



**HAL**  
open science

# Bone regeneration into 3D architected and osteoinductive titanium scaffolds

Antalya Ho-Shui-Ling

► **To cite this version:**

Antalya Ho-Shui-Ling. Bone regeneration into 3D architected and osteoinductive titanium scaffolds. Medical Physics [physics.med-ph]. Université Grenoble Alpes, 2018. English. NNT : 2018GREAI087 . tel-02887097

**HAL Id: tel-02887097**

**<https://theses.hal.science/tel-02887097v1>**

Submitted on 2 Jul 2020

**HAL** is a multi-disciplinary open access archive for the deposit and dissemination of scientific research documents, whether they are published or not. The documents may come from teaching and research institutions in France or abroad, or from public or private research centers.

L'archive ouverte pluridisciplinaire **HAL**, est destinée au dépôt et à la diffusion de documents scientifiques de niveau recherche, publiés ou non, émanant des établissements d'enseignement et de recherche français ou étrangers, des laboratoires publics ou privés.

## THÈSE

Pour obtenir le grade de

### **DOCTEUR DE LA COMMUNAUTE UNIVERSITE GRENOBLE ALPES**

Spécialité : **2MGE : Matériaux, Mécanique, Génie civil,  
Electrochimie**

Arrêté ministériel : 25 mai 2016

Présentée par

**Antalya HO-SHUI-LING**

Thèse dirigée par **Catherine PICART** et codirigée par **Rémy  
DENDIEVEL**

préparée au sein du **Laboratoire des Matériaux et du Génie  
Physique**  
dans l'**École Doctorale I-MEP2 - Ingénierie - Matériaux,  
Mécanique, Environnement, Energétique, Procédés,  
Production**

## **Etude 2D et 3D de la régénération osseuse à la surface et au sein de biomatériaux architecturés et ostéo-inductifs**

Thèse soutenue publiquement le **5 décembre 2018**  
devant le jury composé de :

**Madame Karine ANSELME**

Directeur de Recherche,  
CNRS, Mulhouse

Présidente du Jury  
Rapporteur

**Monsieur Jérôme CHEVALIER**

Professeur des Universités, INSA Lyon

Rapporteur

**Madame Amaïa CIPITRIA**

Group Leader, MPIKG, Allemagne

Examineur

**Monsieur Nicolas COURTOIS**

Responsable R&T, Anthogyr, Sallanches

Examineur

**Madame Liesbet GERIS**

Professor, University of Liège, Belgique

Examineur

**Madame Catherine PICART**

Professeur des Universités,  
Institut Polytechnique, Grenoble

Directrice de thèse

**Monsieur Remy DENDIEVEL**

Professeur des Universités,  
Institut Polytechnique, Grenoble

Co-directeur de thèse



# **Bone regeneration into 3D architected and osteoinductive titanium scaffolds**

## Acknowledgments

I still remember clearly the first time that I had an interview with Pr Catherine Picart for my second year engineering school internship. Thanks to one friend at the engineering school, that was previously a student of Catherine, I was introduced to the biomaterial field and the possibility to do research in China. Even if I was studying only material science at that time, I am still glad that you selected me for this training. Through it, I discovered the research work in a nice laboratory, with not so much fancy equipment, but with the mutual aid, the sharing of knowledge and passion for science. The discovery of research, but also the discovery of China because yes, Ho-Shui-Ling is indeed Chinese, my name coming from my mother side great grandfather. I would like to thank you Catherine for this introduction to this field, to research and for those 3 years of supervision, even though at that time, I didn't know I would do a PhD with you.

After another research experience, in both in a company and a laboratory, many doubts and questions about doing a PhD. I'm able to do it? Do I really like research? What should I do with my professional life? I was not interested in making personal profits, I wanted to contribute to something more meaningful for "us" at the huge scale, except that it would be at my small individual scale and with my modest abilities. At this huge moment of doubts, one friend/mentor/colleague at my 3SR lab time, who had already his PhD simply told me: do you like what you are doing now? I said: yes really, but I'm not sure if I'm clever enough. Then he said: it's okay to make mistakes. Just try, otherwise you will regret it. That's how I decided to find a PhD project.

Things went fast and not so linearly but I finally got this PhD project, with Catherine and Pr Remy Dendievel, which I already knew as a professor since I was one of his students for 2 years. I'm really glad, thankful and happy that you selected me too Remy, that I was able to learn from you as an engineer student and then as a PhD student, to finally teach you back some few things about cellular biology! It's worth investing into students, right?! I'm joking of course. Discovering, learning every day and sharing knowledge with you were the best during those 3 years.

Even if a PhD project is personal and defended by only one person, it's the result of a collective work, depending a lot on its own abilities but also on many external factors, the same as running our own life in fact. For me, more than a scientific project, this PhD was a great life lesson, with many bad moments, making me rediscovering life, myself and what is important for me in the future. But, with also very great moments with amazing people. So now, I would like to thank everyone in a nutshell: Mirasbek, Klaasjan and Leïla for unconditional support. Vincent and Anne for the scientific and funny moments. Michèle and Daniel that were like my parents, except that you were at the LMGP. Dorina, João and Raquel, my Grenoble family. Paul for his great mood, positive attitude and technical help during the last two years of this project. Jie for fruitful scientific discussions and heartless comments that I liked so much.



Marianne for spiritual support, Franz for attentiveness, even if you are buried under the work that it represents to run a laboratory.

I wanted this acknowledgments section to fit only one page, but since I will only do it once in my life, I can write more no? I'm sure dear reader that you agree to it... If not, then you can just stop reading now, sorry and thank you for reading so far...

So where was I? Ah yes, acknowledgments. So I would also like to thank my French Guianese friends, from secondary school and high-school that supported me from far, but still in the same continent and the same country, in France. Because yes, it's sad but true that we just can't find jobs in our hometown: Julien, Raphaël, Kévin, Hector, Benoît, Vaïmiti and Yvanna. Making me remember that we should stick to the basics when you lost all your landmarks and when your family is not near you.

And finally, in French for my family: merci Maman, Eurydice, Lenny, à mes neveux de 2 ans et 11 mois, Liam et Sully, qui m'ont fait sourire à distance par vidéos, d'être là malgré la distance; à mon grand-père, à toi Tatie véro, pour ta sagesse et ta bienveillance, toi qui me rappelle que j'ai bien eu un père. Merci à toi, mon compagnon favori de mes cafés crèmes en terrasse, que je ne prenais jamais avant, et que maintenant je prendrais jusqu'à la fin de mes jours...

## Abbreviations

### Materials/Chemicals

ABG: Autologous bone graft  
Al<sub>2</sub>O<sub>3</sub>: Alumina  
β-TCP: β-tricalcium phosphate Ca<sub>3</sub>(PO<sub>4</sub>)<sub>2</sub>  
BCA: Bicinchoninic acid  
BCP: Biphasic calcium phosphate  
BGS: Bone graft substitute  
EDC: 1-Ethyl-3-(3-dimethylamino-propyl) carbodiimide  
FITC: Fluorescein isothiocyanate  
HA: Hyaluronic acid or sodium hyaluronate  
HAP: Hydroxyapatite (Ca<sub>10</sub>(PO<sub>4</sub>)<sub>6</sub>(OH)<sub>2</sub>)  
HEPES: 4-(2-Hydroxyethyl)-1-piperazine ethane sulfonic acid  
PBS: Phosphate buffered saline  
PCL: Polycaprolactone  
PDMS: Polydimethylsiloxane  
PE: Polyethylene  
PEEK: Polyetheretherketone  
PEI: Poly(ethylene imine)  
PEM: Polyelectrolyte multilayer films  
PLGA: Poly(lactic-co-glycolic) acid  
PLL: Poly(L-lysine)  
PMMA: Polymethylmethacrylate  
pNP: p-nitrophenol  
pNPP: p-nitrophenylphosphate  
S-NHS: N-hydroxysulfo succinimide  
TCP: Tri-calcium phosphate  
Ti: Titanium  
Ti-6Al-4V: Titanium-aluminium-vanadium alloy containing 6% of Al and 4% of V  
TiN: Titanium nitride  
ZrN: Zirconium nitride  
ZrO<sub>2</sub>: Zirconia

### Techniques and equipment

AM: Additive manufacturing  
CAD: Computed aided design  
CVD: Chemical vapour deposition  
CT: Computed tomography  
DLC: Diamond-like carbon  
EBM: Electron beam melting  
EDM: Electrical discharge machining  
LbL: Layer-by-layer  
PM: Powder metallurgy  
PVD: Physical vapour deposition  
SEM: Scanning electron microscopy  
SLM: Selective laser beam melting

### Proteins and cells

ALP: Alkaline phosphatase  
BMP: Bone morphogenetic protein  
BSA: Bovine serum albumin  
CCL2: Chemokine ligand 2  
DM: Differentiation medium  
ECM: Extracellular matrix  
FGF: Fibroblast growth factors  
GM: Growth medium  
HSC: Haematopoietic stem cells  
IGF-1: Insulin like growth factor 1  
IL-6: Interleukin-6  
IL1β: Interleukin 1 beta  
MMTV: Mouse mammary tumour virus  
MP: Mesenchymal progenitor  
MSC: Mesenchymal stem cells  
PDSC: Periosteum-derived cells  
PDGF: Platelet-derived growth factor  
PTH: Parathyroid hormone  
SDF-1α: Stromal derived factor-1α  
TGF-β: Transforming growth factor-beta  
TNF-α: Tumour necrosis factor alpha  
VEGF: Vascular endothelial growth factor  
Wnt: Wingless/Integrated protein

## Glossary

**Architected:** product of an ingenious combination of two or more materials or, a combination of materials and space arranged in a way to obtain properties not attainable by any material on its own

**Growth factor:** natural molecule that regulates the growth and development of an organism. They are secreted by the cells and bind to transmembrane growth factor receptors to stimulate cell signalling cascades that promote proliferation, apoptosis and differentiation

**Osteoconduction:** term used for any material triggering the bone growth at its surface, supporting bone growth and encouraging the ingrowth of surrounding bone. This is generally achieved with materials of similar composition to bone tissue

**Osteoinduction:** term used for any material triggering osteogenesis, with the cells recruitment and differentiation into bone progenitor cells, leading eventually to bone tissue formation. This is generally achieved with the addition of a bioactive molecule

**Osseointegration:** stable anchorage of an implant achieved by new bone formation resulting in a direct bone-to-implant contact

**Scaffold:** 3D structure made of stacking or meshes of any material used as support

## Table of contents

Acknowledgments .....	2
Abbreviations .....	4
Glossary .....	5
Table of contents.....	6
Chapter 1. Introduction.....	10
1.1 Bone tissue .....	10
1.1.1 Multiscale bone structure .....	10
1.1.2 Mechanism of bone repair (from Biomaterial review <sup>21</sup> ) .....	26
1.1.3 Current strategies to repair bone (adapted from Biomaterial review <sup>21</sup> ).....	30
1.2 Biomaterials for bone graft substitutes.....	32
1.2.1 Ceramics .....	32
1.2.2 Polymers.....	33
1.2.3 Metals.....	35
1.2.4 Titanium alloys for bone graft substitutes .....	37
1.2.5 Manufacturing processes of titanium bone graft substitutes .....	38
1.3 Structural optimization of bone graft substitutes.....	43
1.4 Bioactive molecules used in bone graft substitutes.....	58
1.4.1 BMP-2 (adapted from Biomaterials review <sup>21</sup> ).....	58
1.4.2 BMP-7 (adapted from Biomaterials review <sup>21</sup> ).....	60
1.4.3 PDGF (from Biomaterials review <sup>21</sup> ) .....	62
1.4.4 Parathyroid hormone PTH (from Biomaterials review <sup>21</sup> ) .....	63
1.4.5 Bioactive molecules in AM-built titanium bone graft substitutes .....	64
1.4.6 Bioactive molecules on bone graft substitutes in the team .....	67
1.5 Remaining challenges for clinical translation of bone graft substitutes (from Biomaterials review <sup>21</sup> ).....	74
1.5.1 Important steps in clinical translation .....	74
1.5.2 Optimization of the bone graft substitute mechanical properties .....	76
1.5.3 Better understanding the biological mechanisms .....	76
1.5.4 Controlling the dose and delivery of bioactive molecules.....	76
1.5.5 Modulating the material/bioactivity couple .....	76
1.6 PhD Objectives.....	77
Chapter 2. Materials and methods .....	80

2.1	Building and characterization of Ti-6Al-4V architected scaffolds.....	80
2.1.1	Ti-6Al-4V alloy .....	80
2.1.2	Scaffolds building by electron beam melting (EBM).....	81
2.1.3	Dimensional characterization .....	85
2.1.4	Mechanical characterization by uniaxial compression test.....	87
2.2	Deposition of the polyelectrolyte multilayer (PEM) film .....	88
2.2.1	PEM film deposition methods.....	88
2.2.2	Loading of BMP-7 into PEM film .....	92
2.3	Characterization of the film deposition and the BMP-7 loading.....	92
2.3.1	Film labelling with Rhodamine and FITC.....	92
2.3.2	BMP-7 labelling with NHS-fluorescein .....	93
2.3.3	Spectrophotometry.....	94
2.3.4	BMP-7 quantification with BCA assay .....	95
2.3.5	Fluorescence macroscopy and microscopy.....	95
2.3.6	Scanning electron microscopy .....	98
2.4	Cell culture and biological investigations .....	100
2.4.1	D1 cell culture.....	101
2.4.2	Cell quantification with DNA-based cell proliferation assay.....	103
2.4.3	Qualitative cell colonization evaluation with epifluorescence microscopy.....	104
2.4.4	Cell morphology with scanning electron microscopy .....	104
2.4.5	Evaluation of BMP-7 osteoinductivity with ALP expression .....	105
2.4.6	Evaluation of the mineralization of the D1 cells extracellular matrix.....	109
2.4.7	Statistical analysis.....	111
Chapter 3.	Results: Osteoinductive coating on architected Ti-6Al-4V implants for bone regeneration (research article in preparation) .....	113
3.1	Preamble.....	113
3.2	Abstract.....	113
3.3	Introduction.....	114
3.4	Results.....	115
3.4.1	Architected Ti-6Al-4V scaffolds built by EBM additive manufacturing process	115
3.4.2	2D in vitro osteoinductive capacity of PEM film loaded with BMP-7 .....	118
3.4.3	Extracellular matrix mineralization of D1 cells in response to BMP-7.....	122
3.4.4	3D in vitro osteoinductivity of Ti-6Al-4V scaffolds coated with BMP-7.....	129

3.4.5	3D <i>in vitro</i> extracellular matrix mineralization on bare Ti-6Al-4V scaffolds ....	132
3.4.1	Design strategy for <i>in vivo</i> architected and osteoinductive Ti-6Al-4V implant for a critical size femoral bone defect in rat .....	134
3.5	Discussion .....	137
3.5.1	Better knowledge of the mechanical properties of EBM built cubic unit cell Ti-6Al-4V scaffolds .....	137
3.5.2	BMP-7 incorporation into (PLL/HA) polyelectrolytes films .....	138
3.5.3	(PLL/HA) polyelectrolytes films as BMP-7 carrier for human clinical trials .....	138
3.5.4	BMP-7 bioactivity preserved into (PLL/HA) films for short term cell culture ..	139
3.5.5	Non BMP-7 dependant extracellular matrix mineralization of D1 cells .....	139
3.5.6	Effect of (PLL/HA) films on the topography of EBM built Ti-6Al-4V implants .	139
3.5.7	BMP-7 surface delivery from porous and architected EBM built Ti-6Al-4V implants .....	140
3.5.8	Potential advantages of the combination of our architected and osteoinductive strategies .....	140
3.6	Conclusions .....	141
3.7	Acknowledgements .....	141
Chapter 4.	Conclusions and perspectives .....	142
4.1	Conclusions .....	142
4.1.1	Architected Ti-6Al-4V scaffolds built by EBM additive manufacturing process	142
4.1.2	2D <i>in vitro</i> osteoinductive capacity of PEM film loaded with BMP-7 .....	142
4.1.3	Extracellular matrix mineralization of D1 cells in response to BMP-7 .....	143
4.1.4	3D <i>in vitro</i> osteoinductivity of Ti-6Al-4V scaffolds coated with BMP-7 .....	143
4.2	Perspectives .....	143
4.2.1	Architectural characterization of EBM-built scaffolds .....	143
4.2.2	Assessment of the film osteoinductivity .....	144
	Bibliographic References .....	147
	Curriculum Vitae .....	159
	Abstract .....	161
	Résumé .....	161



# Chapter 1. Introduction

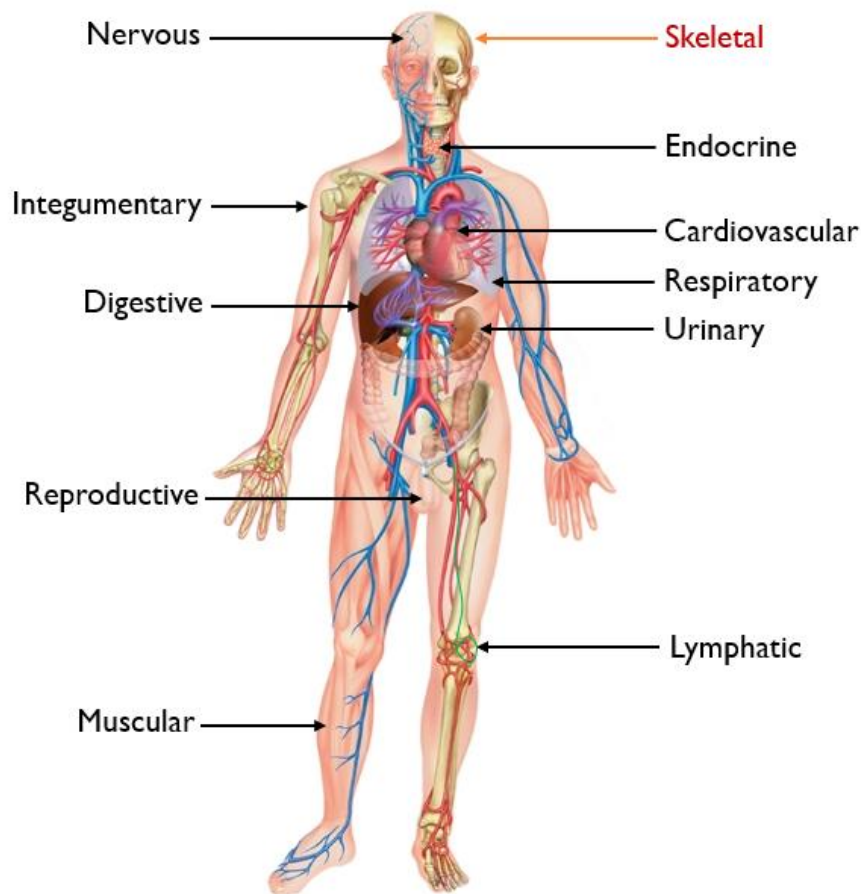
## 1.1 Bone tissue

In the human body, bones have important functions which require them to have specific structures at different scales, and an intricate relationship with other anatomic systems. An overview of their functions, their constituents, their structure, their mechanisms of formation and the existing strategies to repair them will be presented as the first part of this manuscript.

### 1.1.1 Multiscale bone structure





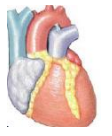





#### 1.1.1.1 Human skeleton: overview and functions

The human skeleton is made of 270 different bones at birth, 206 at the adulthood, and brings to human body the structural support against gravity. In addition to this crucial function, the skeletal system protects soft internal organs, acts as lever for the muscles actions, serves as storage for calcium and fat, and is also implicated in the blood cells production. In fact, the skeletal system is dependent on other anatomic systems, receives biological signals from them and adapts constantly depending on them. The anatomic systems acting on bones are represented in **Figure 1** and their interactions are detailed in **Table 1**.



*Figure 1: Anatomic systems involved in the formation and regulation of bone tissue<sup>1</sup>*



Anatomic system	Effects on bones	Actions of bones
Integumentary 	Synthesize vitamin D3 (calcium absorption promoter)	Structural support
Muscular 	Stabilizes bone position Stimulates bone growth	Calcium for muscle contractions Levers for body movements
Nervous 	Regulates bone position by muscle contractions	Calcium for neural function Brain and spinal cord protection
Endocrine 	Provides hormones: <ul style="list-style-type: none"> <li>– calcitonin (growth hormone)</li> <li>– PTH (parathyroid hormone)</li> <li>– oestrogen (sex hormone)</li> </ul> Regulates bone growth, calcium absorption and mobilisation	Endocrine organs protection
Cardiovascular 	Provides O <sub>2</sub> , nutrients, hormones and blood cells Removes waste products and CO <sub>2</sub>	Calcium for cardiac muscle contractions Blood cells produced and stored in bone marrow
Lymphatic 	Lymphocytes assist in the defence and repair of bone injuries	Cells of the immune response produced and stored in bone marrow
Respiratory 	Provides O <sub>2</sub> and eliminates CO <sub>2</sub>	Ribs movements for breathing Lungs protection
Digestive 	Provides nutrients, calcium and phosphate	Portions of liver, stomach, and intestines protection
Urinary 	Conserves calcium and phosphate Disposes of waste products	Kidneys, ureters, urinary bladder and proximal urethra protection
Reproductive 	Provides sex hormones Stimulates bone growth and maintenance	Reproductive organs protection

*Table 1: Effects and action of bone on the different anatomic systems<sup>2</sup>*

Bones are hard and highly mineralized living tissues composed at 75% of an inorganic phase mainly containing hydroxyapatite (HAP) mineral crystals ( $\text{Ca}_{10}(\text{PO}_4)_6(\text{OH})_2$ ). Those crystals constituting bones store 99% of the calcium of the human body. Calcium ion is a necessary element for important basic biological functions such as transmission of nerve impulses, muscle contractions, blood coagulation and cell division.

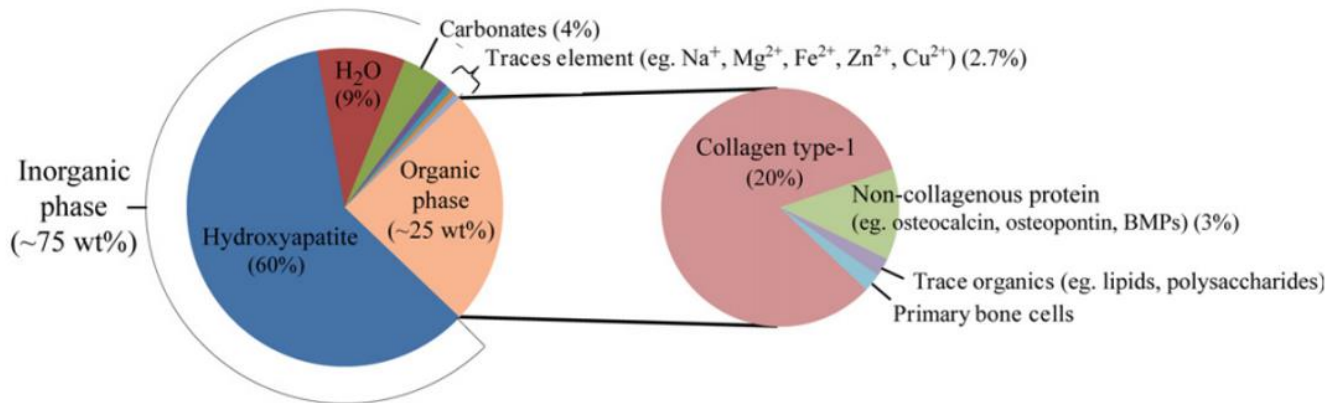


**Figure 2: Composition of human bones.** Bones are composed of two main phases: an organic phase of 25wt% and an inorganic phase at 75wt%. The inorganic phase is mainly composed of hydroxyapatite (HAP) crystals<sup>3</sup>

The remaining 30% part of the bone is the organic phase composed of several proteins, such as type I collagen, osteopontin, osteocalcin, bone morphogenetic proteins (BMPs), and bone cells (osteoblasts, osteoclasts and osteocytes). All those components are highly entangled and organised at the macro, micro and nano scales, as represented in **Figure 3**.

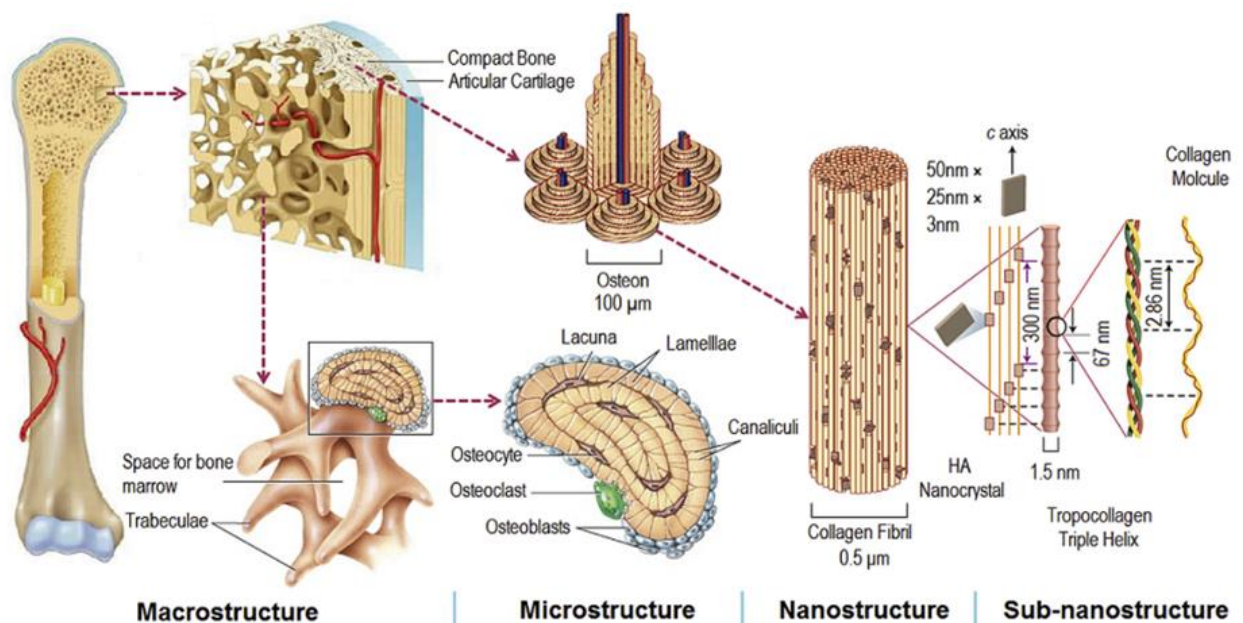


**Figure 3: Multiscale structural organization of bones.** At the macroscale, bones have cortical (dense) and trabecular (porous) areas. At the microscale, bone cells are tightly organized in osteons which are crossed by blood vessels and nerves. At the nanoscale and sub-nanoscale, hydroxyapatite crystals are distributed into collagen fibrils<sup>4</sup>

At the macroscale, bone displays two types of architecture:

- a dense and compact part often located on their outer parts, called the **cortical bone**
- a porous and spongy part often located inside, called the **trabecular bone**

At the tips and inside bones, an important component is stored: the bone marrows. Bones contain two types of bone marrow, the yellow marrow which is composed of fat (adipose tissue) and the red marrow composed of mesenchymal stem cells (MSCs) and blood cells. The yellow marrow is mostly located inside long bones and is used as a source of energy. Whereas the red bone marrow, mostly located in trabeculae spaces of bones, is the place where red blood cells, white blood cells and platelets are produced (haematopoiesis). As a consequence, bones have a close interaction with the vascular system and are full of blood vessels but also nerves. Blood vessels supply to bones O<sub>2</sub>, nutrients, hormones and cells while bones and bone marrows produce and store blood cells, and supply calcium ions through blood vessels for other organs.

#### 1.1.1.2 Cellular environment

In any biological environment, cells are inside a 3D environment commonly called the **extracellular matrix (ECM, Figure 4)**. In their ECM, cells are subjected to several chemical and mechanical factors that dictate their replication, differentiation (specialisation), migration or apoptosis (death). The ECM is the principal extracellular component of all tissues and organs, and provides a physical support to the cells. At the molecular scale, its principal components are collagens, elastins, proteoglycans (chondroitin and heparan sulfates, hyaluronic acid ...), fibronectin, vitronectin and laminin<sup>5</sup>. Those molecules contain cellular binding sites and also small amino acids chains (cryptic peptides, **Figure 4**) storing information for cells.

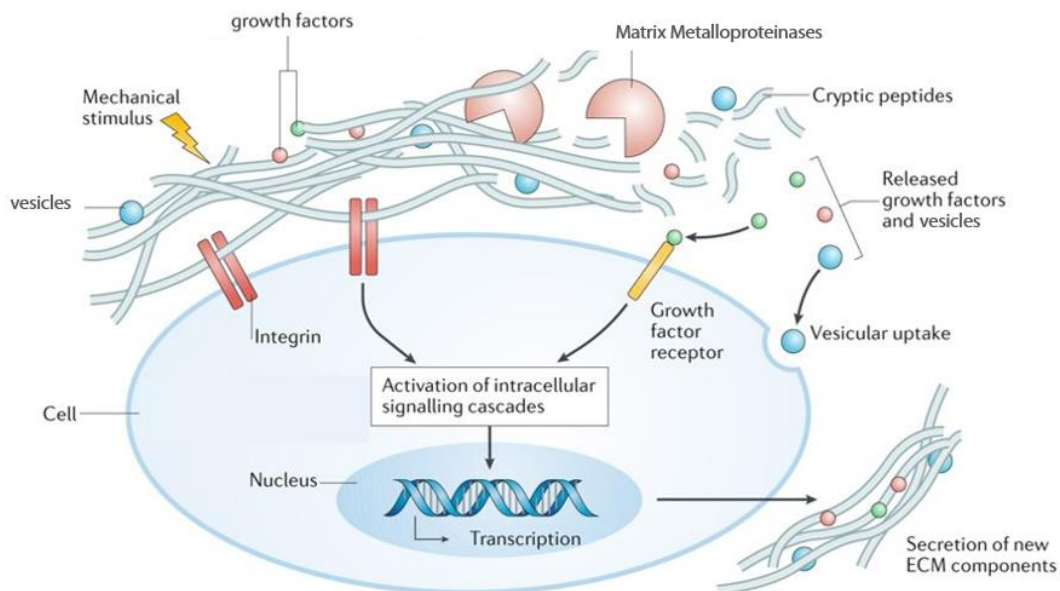


**Figure 4: Schematic representation of a cell surrounded by the extracellular matrix.** The extracellular matrix (ECM) provides to cells physical support, mechanical and biological signals (cryptic peptides, vesicles and growth factors) to dictate their behaviour. The ECM is constantly remodelled by matrix metalloproteinases and new ECM secretion from cells. Mechanical stimulus are transmitted to cells via integrins while biological signals are sensed via either endocytosis (vesicular uptake) or growth factor receptors at the cellular membrane (adapted from<sup>6</sup>)

In addition to its structural role, the ECM is able to store external bioactive products (**growth factors** or vesicles, **Figure 4**), deliver mechanical information (compression, tension, fluid shear stress and hydrostatic pressure) and control their presentations to the cells<sup>5</sup>. The ECM organization is dynamic, evolving and remodelled through a balance between the secretion of new ECM components by the cells and its degradation by matrix metalloproteinases and enzymes (such as lysyl oxidase, collagen/elastin cross linker)<sup>5</sup>. This reorganization releases bioactive products, which are then presented to cells (growth factor receptor, **Figure 4**) and changes the ECM mechanical properties. The physical and chemical signals are translated to the cells nuclei via intracellular signalling reactions (signalling pathways, **Figure 5**). These signalling cascades activate gene transcription and synthesis, which induce secretion of new ECM components and new cellular behaviours<sup>6</sup>.

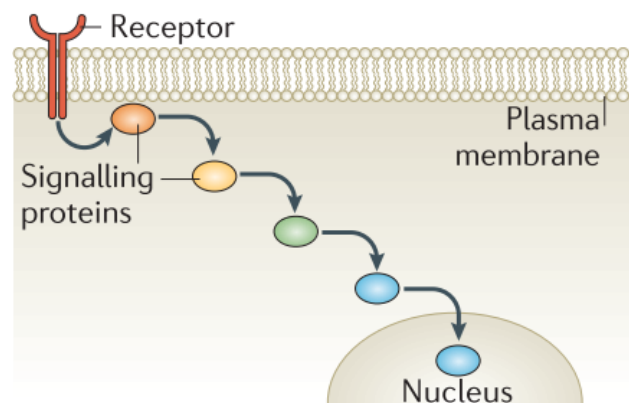


*Figure 5: Schematic representation of a signalling pathway induced by an activated cell receptor at the cellular plasma membrane<sup>5</sup>*

In order to sense those physical and chemical signals, cells possess surface receptors located in their membranes which interacts with external (ECM) and internal (cytoplasm) molecules. Among all cell surface receptors, **integrins** are considered as the cellular mechano-sensor. They are responsible of the cellular binding to the ECM via focal adhesion sites (focal adhesion, **Figure 6**) and are composed of two sub-units  $\alpha$  and  $\beta$ . **Cadherins** are responsible of adherens junctions between cells and participate to the intracellular communication (adherens junctions, **Figure 6**). And finally, growth factor receptors (tyrosine kinases receptors) are activated by specific growth factors and activate associated signalling pathways (growth factor receptor, **Figure 4**)<sup>7</sup>.



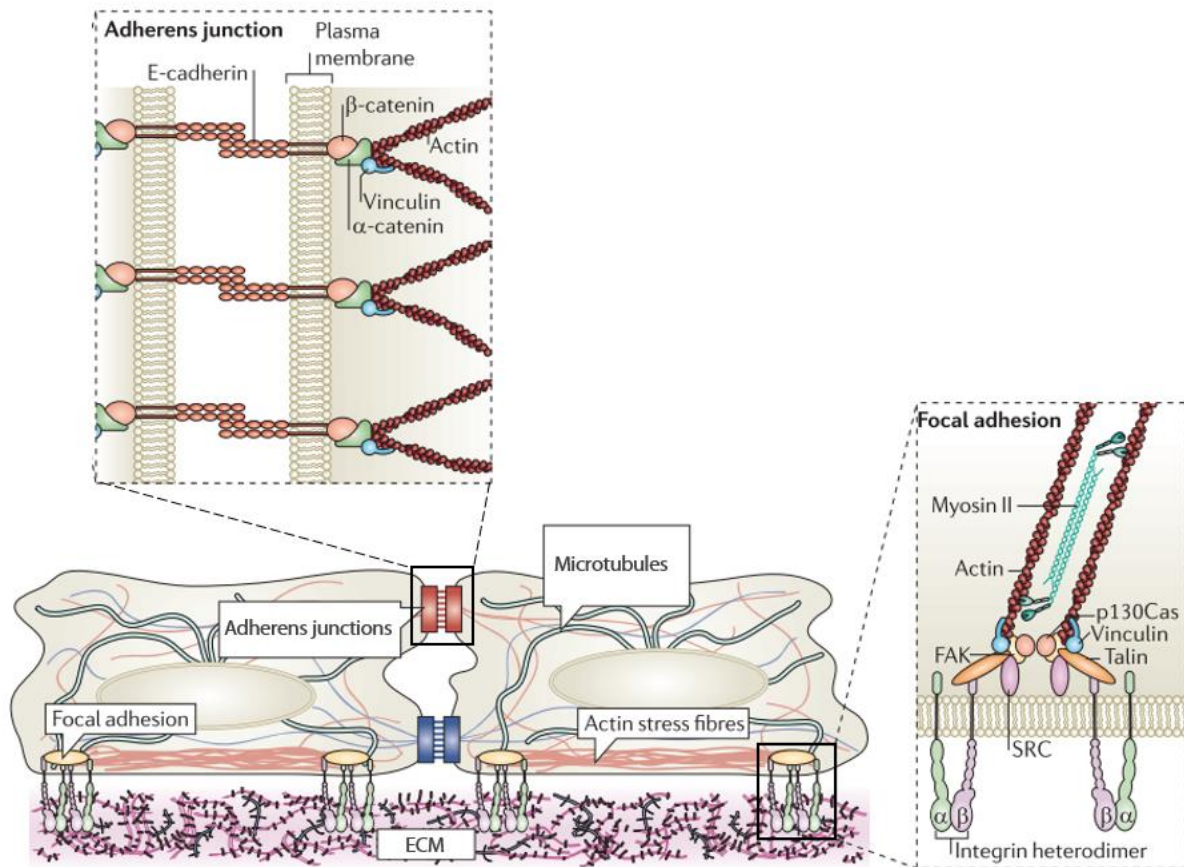


**Figure 6: Schematic representation of the cellular interactions with the ECM and neighbouring cells.** Cells are bound to their ECM via focal adhesion sites comprised of integrins proteins complexes ( $\alpha$ ,  $\beta$ , SRC, FAK, talin, vinculin and p130Cas). Cells are adhering to each other via adherens junction sites comprised of cadherins proteins complexes (E-cadherin,  $\beta$ -catenin,  $\alpha$ -catenin and vinculin, adapted from<sup>5</sup>)

Integrins and cadherins proteins complexes are respectively located at focal adhesion and adherens junction sites. Both proteins complexes are bound to actin filaments via SRC (proto-oncogene tyrosine-protein kinase), FAK (focal adhesion kinase), talin, vinculin and p130Cas proteins in the case of integrins, and via  $\beta$ -catenin,  $\alpha$ -catenin and vinculin in the case of cadherins (**Figure 6**). Actin is one of the main component of the cellular skeleton, the cytoskeleton, and forms a network of filaments with microtubules and others intermediates filaments. The cytoskeleton with motors molecules, such as myosin II (focal adhesion, **Figure 6**), is responsible for the cell structure, motility and contractility<sup>5</sup>. Through integrins complexes, the cytoskeleton is mechanically linked to the ECM and acts as a sensor of external physical forces.

#### 1.1.1.3 Signal transduction

Signal transduction is the molecular mechanism to transmit the information given by any external signals (chemical or physical) to induce cellular responses. This mechanism often consists in a series of protein phosphorylation (addition of phosphate groups on the protein side chain) which induces a cascade of molecular reactions that ultimately changes gene transcription, protein conformation and location. A specific series of molecular events linked

to one signal is called a signalling pathway (signal transduction pathway) and several pathways can induce a unique cellular effect.

In the case of BMPs, the growth factor receptor is the combination of two types of receptors. The type I receptor is either ALK1, 2, 3 or 6 proteins depending on the BMP, while the type II receptor (BMPRII, **Figure 7**) is common to all BMPs<sup>8</sup>. The canonical BMPs signalling pathway is shown in **Figure 7**.

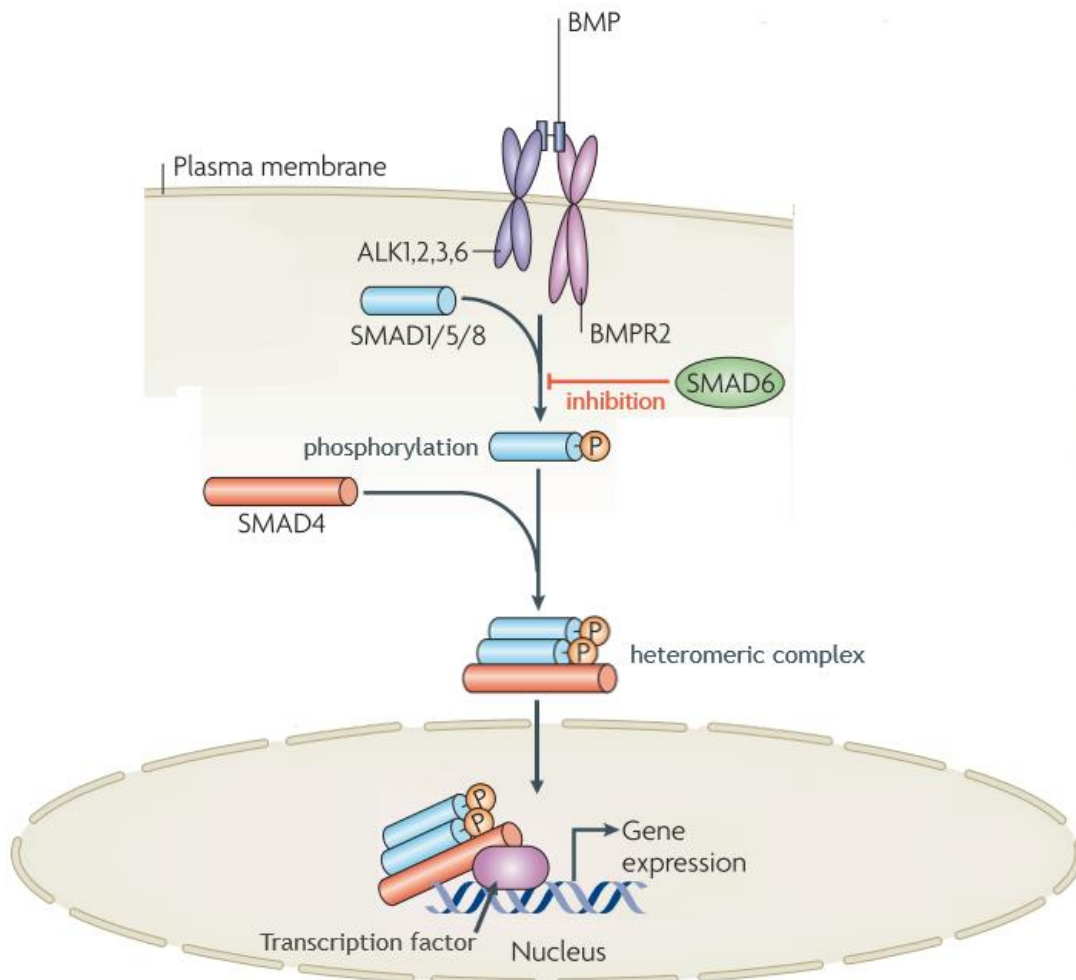


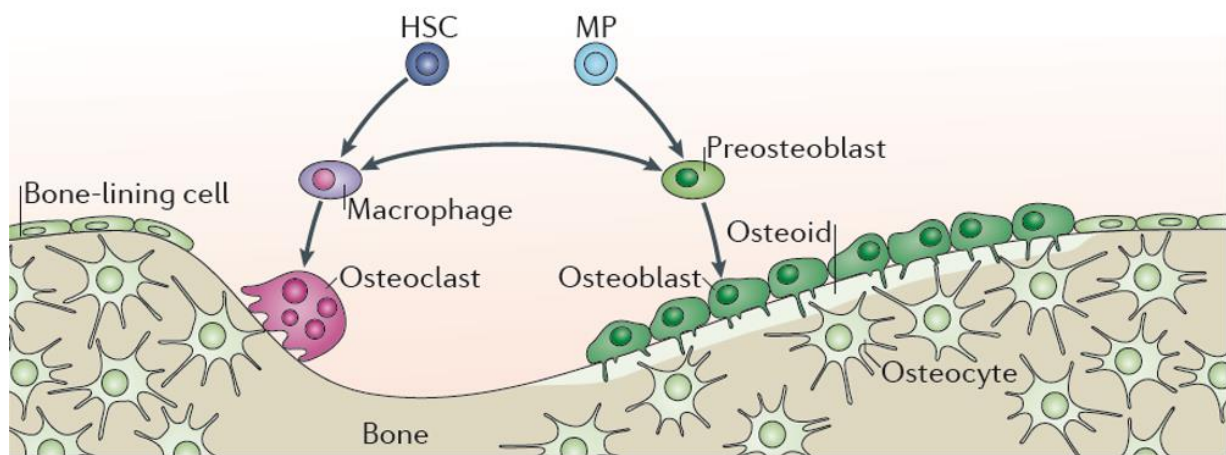
**Figure 7: Example of the canonical signal transduction of BMPs family members.** When BMP binds to a type of BMPs receptors, the second one is recruited. The type I receptor is phosphorylated and activated to phosphorylate Smad1/5/8. Phosphorylated Smads are associated to Smad4 to form a heteromeric complex translocated into the cell nucleus. In the nucleus, the complex associates with a transcription factor (coactivators or corepressors) to regulate gene expression (adapted from<sup>8</sup>)

Once a BMP binds to a type of BMPs receptors, the second one is recruited. Upon the complex formation, the type I receptor is phosphorylated and activated to phosphorylate in turn receptor regulated proteins Smads. The Smads involved in the canonical BMPs signalling pathways are Smad1, 5 and 8. They are phosphorylated and associated to the common mediator Smad4 to form a heteromeric complex that will be translocated into the cell nucleus. Other smads, such as Smad6, have an inhibitory role in the signalling pathway. Once in the nucleus, the complex associates with transcription factor (coactivators or corepressors) to regulate gene expression (**Figure 7**)<sup>8,9</sup>.

The interaction of BMPs with their growth factors receptors is considered as a chemical signalling. Signalling pathways induced by physical signals such as compressive, tensile, fluid shear stresses and hydrostatic pressure are defined as mechanotransduced signals. The mechanotransduction relates to how mechanical signals are sensed and interpreted by cells through signalling pathways<sup>5</sup>. Integrins are the first receptors to sense them and also, it was found that crosstalks between integrins and growth factors receptors can also mediate some signalling pathways<sup>10</sup>.

#### 1.1.1.4 Cellular bone organization

At the microscale, bone tissue is organized in lamellae of mineralized matrix containing canaliculi to allow bones cells to communicate, have access to O<sub>2</sub>, nutrients and evacuate waste products and CO<sub>2</sub> through blood vessels. There are 4 types of cells contained in bones: **osteoblasts**, **bone-lining cells** (periosteum cells), **osteocytes** and **osteoclasts** (**Figure 8**). Each of them have a different role in bone tissue growth, maintenance and evolution.



Cell type	Function
Osteoblasts	Secrete osteoid, the organic bone matrix mainly composed of type I collagen
Bone-lining cells	Inactive non-remodelling form of osteoblasts, found in the periosteum
Osteocytes	Previously osteoblasts, mechanical and hormonal sensors to regulate bone deposition/resorption
Osteoclasts	Resorb bone matrix

**Figure 8: Different types of bone cells and their functions.** Osteoblasts are derived from mesenchymal progenitors (MPs) while osteoclasts are derived from macrophages differentiated from haematopoietic stem cells (HSCs). Osteoblasts and osteoclasts mutually control their production and functions<sup>11</sup>

The matrix secreted by osteoblasts named osteoid, is crucial for the mineralization of bone tissues. Osteoid is mainly composed of type I collagen, proteoglycans and specific bone extracellular matrix proteins (osteopontin, osteocalcin, bone sialoprotein...). The mineralization of this matrix occurs through the nucleation and growth of hydroxyapatite crystals. The crystals formation is induced by the local release of phosphate ions due to an enzymatic action from phosphatases, (such as alkaline phosphatase) present in osteoblast-

generated vesicles, and calcium ions available in the extracellular fluids<sup>12</sup>. The actual shape and structure of those hydroxyapatite crystals is illustrated in **Figure 9**.

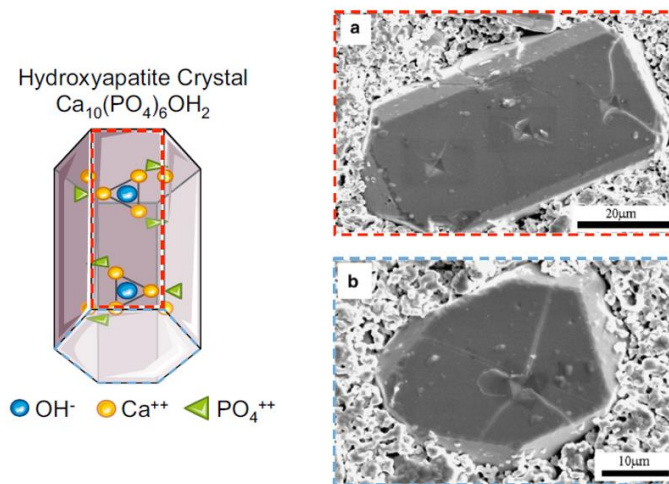


**Figure 9: Chemical formula, structure and shape of hydroxyapatite crystals.** The left scheme represents the spatial distribution of a hydroxyapatite element and its global crystalline structure. Scanning electron microscopy images at the right represent the lateral (a, red) and cross section (b, blue) views of a hydroxyapatite crystal (adapted by Bala from<sup>13</sup>)

Scaling down to the nanoscale, hydroxyapatite crystals are distributed into collagen fibrils which form collagen fibres (**Figure 10**). Mineral crystals in fibrils are bound to osteocalcin proteins which are themselves bound to osteopontin proteins. Those osteocalcin-osteopontin-osteocalcin complexes unfold and elongate when the fibre is under tension and thus protect hydroxyapatite crystals<sup>14</sup>.

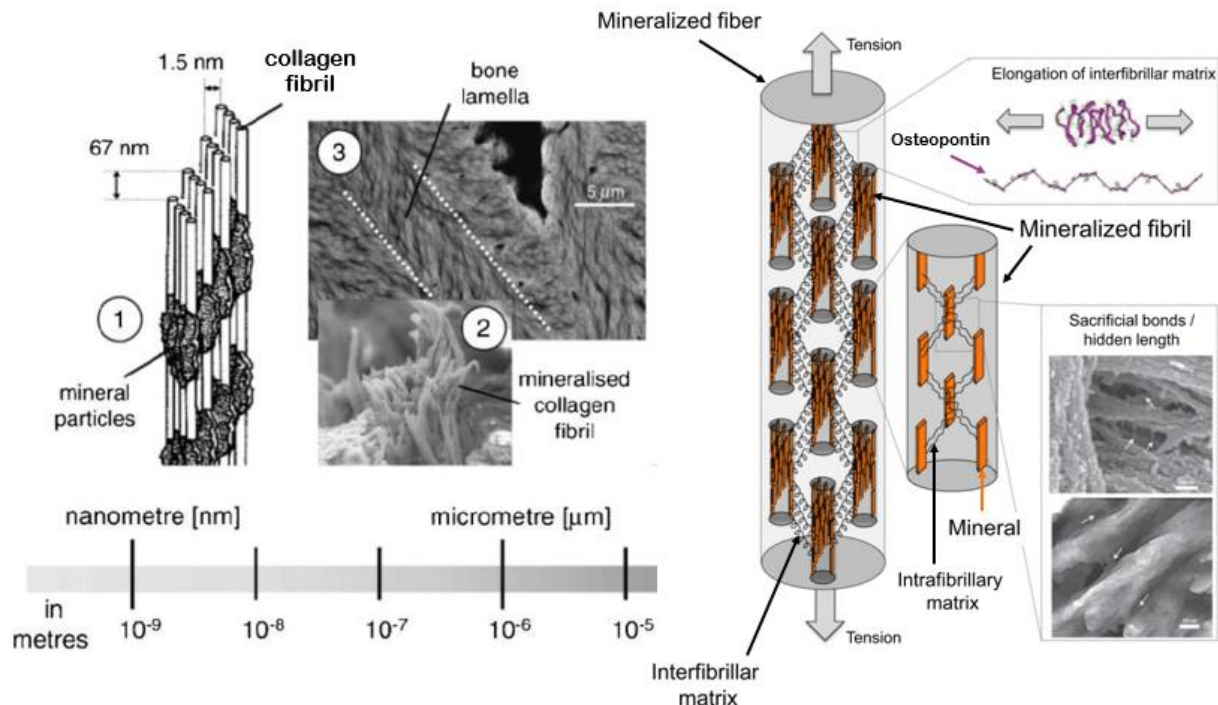


**Figure 10: Structural organization of hydroxyapatite crystals into the collagenous matrix.** From left to right: hydroxyapatite crystals are distributed into collagen fibrils (1) which form bone lamella as seen on scanning electron microscopy images (2,3). Hydroxyapatite minerals are linked between themselves into fibrils with interfibrillar matrix composed of osteopontin-osteocalcin complexes (adapted from<sup>14,15</sup>)



This structural organization of minerals and organic matrix confers to bones enough strength and stiffness to sustain the body, while maintaining some lightness and flexibility. Those contradictories properties are achievable by the appropriate combination and spatial arrangement of organic and inorganic matter depending on the hormonal and mechanical signals received by bone tissues.

#### 1.1.1.5 Bone formation

In human development, bone formation starts at the fifth week of the embryonic life period. Embryonic mesenchymal stem cells (MSC) constituting the mesoderm in the foetus are at the origin of the first bone tissues via two different bone formation mechanisms: the **intramembranous ossification** and **endochondral ossification**.

In **intramembranous ossification**, MSCs located in the collagenous and fibrous matrix directly differentiate into osteoblast cells. The osteoblasts condense and secrete an organic matrix, the osteoid, mainly composed of type I collagen (**Figure 11a**). The secreted matrix mineralizes and gives birth to entrapped osteocytes, former osteoblasts, which are stored in the bone matrix (**Figure 11b**). After several sites of mineralization, the bone tissue forms a network called the trabeculae (**Figure 11c**). Near blood vessels, the remaining non-mineralized matrix condenses blood vessels and creates red bone marrow. And finally, external MSCs and fibroblast cells surround the newly formed bone tissue and form the periosteum (**Figure 11d**). This first mechanism of bone formation is at the origin of the clavicle formation. Between the ninth and twelfth week of the foetal life, the clavicle continues to grow by endochondral ossification<sup>16,17</sup>.

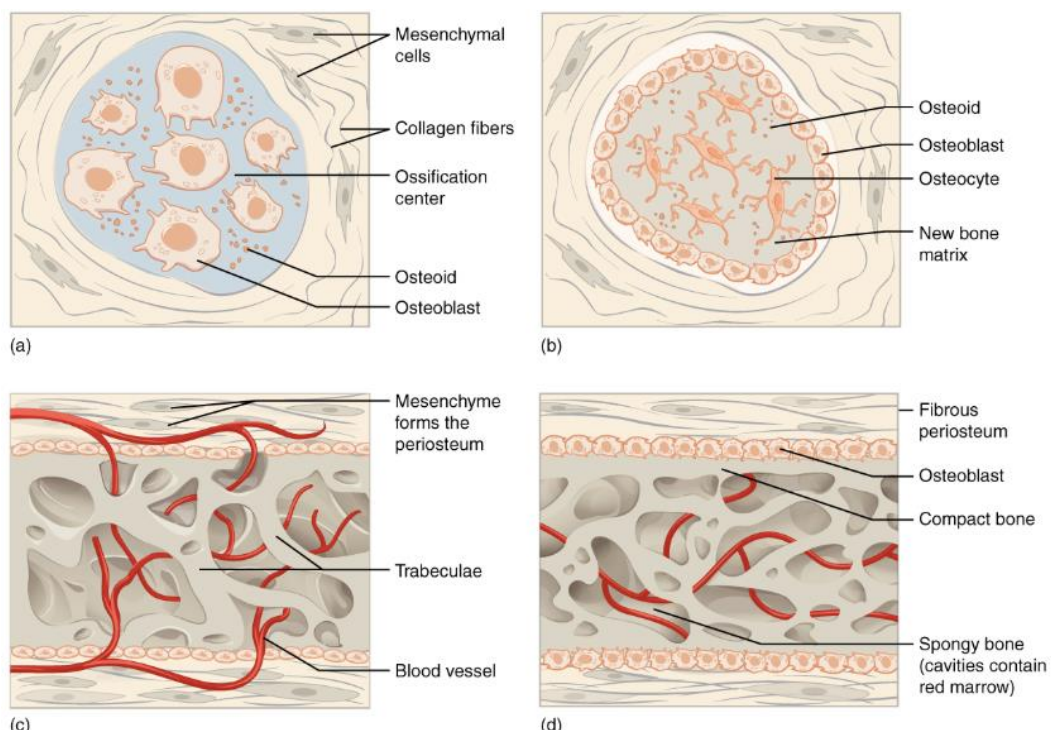


**Figure 11: Stages of the intramembranous ossification.** Mesenchymal stem cells differentiate into osteoblasts. Those osteoblasts condense and secrete osteoid to form an ossification center (a). Entrapped osteoblasts become osteocytes and the osteoid mineralizes (b). Several mineralization sites give rise to the trabeculae bone tissue network (c). Entrapped blood vessels condense and form the spongy bone marrow (d)<sup>18</sup>

In **endochondral ossification**, which is the mechanism at the origin of axial vertebrae and limb bones, MSCs condense in compact nodules and differentiate into cartilaginous cells called chondrocytes. Chondrocytes produce the hyaline cartilage matrix composed of type II collagen and chondroitin sulphate (**Figure 12a**). Among those chondrocytes, some are hypertrophied during this matrix production process. Those hypertrophied chondrocytes are at the origin of the calcified matrix (**Figure 12b**) which will be later the primary ossification center (**Figure 12c**). In this ossification center, late stages of the intramembranous ossification occur. More specifically, an artery invades the ossification center and brings osteogenic cells that will become osteoblasts and form the spongy bone. With the ongoing mineralization, internal nutrients can no longer reach the surrounding chondrocytes and induces the cartilage disintegration. A denser bone is formed inside, more blood vessels invade the resulting spaces, enlarge the cavities which will then form the medullary cavity (**Figure 12d**). Then, a second ossification center forms at the newly formed bone heads (**Figure 12e**). Finally trabeculae are formed into the bone heads, former hyaline cartilage remains in the epiphyseal plate and articular cartilage is formed at the bone head external parts (**Figure 12f**).

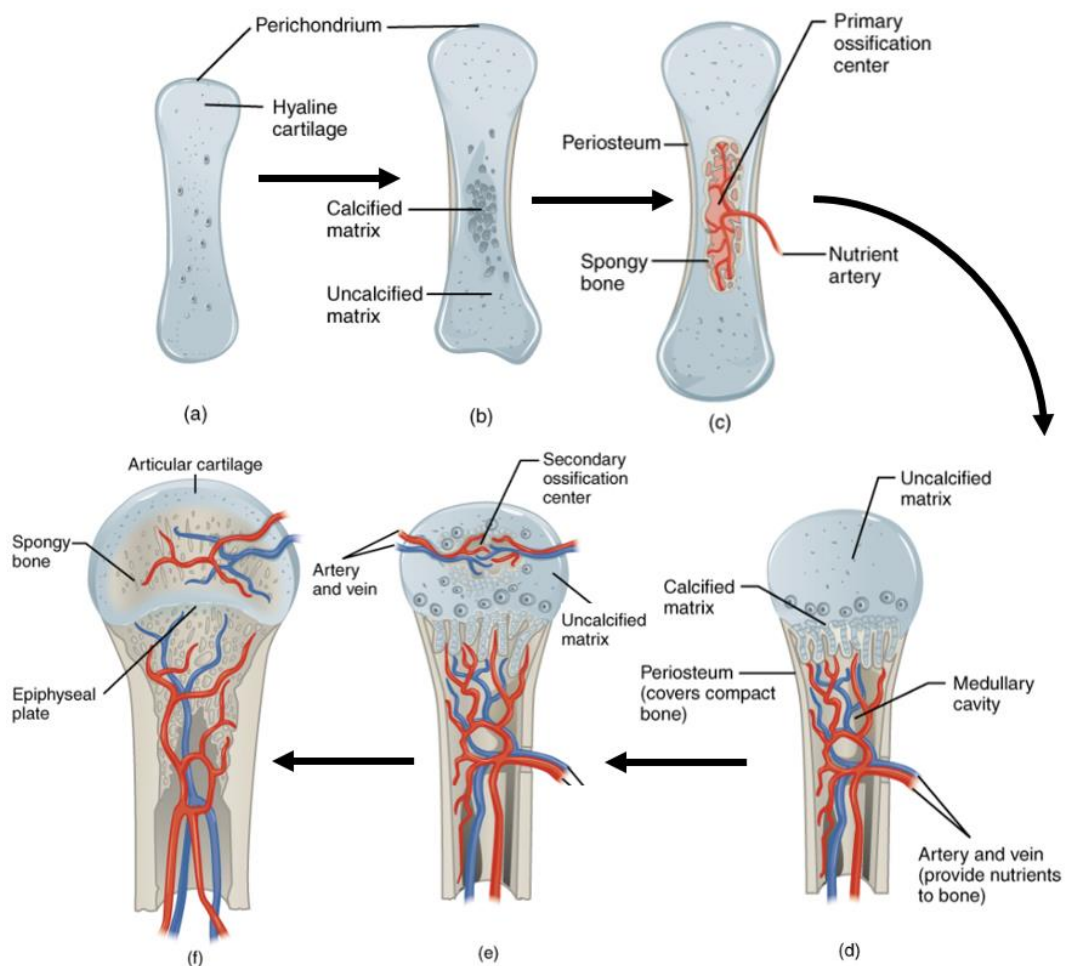


**Figure 12: Different stages of endochondral ossification.** Chondrocytes differentiated from mesenchymal stem cells aggregate and produce the hyaline cartilage (a). Hypertrophied chondrocytes generate the calcified matrix at the center of the cartilage (b) which then become the primary ossification center (c). The center evolves into a medullary cavity (d) and a second ossification center forms in the bone heads (e). Spongy bone is formed at this location and articular cartilage forms at the bone head external parts (f)<sup>18</sup>

This second mechanism of bone formation begins at the sixth week of the embryonic life. Limb buds in the embryo are formed from MSC condensation and are then constituted of chondrocytes and hyaline cartilage. At the seventh week, the primary ossification center forms and limbs rotate. At the eighth week, further vascularisation of the limbs starts. At birth, all bones are formed but not completely ossified, their growth continues until the 25 years-old and they evolve during all our life time.

#### 1.1.1.6 Bone growth

Bone growth in length starts at the epiphyseal plate (**Figure 12f**), **Figure 13** top part displays a zoomed view of this plate. In reserve zone, chondrocytes produce a cartilaginous matrix which induce the storage of some of them. Then in the proliferative zone, stacks of chondrocytes are formed by cellular division (mitosis). Older chondrocytes, located in the maturation zone, accumulate and the surrounding matrix mineralizes and causes their hypertrophy. In the end, the calcified cartilaginous matrix induces their death and the left space is invaded by capillaries and osteoblasts from the medullary cavity (bottom part, **Figure 13**) for further mineralization. Osteoblasts generate new bone tissue on the ossification zone which leads to the global bone growth.

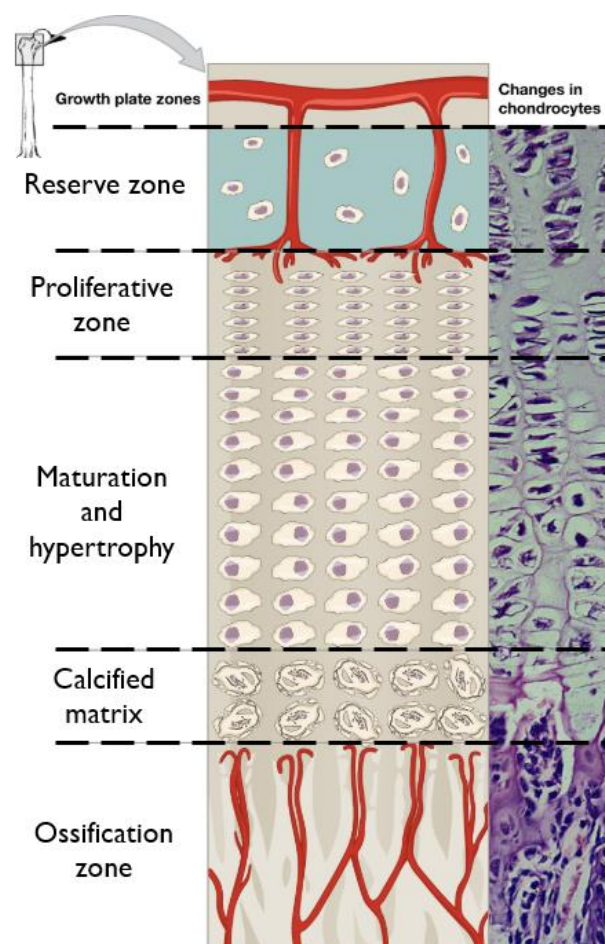


**Figure 13: Epiphyseal long bone growth.** The growth starts at the epiphyseal plate and remaining chondrocytes produce cartilaginous matrix to form a reserve zone. At this zone extremity, they proliferate (proliferative zone) to finally mature and become hypertrophied in the calcified matrix. Dead chondrocytes leave space for the invasion of capillaries and osteoblasts from the medullary cavity leading to new bone tissue (ossification zone)<sup>18</sup>

At the end of the bone growth, chondrocytes stop proliferating and die, and only a layer of cartilage called the epiphyseal line remains. This mechanism of bone growth explains their growth in length, however bones also grow in diameter. Their diameter evolves by appositional growth through bone remodelling.

#### 1.1.1.7 Bone remodelling cycle

After their formation, bones evolve constantly in response to external stresses applied either during basic activities (such as sitting, standing or walking) or exercises. The adaptation of the bone tissue is possible through the bone remodelling process, as represented in **Figure 14**. The bone remodelling cycle is based on the removal and reformation of bone tissue depending on hormonal and mechanical stimuli.

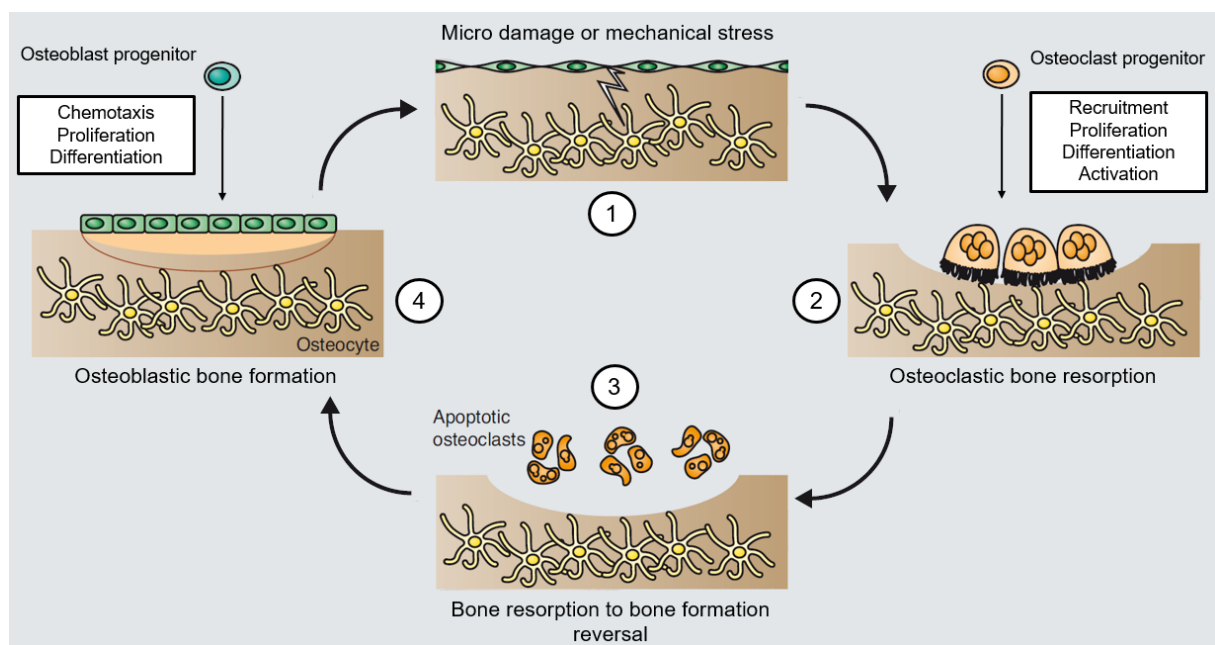


**Figure 14: Representation of the bone remodelling cycle.** Osteocytes sense micro damages or mechanical stresses and release growth factors to trigger the remodelling process (1, **Figure 14**). Haematopoietic stem cells are recruited and differentiated into osteoclast cells which resorb bone matrix (2). Hormonal regulation triggers the osteoclasts death (3) and osteoblast progenitor cells differentiate into osteoblast cells and secrete the new bone matrix (4), adapted from<sup>12</sup>

First, osteocytes within the organic bone matrix sense either micro damages or mechanical stresses and release growth factors to trigger the remodelling process (1, **Figure 14**). Second, haematopoietic stem cells and stem cells from blood vessels are recruited and differentiated into osteoclast cells at the remodelling site. Osteoclasts are activated to resorb bone matrix and secrete enzymes and acids to respectively digest the organic matrix and solubilize hydroxyapatite crystals. The dissolution by-products are then transported (transcytosed) by osteoclasts and secreted into interstitial fluids and blood vessels (2, **Figure 14**). As a consequence to the increasing level of calcium in blood, hormonal regulation triggers the osteoclasts death (apoptosis, 3, **Figure 14**). The growth factors previously released from the dissolved matrix or secreted by osteoclasts (**Figure 15**), attract osteoblast progenitor cells (4, **Figure 14**). Finally, those cells differentiate into osteoblasts and secrete new bone matrix (4, **Figure 14**)<sup>12,19</sup>.



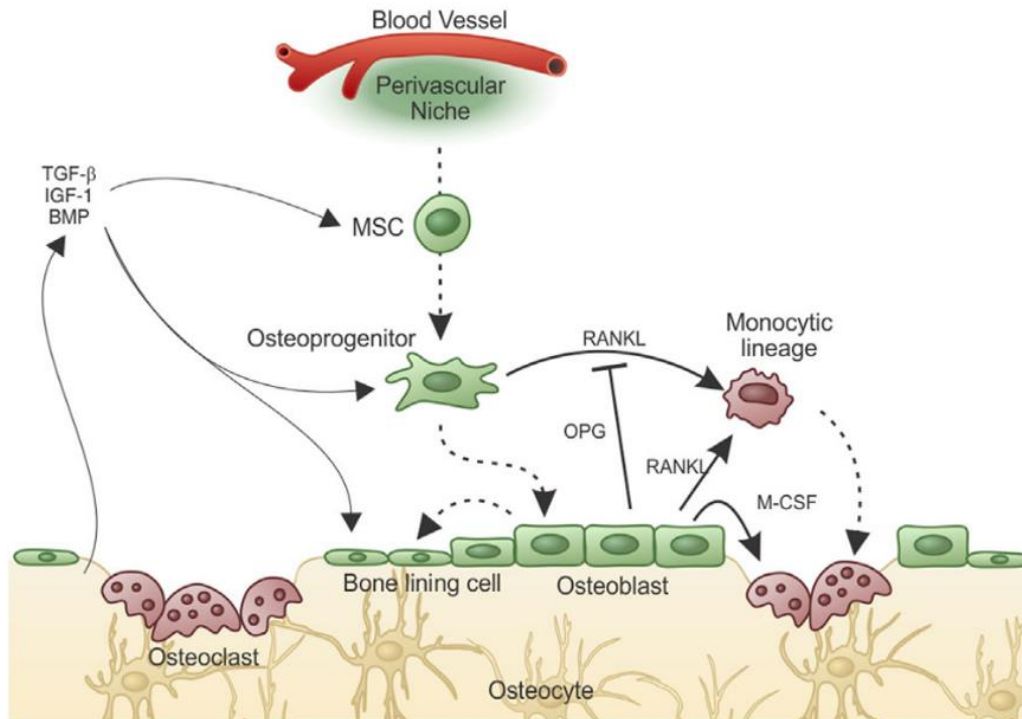


**Figure 15: Simplified representation of the growth factors role in the bone remodelling process.** Transforming growth factor beta (TGF- $\beta$ ), insulin-like growth factor-1 (IGF-1), bone morphogenetic proteins (BMP) growth factors produced by bone lining cells guide the mesenchymal, osteoprogenitor and bone lining cells differentiation. Receptor activator of nuclear factor kappa-B ligand (RANKL), macrophage colony-stimulating factor (M-CSF) and osteoprotegerin (OPG) growth factors are involved in osteoclastic differentiation<sup>19</sup>

Thus, the bone remodelling regulation relies on growth factors production (**Figure 15**), hormonal and mechanical controlling loops through calcium homeostasis in blood and the required skeleton resistance to mechanical and gravitational forces.

#### 1.1.1.8 Mechanical loads in bone

Mechanical forces are known to play an important role in the bone remodelling process, which adjusts the bone structure to ensure the fulfilment of its load-bearing functions (Wolff's law). In daily activities such as standing and walking, bones are subjected to tensile and compressive stresses (**Figure 16**).

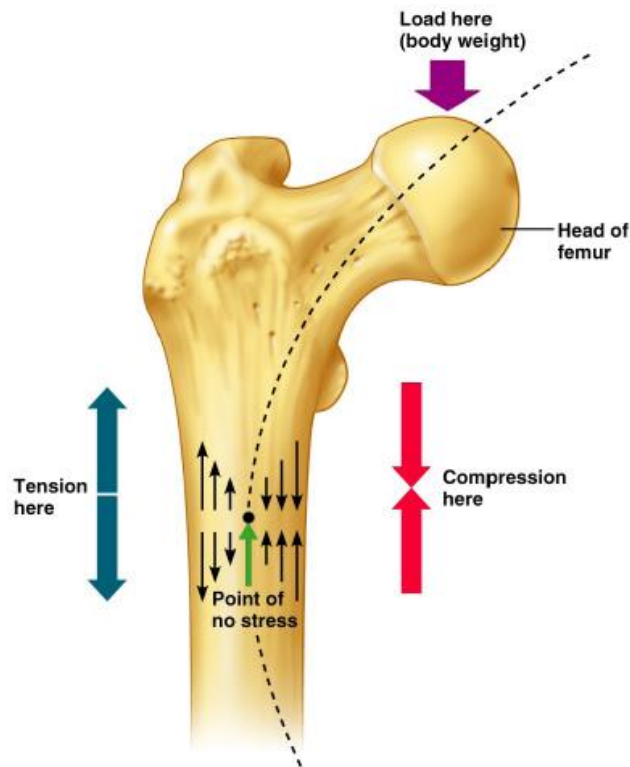


*Figure 16: Representation of the tensile and compressive stresses distribution in a femur subjected to mechanical load (Pearson Education)*

Depending on their location and the specific structural function to fulfil, bones have different shapes and are subjected to different types of loads. Those loads are generated from the body weight subjected to gravity and from muscular contractions. They are applied in different directions which in total generate 5 types of different mechanical loads namely: compression, tension, shear, torsion and bending (**Figure 17**).

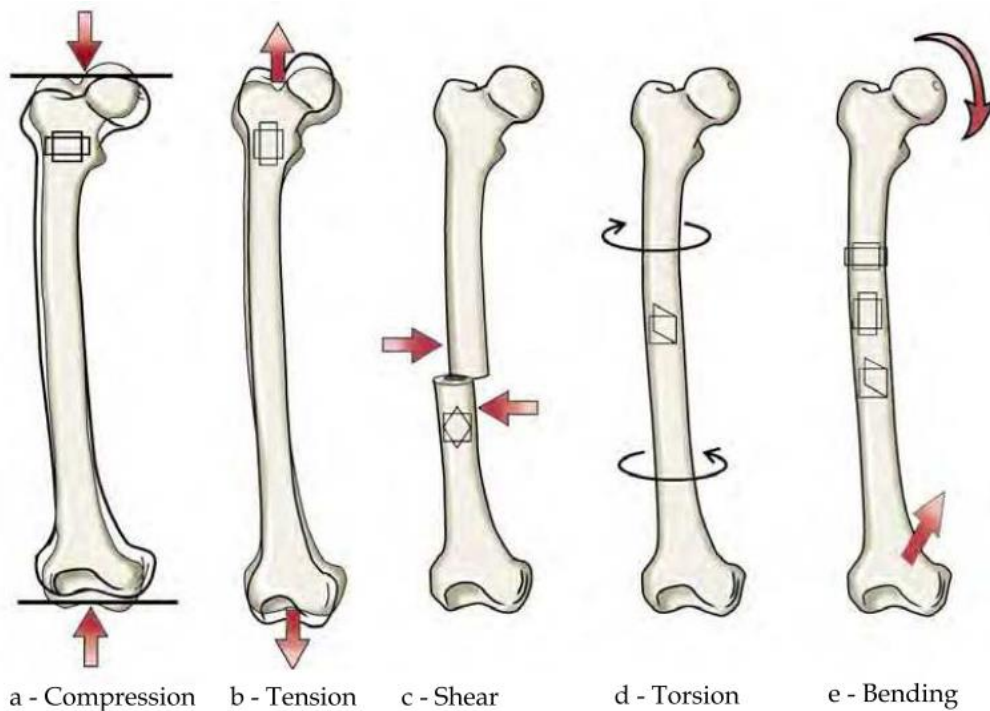


*Figure 17: Illustration of mechanical loads applied to a femur<sup>20</sup>*

As the bone structure is highly anisotropic, with cortical and trabecular areas in different directions, the resulting mechanical properties are also anisotropic and strongly depend on the loading directions.

1.1.1.9 Bone fracture (adapted from Biomaterial review <sup>21</sup>)

Bone fractures are one of the most common organ injuries that can result from high energy trauma such as car and motorbike accidents or sport injuries (rugby, mountain bike, paraglide...). In developing countries, due to the boom of economic activity and the resulting working conditions, work accidents are also an important cause of fractures<sup>22</sup>.

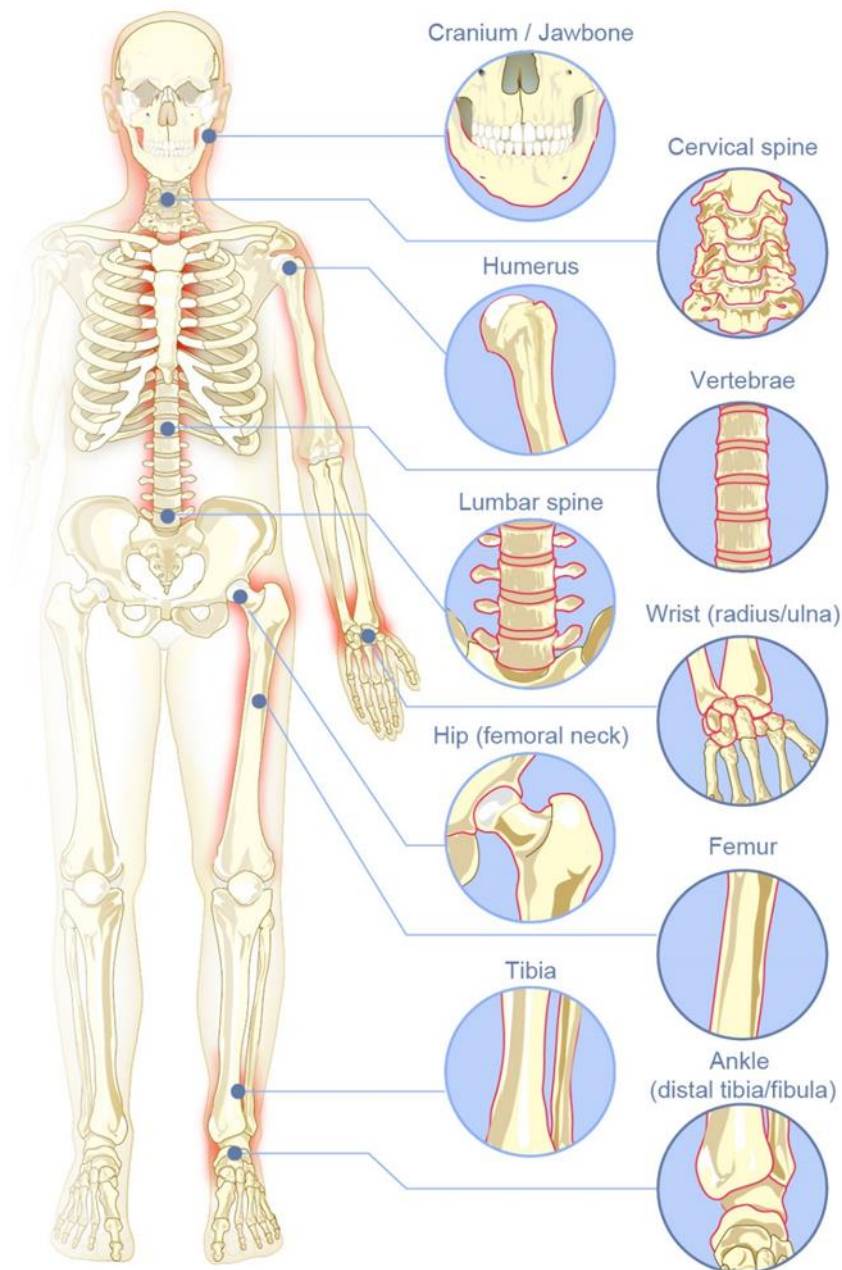


**Figure 18: Human skeleton and common sites of bone fractures in the body** where strategies using synthetic bone graft substitutes, bioactive molecules and/or stem cells are needed to repair bones in difficult clinical situations<sup>21</sup>

Typically, bone defects can be segmented into different subfields depending on their location: long bones and spine, maxillofacial and craniofacial. The most common bone fracture sites are (**Figure 18**): the femur, shoulder (mostly humerus), hip (femoral neck), wrist (radius/ulna), tibia (distal third), ankle (above the joint, distal tibia/fibula fractures) together with vertebral fractures, maxillo and cranio facial (jawbone, calvaria). Depending on bones and mechanical stresses, there are different types of fracture. The common types of fractures are illustrated and detailed in **Figure 19**.



**Figure 19: Common types of bone fractures.** *Spiral fractures refer to a ragged break and occur when bone is excessively twisted which is common for sports injuries. Greenstick fractures refer to an incomplete fracture when one side broke and the other side bent, this is common for children fractures. Communitied fractures refer to the case where bone fragments are into three or more pieces, commonly found in elderly fractures. Depressed fractures refer to broken bone portions pressed inward, common for skull fractures. Epiphysal fractures refer to the epiphysis separation from diaphysis along the epiphyseal line, commonly found in dead cartilage areas. Compression fractures refer to bone crushing which is common in porous bones<sup>23</sup>*

Under healthy circumstances, bone has a unique healing capacity without inducing scar tissue formation. However, complex or compromised bone fractures (i.e. fractures of critical size, severely damaged surrounding environment) can fail to heal, leading to a non-union fracture (**Figure 20A**).

### 1.1.2 Mechanism of bone repair (from Biomaterial review<sup>21</sup>)

Bone fracture healing is a complex, orchestrated, regenerative process that involves a crucial number of progenitor cells as well as inflammatory, endothelial and haematopoietic cells. The cellular and molecular events are strictly regulated during the healing cascade which includes the initial inflammatory phase, hematoma formation and progenitor cell recruitment (**Figure 20A**), formation of an intermediate callus (**Figure 20B**), maturation of the callus (**Figure 20C**) and the final remodelling of the bony callus to the original bone's structure and shape (**Figure 20D**)<sup>24</sup>.



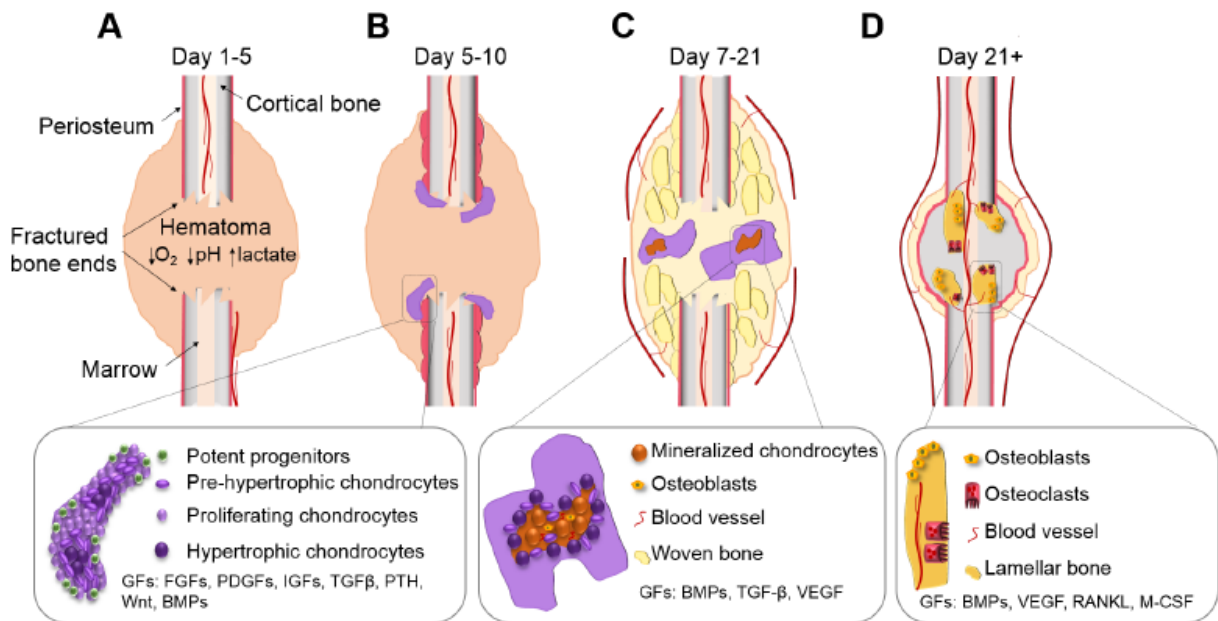


**Figure 20: Healing of a non-stabilized long bone fracture through the formation of a cartilaginous callus.** The major biological phases during healthy fracture healing go through the chronological stages of inflammation, the formation of a cartilaginous callus and remodelling of the callus into bone. The primary cell types that are found at each stage include inflammatory cells, chondrocytes, osteoblasts, osteoclasts, hematopoietic cells and osteocytes. (A) Upon fracture, the hematoma forms, associated with reduced  $O_2$  and pH levels as well as increased lactate. At this stage, the inflammatory cells remove injured tissue and secrete stimulatory factors to recruit cells from the environment including the periosteum. (B) A callus forms due to the massive progenitor cell expansion leading to cellular condensation and initiation of chondrogenic differentiation. (C) Hypertrophic chondrocytes in the callus mineralize and osteoblasts enter to subsequently form woven bone. The woven bone remodels through osteoclast-osteoblast coupling and the lamellar bone eventually bridges the fracture (D)<sup>21</sup>

The concerted action of the cells is strictly regulated by a crucial interplay of biochemical, physical and mechanical factors<sup>25</sup>, and largely recapitulating phenomenological events of **endochondral ossification** during embryogenesis<sup>26</sup>. As a result, many of the homeotic genes and primary morphogenetic pathways that are active during skeletal development also play a role during fracture healing<sup>27</sup>.

#### 1.1.2.1 Initial inflammatory phase and hematoma formation

The initial fracture causes a local disruption of the vascular network and surrounding tissues, which leads to hematoma formation and this is closely followed by the acute inflammatory phase<sup>28</sup>. The hematoma forms by cells from the peripheral blood and the intramedullary hematopoietic compartment<sup>29</sup>. This process occurs due to the plasma coagulation and platelet exposure to the extravascular environment, which together provide a fibrin network as a first provisional matrix. As a result, the hematoma has a high concentration of angiogenic growth factors, explaining its strong pro-angiogenic activity. The importance of the hematoma has been confirmed; its removal attenuates repair, whereas transplantation stimulates new bone formation<sup>30</sup>. The soft matrix of the hematoma allows recruitment and infiltration of the first inflammatory cells, neutrophils, within 24 h post fracture. By secreting inflammatory and chemotactic mediators such as Interleukin (IL)-6 and Chemokine ligand 2 (CCL2), the

neutrophils recruit the second wave of inflammatory cells, the monocytes and macrophages<sup>26,28,31</sup>. From this inflammatory environment, macrophages are polarized to a predominantly pro-inflammatory M1 phenotype, a specific type of macrophages<sup>32</sup>.

Next, the inflammatory cells that migrated to the site function remove the provisional fibrin matrix and necrotic cells, as well as to resorb necrotic bone fragments. In addition, macrophages, increasingly assuming the anti-inflammatory phenotype, known as M2 macrophages<sup>32</sup>, secrete a repertoire of inflammatory, chemotactic and progenitor mediators including stromal derived factor-1 $\alpha$  (SDF-1 $\alpha$ ), tumor necrosis factor alpha (TNF- $\alpha$ ), IL1 $\beta$ , IL-6, CCL2, bone morphogenetic protein (BMP)s, fibroblast growth factors (FGF)s and Wingless-type MMTV integration site family of proteins (Wnt)s to initiate the recruitment of progenitor cells from the bone marrow, periosteum and the cortical bone<sup>26</sup>.

As a result, the hematoma and the acute inflammatory reaction are cleared after a week and the hematoma is then replaced by granulation tissue, which consists of proliferating progenitor cells and neovasculature embedded in an unorganized ECM. Of note, a balanced acute inflammatory response has been shown to be crucial for healthy fracture healing, since macrophage depletion or knock out of inflammatory cytokines impairs the healing cascade<sup>32-35</sup>. In addition, the important switch between the pro-inflammatory M1 and anti-inflammatory M2 macrophages phenotypes is likely mediated by both macrophage autocrine signalling as well as paracrine signalling from other cells at the fracture site, including the recruited progenitors<sup>32</sup>.

#### *1.1.2.2 Callus formation*

After the inflammatory stage, the following fracture healing process largely recapitulates the process of long bone development in the embryo, including: 1) migration of skeletal precursors to the site of skeletogenesis followed by 2) cellular condensation, leading to the subsequent 3) differentiation towards chondrocytes and/or osteoblasts<sup>36-38</sup>. Skeletal progenitor cells have been found to be recruited locally and concurrently from periosteum, bone marrow/endosteum and/or dura mater during bone repair. All tissue sources give rise to osteoblasts, whereas the periosteum is the major source of chondrocytes<sup>39,40</sup>.

Importantly, intrinsic and environmental signals modulate cell fate decisions within these tissues. It is believed that depending on the relative distance to the blood vessels, combined with the release profiles of cytokines and growth factors, progenitor cells either first differentiate into chondrocytes, or directly mature into bone-forming osteoblasts. Due to the adapted metabolism in chondrocytes, designed to survive and function in poorly vascularized environments, these cells are located furthest away from the blood vessels<sup>26,41</sup>. The local hypoxia at the fracture site induces production of angiogenic factors such as VEGF to stimulate neo-angiogenesis<sup>42</sup>. Osteoblasts are dependent on oxidative metabolism and require a constant and substantial supply of oxygen and nutrients. Therefore, they accumulate in the vicinity of the newly formed blood vessels near the fracture extremities<sup>43</sup>.

### 1.1.2.3 Intramembranous and endochondral ossification

The success of fracture healing, bone integration and remodelling is also highly dependent on the biomechanics of the fracture site. Stabilized fractures in which the bone ends are closely opposed, mechanically stabilized and with limited vascular disruption, mainly heal through intramembranous ossification (**Figure 21A**)<sup>44</sup>.

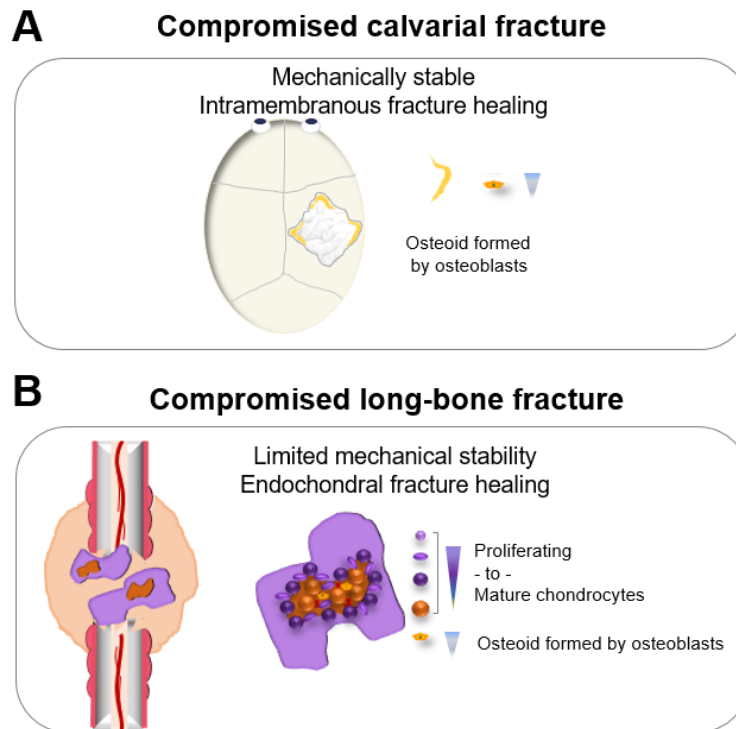


**Figure 21: Healing mechanism of compromised long-bone fracture and calvarial fracture.** (A) A compromised calvarial fracture in a mechanically stable environment mainly heals through direct ossification. In this process, cells from the periosteum, bone marrow (long bones) and dura mater (calvarial) contribute to the defect healing<sup>21</sup>. (B) A mechanically unstable long bone fracture heals through the formation of an intermediate cartilaginous callus that subsequently remodels into bone and the native bone structure and shape. The initial cartilaginous callus is mainly formed by cells recruited from the periosteum, and provides initial stabilization to the fracture. This allows blood vessel ingrowth closely followed by remodelling by cartilage-resorbing chondroclasts. Thereafter, progenitor cells recruited from the periosteum and bone marrow differentiate into osteoblasts that deposit new bone<sup>21</sup>

Partially stabilized or non-stabilized fractures on the other hand, with damaged vasculature, heal through rapid formation of a cartilaginous intermediate to provide initial stabilization (**Figure 21B**). This stabilization allows sufficient rigidity for blood vessel ingrowth, closely followed by invasion of bone forming osteoblasts that transform the soft callus into bone in collaboration with chondroclasts<sup>45</sup>.

### 1.1.2.4 Growth factors involved in fracture healing

Similarly to embryonic bone development, fracture healing is directly regulated by crucial factors from - and related to - the bone morphogenetic proteins (BMPs), transforming growth factor-beta (TGF- $\beta$ ), fibroblast growth factors (FGFs), parathyroid hormone (PTH), protein

wingless morphogenetic factors (Wnt), platelet-derived growth factors (PDGFs) and insulin like growth factor 1 (IGF-1) families<sup>27</sup>.

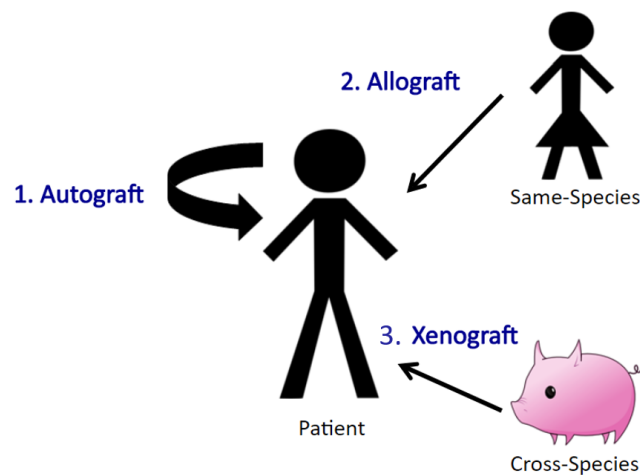
During the fracture healing cascade, TGF- $\beta$  and BMPs are secreted to help recruit progenitor cells. Thereafter, together with FGF, PDGF and IGF, they induce proliferation that is followed by cell differentiation, the latter being largely driven by BMPs<sup>42,45–48</sup>.

Several of these morphogenetic processes form interactive feedback loops, including co-regulation and regulation between different cell and tissue types during fracture repair. This elegant balance of complex interplay can be interrupted in a compromised biological environment due to severe damage, co-morbidities or the large size of the defect. This impaired signalling and or lack of progenitors leads to insufficient regenerative potential and the need to boost bone repair using other means.

### 1.1.3 Current strategies to repair bone (adapted from Biomaterial review<sup>21</sup>)

#### 1.1.3.1 Autograft, allograft and xenograft

Currently, the “gold standard” treatment of patients suffering from slow or incomplete bone healing is to perform bone grafting, using either an autograft or an allograft (**Figure 22**). However, there are drawbacks to bone grafting. Autograft treatment is limited by the volume of bone that can be harvested from the iliac crest and subsequently transplanted to the defect site. Complications include morbidity at the harvest site, local hematoma and remodelling issues of the implanted bone<sup>49,50</sup>. Allograft is hampered by bone tissue integration from the host and vascularization issues.





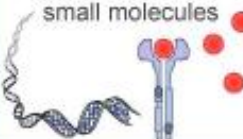









**Figure 22: Schematic representation of the different types of grafts.** Autograft represents a graft from another body area of the same patient while allograft is harvested from another patient and xenograft from a different species<sup>51</sup>

A last resort treatment strategy is distraction osteogenesis, which is a largely successful, but long, painful and dependent on the availability of a competent medical team. This technique has also been associated with poor healing and re-fracture<sup>52,53</sup>.

### 1.1.3.2 Bone graft substitutes

Consequently, a more sustainable, long term treatment strategy is required. To that end, bone graft substitutes (BGS) are being engineered to help impaired fracture healing. Depending on the trauma severity, we can distinguish three main strategies for bone repair (**Figure 23**): i) synthetic scaffolds alone, ii) scaffolds combined with active molecules and iii) cell-based combination products with cells from various sources.

Class	MD Class II	MD Class III	ATMP
Scaffold	3D Scaffold 	Collagen sponges, bioceramic granules 	Bone grafts, bioceramic granules 
Additional functionality	Surface modification 	Growth factors BMPs, PDGF, genes, small molecules 	STEM cells BMSCs, ASCs, PDCs 
Bone defect	in situ  small < 2 cm	in situ  intermediate 2-4 cm	ex situ / in situ  large and compromised > 4cm
Clinical observation			

**Figure 23: The three major strategies currently used and developed to repair bone.** The first (left column) relies on using only synthetic bone graft substitutes (BGS). The second (middle column) relies on combining bioactive molecules with a carrier that is mostly an extracellular matrix protein or a ceramic-based carrier. The third (right column) consists of combining stem cells with a carrier, possibly with the use of additional bioactive molecules. Each of these approaches is more appropriate for the healing of bone defects depending on their severity. When the healing of a defect is compromised, there is a need to have a biological functionality in addition to the BGS, which is provided either by bioactive molecules, stem cells, or a combination of both<sup>21</sup>

Once implanted, the different types of BGS can either lead to **osteoconduction**, the growth of bone tissue at their surface, or **osteoinduction**, the cells recruitment and differentiation into bone progenitor cells leading to bone tissue formation. In both case, the BGS **osseointegration** is the main objective with the stable anchorage of the BGS with a direct bone-BGS contact<sup>54</sup>.

The first generation of these strategies are currently in clinical trials at different phases (I, II, or III) and some have even made it to the clinic. In addition, the next generation of implants are currently being developed at the pre-clinical stage. Traditionally, scaffolds are used in trauma or spine fusion markets, while the combination of scaffolds with active molecules and/or stem cells is typically classified in the “orthobiologics” field.

#### 1.1.3.3 Industrial market

In terms of industrial markets, fracture treatments and bone bridging/repair solutions are classified in different application fields generating important revenues. The worldwide orthopaedic product sales are segmented as fracture repair, a market estimated at \$5.5 billion that includes all products used to repair fractures internally or externally: plates, screws, intramedullary nails, pins, wires, staples, and external fixators; spinal implant and instrumentation at ~\$7 billion market that includes spinal fusion; and orthobiologics at \$4.7 billion market that includes different strategies used to repair bone or fuse joints<sup>22</sup>. To note, orthobiologics are biological substances, either active molecules, stem cells or demineralized bone grafts that are used to help bone defects heal more quickly. The term orthobiologics is specific to bone, while tissue engineering is a more generic term that can be applied to the repair of all tissues, including bones.

## 1.2 Biomaterials for bone graft substitutes

As described in the section 1.1, bone tissue is mainly composed of hydroxyapatite crystals and collagen, organized in a specific manner to reach the biological and mechanical requirements. Materials used for bone graft substitutes are first selected for their biocompatibility, which is why they are named after biomaterials, but should also substitute as much as possible the bone functions there are aimed at. In general, the different types of biomaterials used in orthopaedics are combined to fit the target bones that are substituted.

### 1.2.1 Ceramics

Ceramics are solid materials composed of inorganic and non-metallic elements linked together via ionic and covalent bonds. They are generally formed and processed at high temperature and their structures can either be highly crystalline, semi-crystalline (porcelain) or completely amorphous (glass). In terms of mechanical properties, ceramics are generally hard and brittle materials with high compressive strength and low tensile strength. Moreover, they possess a higher elastic modulus compared to bone<sup>55</sup>. For bone graft substitutes, two types of ceramics are being employed: **bio inert** and **bioactive/biodegradable** ceramics.

Among **bio inert** ceramics, alumina (Al<sub>2</sub>O<sub>3</sub>) and zirconia (ZrO<sub>2</sub>) are the most used for clinical applications. When implanted, they are not directly bound to surrounding bone tissue due to their high chemical inertness and induce the formation of a non-adherent fibrous connective



tissue. Their main applications as biomaterials in bone graft substitutes are for dental implants and for articular surfaces of joint replacements (**Figure 24**) as they also exhibit a high wear resistance<sup>56</sup>.

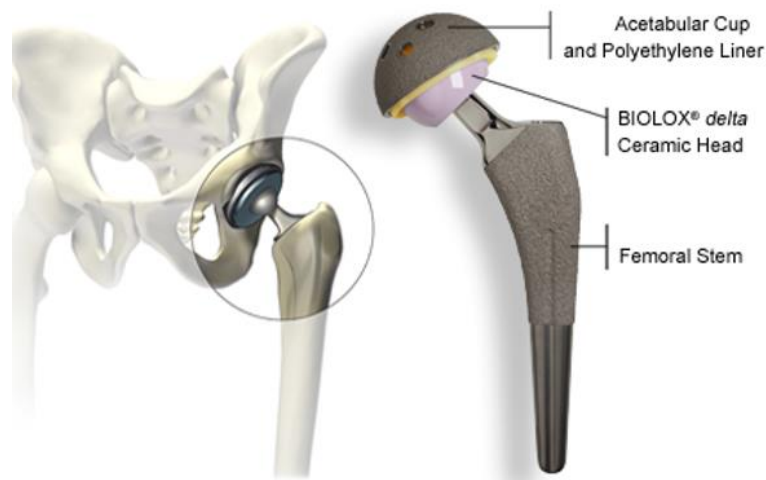


**Figure 24:** Example of alumina use for hip prosthesis head. Renovis<sup>®</sup> surgical hip prosthesis represented in a total hip replacement configuration (left). The acetabular cup, polyethylene liner, ceramic head and femoral stem constituting Renovis<sup>®</sup> hip prosthesis are represented (right)<sup>57</sup>

**Bioactive** ceramics are osteoconductive ceramics that have the capability to form direct bonds with the surrounding bone tissues<sup>58</sup>. Among them, 45S5 Bioglass<sup>®</sup> (45wt% SiO<sub>2</sub>, 24.5wt% CaO, 6wt% P<sub>2</sub>O<sub>5</sub> and 24.5wt% Na<sub>2</sub>O), hydroxyapatite (HAP, Ca<sub>10</sub>(PO<sub>4</sub>)<sub>6</sub>(OH)<sub>2</sub>),  $\beta$ -tricalcium phosphate ( $\beta$ -TCP, Ca<sub>3</sub>(PO<sub>4</sub>)<sub>2</sub>) or composite of both, biphasic calcium phosphate (BCP), are the most used bioactive ceramics. Those ceramics are also generally biodegradable and are thus resorbed and replaced gradually by new bone tissue. Despite having a real bond with the surrounding bone tissue, those ceramics remain brittle and thus are mostly employed as bone void filler in form of injectable pastes, granules (**Figure 25**), or as surface treatment<sup>59</sup>.

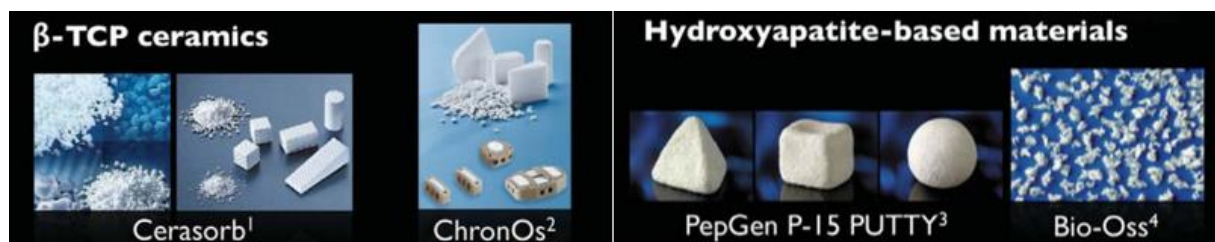


**Figure 25:** Examples of commercialized ceramics. Ceramics composed of  $\beta$ -TCP, Cerasorb and ChronOs commercialized by Curasan AG<sup>1</sup> and Synthes<sup>2</sup> companies. Hydroxyapatite-based materials, P-15 Putty and Bio-Oss commercialized by PepGen<sup>®3</sup> and Geistlich<sup>60</sup>

### 1.2.2 Polymers

Polymers are made by controlled polymerisation of small molecular units, the monomers. The polymers physico-chemical properties as well as mechanical properties depend on their molecular structure, weight and dispersity as well as their synthesis route. Polymers can either be natural (ie made of natural biomolecules such as type I collagen or fibrin) or synthetic. In this later case, they can either be degradable or non-degradable. In the case of biodegradable polymers, the main degradation mechanism is the chemical hydrolysis of monomers bonds.

Those kind of polymers are interesting for short term applications such as drug delivery or for mechanical stabilization until the body regenerates on its own. When the body is not able to restore the damaged area, non-degradable polymers are employed as a long term strategy<sup>61</sup>.

All types of polymers are employed in bone graft substitutes either as a part, entirely or also as cement around bone substitutes, to enhance their anchorage to the surrounding tissue. Among non-degradable polymers, synthetic polymers such as polyethylene (PE) and polyetheretherketone (PEEK) are used as liner in acetabular cups (**Figure 24**) or as a spacers in intervertebral disc replacement (**Figure 26**). Polymethylmethacrylate (PMMA), silicon rubber (such as PDMS), acrylic resins and polyurethanes are often used as bone cements (**Figure 26**)<sup>62</sup>.



**Figure 26:** PEEK Clydesdale™ Spinal System (left, Medtronic) and CEMFIX® 1 PMMA bone cement (right, Teknimed)

Among biodegradable polymers, synthetic polymers such as poly(lactic-co-glycolic acid) (PLGA), polylactic acid (PLA), polycaprolactone (PCL) or polyethylene glycol (PEG) are mostly used as pins, sutures wires, membranes, plates or screws to provide mechanical strength near newly implanted bone substitutes<sup>62,63</sup>.

Natural polymers, such as type I collagen, fibrin, hyaluronic acid and chitosan have lower mechanical stability. Thus, they are rather used as space filler, lubricant or matrix carrying HAP or bioactive molecules (**Figure 27**)<sup>21,64</sup>.



**Figure 27:** Monovisc® Acid hyaluronic lubricant for knee joint (left, DePuy Synthes) and Bio-Oss® Collagen for dental bone substitute (right, Geistlich)

Composites materials made of polymers and bioactive ceramics are interesting for bone graft substitutes since they can mimic bone composition (mostly HAP and type I collagen) and



combine the properties of each materials, notably biodegradability, mechanical stability and better osteoconductivity in the case of bioactive ceramics<sup>65</sup>.

### 1.2.3 Metals

Metals are all elements forming an attractive electrostatic bond between themselves with clouds of free electrons (valence shell electrons) and their positively charged ionic form. This metallic bond gives to metals specific physical properties such as high thermal and electrical conductivity, opacity and ductility<sup>66</sup>.

For load-bearing applications, metallic materials remain the first choice for bone graft substitutes in view of their high compressive strength (**Table 2**) and fatigue resistance. The main metallic materials used as bone graft substitutes are stainless steel, cobalt-chromium-based and titanium-based alloys<sup>67</sup>.

	Porosity	Elastic Modulus (GPa)		Ultimate Strength (MPa)	
Cortical bone	3 - 5%	Tension	18.5 ± 4.2	Tension	125.4 ± 35.5
		Compression	22.4 ± 5.9	Compression	194.7 ± 11.2
Trabecular bone	Up to 90%	Compression	0.27 ± 0.25	Compression	4.89 ± 2.46
Stainless steel 316L	Bulk		210		170 – 750
Co-Cr-Mo			240		275 – 1585
Ti-6Al-4V			110		850 - 900

**Table 2: Average mechanical properties of bones and metallic materials used for bone graft substitutes.** The elastic modulus, compressive, shear and tensile strengths and Poisson's ratio of compact and trabecular bones, stainless steel, cobalt-chromium-molybdenum and titanium-aluminium-vanadium alloys (adapted from<sup>62,68</sup>)

The first metallic materials successfully used in orthopaedic applications were the 316L stainless steel (316LSS, composed mainly of Fe, C <0.03wt%, Cr 17-20wt%, Ni 12-14 wt%) and cobalt–chromium (Co-Cr) alloys. Those alloys exhibit a good corrosion resistance due to their high Cr content (more than 12wt%) allowing the formation of a corrosion resistant coating oxide of Cr<sub>2</sub>O<sub>3</sub><sup>62</sup>. However, Cr and Co released from those alloys were proven to have toxic effects on the body, in addition to their relatively high elastic modulus (respectively 210 GPa and 240 GPa, **Figure 28**) compared to bone, inducing higher stress shielding effect<sup>67</sup>.

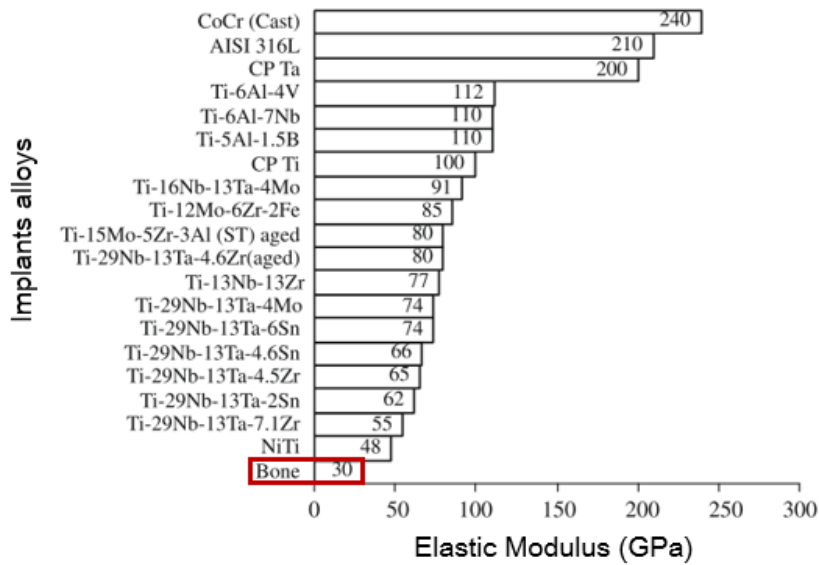


Figure 28: Elastic modulus of alloys used for bone implant<sup>67</sup>

The stress shielding effect refers to the bone resorption occurring when there is insufficient transfer of stresses in bone (Figure 29). The decrease of stresses in the surrounding bone around the implant leads to its resorption and can eventually cause the substitute loosening in the following years after implantation<sup>67</sup>.

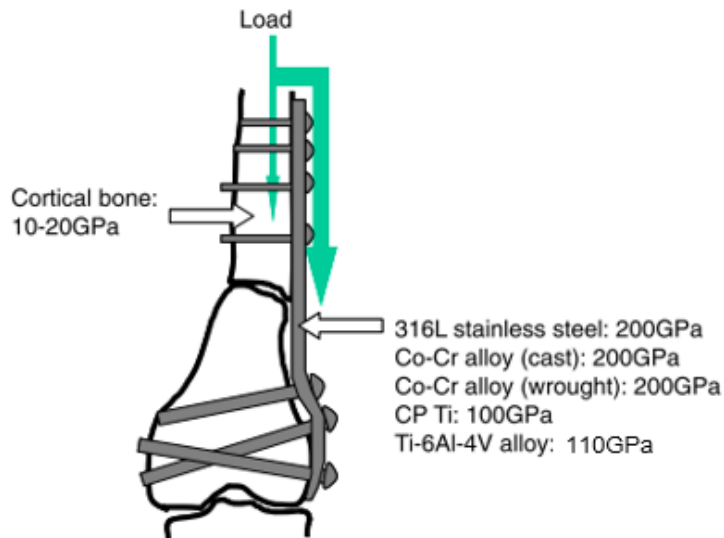


Figure 29: Illustration of the load distribution in presence of metallic bone fixation which can induce a stress shielding effect. Elastic modulus of cortical bone and the possible different material that can be used as metallic fixation are listed in GPa<sup>69</sup>

Titanium (Ti) and its alloys were originally developed and used for aeronautic applications. Because of their remarkable properties in terms of strength, low density, moderate elastic modulus (110 GPa, Figure 28), corrosion resistance and complete inertness to biological environments, they were introduced in the biomedical field<sup>67</sup>.

Other alloys, such as the nickel-titanium (NiTi) shape memory alloy and biodegradable alloys (magnesium, iron and zinc-based) are also investigated as potential metallic materials for

medical devices. In the case of NiTi alloy, unsolved allergenic effect of Ni has hampered its use<sup>62</sup> whereas for biodegradable metals, the control of their corrosion rate still remains a crucial safety issue<sup>70</sup>.

#### 1.2.4 Titanium alloys for bone graft substitutes

Ti and Ti based alloys are lightweight materials with high strength and corrosion resistance with higher melting point than iron, nickel and aluminium (Al) based alloys, which made them at first, the best candidates for aeronautics application despite their high price. Due to their low electrical conductivity, Ti and Ti based alloys are subjected to electrochemical oxidation leading to the formation of a thin passive oxide layer<sup>71</sup>. In addition to contribute to their corrosion resistance, this protective oxide layer is stable at physiological pH with an isoelectric point around 5-6. The latter gives to Ti materials a low tendency to form ions in aqueous environment which make them biocompatible<sup>72</sup>. After the discovery of the Ti biocompatibility and especially osseointegration, the tight integration of the material around bone tissue by Branemark, the interest for Ti and its alloys for dental and orthopaedics implants started<sup>62</sup>. Commercially pure Ti (CP Ti) was first used for cardiovascular stents, lead wires and spinal/trauma fixation devices. To increase its mechanical performances (yield strength), four different grades of CP Ti were developed with increasing oxygen content. However, even if CP Ti (grade 1-4) mechanical properties were suitable for dental applications, they were below the requirements for orthopaedic applications<sup>73</sup>.

This need led to the introduction of Ti-6Al-4V ELI (Extra Low interstitial oxygen) alloy composed of aluminium (Al, hexagonal crystallographic structure  $\alpha$  stabilizer, ~6wt%) and vanadium (V, body centered cubic crystallographic structure  $\beta$  phase stabilizer, ~4wt%) which presents a higher tensile strength than CP Ti, as shown in **Table 3**. Today, Ti-6Al-4V remains the largest titanium alloy used for biomedical devices such as hip joints, bone screws, knee joints, bone plates, dental implants and surgical devices, but health and safety concerns are raising from the release of Al and V ions. Those ions were found to be associated with long-term health problems, such as Alzheimer disease, neuropathy and osteomalacia<sup>67</sup>. To answer this issue, other Ti alloys such as Ti-6Al-7Nb or Ti-5Al-2.5Fe were developed by substituting vanadium with niobium or iron while keeping the same  $\alpha/\beta$  phase microstructure of Ti-6Al-4V.

Material	Standard	Modulus (GPa)	Tensile strength (Mpa)	Alloy type
<i>First generation biomaterials (1950–1990)</i>				
Commercially pure Ti (Cp grade 1–4)	ASTM 1341	100	240–550	$\alpha$
Ti–6Al–4V ELI wrought	ASTM F136	110	860–965	$\alpha + \beta$
Ti–6Al–4V ELI Standard grade	ASTM F1472	112	895–930	$\alpha + \beta$
Ti–6Al–7Nb Wrought	ASTM F1295	110	900–1050	$\alpha + \beta$
Ti–5Al–2.5Fe	–	110	1020	$\alpha + \beta$
<i>Second generation biomaterials (1990–till date)</i>				
Ti–13Nb–13Zr Wrought	ASTM F1713	79–84	973–1037	Metastable $\beta$
Ti–12Mo–6Zr–2Fe (TMZF)	ASTM F1813	74–85	1060–1100	$\beta$
Ti–35Nb–7Zr–5Ta (TNZT)		<b>55</b>	596	$\beta$
Ti–29Nb–13Ta–4.6Zr	–	65	911	$\beta$
Ti–35Nb–5Ta–7Zr–0.40 (TNZTO)		66	1010	$\beta$
Ti–15Mo–5Zr–3Al		82		$\beta$
Ti–Mo	ASTM F2066			$\beta$

**Table 3: Main titanium alloys and their mechanical properties used in the biomedical field.** The first generation of titanium alloy exhibit relatively higher elastic modulus than the second generation which composition has been modified to reduce the elastic modulus<sup>67</sup>

Additional concerns to have an elastic modulus lower and closer to human bone led to the development of low modulus  $\beta$  Ti alloy such as Ti–13Nb–13Zr or Ti–35Nb–7Zr–5Ta, while using only biocompatible alloying elements (niobium Nb, zirconium Zr, tantalum Ta) and keeping strength properties comparable to Ti–6Al–4V<sup>73</sup>. Another limitations of Ti materials are their poor shear strength and their high coefficient of friction which can lead to the wear debris formation. Wear debris are known to trigger an acute inflammatory reaction causing pain and the implants loosening by osteolysis. Those limitations are the reasons why the time service period of Ti implants has been restricted to 10–15 years<sup>67</sup> but still, Ti and its alloys remain the most used metallic materials for load-bearing bone graft substitutes.

### 1.2.5 Manufacturing processes of titanium bone graft substitutes

#### 1.2.5.1 Wrought and cast

Wrought manufacturing processes consist in the shaping of metals with compressive mechanical pressures provided either by hammers, rolls or presses. Wrought is either applied in hot or cold working conditions. In contrast, cast consists in melting raw material to obtain a liquid, pour it into a hollow mould and let the material solidify inside it. The solidified part is the final object and is recovered from the mould for eventual post-treatments.

The starting material form of Ti for bone graft substitutes are annealed bar stock, which are derived from wrought and annealed Ti ingots as detailed in **Figure 30**. First, Ti sponge are compacted and made into consumable electrodes with alloying elements for the vacuum arc furnace. Vacuum is applied in the furnace and the atmosphere is filled with argon to prevent contamination. Then, the Ti electrode is remelted into this furnace with an electric arc to form an ingot, which is further manufactured (hot rolled and annealed) to obtain bars<sup>74</sup>.

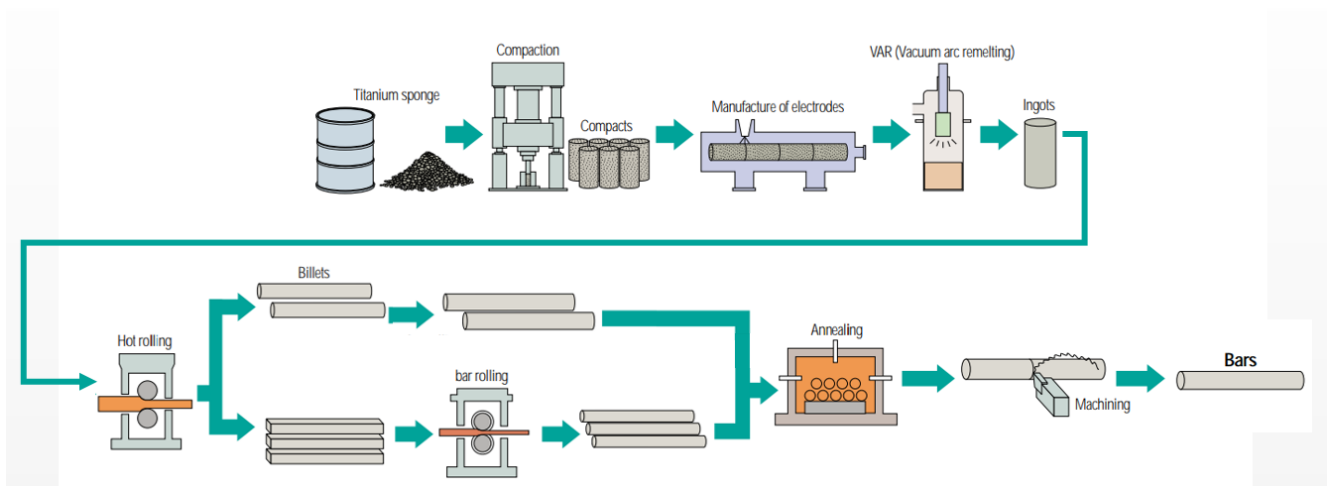


**Figure 30: Manufacturing processes to obtain Titanium bar stocks.** Titanium sponge are mixed with alloying elements and prepared as electrodes for their melting. The obtained ingot is further processed with hot rolling and annealing steps to obtain titanium bars (adapted from<sup>74</sup>)

Dental implants are machined by computer numerical controlled (CNC) multi-axis machine tools directly from Ti bars, hip stems are generally wrought, machined and polished, cranial plates implants are produced from Ti sheets that are reshaped around the patient model and pressed with a hydraulic press<sup>75-77</sup>.

Still both types of processes require relatively long product-cycle time and complex post-treatments, without mentioning the loss of material. Moreover, bulk Ti parts still have higher elastic modulus than bone which can lead to stress shielding effects at the implantation site. To solve this issue, interconnected porous structures in Ti bone substitutes are a promising solution to lower their elastic modulus and better match the local osseous environment. As a result, research efforts have been directed towards developing fabrication technologies able to produce porous Ti implants<sup>78</sup>.

#### 1.2.5.2 Powder metallurgy

Powder metallurgy (PM) is a manufacturing process that uses metallic powders as starting material. Pure metallic elements or alloy powders are mixed and compacted into a designed mould. This mould is heated to partially or totally sinter powders in a controlled atmosphere to bind the particles (**Figure 31**).

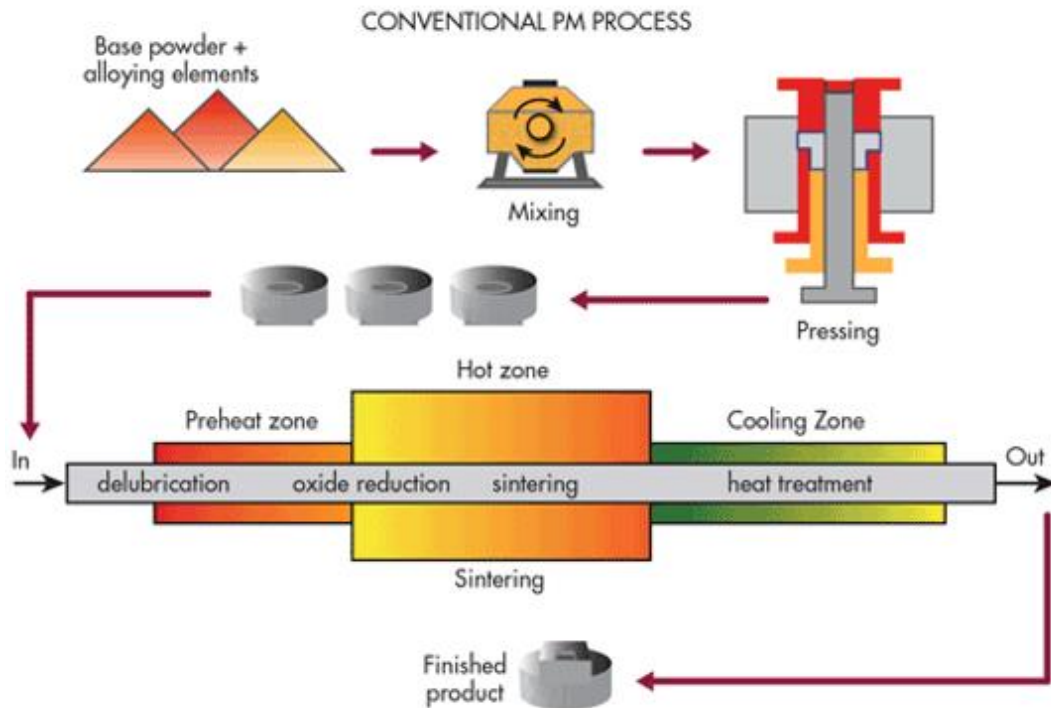


**Figure 31: Representation of powder metallurgy manufacturing process.** Powders are mixed and pressed into a designed mould. Moulds are heated to sinter powders before obtaining the finished product<sup>79</sup>

This manufacturing process has the advantage to allow a low-cost fabrication of Ti parts while achieving a nearly waste-free and net-shape forming. In addition, those parts can be produced with the combination of small and large pores by adjusting processing parameters such as the powder size, the temperature and pressure. Porous structures do not only decrease the elastic modulus but also increase the bone substitute surface area. This last feature allows a higher cells and blood vessels penetration which can induce a better implant integration than wrought or cast substitutes<sup>78</sup>.

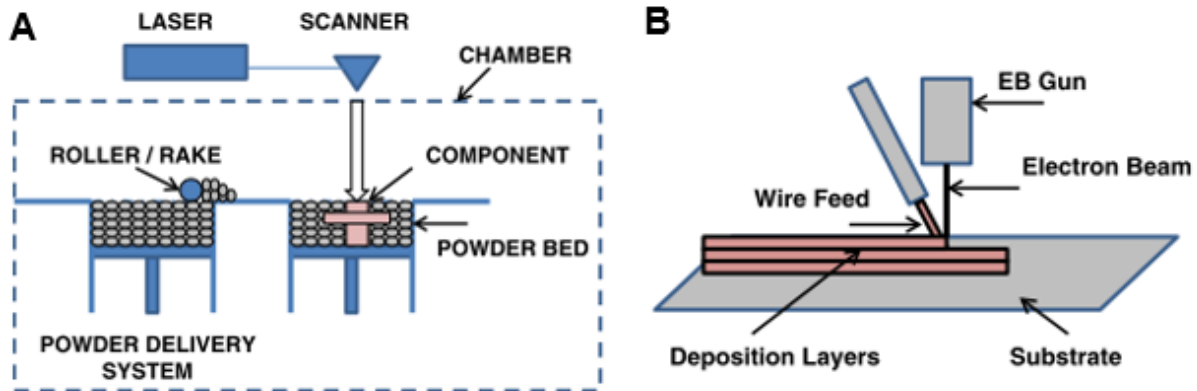
The use of PM on Ti and its alloys began in the mid-1970s. The PM technique not only helped to lower the fabrication costs but was also found to produce fine-grained structures which contribute to better fatigue properties. In addition, higher porosities in Ti substitutes enhance their corrosion resistance with higher internal supply of oxygen for the passivation of their surface. However, limitations for manufacturing orthopaedic implants with PM remain. The size limitation due to the press, the high energy consumption to compact the powder mixture or the non-avoidable post-fabrication processes such as polishing are some of them<sup>78</sup>.

#### 1.2.5.3 Additive manufacturing (AM)

Additive manufacturing (AM) technologies emerged in the 1980s and are defined by the American Society for Testing and Materials (ASTM) as processes consisting in building materials layer by layer, to create an object from 3D model data, as opposed to subtractive manufacturing methodologies (ASTM F2792). Among AM technologies, two main types of processes are available: powder bed fusion systems (**Figure 32A**) and wire fed systems (**Figure**



**32B).** The energy source to melt the starting material can either be a laser, an electron beam or a plasma arc.

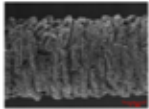
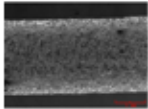


*Figure 32: Schematic representation of powder bed fusion (A) and wire based (B) additive manufacturing systems. In powder bed fusion systems, the starting material is a powder that is deposited on the build platform for further melting. In wire based systems, the starting material is a wire directly deposited and melted after deposition<sup>80</sup>*

In powder bed fusion systems, the starting material is in powder form. First, a powder bed is deposited for each layer by a raking delivery system. Then, the energy source melts locally the powder according to the 3D model and a new powder bed is added and melted for each layer until building the complete object. Whereas in wire fed systems, the starting material, which is a wire, is directly deposited and melted after its deposition<sup>80</sup>.

In the case of titanium-based bone substitutes, two powder bed techniques are used: the **electron beam melting (EBM)** and **selective laser beam melting (SLM)**. Their main characteristics are described in **Table 4**. Both techniques have been commercialized at the same time and proven to be efficient for the building of Ti-6Al-4V orthopaedic implants<sup>81</sup>. Even if SLM allows a better control of the spatial resolution and surface features (**Table 4**), the EBM technique stands out in terms of production rates (80 cm<sup>3</sup>/h over 40 cm<sup>3</sup>/h for SLM), control of the alloy microstructure ( $\alpha/\beta$  over  $\alpha'$ ) and purity (vacuum in the build atmosphere)<sup>68</sup>.

In terms of mechanical properties, Ti-6Al-4V built by SLM and EBM have enhanced mechanical strengths compared to cast alloys (typical values for EBM vs casting: 950 MPa vs 800 MPa for yield strength, 1020 MPa vs 850 MPa for Ultimate Tensile Strength (data given by ARCAM). Compared to SLM, the EBM process allows to obtain a more ductile material as demonstrated by the elongation (14 % over 7-8% for SLM or casting)<sup>81</sup>.

	<b>EBM</b>	<b>SLM</b>
<b>Company</b>	Arcam AB (2005)	EOS GmbH (2005)
<b>Build atmosphere</b>	Column < 10 <sup>-4</sup> mBar Building area < 10 <sup>-2</sup> mBar with He gas	Purified Ar or N <sub>2</sub>
<b>Powder size</b>	45 - 100 μm	25 - 45 μm
<b>Layer thickness</b>	100 μm	20 - 100 μm
<b>T<sub>Build platform</sub></b>	700°C	90°C
<b>T<sub>Build atmosphere</sub></b>	700°C	700°C
<b>Scan rates</b>	10 <sup>2</sup> to 10 <sup>4</sup> mm/s	8 to 12 x 10 <sup>2</sup> mm/s
<b>Ti-6Al-4V microstructure</b>	α/β or α'	α' or α/α'
<b>Geometry accuracy</b>	+	++
<b>Roughness</b>	++ 	+ 

*Table 4: Comparison of the EBM and SLM additive manufacturing techniques<sup>82</sup>*

The main advantages of AM techniques for bone graft substitutes are: the possibility to easily produce at once highly porous or dense parts in a unique construct, the ability to build customized substitutes according to the patient anatomical data and the saving of material compared to conventional manufacturing processes. More specifically in the case of EBM, a high temperature is used during the build process. As a consequence, no residual stresses accumulate in the structure, which allow to avoid post treatment such as annealing. However, the production volumes are low compared to conventional manufacturing techniques and surface finishing processes, such as grinding or polishing, are still required especially with the inherent roughness which ranges between 30 to 40 μm<sup>78,81</sup>.

The first bone graft substitute part built by AM technique was an acetabular cup produced by Lima Corporate and Arcam with EBM and the Ti-6Al-4V alloy in 2007. Nowadays, several interbody cages built by EBM have been approved by the USA Food and Drug Administration (FDA) and used in more than 10 000 patients in 15 different countries (**Figure 33**)<sup>68</sup>. Despite this increasing use of Ti-6Al-4V alloy with AM processes for bone graft substitutes, several challenges remain in this manufacturing field such as: the reproducibility of each built part, the control of the mechanical properties to avoid the stress shielding effect and increase the substitute life expectancy or more, the optimization of the structure and surface to ensure an efficient implant integration and bone ingrowth.

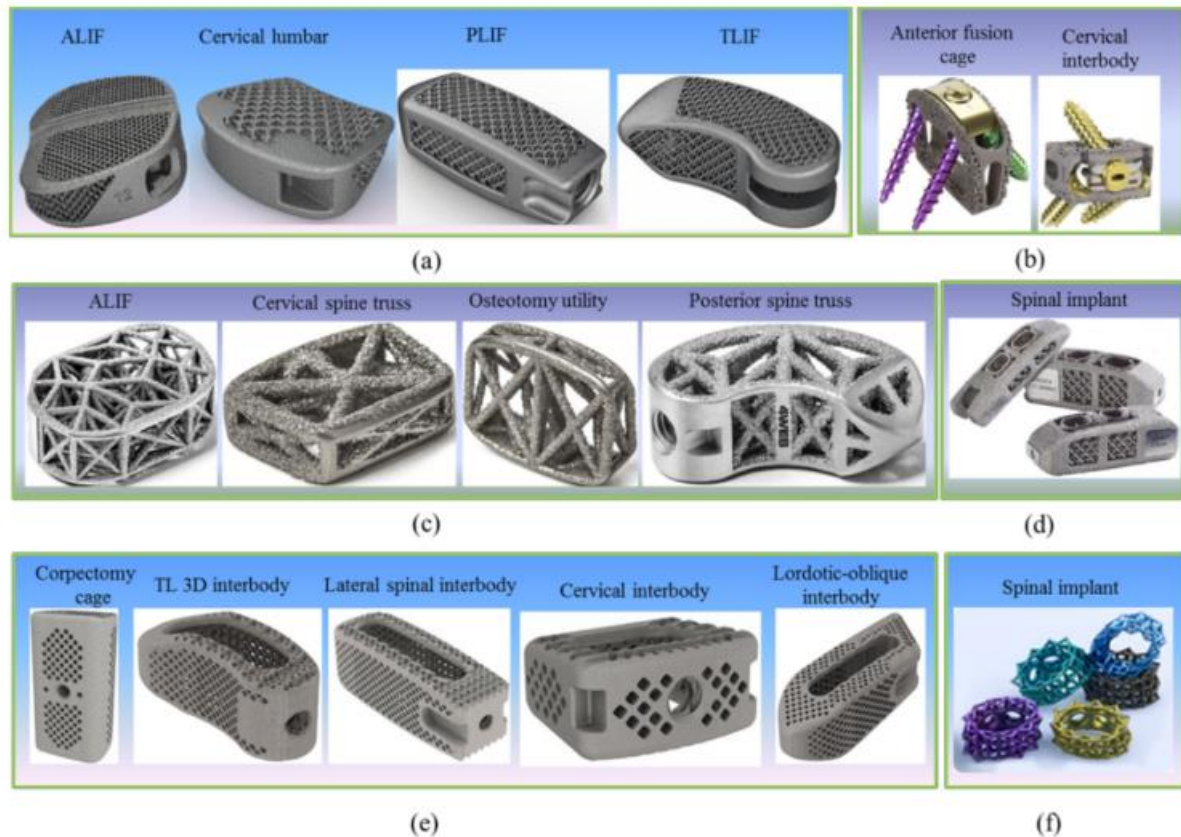


**Figure 33: Examples of Food and Drug Administration (FDA) approved Ti-6Al-4V bone graft substitutes manufactured by EBM. (a) By EIT, Germany. (b) By Renovis, USA (c) By 4WEB Medical, USA. (d) By Joimax, Germany. (e) By K2M, USA. (f) By Solidscape, USA<sup>68</sup>**

### 1.3 Structural optimization of bone graft substitutes

The first strategy to improve the integration of bone substitutes is to use 3D geometries that favour bone ingrowth, while being as close as possible to the target bone and without impeding the natural bone regeneration and remodelling process. Currently, the identified structural features recognized as crucial in bone tissue regeneration and substitutes osseointegration are: mechanical properties, porosity, surface curvature and topography<sup>83,84</sup>.

#### 1.3.1.1 Mechanical properties

Mechanical properties of human bones are highly dependent on the age, gender and the specific bone in either its cortical or trabecular areas. The main mechanical properties measured for bones in the literature are: tensile yield strength, ultimate tensile and compressive strengths, tensile and compressive elastic moduli, ultimate strain and density.

With the emergence of AM technologies for metallic materials, several open-cells porous structures have been constructed and characterized in view to match bone mechanical properties. More particularly, a focus has been made on lattice structures built from repetitions of a unit cell. The four mostly investigated lattice structures were built by EBM using the cubic, dodecahedron, diamond and hexagonal unit cells (**Figure 34**). Parameters such as the unit cell type, porosity/density, elastic modulus and strengths (tensile, compressive or

fatigue) are measured to characterize lattice structures and then compared to human bones properties<sup>68</sup>.

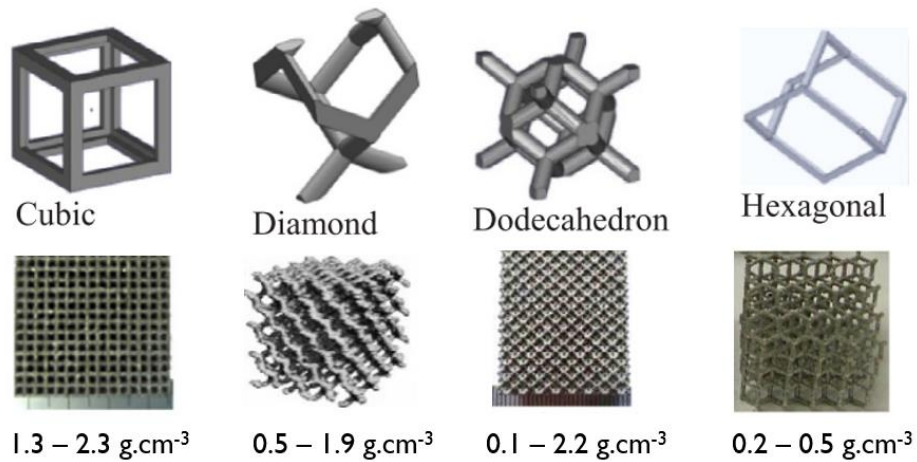


**Figure 34: Unit cells and corresponding lattices built by EBM with Ti-6Al-4V alloy.** Obtained lattices densities are close to human bone average densities which range from 0.19 to 1.99 g.cm<sup>-3</sup> (adapted from<sup>68</sup>)

Due to the fact that the used unit cells are open cells, built lattices can reach very low densities (from 0.1 to 2.3 g.cm<sup>-3</sup>, translated in terms of porosities from 96% to 50%) close to the human bones average density ranging from 0.19 to 1.99 g.cm<sup>-3</sup> and with porosities ranging from 3% to 95% depending on the bone type. The different distributions of void and matter in those structures enable the tuning of the global properties and mechanical behaviour of the lattice. For instance, considering the compressive strength ( $\approx 156$  MPa), elastic modulus ( $\approx 15$  GPa) and fatigue strength ( $\approx 105 \cdot 10^6$  MPa) of a cubic lattice with a 63% porosity, the Ti-6Al-4V cubic lattice can successfully replace human cortical tibia and femur<sup>68</sup>.

Knowing that ultimate strengths and elastic modulus of cortical areas are much higher than those from trabecular areas, bi-structural bone implant could be accurately subjected to stresses as native bones. This bi-structural architecture is currently achievable with the EBM process (**Figure 35**).



**Figure 35: Illustration of multi-structural stem with dense ( $1.06 \text{ g.cm}^{-3}$ ) and less dense ( $0.58 \text{ g.cm}^{-3}$ ) areas for femoral implantation. The CAD (b) and EBM-built prototype (c) were derived from femoral model (a). Scale bars of (a), (c) = 2 cm and (b) = 1 cm from<sup>85</sup>**

However, simply mimicking native bones structures and translating it to Ti-6Al-4V scaffolds might raise some mechanical issues. Indeed, highly porous structures derived from trabecular bones might not reach the very low trabecular elastic modulus (0.02 to 0.65 GPa)<sup>68</sup> but also display very poor fatigue strength<sup>86,87</sup>. Currently, porous Ti-6Al-4V lattices have been well characterized by compression tests. However, few tensile data are now available in the literature. Knowing the fact that human bones experiences both compressive and tensile stresses, deeper mechanical characterization in tension is needed to obtain the tensile properties<sup>68</sup>.

### 1.3.1.2 Porosity

According to the porous architecture of native bones, the effect of porosity on bone formation was assessed *in vitro* and *in vivo* with various pore sizes and shapes. The first study demonstrating the necessity to use pores for bone regeneration was done with three types of hydroxyapatite ceramics (solid, porous, coral-replicated porous tablets) in a rat ectopic bone model<sup>88</sup>. New bone only formed in porous scaffolds while no bone formed on the solid particles. In another major study where investigators used porous ceramics granules, the effect of pore sizes on the bone formation was investigated in dog femur<sup>89</sup>. For small granules (10 - 44  $\mu\text{m}$  and 44 - 75  $\mu\text{m}$ ) no bone tissue was able to grow inside the ceramics, while it was

the case for larger pores (100 - 150  $\mu\text{m}$ ). From those two major studies, resulted other studies focused on the effect of the global porosity and the pore sizes of implants on bone regeneration.

Currently, the commonly approved minimum pore size for bone regeneration in a porous material is set at 100  $\mu\text{m}$ <sup>83</sup>. At the research stage, pores between 150-250  $\mu\text{m}$  were found to be favourable for the expression and production of collagen and aggrecan, and for oxygen supply<sup>90</sup>. While larger pores < 300-400  $\mu\text{m}$  were reported to be more suitable for blood vessels formation and bone ingrowth<sup>88</sup>. With the EBM process, the minimum pore size reached until now is at 450  $\mu\text{m}$ , which is slightly greater than most pores in human bone (from 50  $\mu\text{m}$  to 300  $\mu\text{m}$  in trabecular human femur for instance)<sup>91</sup>.

Pore sizes requirements for *in vitro* and *in vivo* studies are different. Indeed, *in vitro* investigations need to be adapted to the cellular scale. This means that the investigated structural parameters should make possible to fulfil essential requirements such as cellular aggregation or low fluid velocity, for the appropriate cellular proliferation and viability<sup>84</sup>. While *in vivo*, there is a need for the implant to be sufficiently invaded by body fluids in order to have clots formation and stem cells recruitment for future bone formation<sup>83</sup>. Also, the introduction of porosities into a material decreases its mechanical performances. A compromise between high porosity and mechanical properties of the selected material should be done in regards to the target bone to be replaced.

#### 1.3.1.3 Surface curvature

Surface curvature was found to guide and control tissue formation *in vitro*. One of the major study conducted by Rumpler and co-workers, with long term cultures of murine pre-osteoblastic cells (MC3T3-E1) into 2 mm thick hydroxyapatite plates of 4 different types of shapes (triangular, square, hexagonal and circular), revealed this curvature dependency (**Figure 36**)<sup>92</sup>. Even though the total amount of new tissue was independent of the shape, the tissue formation kinetic was affected by the local curvature. Indeed, in the case of triangular, square and hexagonal plates, tissue formation started in the corners while it was directly uniform for circular ones. After, all the corners were filled with tissue, tissues formed a uniform concentric opening occurred in all shape types.



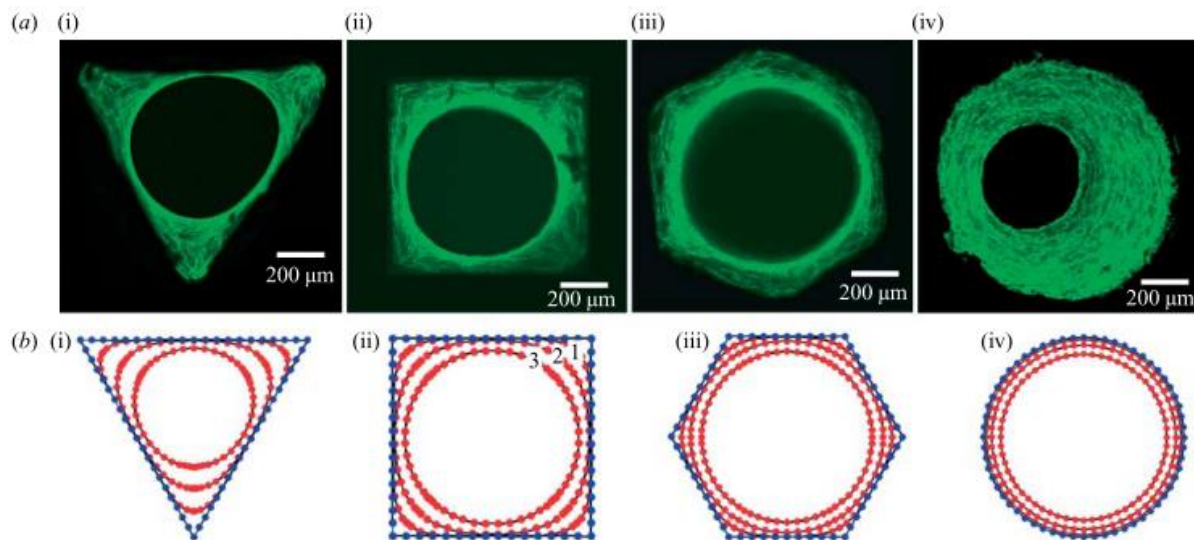


**Figure 36:** Actin stress fibres of MC3T3-E1 cells after 21 days (i-iii) and 30 days (iv) of cell culture (a) and the corresponding numerical simulation of tissue formation with a linear curvature dependent theoretical model (b). The fibres were stained with phalloidin-FITC and visualized under confocal laser scanning microscopy (from<sup>92</sup>)

This *in vitro* study confirmed that tissue formation occurs preferentially on concave surfaces instead of flat or convex ones, and that the rate of this formation increases almost linearly with curvature. This curvature driven tissue formation was also confirmed *in vivo* with mPCL- $\beta$ -TCP scaffolds in 30 mm segmental defect in sheep tibia mid-diaphysis<sup>93</sup>. The employed scaffolds contained regions with two different mean surface curvatures (**Figure 37**). The first type of regions had concave curvature (negative,  $-0.0295 \mu\text{m}^{-1}$ ) and were located at the intersection of two struts (**Figure 37B & C**, red lines). The second type of regions displayed convex curvature (positive,  $0.0055 \mu\text{m}^{-1}$ ) and were located on the strut surfaces (**Figure 37B & C**, blue lines).

After 12 months, implanted scaffolds were retrieved and the ECM formation was analysed, in regards to the simulated tissue formation obtained from a 3D curvature-driven model. The input geometry was a micro tomography representation of the initial scaffold. Histological and second-harmonic generation images revealed a high density of collagen fibres in regions of concave curvature and this ECM formation matched with the simulated tissue growth<sup>93</sup>. In this same study, they also used this 3D curvature-driven model to investigate the effect of pore size ( $300 \times 300$ ,  $600 \times 600$  and  $1200 \times 1200 \mu\text{m}^2$ ) and shape ( $0/90^\circ$  and  $0/60^\circ$  strut laydown patterns) on tissue growth. The model predicted pore filling for the smallest pore size of  $300 \mu\text{m}$  while no differences in the tissue rate formation were observed between the two types of pore shapes<sup>93</sup>.

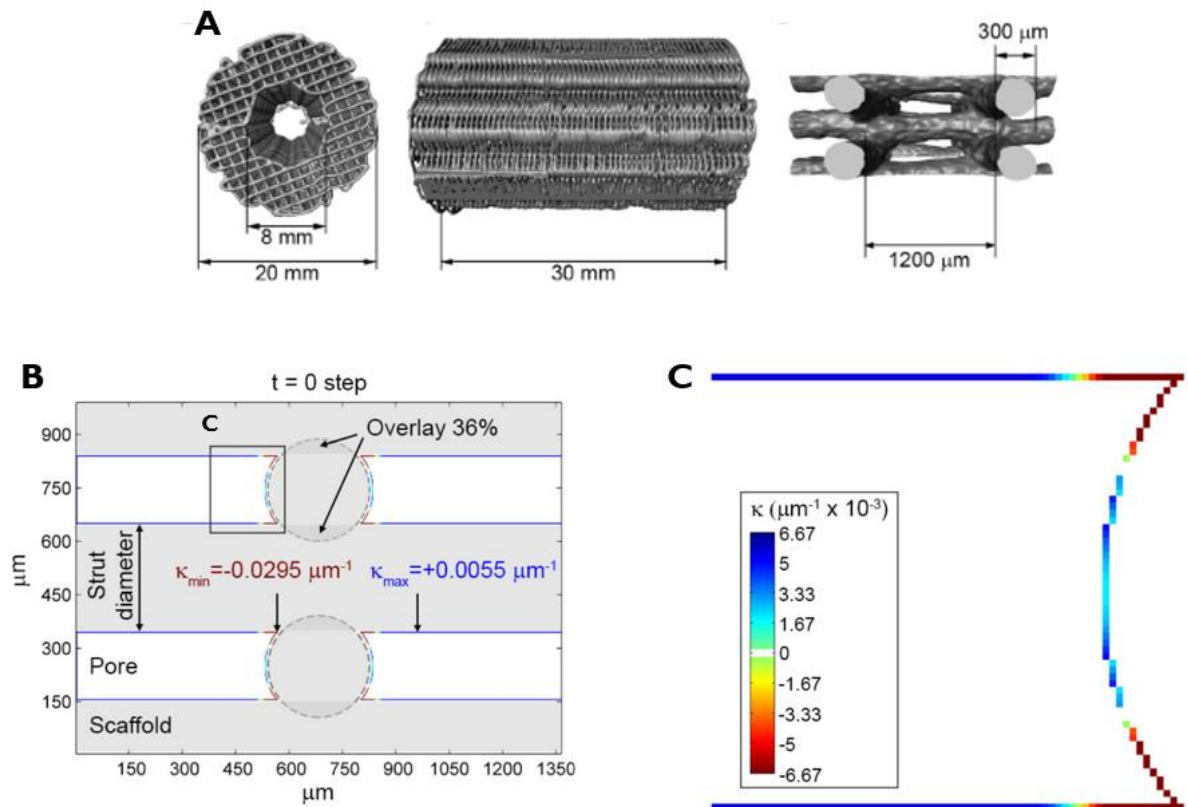


**Figure 37:** Representation of mPCL- $\beta$ -TCP scaffolds with 0/90° strut laydown pattern (A) and the corresponding mean surface curvature estimations (B) and zoom (C) in a unit volume of those scaffolds (adapted from<sup>93</sup>)

Bone graft substitutes with optimized surface curvature could accelerate the bone tissue regeneration within them. However, other structural parameters such as mechanical properties and pore size should not be omitted while designing the substitute.

#### 1.3.1.4 Topography

Topography relates to all different geometrical features that a surface can display. In regards to the cellular environment, a given surface can have four types of topographical features: macroscale ( $>100 \mu\text{m}$ ) that mainly affects cells at the colony level, microscale and submicroscale ( $0.1 - 100 \mu\text{m}$ ) that can influence a single cell, and nanoscale ( $1 - 100 \text{nm}$ ) which may interact with individual cell receptors (Figure 38)<sup>94,95</sup>.

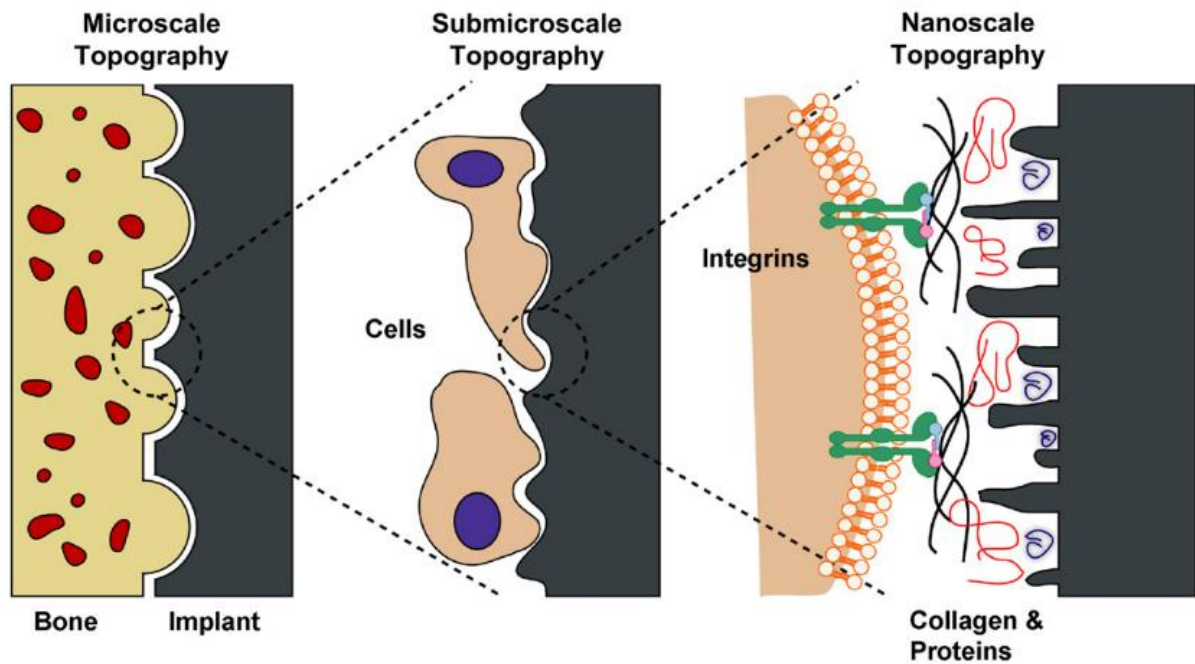


**Figure 38: Schematic representation of the topographical scales and their interactions with bone tissue constituents.** The macroscale ( $>100\ \mu\text{m}$ ) mainly affects cells at the colony level. The microscale and submicroscale topographies ( $0.1 - 100\ \mu\text{m}$ ) can influence a single cell while the nanoscale ( $1 - 100\ \text{nm}$ ) topography may interact with individual cell receptors (from<sup>95</sup>)

At the nanoscale, topographical effects are translated to the cells via the ECM distribution and the adsorbed proteins orientation and conformation in regards to the topography<sup>96</sup>. *In vivo*, the native ECM contains pits, pores, protrusions and fibres in the length scale of 5 to 200 nm<sup>97</sup>. Cell surface receptors such as integrins or growth factor receptors, are responsible for the cellular adhesion and response to the surrounding environment. The presentation of binding and signalling sites of adsorbed biomolecules to the cells is dependent on the effects of the nanofeature on the biomolecule, but also on the biomolecule size<sup>96</sup>.

Indeed, several studies on nano-rough surfaces highlighted the fact that proteins with dimensions in the same order of the roughness did not experience conformational changes. While proteins with much smaller or larger dimensions than the roughness experienced conformational alterations<sup>96</sup>. Conformational changes in proteins might interfere in their interaction with other molecules such as cellular receptors. With possible binding sites being hidden or more exposed with the nanotopography. The general trend is that nanotopography mainly influences the cellular adhesion, orientation and short and medium term responses<sup>96</sup>.

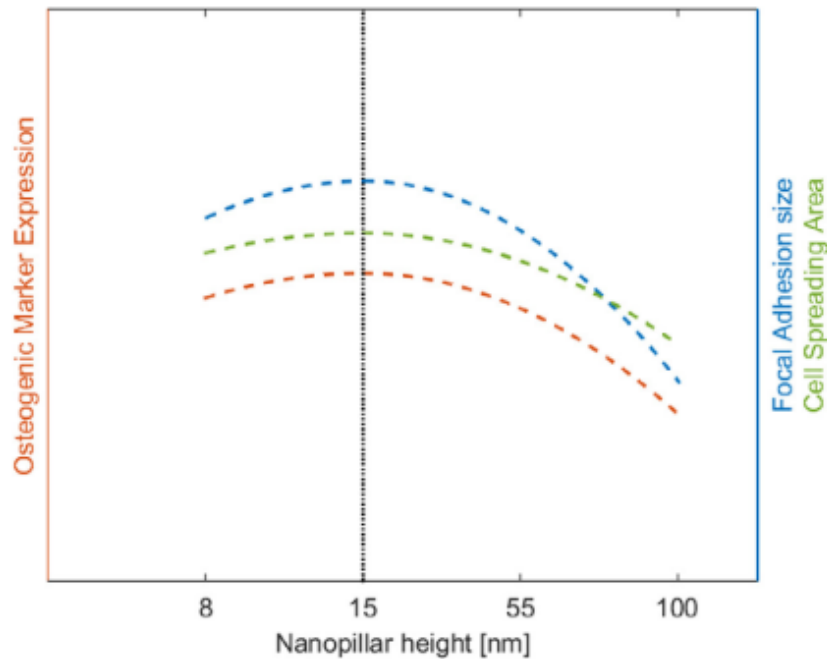


**Figure 39: Schematic representation of the relationship between nanopillar height and osteogenic marker expression, focal adhesion site and cell spreading area.** Derived from 20 articles (10 reviews and 10 singles studies investigating the effects of nanofeatures on the hMSCs osteogenic differentiation without osteogenic supplements in the culture medium (from<sup>94</sup>)

In the case of human mesenchymal stem cells (hMSCs), nanopatterns recognized to have the highest effect on their osteogenic differentiation was 15 nm high pillars compared to smaller (8 nm) and higher pillars (55 nm, 90 nm and 100 nm)<sup>94</sup>. As seen in **Figure 39**, this nanopattern induced osteogenic potential is correlated with a high focal adhesion size and cell spreading area. Those results, derived from the analysis of 10 reviews and 10 singles studies which investigated the effects of nanofeatures on the hMSCs osteogenic differentiation, suggest that this osteogenic induction might be partly regulated via cellular tension and mechanotransduction<sup>94</sup>.

In native ECM, microscale organization is known to influence cell morphology, migration and tissue organization. To study the effect of microscale topographies on cellular behaviour, the most commonly fabricated and employed micro patterns are grooves and pits with various width and depth<sup>98</sup> (**Figure 40**). Cellular migration is driven by asymmetrical chemical, mechanical or electrical external signals. In response to asymmetrical signals, cell morphology adapts and displays a leading and trailing edge.

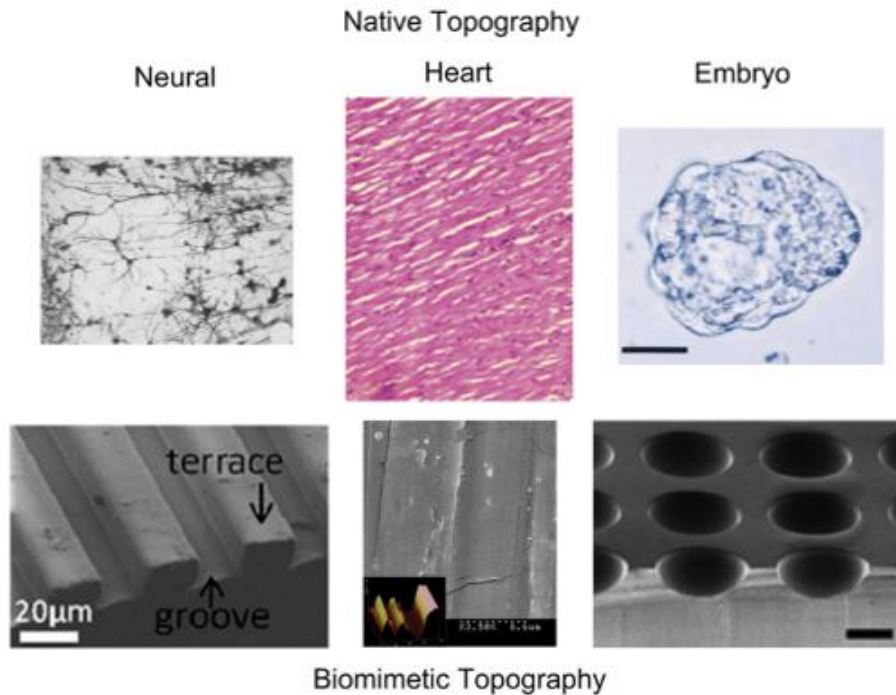


**Figure 40: Representation of native topography of neural, cardiac and embryonic tissues and the associated *in vitro* biomimetic topography approaches. The embryo scale bar is at 20  $\mu\text{m}$  and the pits scale bar at 500  $\mu\text{m}$  (adapted from<sup>98</sup>)**

Even if the microscale topography effects are highly dependent on the cell type, fibroblast, neuron, epithelial, endothelial and smooth muscle cells presented a higher average migration speed on grooved substrates than on flat ones. With a majority of cell types aligning and migrating along the major axis of the grooves<sup>98</sup>. In the case of osteoblasts, two studies using microscale grooves with widths between 10 to 76  $\mu\text{m}$  showed that only grooves with widths between 10 to 30  $\mu\text{m}$  influenced osteoblasts migration along the long axis. For bigger widths, no significant differences were seen on their orientation and migration. However in both cases, their osteogenic capacities were not affected<sup>99,100</sup>.

Pillars are another type of microscale topographical pattern used to study cellular behaviour. By modulating their spatial organization and dimensions, it is possible to generate a substrate with mechanical gradient (from softer to stiffer surface)<sup>98</sup>. A study using pillars of fixed diameter (2  $\mu\text{m}$ ) and increasing heights (0.97, 6.1 and 12.9  $\mu\text{m}$ ) on human MSCs, highlighted the fact that MSCs differentiation can be regulated with the substrate stiffness<sup>101</sup>. In an osteogenic and adipogenic bipotential medium, the osteogenic differentiation of hMSCs was favoured on rigid pillars (1566  $\text{nN}\cdot\mu\text{m}^{-2}$ , 483 kPa) after 14 days of culture. While the adipogenic differentiation was favoured on soft pillars (1.90  $\text{nN}\cdot\mu\text{m}^{-2}$ , 7 kPa)<sup>101</sup>. Well defined microscale topographies are great *in vitro* tools to study the adhesion, migration and differentiation of one cell type. In the case of bone substitutes, microscale topographies are the most investigated and used. There are produced through various surface treatments.

### 1.3.1.5 Surface treatment of metallic bone graft substitutes

The second important strategy to improve metallic bone substitute integration is the use of surface treatment. Those 2D treatments consist in modifying the surface reactivity to guide the material interactions with the surrounding living matter. Once implanted, implants are subjected to non-specific protein adsorption. In some cases, this adsorption can induce an excessive fibroblast recruitment and action, which can lead to a fibrous encapsulation process<sup>102</sup>. To avoid this fibrous encapsulation scenario, several surface treatment processes have been developed and are divided into two main categories: dry and wet processes (**Figure 41**). The surface can be mechanically modified to act as an anchoring layer, or chemically modified to form an additional layer with specific chemical properties.

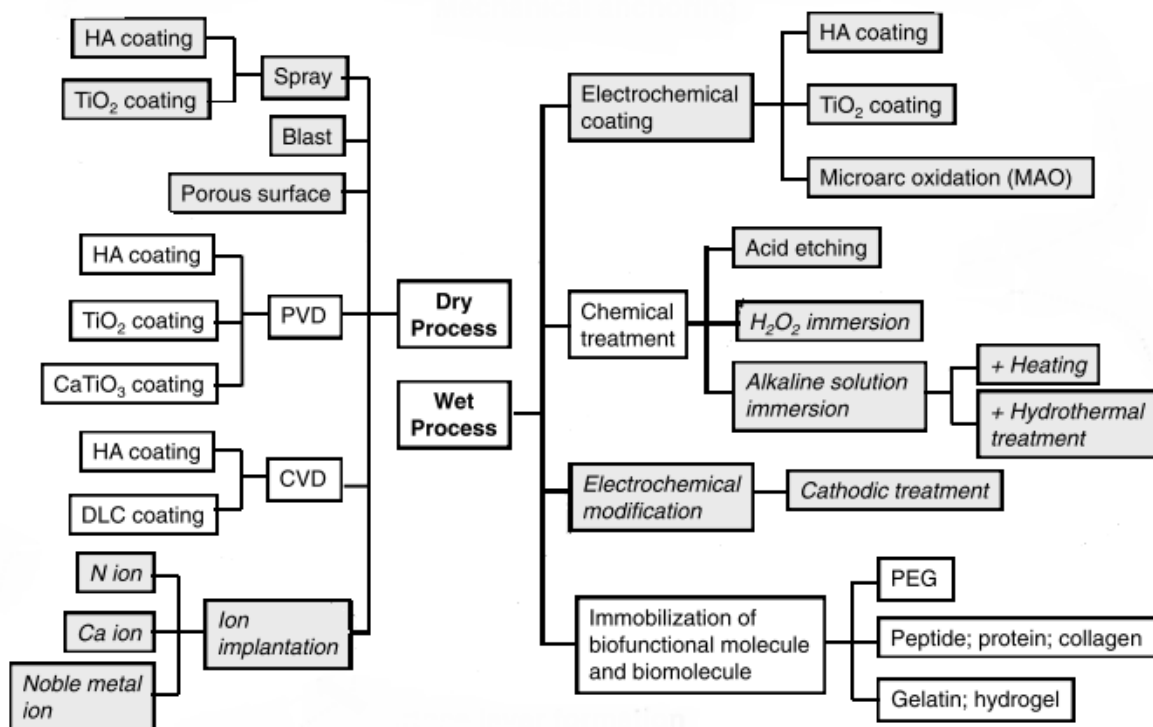


**Figure 41: Overview of the existing surface treatment processes used for metallic bone substitutes at the research and clinical stages<sup>69</sup>**

Thermal spray, physical vapour deposition (PVD) and ion implantation are physical methods that enable the surface roughness modification and the deposition of inorganic layers such as hydroxyapatite (HAP) or additional TiO<sub>2</sub>. Chemical methods such as chemical vapour deposition (CVD) of HAP or “Diamond like Carbon” (DLC) allow the deposition of HAP or carbon layers. Acid etching (using HCl), alkaline solution immersion (using NaOH), heat treatment and anodic oxidation modify the surface roughness but more specifically change the chemical composition with the introduction of OH groups. Those hydroxyls groups with their negative charges, are known to improve the surface hydrophilicity, attract calcium and phosphate ions and thus favouring proteins adsorption, bone tissue formation and mineralization at the surface<sup>103</sup>.



In the case of titanium alloys, they are naturally covered by a 3 to 7 nm layer of TiO<sub>2</sub>, which provides them their chemical inertness and corrosion resistance. Nevertheless, surface treatments are still employed to tune the microscale topography and increase the surface roughness. The surface roughness is commonly measured with a parameter called R<sub>a</sub>. This parameter represents an arithmetic average of the roughness profile in height. Surfaces with R<sub>a</sub> < 0.5 μm are considered as smooth, while minimally rough surfaces have R<sub>a</sub> between 0.5 to 1 μm. Moderately rough surfaces have a R<sub>a</sub> between 1 to 2 μm and those with a R<sub>a</sub> > 2 μm are strictly rough<sup>104</sup>.

This is done mostly via surface modification techniques such as acid etching, sand blasting, heat treatments and anodic oxidation (**Figure 42**)<sup>105</sup>. The aim of those modifications is to reduce the fibrous encapsulation that can occur at the implantation site, increase the bone-to-implant contact (BIC) and finally obtain a tightly fused and osseointegrated implant.

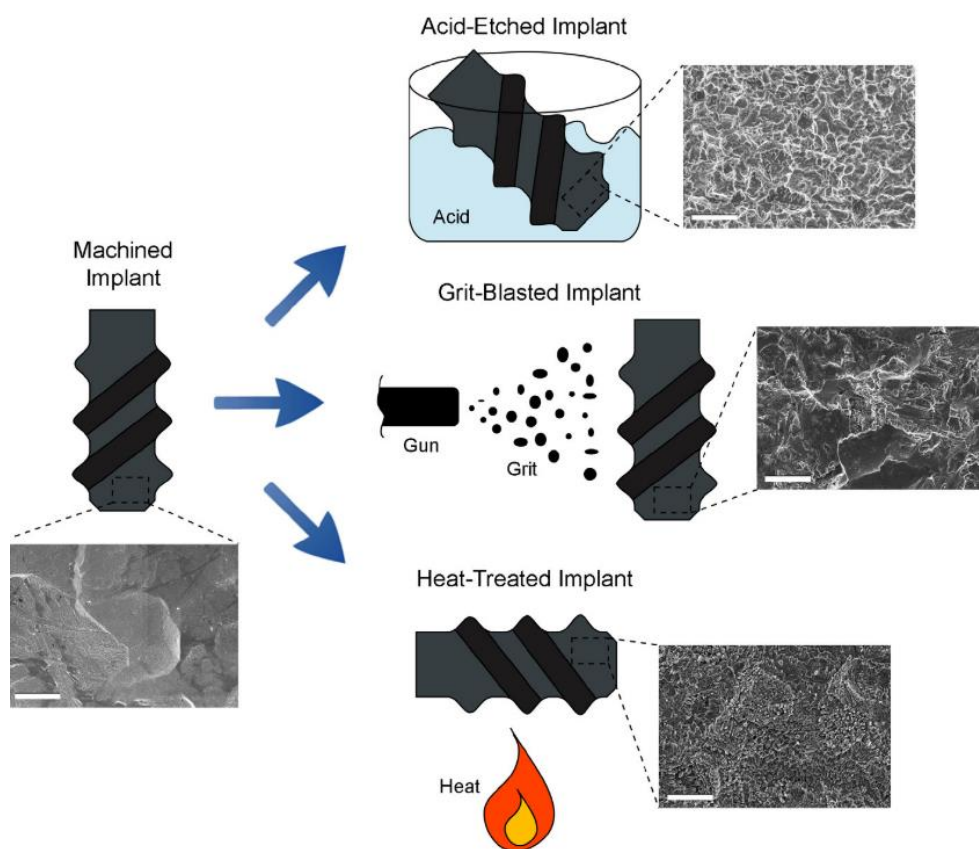


**Figure 42:** Schematic representation and corresponding SEM images of three main surface modification techniques applied to titanium implants to increase the surface roughness: acid-etching, grit-blasting, heat-treatment. Scale bar = 3 μm from<sup>105</sup>

#### 1.3.1.6 Surface treatment on AM-built titanium bone graft substitutes

At the research stage, various surface treatments have been tested on EBM-built Ti-6Al-4V structures to improve their osteoconduction. Heini et al built two types of Ti-6Al-4V lattice structure (diamond and hatched, **Figure 43**) by EBM and modified their surfaces with two chemical treatments, an acid etching in 37% HCl and an alkaline immersion in 10 M NaOH. They tested their bioactivity in simulated body fluid (SBF) dynamic immersion for 6 days (**Figure 43**)<sup>106</sup>. Both structures were successfully treated and the successive chemical surface

modification using HCl and NaOH induced *in vitro* apatite formation, as seen on the second EDX spectrum with the calcium and phosphate peaks (2, **Figure 43**).

Similar results were obtained in the study of Li et al on Ti-6Al-4V lattices built by EBM with honeycomb-like, orthogonal and layer structures after an alkali treatment in 10 M NaOH for 24h, a heat treatment at 600°C for 1h and an immersion in SBF for 14 days<sup>107</sup>. The osteoconductivity of treated lattices was then evaluated *in vitro* with the culture of osteoblast cells for 14 days and *in vivo* during 12 weeks in a cranial calvaria defect in rabbits<sup>107</sup>. Unfortunately in this case, non-statistical differences in cell morphology, viability and bone formation were observed between bare and apatite coated titanium implants.

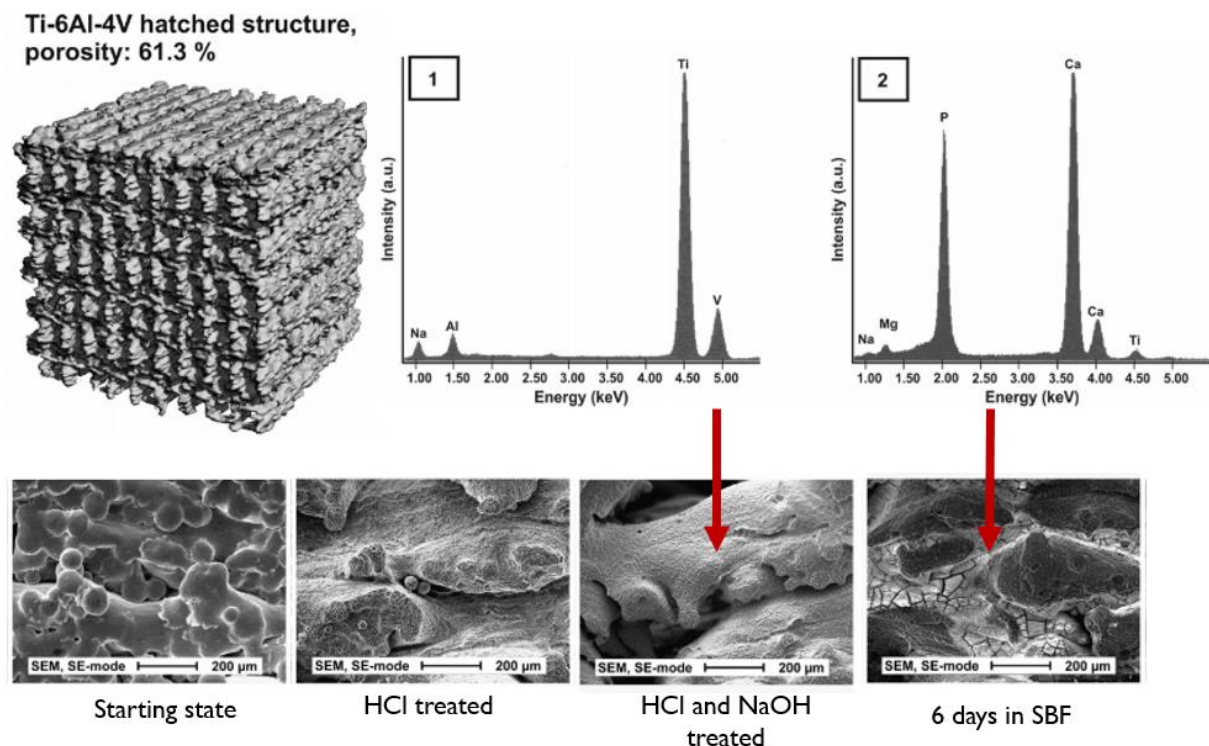


**Figure 43: Representation of the EBM built Ti-6Al-4V hatched lattice.** Scanning electron microscopy images of non-treated, acid treated (HCl), acid and alkali treated (NaOH) and simulated body fluid treated (SBF) surfaces and the corresponding EDX analysis for HCl/NaOH treated (1) and SBF treated (2) surface (adapted from<sup>106</sup>)

Amin Yavari et al also investigated the effects of different surface treatments on Ti-6Al-4V porous structures by comparing *in vitro* and *in vivo* bone regeneration performance of three surface treatments: acid-alkali (AcAl, c and g **Figure 44**), alkali-acid-heat (AlAcH, b and f **Figure 44**) and anodizing-heat treatments (AnH, d and h **Figure 44**). The treatment effects on the apatite forming ability, human periosteum-derived cell (hPDC) attachment, proliferation, osteogenic gene expression and bone regeneration were evaluated using an apatite forming ability test, cell culture assays and a critical-size femoral bone defect in rats<sup>108</sup>.

They found that AcAl improved the apatite forming ability even if it did not have any positive effect on cell attachment, proliferation and osteogenic gene expression. In contrast, AnH did not improve the apatite forming ability but showed significantly better cell attachment, cell proliferation and expression of osteogenic markers. The AlAcH treated scaffolds were

between AnH and non-coated scaffolds in terms of apatite forming ability and cell responses. *In vivo*, AcAl resulted in significantly larger volumes of newly formed bone within the pores as compared to AnH (bone volume, b **Figure 44**). After 12 weeks of implantation (bone volume, a **Figure 44**), no differences were seen between the three surface treatments suggesting that the applied surface treatment are important for the early stages of the bone regeneration.

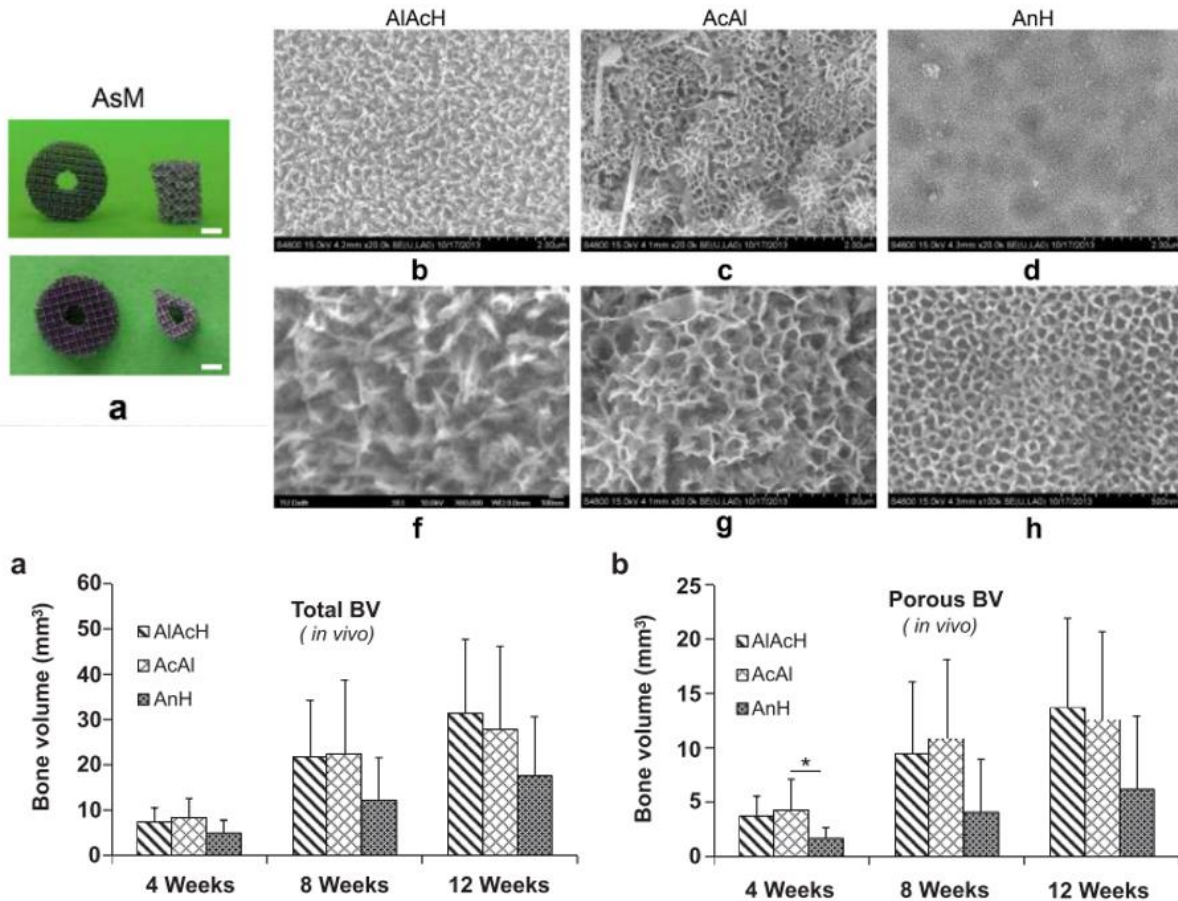


**Figure 44:** As manufactured SLM built Ti-6Al-4V implants (a). Scanning electron microscopy images of acid-alkali (AcAl, c and g), alkali-acid-heat (AlAcH, b and f) and anodizing-heat (AnH, d and h) surface treated samples. *In vivo* total bone volume (a) and porous bone volume (b) of surface treated Ti-6Al-4V scaffolds (adapted from<sup>108</sup>)

A coating made of tantalum by chemical vapor deposition (CVD) was also tested on EBM-built porous Ti-6Al-4V scaffolds by Li et al<sup>109</sup>. The biocompatibility and bone ingrowth of Ta-coated scaffolds were evaluated using mesenchymal stem cells (MSCs) *in vitro* and a goat implantation model *in vivo*. As illustrated in **Figure 45**, the Ta coating was successfully deposited at the scaffold surface (left panel, **Figure 45**). More cells were present on Ta-coated scaffolds compared to non-coated ones (proliferation, **Figure 45**) and the new bone formation percentage (bone volume/pore volume, **Figure 45**) in Ta-coated scaffolds was significantly higher than in porous Ti-6Al-4V scaffolds (24% over 20%) after 12 weeks<sup>109</sup>. EBM-built scaffolds combined with this surface treatment could be potentially used for clinical application in orthopaedics.

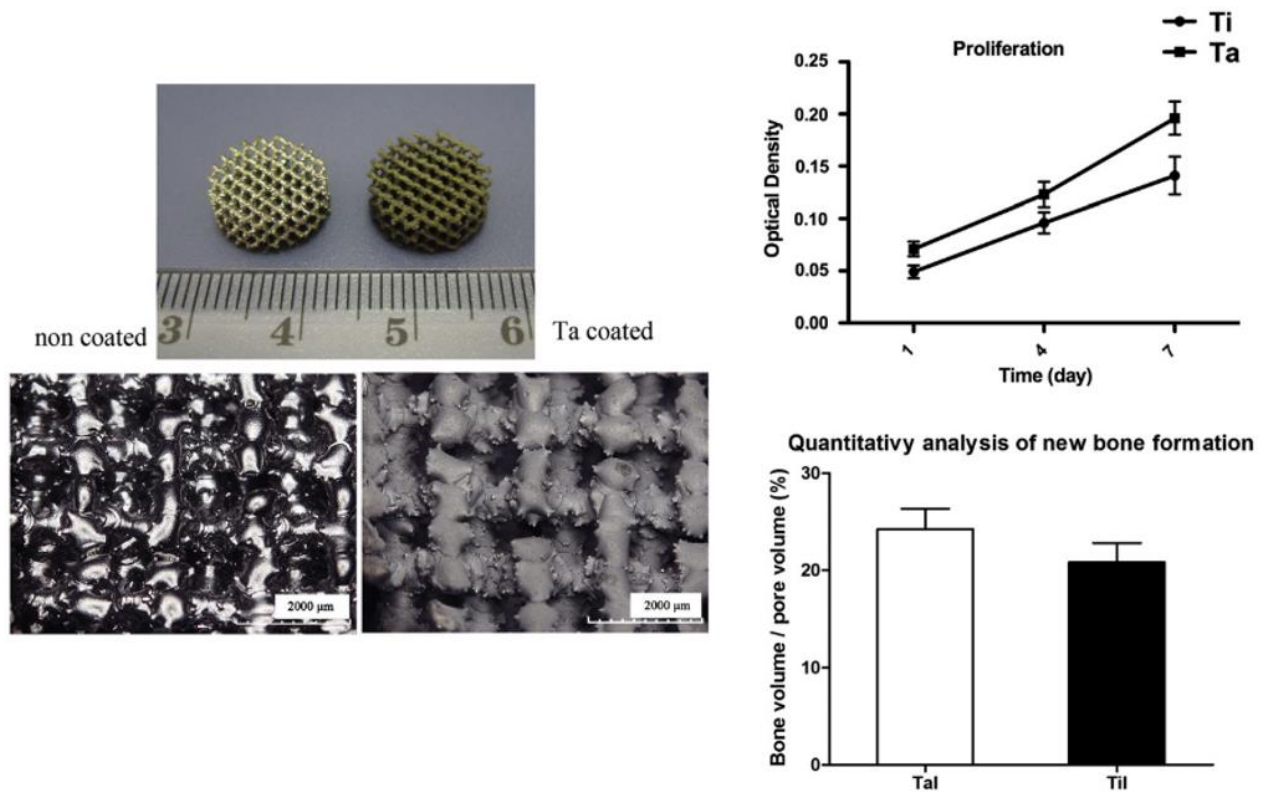


**Figure 45:** Picture of non-coated and Ta-coated EBM-built Ti-6Al-4V scaffolds and their respective surface microscopic images (left panels). Control of the mesenchymal stem cells proliferation on bare and Ta-coated scaffolds after 1, 4 and 7 days (right). Quantitative analysis of the bone formation on Ta-coated and bare scaffolds 12 weeks post-implantation in goat iliac crests (adapted from<sup>109</sup>)

A coating made of magnesium (Mg) deposited by arc ion plating was also investigated for the osteoconduction of porous Ti-6Al-4V implants<sup>110</sup>. The magnesium coating was successfully fabricated on porous Ti-6Al-4V scaffolds, *in vitro* studies on scaffolds of the cytotoxicity and proliferation of MC3T3-E1 cells showed that the coating is biocompatible and induces a significant increase of proliferation at 7 days (CCK8 assay, **Figure 46**). And finally, *in vivo* studies in rabbit femoral condylar defects proved that the coating could significantly promote bone regeneration after implantation for 4 and 8 weeks, compared to bare porous Ti-6Al-4V (A1,B1,C1 and D1, bone volume fraction, **Figure 46**)<sup>110</sup>.



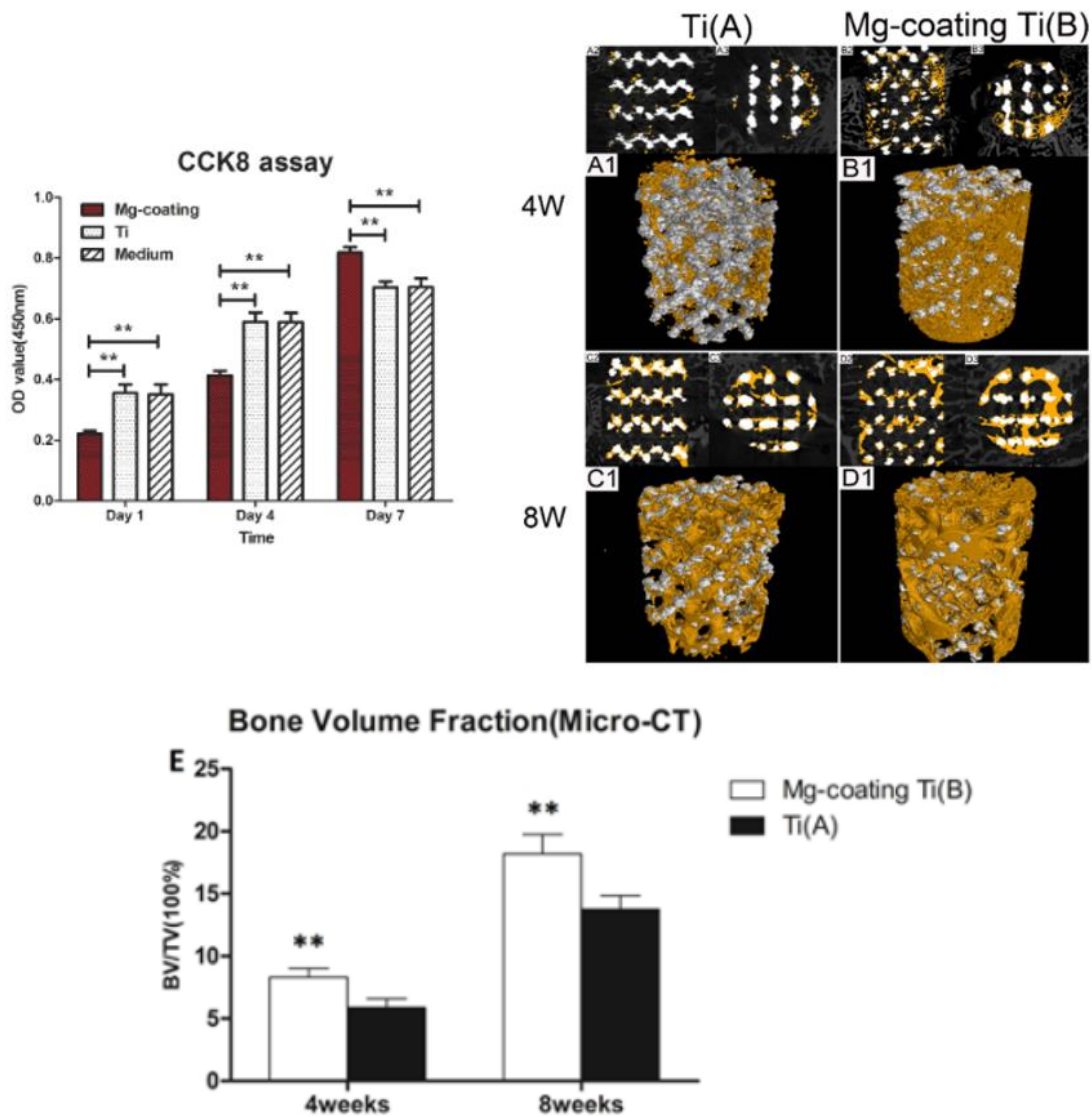


**Figure 46:** Control of MC3T3 cells proliferation with CCK8 assay on magnesium (Mg) coated and bare Ti-6Al-4V scaffolds (left). Bone volume fraction on bare and magnesium coated Ti-6Al-4V scaffolds implanted for 4 and 8 week in rabbit femoral condylar defects: micro CT representation (right) and the corresponding quantification (bone volume/total volume, BV/TV) (bottom, adapted from<sup>110</sup>)

At the clinical and market stages, surface treatments without bioactive molecules that are investigated or used, are in the same range as the studies detailed in this part. Clinical trials with micro and nanostructured surface roughness, with metallic bone graft substitutes coated with ceramic or another metallic layer, or with morphological changes through acid etching or alkali and heat treatments (to improve and promote the apatite layer formation) are on-going<sup>21</sup>. Plasma, PVD and anodization surface treatment techniques are already used for either HAP, TiN, ZrN or DLC layers deposition on commercialized medical devices and implants (Ceramed®, DOT medical implant solutions)<sup>111,112</sup>.

## 1.4 Bioactive molecules used in bone graft substitutes

The mechanism of bone repair is complex and involves several important growth factors. As presented in the last two previous sections (1.3.1.5, 1.3.1.6), structural optimization and surface properties modification are employed to enhance the integration of titanium bone graft substitutes. In order to actively trigger bone regeneration, specific bioactive molecules can be used. These bioactive molecules can interact with stem cells and inflammatory cells that are at the origin of the bone formation and regeneration via cell surface receptors. The interaction of the bioactive molecules with the cell surface receptors trigger biochemical signalling. In this part, the bioactive molecules currently used, the strategies to incorporate them and deliver them through bone substitutes will be detailed.

### 1.4.1 BMP-2 (adapted from Biomaterials review<sup>21</sup>)

Bone morphogenetic proteins (BMPs) belong to the transforming growth factor (TGF)  $\beta$  superfamily of proteins and are synthesized by osteoprogenitor cells, osteoblasts, chondrocytes and platelets. BMPs, and other growth factors used for bone repair, are obtained through protein purification, using cDNA cloning and protein expression in bacterial or mammalian cells<sup>113</sup>.

BMP-2 is an important osteogenic factor that induces endochondral and intramembranous ossification, chondrogenesis and triggers mesenchymal stem cells differentiation towards the osteoblastic lineage. This protein is critical for the maintenance of the skeleton integrity and for bone fracture healing. BMPs are dimeric molecules constituted by two polypeptides chains of about 120 amino acids.

More particularly, BMP-2 has two polypeptides chains of 115 amino acids with a total molecular weight of 44kDa. This protein has an isoelectric point is at 9.15 and is soluble at pH below 6<sup>113</sup>. The BMP-2 protein monomer is stabilized by three disulphide bonds, represented by white and yellow bridges in the tertiary structure (**Figure 47**) and more generally, BMPs are naturally found in their dimeric form<sup>113,114</sup>.



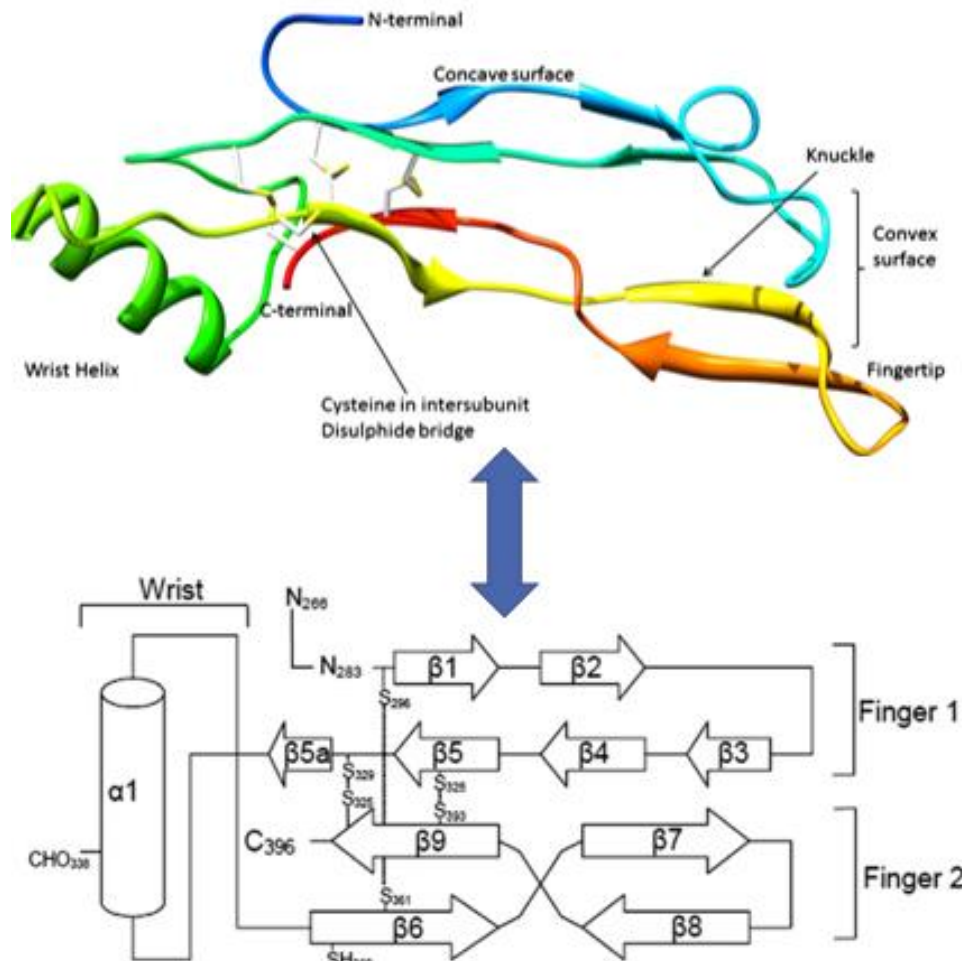


**Figure 47: BMP-2 monomer protein tertiary structure (top) and its schematic diagram representation (bottom).** The protein structure is stabilized by three disulphides bonds, represented in white and yellow in the tertiary structure and by S-S links in the corresponding schematic diagram<sup>113,114</sup>

A large amount of literature has already been published on BMP-2 combined with a type I collagen sponge as carrier, for uses in open tibial shaft fractures and in spinal fusion. In this case, BMP-2 is associated with a titanium or PEEK cage for interbody fusion use (**Figure 48**). A controversy related to this product emerged in 2011 after adverse effects were reported in response to the supra-physiological doses delivered (1/5 mg/mL of BMP-2 for human use), and off-label use (~ 85%), including inflammation and pain<sup>115,116</sup>. It is now known that bone repair in response to BMP-2 is dose-dependent<sup>117</sup> and that high doses can lead to osteolysis.

However, to date, it is also acknowledged that BMP-2 remains a powerful activator of bone repair, whose delivery needs to be further optimized. Alternative sources of BMP-2 combined with ceramics are emerging, such as those produced in CHO-cells<sup>118</sup> or in E-coli<sup>119,120</sup>.

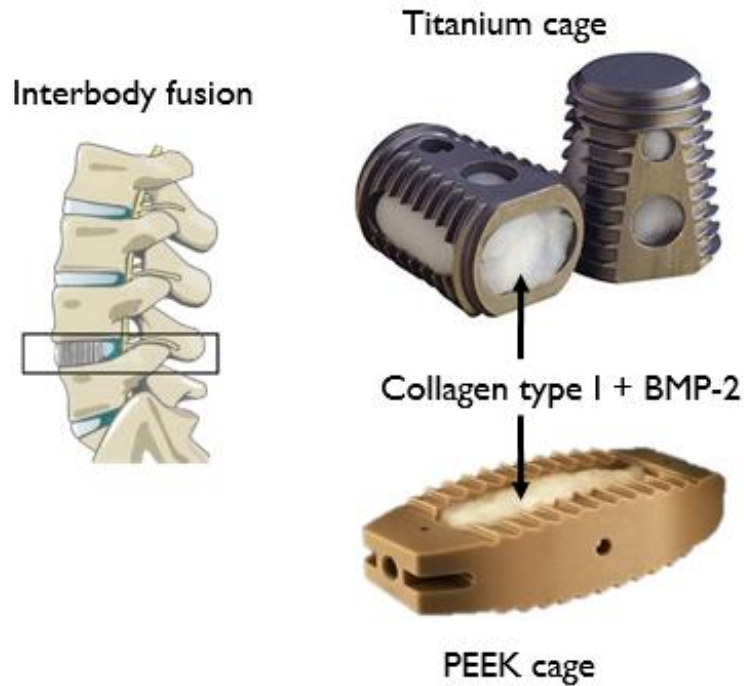


**Figure 48: Commercial use of BMP-2 in infuse® Bone Graft in combination with LT-CAGE® for anterior lumbar interbody fusion (ALIF) procedure. Illustration of the interbody fusion procedure (left) and the infuse® Bone Graft in combination with LT-CAGE® (right, adapted from Medtronic)**

At the research stage, intensive studies are carried out in order to better understand how growth factors, especially BMP-2, can be efficiently trapped by materials or immobilized at their surface<sup>121</sup> and how they interact<sup>122</sup>, in order to improve the *in vivo* delivery and release profiles. Once *in vivo*, the pathophysiological context can greatly influence the release of bioactive molecules from the biomaterial<sup>123</sup>.

#### 1.4.2 BMP-7 (adapted from Biomaterials review<sup>21</sup>)

BMP-7 is the second bone morphogenetic protein used as an osteoinductive growth factor in bone repair and is especially active in mature osteoblasts. BMP-7 has two polypeptides chains of 139 amino acids subunits with a total molecular weight of 49kDa. This protein has an isoelectric point at 7.74 and is soluble in acidic conditions<sup>124</sup>.

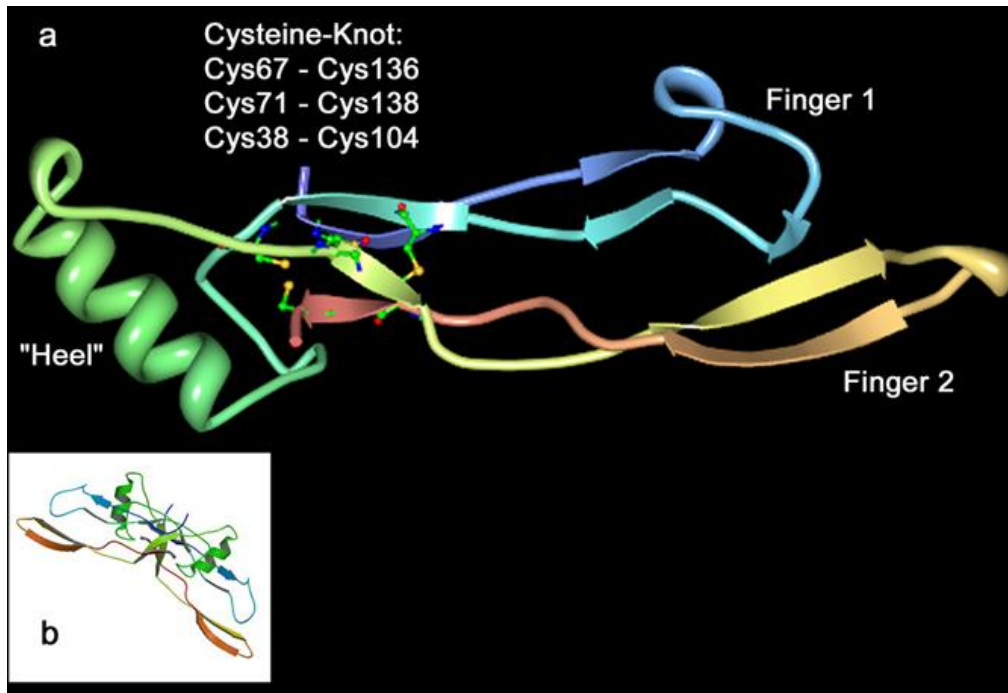


**Figure 49: Tertiary structure of the BMP-7 monomer (a) and dimer (b).** As BMP-2, BMP-7 monomer is stabilized by three disulphides bonds located at the listed cysteine-knots (a)<sup>125</sup>

As BMP-2, BMP-7 has also been investigated for clinical trials in bone reconstruction. BMP-7 was associated with type I collagen in the form of a paste (OP-1 putty, Olympus Biotech) and used under a humanitarian device exemption (< 4000 patients) for recalcitrant long bone non-unions and spine surgery. When the production stopped, the reports about its efficacy and safety were satisfactory<sup>126</sup>. Interestingly, a recent review highlighted the important role of kidneys in bone metabolism and BMP-7 emerged as one of the important active molecules produced in the kidneys that is involved in different pathways associated with bone formation<sup>127</sup>. Experiments in a sheep model showed that the BMP-7 paste can be combined with an architected scaffold to trigger efficiently the repair of long bones (**Figure 50**)<sup>128</sup>.

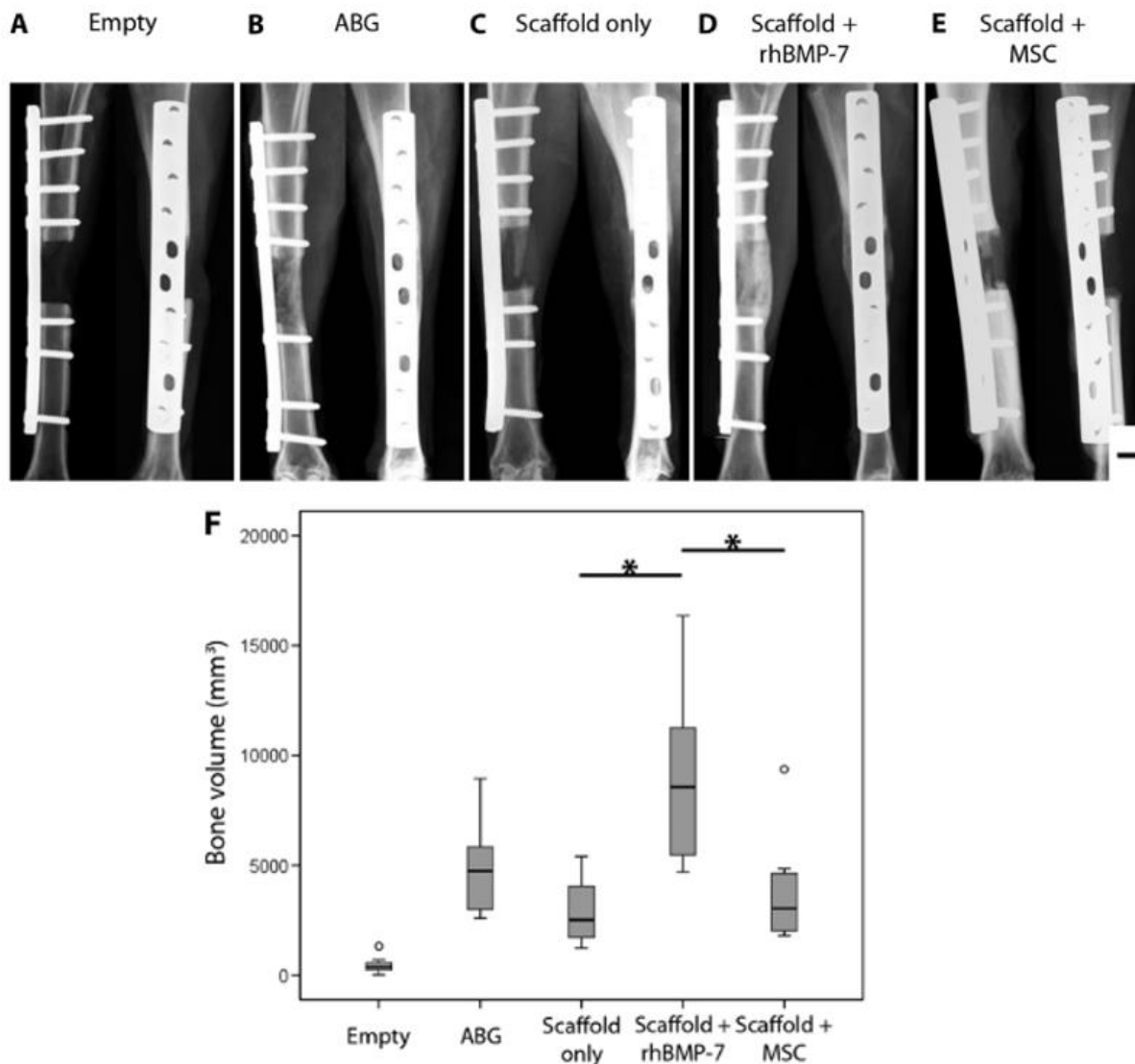


**Figure 50: Evaluation of the bone regeneration in mPCL-TCP scaffold filled with collagen containing BMP-7 after 3 months in a critical size sheep bone defect. (A to E) Representative x-ray images showing an empty control defect (A) Defect reconstructed with cancellous bone graft from the iliac crest (B) Defect treated with the mPCL-TCP scaffold only (C) Defects augmented with scaffold + rhBMP-7 (D) or scaffold + MSCs (E). Scale bar, 1 cm. (F) Median bone volumes were determined by CT (adapted from<sup>128</sup>)**

#### 1.4.3 PDGF (from Biomaterials review<sup>21</sup>)

Recombinant human platelet-derived growth factor BB (rhPDGF-BB), also known as becaplermin, stimulates the recruitment and proliferation of osteoblastic cells and mesenchymal stem cells<sup>129</sup>. It also promotes the formation of new blood vessels at the site of healing by increasing vascular endothelial cells, pericytes and smooth muscle cells responses. rhPDGF-BB was approved as a Class III combination medical device/drug product in 2015 for hindfoot and ankle fusion in specific categories of patients suffering from different types of arthritis with operative evidence indicating the need for a supplemental graft material. Currently, a solution of PDGF is associated to  $\beta$ -TCP particles, a scaffold that provides osteoconductivity for new bone formation.



**Figure 51: Clinical use of PDGF-BB in Augment® Bone Graft.** Augment® bone graft is composed of  $\beta$ -TCP particles and recombinant human PDGF-BB in solution (Wright Medical Group)

A recent clinical study on 434 patients dedicated to hindfoot or ankle arthrodesis, treated with rhPDGF-BB/ $\beta$ -TCP, resulted in comparable fusion rates, less pain, and fewer side effects as compared with treatment with autograft<sup>130</sup>. In particular, the safety profile was improved and compared to autograft due to the elimination of harvest site pain and morbidity, since there is no need to graft bone. More recently, a comparative study between PDGF-BB/ $\beta$ -TCP and autograft showed that there is a relation between the amount of graft material and successful hindfoot and ankle arthrodesis. Graft material filling > 50% of the fusion space at 9 weeks, regardless of type or origin, was associated with significantly higher fusion rates at 24 weeks<sup>131</sup>.

#### 1.4.4 Parathyroid hormone PTH (from Biomaterials review<sup>21</sup>)

Parathyroid hormone (PTH) plays a central role in regulating calcium-phosphate metabolism. Its production increases in response to low serum calcium levels. Moreover PTH enhances the Wnt-beta catenin pathway that is central to osteogenesis and bone formation. It is also used as a drug to treat osteoporosis. The products developed by Kuros (KUR-111/112/113) contains PTH trapped in a natural fibrin matrix combined with a structural ceramic component (HAP/TCP granules), to provide mechanical stability during healing. To date, only their MagnetOs granules (granules containing magnetic particles) have obtained CE mark approval in the EU and 510(k) approval in the US. The bioactive products are based on an engineered active fragment of human parathyroid hormone (PTH(1-34)), linked to a transglutaminase substrate for binding to fibrin as a delivery mechanism, and cell-invasion matrix with an intervening plasmin-sensitive link. It was initially tested in femur and humerus defects of female sheep<sup>132</sup>, where it was both osteoconductive and osteoinductive. KUR-111 is a bone graft substitute and was initially developed for the treatment of tibial plateau fractures, where success was reported in a Phase IIb clinical study (NCT00533793, ended in 2011).



**Figure 52: Fracture treatment with KUR-111.** KUR-111 is composed of a fibrin matrix and HA/TCP granules with a paste of parathyroid hormone (PTH) (Kuros<sup>133</sup>)

This study assessed the safety and efficacy of KUR-111 in 183 patients across 30 centers in Europe and Australia. At 16 weeks, 84% of autograft treated patients and 84% of patients treated with the higher dose of KUR-111 had radiological fracture healing, but no results were published in a peer-reviewed article. KUR-113 was developed for fractures at risk for incomplete healing. It was initially tested in tibial shaft fractures in a Phase II clinical study and is now being tested for spinal fusion in patients with degenerative disc disease. KUR-112 is a candidate product for patients with solitary bone cysts and was tested pre-clinically in horse model<sup>134</sup>.

#### 1.4.5 Bioactive molecules in AM-built titanium bone graft substitutes

At the research stage, several strategies are investigated to incorporate and then deliver bioactive molecules directly from bone graft substitutes in order to help the bone repair and regeneration at the implantation site. For instance, bioactive molecules can be adsorbed at the surface by dip coating. In this case, the rate of adsorption and release will depend on the molecule affinity with the surface. They can also be co-precipitated in mineral materials, in this case they are released by the material degradation. Another strategy is to encapsulate the molecules in natural or synthetic degradable polymers. Similarly, natural extracellular matrix molecules (such as fibronectin, fibrin or acid hyaluronic), which can have natural binding sites with some of the bioactive molecules, are also used either as carrier or as coating on the substitute. And finally, chemical immobilization with covalent tethering is also investigated even though, in some cases, this method reduced the molecule bioactivity<sup>123</sup>. In the case of porous titanium bone graft substitutes, the incorporation of bioactive molecules is either done by adsorption or by the use of natural ECM molecules.

For instance, in the study of Van der Stok et al.<sup>135</sup>, they investigated the osteoinductivity of porous Ti-6Al-4V scaffolds with incorporated gelatine gels containing either BMP-2, fibroblast growth factor-2 (FGF-2) or both growth factors in critical femoral bone defects in rats (A, B, C and D, **Figure 53**). Scaffolds with BMP-2 gels gave an early increase of the bone regeneration (0–4 weeks) whereas those with FGF-2 gels gave a late increase (8–12 weeks, not shown here). They observed that stimulatory effects of 0.6  $\mu\text{g}$  FGF-2 were similar to a fivefold higher dose of BMP-2 (3  $\mu\text{g}$ ) and that BMP-2/FGF-2 gels gave more bone outside the porous titanium scaffolds than gels with only BMP-2 or FGF-2 (E, **Figure 53**).



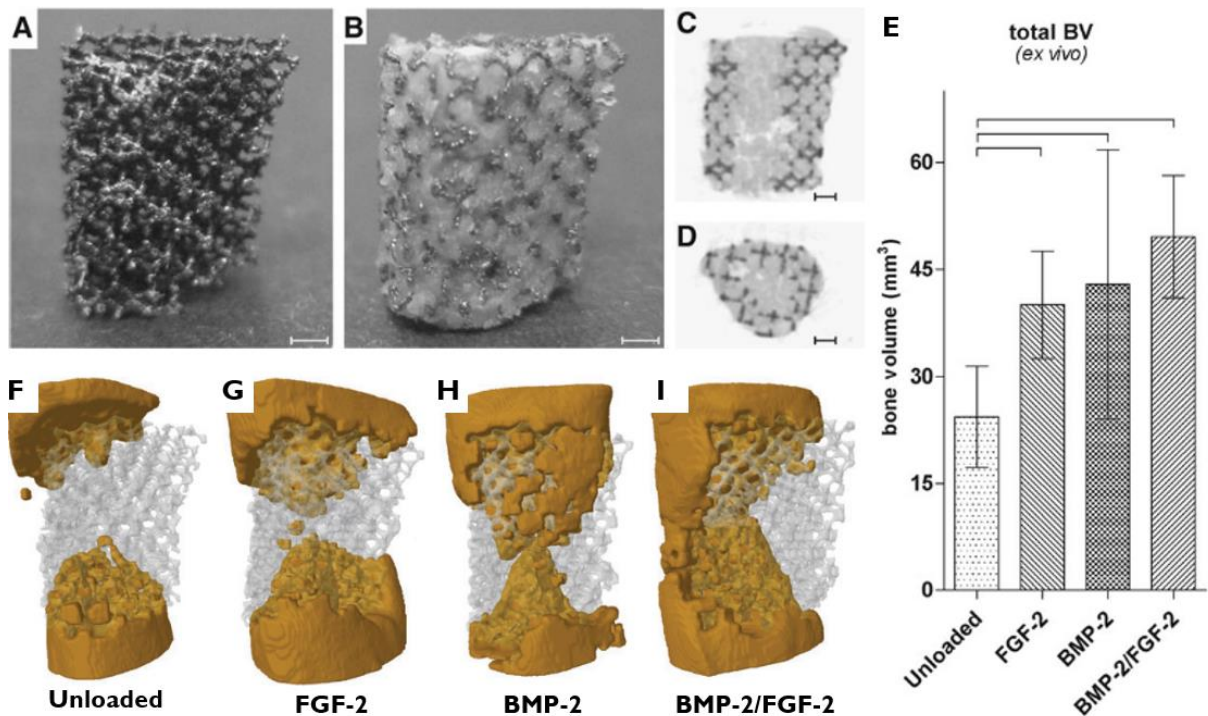


**Figure 53: Evaluation of the bone regeneration 12 weeks after implantation in critical size rat femoral bone defect into Ti-6Al-4V scaffolds with FGF-2 and BMP-2 growth factors incorporated into gelatine gel.** Photographs of porous titanium scaffolds in the shape of the 6-mm bone segment that was replaced during the animal experiment before (A) and after (B) incorporation with colloidal gelatine gels. Micro-CT images of perpendicular (C) and horizontal (D) cross sections of porous titanium scaffold (black) incorporated with colloidal gelatine gels containing iodine-based radiographic contrast agent ioxaglate (gray). Scale bar = 1mm. Representative 3D micro-CT images of bone bridging the porous titanium scaffolds containing unloaded (F), FGF-2 (G), BMP-2 (H), or BMP-2/FGF-2 (I) gels after 12 weeks. Ex vivo micro-CT quantification of total BV after 12 weeks ( $p < 0.05$ ) (adapted from<sup>135</sup>)

In another work, they studied the bone regeneration into porous titanium scaffolds coated with osteostatin, an osteoinductive peptide composed of the 107–111 domain of the parathyroid hormone (PTH)-related protein (PTHrP)<sup>136</sup>. The scaffolds were built by SLM, their surface were treated with an alkali-acid-heat treatment and then coated with osteostatin through soaking in a 100nM solution for 24h. Osteostatin-coated scaffolds contained 0.1  $\mu\text{g}$  peptide/g of titanium and 81% of the protein was released *in vitro* within 24h (A, **Figure 54**). *In vivo* experiments showed that the osteostatin-coated porous titanium scaffolds enhanced early bone regeneration in critical-sized rat femoral bone defects (B, **Figure 54**).

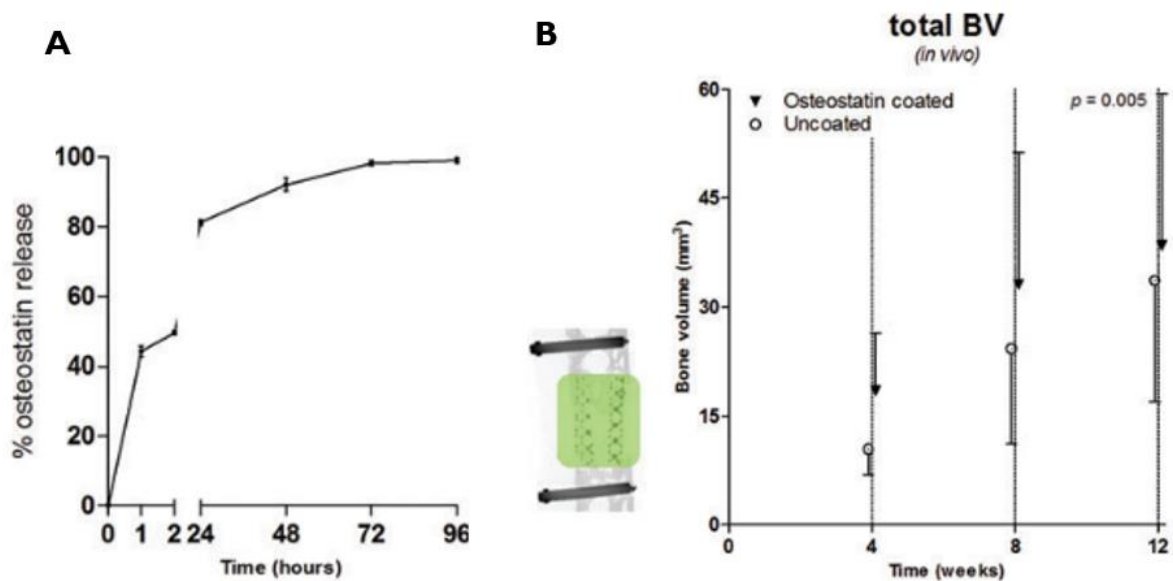


**Figure 54: Evaluation of the in vitro osteostatin release and in vivo bone regeneration of osteostatin-coated Ti-6Al-4V scaffolds 12 week after implantation in critical size rat femoral bone defect.** In vitro osteostatin release after loading femur-shaped titanium implants for 24 h in 100nM osteostatin in phosphate-buffered saline solution (A). Total bone volume on in vivo microcomputed tomography (mCT) scans made after 4, 8, and 12 weeks (B) (adapted from<sup>136</sup>)

In a more recent study, Van der stok et al. used a physiologically concentrated fibrin gel loaded with bone morphogenetic protein-2 (3  $\mu\text{g}$  of BMP-2) in porous titanium scaffolds<sup>137</sup>. The implants were used in a critical size femoral bone defect in rat and as a control, some implants were either left empty or filled with fibrin gels without BMP-2 (**Figure 55**). The bioactive bone substitute completely regenerated and bridged the critical-sized bone defects within 8 weeks. After 12 weeks, femora were anatomically re-shaped and revealed open medullary cavities in the case of the implants containing BMP-2<sup>137</sup>.

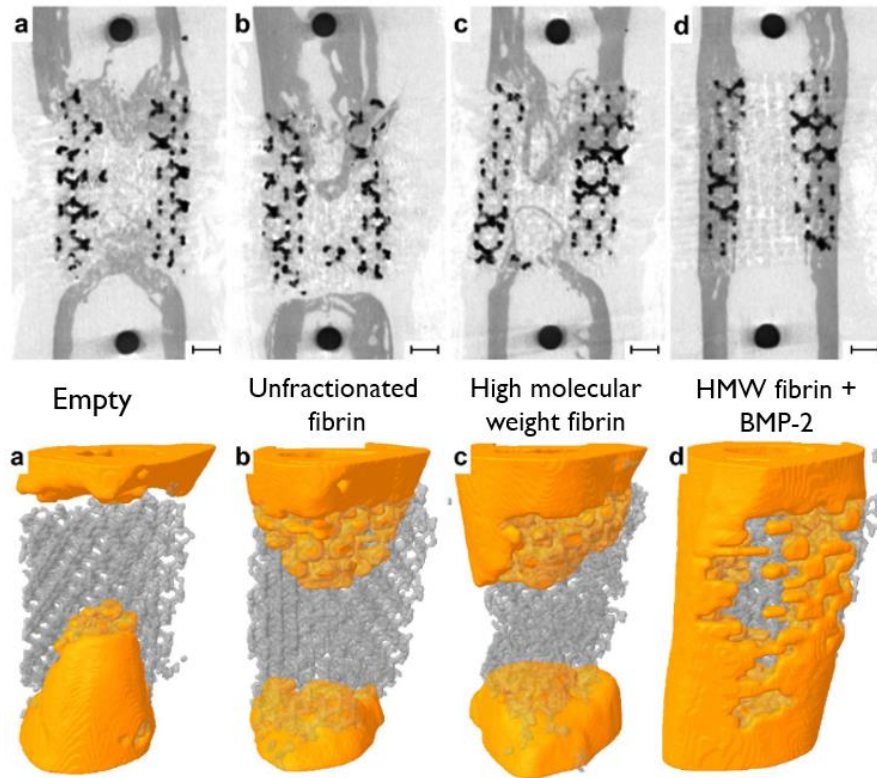


**Figure 55: Evaluation of the bone regeneration of porous Ti-6Al-4V scaffolds filled with fibrin containing BMP-2 after a 12 week implantation in critical size femoral bone defect in rat. Representative transversal ex vivo  $\mu$ CT images of grafted segmental femur defects and the corresponding 3D  $\mu$ CT images showing the average extend of bone bridging of the empty (a), unfractionated fibrin (UNF-Fb, b), high molecular weight fibrin (HMW-Fb, c), as well as the HMW-Fb-BMP-2 (d) group (adapted from<sup>137</sup>)**

#### 1.4.6 Bioactive molecules on bone graft substitutes in the team

##### 1.4.6.1 Polyelectrolyte multilayer (PEM) films

Polyelectrolytes are a subclass of polymers made of macromolecules containing in their repeat unit an electrolyte group. Like electrolytes, when polyelectrolytes are dissolved into an aqueous solution, they dissociate into charged polymers. The resulting solution is electrically conductive even though it remains electrically neutral from the presence of counter ions either positively or negatively charged<sup>138</sup>. The formation of polyelectrolyte multilayer (PEM) films is based on the successive adsorption of polyelectrolyte layers that are positively charged (polycation) or negatively charged (polyanion) on a charged substrate (**Figure 56**).

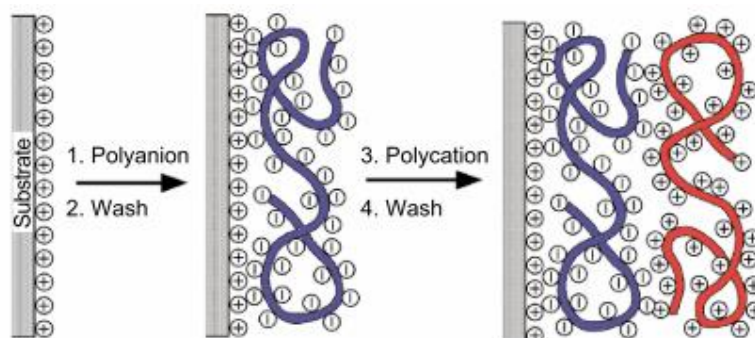


**Figure 56: Schematic representation of PEM film formation.** The polyanion is represented in blue and the polycation is represented in red<sup>139</sup>

The film self-assembles and self-organizes through mainly electrostatic (ionic) interactions as well as non-electrostatic interactions such as hydrophobicity<sup>140</sup>, hydrogen bonds<sup>141</sup> or Van der Waals forces<sup>142</sup>. The layer-by-layer (LbL) method to build PEM films was introduced more than 20 years ago by M $\ddot{o}$ hwald<sup>143</sup>, Decher<sup>139</sup> and Lvov<sup>144</sup>. This technique can be applied with various polyelectrolytes, the number of layers can be varied and the film can be deposited on top of multiple substrates such as plastic, glass, ceramics and metals<sup>145</sup>.

c Their respective structures are presented in **Figure 57A** and **Figure 57B**.

EDC is a molecule containing a carbodiimide group ( $\text{RN}=\text{C}=\text{NR}$ ), this group causes amide bonds formation by activating carboxyl groups ( $-\text{COOH}$ ) reaction with primary amine ( $-\text{NH}_2$ ). Sulfo-NHS is a sodium salt that forms amine-reactive sulfo-NHS esters in presence of carboxyl-containing molecules. Those sulfo-NHS esters also react with primary amines to form stable covalent amide bonds. In our case, the sulfo-NHS is added to the crosslinking reaction to enhance the formation of amide bonds<sup>146</sup>.

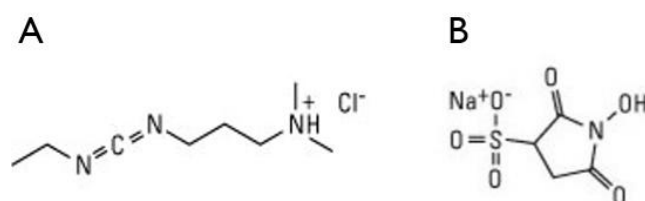


**Figure 57: Chemical structures of 1-ethyl-3-(3-dimethylaminopropyl) carbodiimide EDC (A) and N-hydroxysulfosuccinimide sulfo-NHS (B)**<sup>147</sup>

As schematically represented in **Figure 58**, the cross-linking reaction starts with the EDC carbodiimide group reaction with the carboxyl group formed previously by the ionic link between the polyanion (1, carboxylic acid) and the polycation (2, primary amine).

The ionic link is broken to form the unstable o-Acylisourea intermediate compound. This compound can react directly with the primary amine (polycation) to form the amide bond. It can also react with sulfo-NHS and create amine reactive sulfo-NHS ester which bond to the primary amine. In the end, a stable conjugate made of polycation and polyanion chains is formed with covalent amide bonds via two different mechanisms.

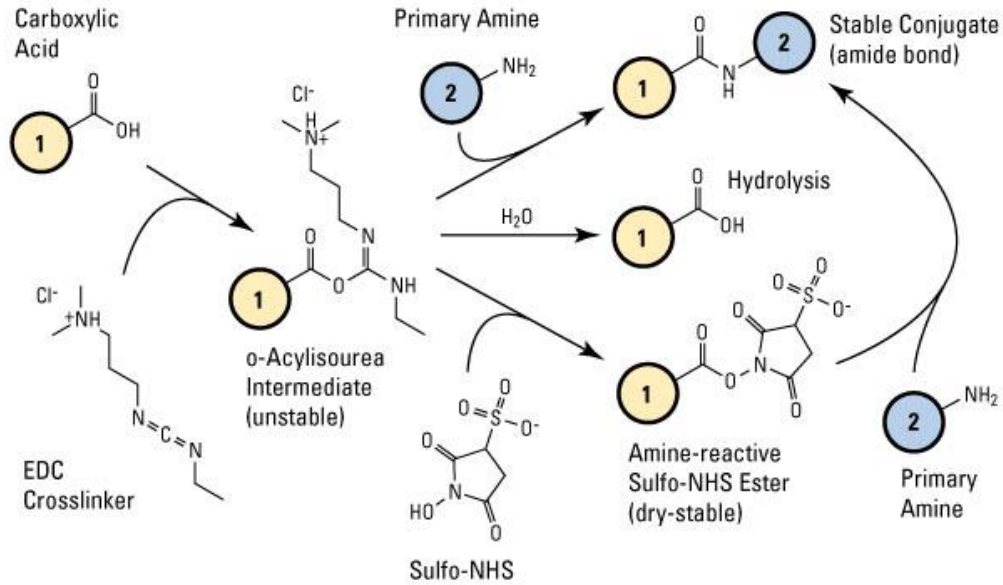


**Figure 58: EDC and Sulfo-NHS chemical cross-linking reaction.** EDC reacts with carboxylic groups to form o-Acylisourea intermediate compound. This compounds reacts either directly with primary amines or with sulfo-NHS to form sulfo-NHS ester. In both cases, a covalent bond will be formed with the primary amine groups<sup>147</sup>

PEM films present the advantages to be versatile, easy to use and tune depending on the desired properties. Their layer-by-layer deposition can be used for various polyelectrolytes, but also for proteins such as collagen<sup>148</sup>, and be carried out in aqueous solutions with mild conditions of pH and temperature. Their thickness can be adjusted by the number of bilayers, the pH or the ionic strength of the build-up solution (**Figure 59A**)<sup>149</sup>. And finally, their stiffness can also be tuned over 100 kPa to 400 kPa depending on their crosslinking levels (**Figure 59B**)<sup>145</sup>. In addition to those intrinsic properties, previous studies have demonstrated their ability to store nanomaterials and biomolecules such as proteins<sup>150</sup>.

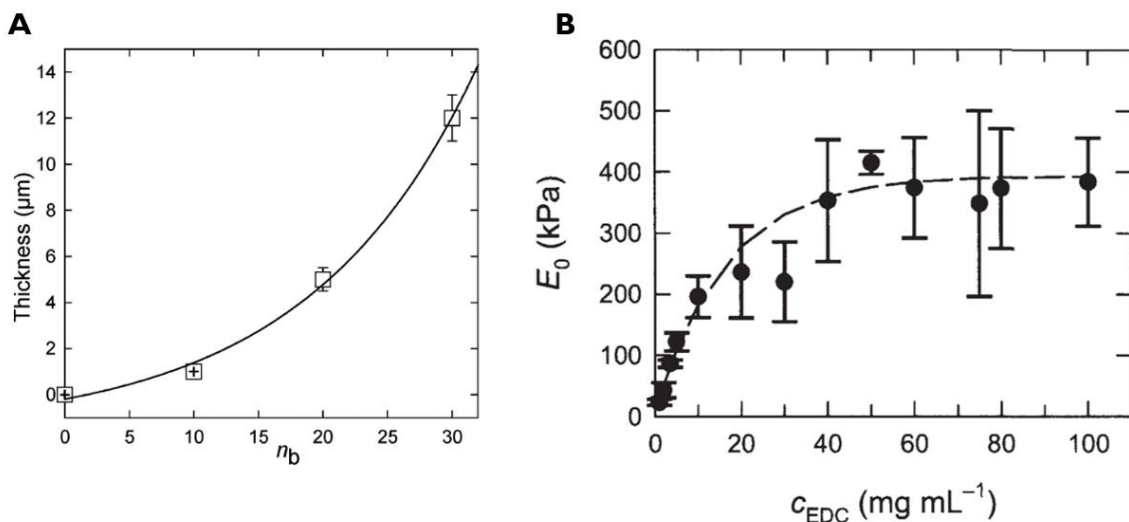


**Figure 59: Evolution of thickness as a function of the number of poly-L-Lysine and hyaluronic (PLL/HA) bilayers (A) Evolution the (PLL/HA) film stiffness as a function of the EDC cross linker concentration (B) from**<sup>146,151</sup>

#### 1.4.6.2 Osteoinductive coating with BMP-2 and BMP-7 in PEM films

In order to deliver bioactive molecules, the IMBM team at LMGP has developed during the past years a polyelectrolyte multilayer film (PEM) made of poly-L-Lysine (PLL) and acid hyaluronic (HA). Those films assemble in a layer-by-layer manner, can be deposited on various type of surfaces and bioactive molecules can be incorporated into them to make them osteoinductive.

The loaded amount of bioactive molecules was optimized with BMP-2 by modulating the pH and ionic strength of the loading solution<sup>150</sup>. Also, loaded and released amounts have been tuned by varying the film thickness and crosslinking level<sup>152</sup>. BMP-2 and BMP-7 were successfully incorporated into those films and induced the osteogenic differentiation of BMP-responsive skeletal muscle cells (C2C12 cells)<sup>153</sup>. In the case of bone graft substitutes, the coating technique was employed with BMP-2 on different types of bone graft substitutes, including porous ceramics<sup>154</sup>, titanium<sup>155</sup> or polymers<sup>152</sup>, and its osteoinductive capacity was evaluated in different bone regeneration models.

In the PhD thesis of Thomas Crouzier (defence in 2010), the loading condition of BMP-2 was optimized<sup>150</sup> and the bioactivity of BMP-2 either by direct adsorption on TCP/HAP porous granules or loaded into PEM film on the ceramic substitute were compared<sup>154</sup>. The BMP-2 adsorbed onto PEM-coated and on bare granules, in a lesser extent, could be stored and remained bioactive over at least 3 weeks (A, **Figure 60**). The BMP-2 bioactivity in the PEM-coated granules was confirmed *in vitro* with the alkaline phosphatase activity expression on C2C12 cells (B, **Figure 60**). *In vivo*, both uncoated and PEM-coated TCP/HAP granules loaded with rhBMP-2 exhibited both osteoconductive and osteoinductive properties (C, D and E, **Figure 60**)<sup>154</sup>.



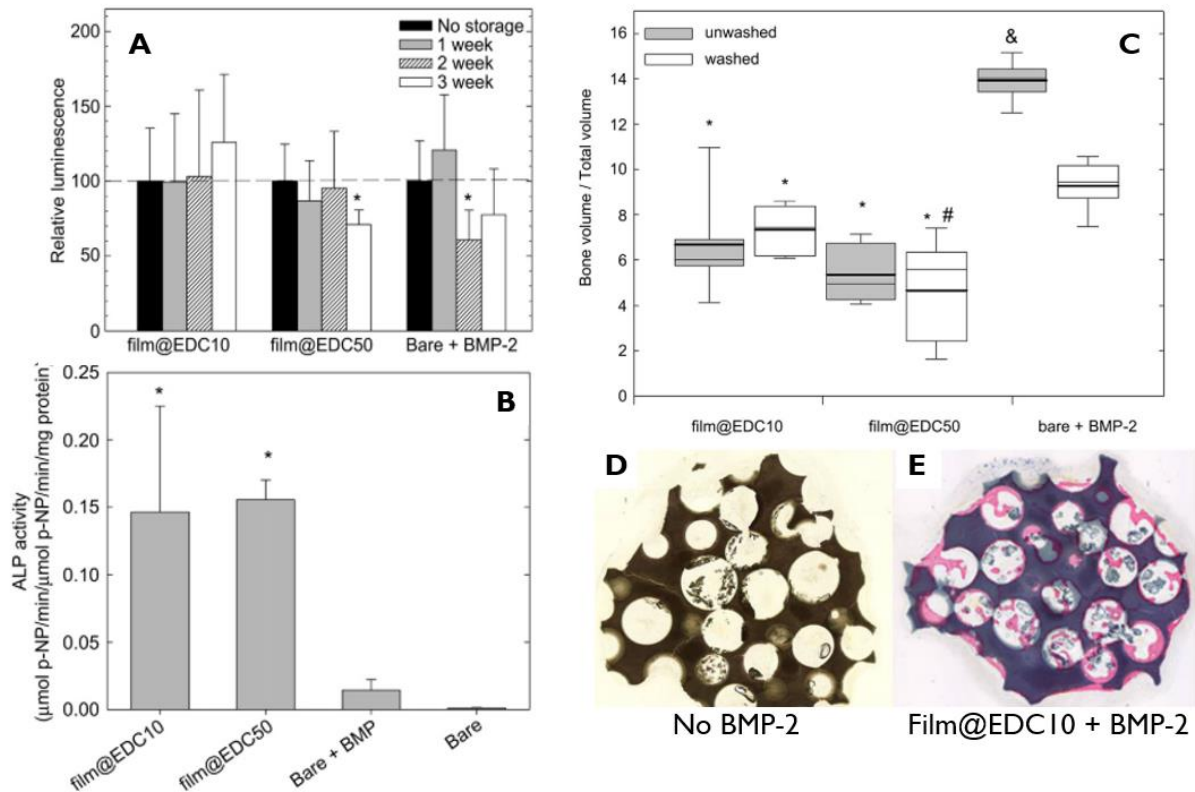


**Figure 60: Evaluation of the BMP-2 bioactivity on bare and film-coated TCP/HAP granule in vitro and in vivo in an ectopic rat bone model after 4 weeks.** The luciferase activity of C2C12 was measured after 1 day of culture on granules that were loaded with rhBMP-2, then air-dried and stored up to 3 weeks (A). Quantification of alkaline phosphatase activity of C2C12 cells cultured for 3 days on the different surfaces (B). Box-and-whisker plot of bone volume (normalized over the total implant volume) determined by micro-CT analysis (C). Histological analysis. Bone tissue cross sections of TCP/HAP granules coated with film@EDC50 without rhBMP-2 (D) and coated with film@EDC10 with rhBMP-2 (E) at 6 weeks post-implantation (X20) (adapted from<sup>154</sup>)

The team began to work on titanium implants in 2011 and designed a custom-made porous Ti-6Al-4V implant with the help of TIMET Savoie S.A (Ugine, France) with open and communicating pores of 500 μm in diameter (B, **Figure 61**)<sup>155</sup>.

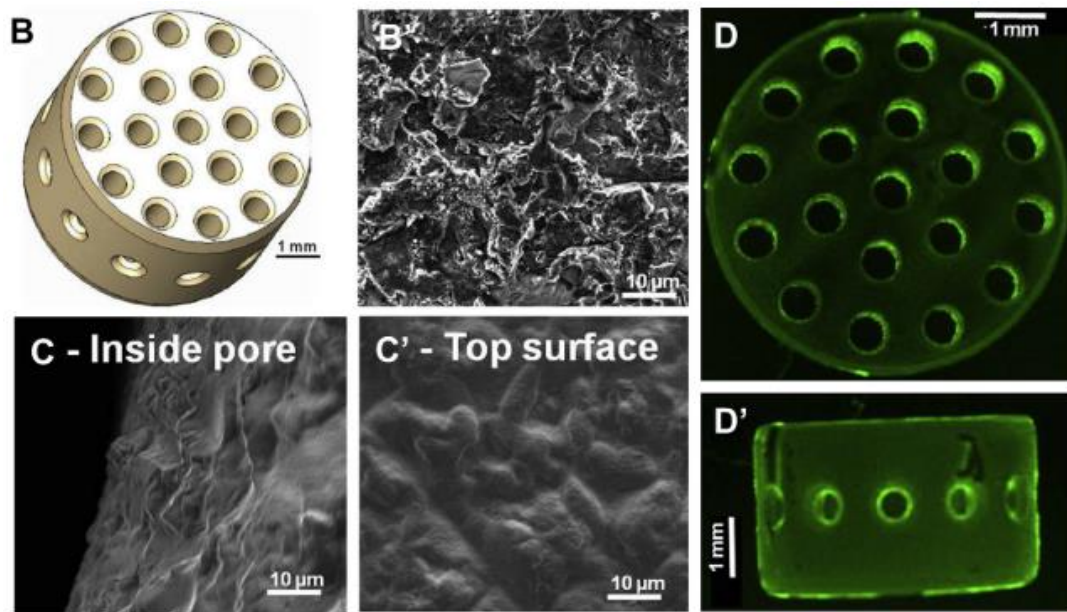


**Figure 61: Illustration of the PEM film coating of porous titanium implant under scanning electron microscopy and macrofluorescence loup.** Schematic of porous Ti-6Al-4V scaffold with 500  $\mu\text{m}$  pore size (B). SEM micrograph of the uncoated Ti-6Al-4V surface imaged at the implant surface (B'). SEM micrographs of (PLL/HA)<sub>24</sub> film-coated surface of the Ti-6Al-4V scaffold either (C) inside a pore channel or (C') at the outer surface. Observation of a PEM-film deposited on the Ti-6Al-4V scaffold by a macroscope: (D) top view and (D') side view<sup>155</sup>

The amount of BMP-2 loaded into these films was tuned over a large range depending on the cross-linking extent of the film and the BMP-2 initial concentration. The stability of the BMP-2 into the film was tested upon one year storage and after sterilization *in vitro*, using C2C12 cells (A and B, **Figure 62**), and *in vivo* with a rat ectopic model for the perspective of industrial and clinical development (D, **Figure 62**). BMP-2 loaded in dried PEM films exhibited shelf-life stability over one year (B, **Figure 62**). However, their bioactivity *in vitro* decreased from 50 to 80% after irradiation depending on the g-irradiation dose (C, **Figure 62**). Nevertheless, the *in vivo* studies showed that the osteoinductive potential of BMP-2 contained in PEM-coated Ti implants was fully preserved after air-drying of the implants and sterilization at 25 kGy. Finally, the film drying or irradiation did not affect the amount of new bone tissue formation (D, **Figure 62**)<sup>155</sup>.

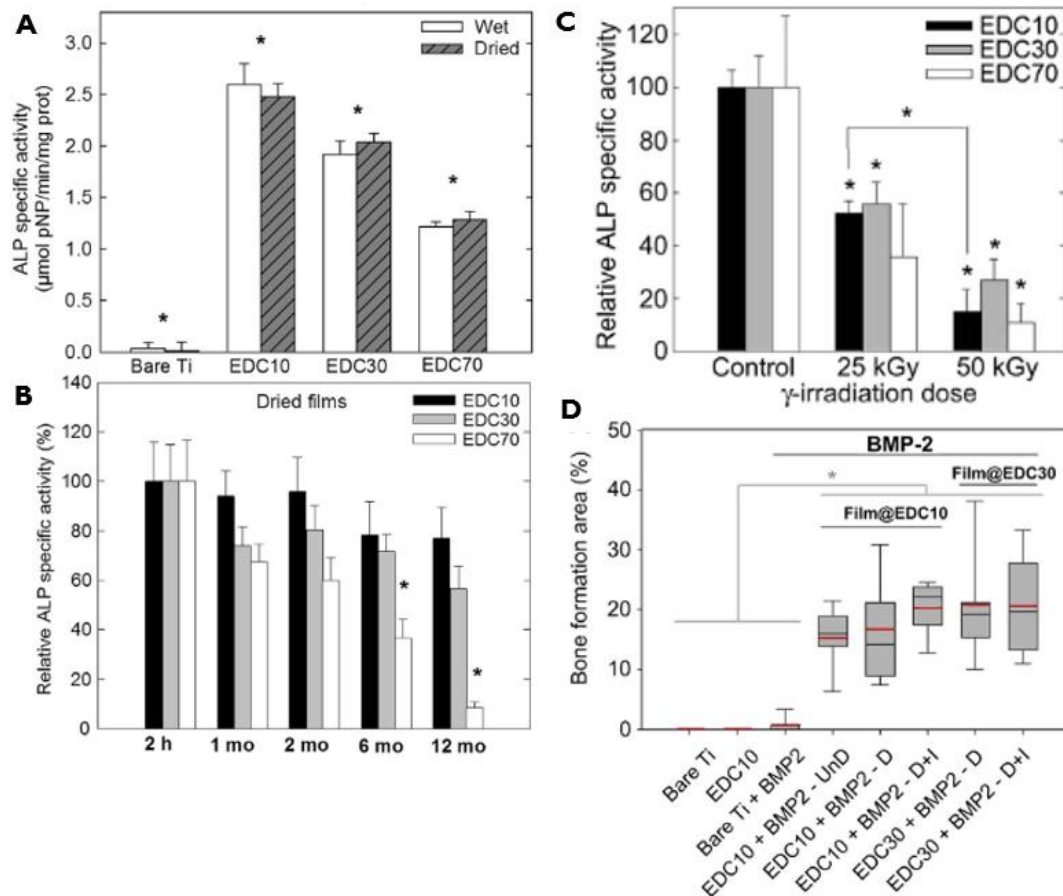


**Figure 62: Evaluation of the bioactivity and stability of BMP-2 loaded into PEM film coated on porous titanium implant in vitro and in vivo in an ectopic rat bone model after 6 weeks.** ALP activity of C2C12 myoblasts cultured for 3 days on either bare or on PEM film coated Ti substrates loaded with BMP-2 at 20 µg/mL (films@EDC10, 30 and 70) (A). Kinetics of ALP activity of BMP-2-loaded PEM films stored in dry state for up to 1 year (B). ALP activity of C2C12 cells cultured on BMP-2-loaded PEM that had been air-dried and g-irradiated at either 25 or 50 kGy (C). Box-and-whisker plots of bone formation area given as a % of the “available area” (D, adapted from<sup>155</sup>)

In a more recent study conducted by Michael Bouyer during his PhD (2015-ongoing. Clinician, plastic and maxilla-facial surgery service in the University Hospital of Grenoble, France), the film containing BMP-2 was deposited on a polymeric hollow tube made of commercially-available PLGA and used for the repair of a critical size femoral bone defect in rat<sup>152</sup>. The amount of BMP-2 loaded was tuned and released from the film over a large extent by controlling the film crosslinking level and initial concentration of BMP-2 in solution. With microcomputed tomography (µCT) and quantitative analysis of the regenerated bone growth kinetics, they showed that the amount of newly formed bone and kinetics could be modulated (**Figure 63**). They obtained an effective and fast repair in the first 1-2 weeks in the best conditions with complete defect bridging, formation of vascularized and mineralized bone tissue. Further analysis with histological staining and high-resolution computed tomography also revealed the presence of bone regeneration inside and around the tube with spatially distinct organization for trabecular-like and cortical bones. Finally, the amount of cortical bone and its thickness was found to be increasing with the BMP-2 dose<sup>152</sup>.

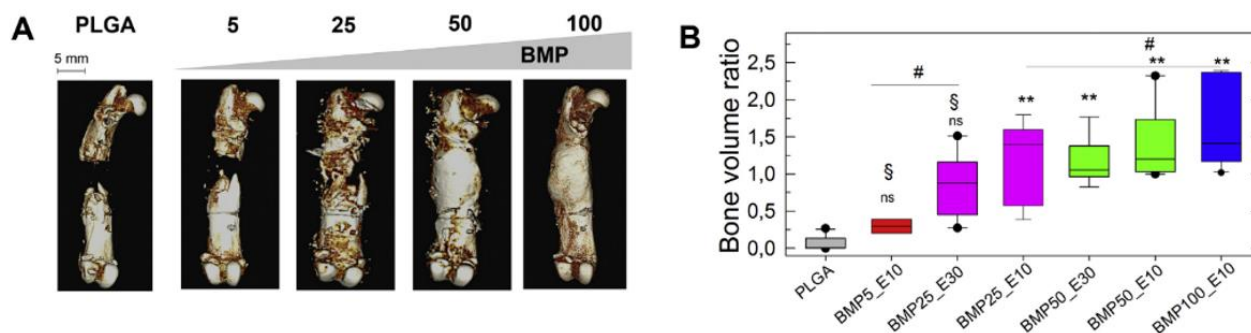


**Figure 63: Quantitative analysis by  $\mu$ CT of the bone regeneration on BMP-2 loaded tube at 8 weeks after implantation.** Representative 3D  $\mu$ CT reconstructions taken at 8 weeks after implantation for EDC with increasing doses of BMP-2 (BMP5 to BMP100) and control PLGA (A). Box plot representation of the bone volume ratio at 8 weeks ( $n = 8$ , except for BMP5/EDC10 with  $n = 2$ ) for the EDC10 and EDC30 films with increasing BMP-2 doses from 5 to 100  $\mu$ g/mL (BMP5 to BMP100, B)<sup>152</sup>

In summary, several bioactive molecules are being used to enhance bone repair. Even though most of the studies focused on BMP-2, other growth factors such as BMP-7, PDGF-BB or FGF-2 also appear promising as shown by the on-going clinical assessments. In the case of porous titanium substitutes, carriers used so far to deliver these bioactive molecules are mainly extracellular matrix proteins (collagen, fibrin gels), or biomimetic calcium phosphate, which provides osteoconduction and better mechanical support than ECM proteins on their own. The use of film coating such as PEM film seems promising in terms of convenience, stability and storage of the bioactive molecule, without neglecting the ability to tune the delivery amount.

In fact, the PEM film coating developed by the IMBM team is now involved into a start-up company project to translate this solution to the clinic. The APIOS project aims at offering the PEM coating solution made of PLL and HA to deliver bioactive molecules for critical size bone defects in patients. Preclinical trials were performed on animals studies, as illustrated with the published articles presented above, and market studies were undertaken to identify the position and the need for this coating. In total, 800k€ was raised for this project and 2 patents were secured for the coating preparation. The APIOS start-up is still on incubation and preclinical trials are still on-going for further translation to the clinical stage.

### 1.5 Remaining challenges for clinical translation of bone graft substitutes (from Biomaterials review<sup>21</sup>)

Researchers and scientists face many barriers for the translation of innovative bone healing strategies to clinical and commercial applications. In this section, the main important steps for clinical translation are presented and remaining limitations and challenges are discussed.

#### 1.5.1 Important steps in clinical translation

The most challenging point for effective translation is understanding the complex regulatory environment, medical device classification and advanced therapeutic medical products. In fact different agencies, especially in the USA versus EU, have different classification systems.

In the USA, a medical device product must receive authorization by the Food and Drug Administration (FDA) prior to being marketed. The FDA classifies medical devices in three categories: Class I, Class II, Class III depending on the risks associated with the devices. For instance, a medical device combined with a drug belong to class III. For combination devices, i.e. devices that contain drugs and/or stem cells, the FDA determines which of three centers, namely the Center for Devices and Radiological Health (CDRH), the Center for Drug Evaluation and Research (CDER) or the Center for Biologics Evaluation and Research (CBER), has primary jurisdiction on the authorization process. The FDA has a specific regulation for Human Cellular and Tissue Products (HCTP). Generally, the CBER has primary jurisdiction on Regenerative Medicine Advanced Therapy (RMAT) products when cells are used.

In Europe, the situation is different. Medical devices do not need to be evaluated by a regulatory agency. Classified as class I, II and III depending on their intended use and risk level, they are simply CE marked by certified notification bodies, a CE mark being the manufacturer's declaration that the product meets the requirement of a European directive. In contrast, drugs are considered as pharmaceutical products and need to have authorization from the European Medicine Agency (EMA). Stem cells also belong to a specific category, the advanced therapeutic medicinal products (ATMP). The more complex the product, the longer the path toward clinical translation and the higher the product will cost. The most complex products are by far the stem-cell based products.

There is a need to define the specific clinical application to address. Who is the patient to be treated? The answer to this question will guide the clinical development steps including implantation site and animal model. Select the most appropriate animal models for the pre-clinical experiments is also an issue. Pre-clinical trials require animal care facilities and veterinary schools or labs. Later, clinical trials of course involve patients in clinics and hospitals. There are several recent reviews on animal models for bone repair from ectopic bone induction (mice), small bone defects (rats) and larger bone defects (rabbit, dog, sheep, goat, mini-pigs and pigs)<sup>156-158</sup>. The selection criteria need to be carefully considered, since each model has pros and cons<sup>159</sup> and each study uses a specific set of parameters for bone scaffold design, which makes comparisons between studies difficult. Furthermore, there is no current consensus about the pre-clinical assessment strategies, including animal implantation site<sup>160</sup>. The efficacy of bone repair, including the amount of regenerated bone, the kinetics of bone formation and mechanical properties of regenerated bone, needs to be assessed as well as, importantly, the safety of the product, including the possible presence of toxic degradation products in the different organs, and the possibility of chronic inflammatory reaction, as examples.

The cost effectiveness of the product and the potential reimbursement by medical care systems should be considered and depend on the specific country. Of note, in Europe, a large part of medical expenses is paid by government bodies, while in the USA, it is paid by private insurances. In view of industrialization, aspects such as large-scale manufacturing, sterilization processes, and mode of storage need to be considered. Last but not least, the quality of both the process and the product needs to be assessed. This includes the sourcing of the raw components, good manufacturing practice (GMP) grade, batch-to-batch reproducibility, the manufacturing process and the respect of standards for production (ISO norms).

### 1.5.2 Optimization of the bone graft substitute mechanical properties

The optimization of the mechanical properties of BGS is important to restore mechanical function by matching, or mimicking, the mechanical properties of the natural tissues. Also, the closer the mechanical properties of the BGS are to those of the natural tissue, the higher the chances of avoiding adverse effects to the surrounding anatomy. Indeed, bone tissue surrounding a metallic implant, such as a hip prosthesis, degrade over time due to stress shielding<sup>161</sup>. This is due to the redistribution of mechanical loads after implantation, whereby the stiffer metal implant bears most of the mechanical stresses, while the surrounding bone tissue is not mechanically loaded, which inhibits the integration and regenerative potential. Similarly, if the BGS material properties are weaker than the surrounding tissue, the tissue will compensate, which may hinder bone regeneration in the BGS and/or cause damage and fatigue to the surrounding tissue.

### 1.5.3 Better understanding the biological mechanisms

Regarding the active biomolecules, it is clear that there is a need to precisely understand what their modes of action are and whether they affect inflammatory or bone precursor cell response. As already suggested by Martino<sup>162</sup>, the role of inflammatory cytokines and immune cells regulated in bone regeneration should be further investigated and exploited. The action of bioactive molecules on osteoblasts versus osteoclasts should also be better understood. In the future, combined strategies targeting growth factor receptors and cellular adhesion receptors may be developed to induce cooperative signalling and optimize bone repair. The specificity of the mechanism of action is key.

### 1.5.4 Controlling the dose and delivery of bioactive molecules

It is also important to precisely control and confine the bioactive molecules *in vivo* to avoid undesirable side effects. Their dose should be optimized to avoid over-dosing, in order to attain a safe but efficient working range to form new bone. Of note, a major difficulty arises from the fact that bioactive molecule delivery is not an intrinsic parameter, but depends on the biodegradability (i.e. kinetics and degradation products) of the biomaterial carrier. Ideally, these two parameters should be uncoupled.

### 1.5.5 Modulating the material/bioactivity couple

To date, the carriers used to deliver the bioactive molecules have typically been biodegradable (matrix proteins, HAP/ $\beta$ -TCP). In the future, it may be beneficial to take advantage of the mechanical properties of the engineered scaffold, which can be non-biodegradable polymeric materials such as PEEK or biodegradable such as PCL and PLGA. Metallic lattices made of titanium may also benefit from an added bioactivity. Depending on each specific clinical situation, the coupled material/bioactive molecule may be adapted in order to provide proper structural, biodegradable and surface characteristics depending on the indication. As mentioned in the section 1.1.2, the stability of the bone regeneration site is also crucial for long bone healing. Improvement in scaffold design and production techniques, such as 3D



printing and fixation techniques, may improve the bone repair efficiency. Such developments require collaborative work between clinicians, engineers and biologists/biochemists to improve the scaffold, the efficacy of incorporated drugs and the surgical procedure itself.

In the field of vascular stents, the combination of metallic or polymeric scaffolds and active molecules has already been implemented in clinics since 2003, where the tubular mesh provides a mechanical support and the anti-proliferative drug embedded in a surface coating, acts on the cells in the vascular wall<sup>163</sup>. Thus, it will be interesting, by taking examples from the vascular field, to further expand the potential of material carriers. For instance, instead of adding ceramic granules inside a PEEK cage, as done currently in clinics, the bioactive molecules may directly be coated at the surface of the carrier, using a spacer or a “cushion”.

Among the numerous technical strategies that are currently developed by academic teams to trap BMPs at the surface of materials, some may well emerge in the near future, provided that they are sufficiently robust to meet the industrial requirements (large-scale industrialization, sterilization, storage...). In terms of regulation and development time, combining an already approved medical device with an already approved active molecule could speed up the translation to clinic.

## 1.6 PhD Objectives

As presented in this first chapter, bone is a complex tissue that fulfils important biological functions of the human body. This tissue is able to remodel and repair itself in case of small fractures. However, for complex or compromised fractures, the use of bone graft substitutes remains the safest way to help the repair and replace temporary or permanently the damaged bones. Numerous research works and clinical trials investigate how to optimize the material composition and structure, the associated biocompatibility and bioactivity those substitutes can have depending on the specific bone repair application.

Emerging additive manufacturing technologies such as EBM, have enabled the generation of highly porous architectures with an already used biocompatible material such as Ti-6Al-4V alloy. With this manufacturing process, it is now possible to mimic the macro scale structural organization of the bone tissue while optimizing the substitute mechanical properties. Several surface treatments, based on the mechanical modification or the addition of calcium phosphate or hydroxyls groups, enhance the biocompatibility of titanium substitutes to make them osteoconductive.

More than osteoconductive, the next generation of bone graft substitutes could also be osteoinductive. The incorporation of bioactive molecules, especially BMP-2 and BMP-7, is a promising option in the field to help the bone repair and regeneration. On-going clinical trials and numerous research studies on osteoinductive bone graft substitutes are the proof of their potential effectiveness and faster regenerative capacities. In the case of metallic and porous bone graft substitutes, most investigated solutions to incorporate and deliver bioactive molecules are using ECM gels filling the porous structure. The latter reduces the available space provided by the porous structures, does not ensure a controlled delivery of the bioactive molecules and may introduce more inflammatory responses.

In this PhD project, the objective was to develop 3D architected and osteoinductive titanium-based scaffolds presenting at the same time a high porosity and a bioactive surface coating. To this end, my project was divided in three parts (**Figure 64**) and conducted with the following objectives:

- i. Build titanium-based architected scaffolds and control their structures: architected scaffolds were built by EBM with medical grade Ti-6Al-4V alloy and structurally characterized (**Figure 64**, part I)
- ii. Obtain an osteoinductive surface coating with BMP-7: the osteoinductive coating was obtained by incorporating BMP-7 into a polyelectrolytes multilayers (PEM) film made of (PLL/HA) bilayers. Its releasing capacity was evaluated *in vitro* (**Figure 64**, part II)
- iii. Assess the coating osteoinductive capacity: the coating ability and its osteoinductive capacity were studied *in vitro* on 2D plastic surfaces and on 3D scaffolds with murine mesenchymal stem cells (**Figure 64**, part III).

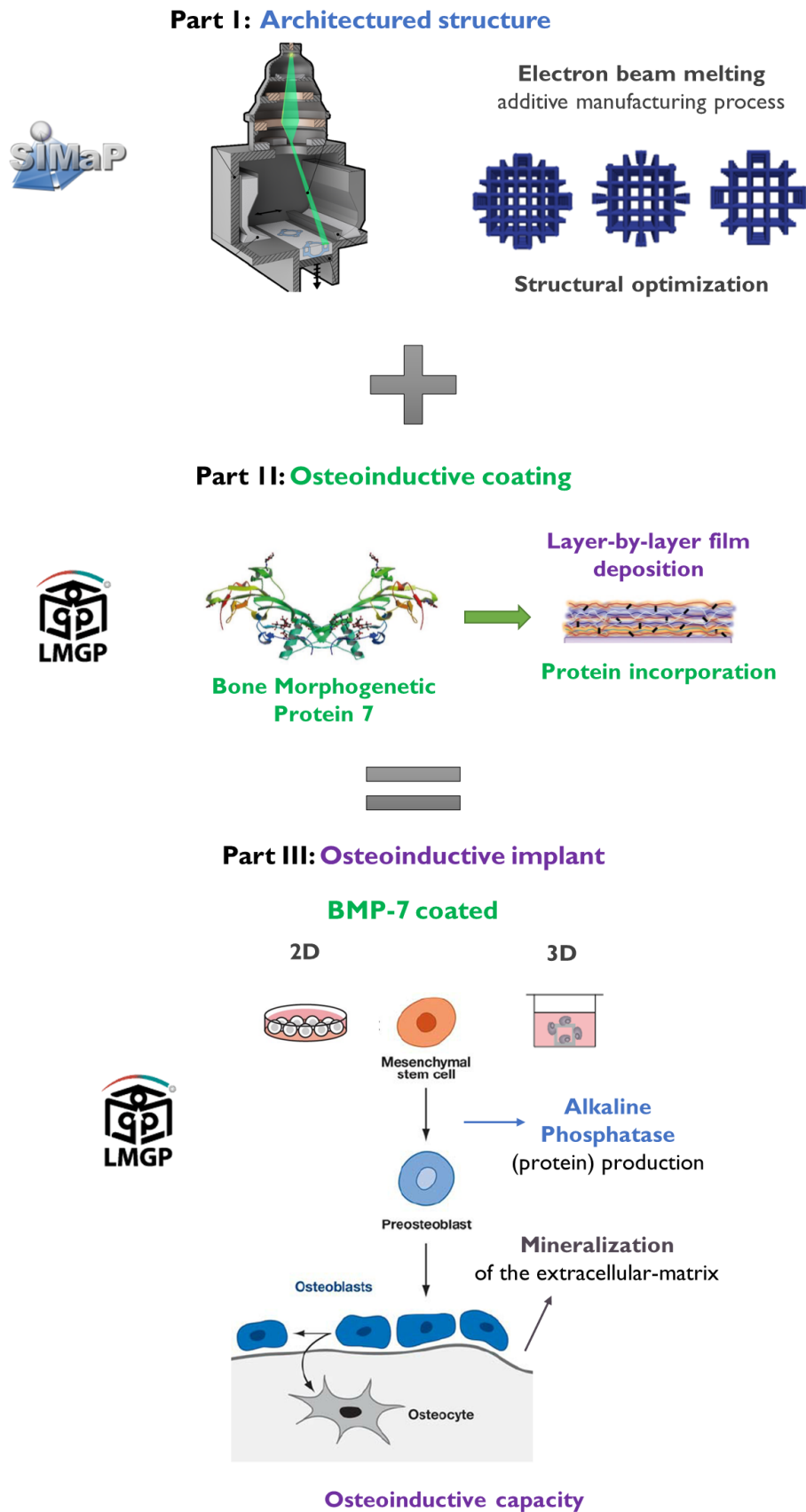


**Figure 64: Schematic representation of the PhD objectives divided into three parts. Part 1: architected Ti-6Al-4V scaffolds scaffold by EBM. Part 2: osteoinductive coating with (PLL/HA) films loaded with BMP-7. Part 3: osteoinductive capacity in vitro on 2D substrates and 3D scaffolds with murine mesenchymal stem cells**

## Chapter 2. Materials and methods

### 2.1 Building and characterization of Ti-6Al-4V architected scaffolds

Architected structures are the product of an ingenious combination of two or more materials or, a combination of materials and space arranged in a way to obtain properties not attainable by any material on its own<sup>164</sup>. This type of structure requires specific starting material and manufacturing process, as well as specific structural characterization methods. The material, the building method and the characterization techniques used in this thesis will be described in this part.

#### 2.1.1 Ti-6Al-4V alloy

Originally, the Ti-6Al-4V alloy was developed for aerospace applications requiring materials with remarkable properties such as high strength for a low density, high corrosion resistance or significant fracture toughness. For medical applications, the selected metals also need to have those properties in addition to a low modulus, to better match the surrounding biological environment, and more importantly a good biocompatibility. The Ti-6Al-4V alloy gathers all those properties which made it currently the most commonly used metallic materials for implants<sup>67</sup>.

In this thesis, we used the extra low interstitial (ELI) Ti-6Al-4V titanium alloy (grade 23) which composition is detailed in **Table 5**. The name ELI refers to the fact that, comparing to the Ti-6Al-4V alloy (grade 5), the ELI alloy contains lower amount of interstitial elements such as mainly oxygen, but also carbon, nitrogen or hydrogen, which improves its ductile behaviour<sup>165</sup>.

Element	Aluminium <i>Al</i>	Vanadium <i>V</i>	Iron <i>Fe</i>	Carbon <i>C</i>	Oxygen <i>O</i>	Titanium <i>Ti</i>
Content (%wt)	5.5 - 6.5	3.5 – 4.5	<0.25	<0.08	<0.13	Balance

**Table 5: Composition of Ti-6Al-4V alloy according to the standard American Society for Testing and Materials (ASTM) F136**

This alloy has generally an  $\alpha$  (hexagonal) +  $\beta$  (cubic) crystallographic microstructure at room temperature, which can change depending on the applied thermo-mechanical treatment<sup>69</sup>. Indeed, depending on heating temperatures and cooling rates, this material can either have an  $\alpha$  +  $\beta$  microstructure, or  $\alpha$  +  $\alpha'$  microstructure with the  $\alpha'$  martensitic phase. **Figure 65** shows a typical  $\alpha$  +  $\beta$  microstructure inherited from EBM process. The different possible microstructures of Ti-6Al-4V have a non-negligible effect on the macroscale properties of the material.

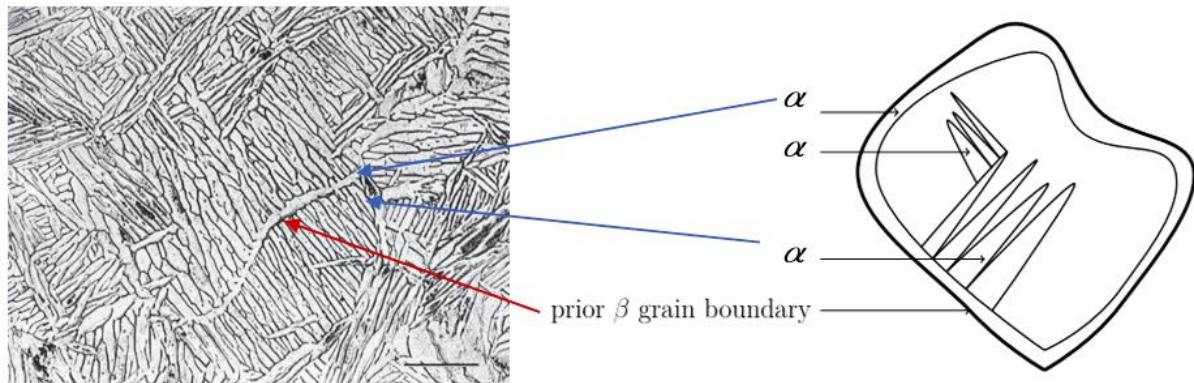


**Figure 65: Micrograph (right) and schematic representation (left) of the typical microstructure of Ti-6Al-4V obtained by EBM, exhibiting the  $\alpha$  (hexagonal) +  $\beta$  (cubic) microstructure (scale bar = 50  $\mu\text{m}$ , from<sup>85,166</sup>)**

## 2.1.2 Scaffolds building by electron beam melting (EBM)

### 2.1.2.1 Electron beam melting manufacturing process

The electron beam melting (EBM) is an additive manufacturing process using an electron beam as source of energy to selectively melt layers of metallic powders in order to generate a 3D structure from a 3D model data<sup>167</sup>.

The starting material is a gas-atomized powder of Ti-6Al-4V with a particle size ranging from 45 to 100  $\mu\text{m}$  as illustrated in **Figure 66**. After one building cycle, the non-melted particles are recovered and re-used for next buildings. The latter can alter their spherical shape and introduce flatter areas corresponding to sintered necks (white arrows, **Figure 66**).

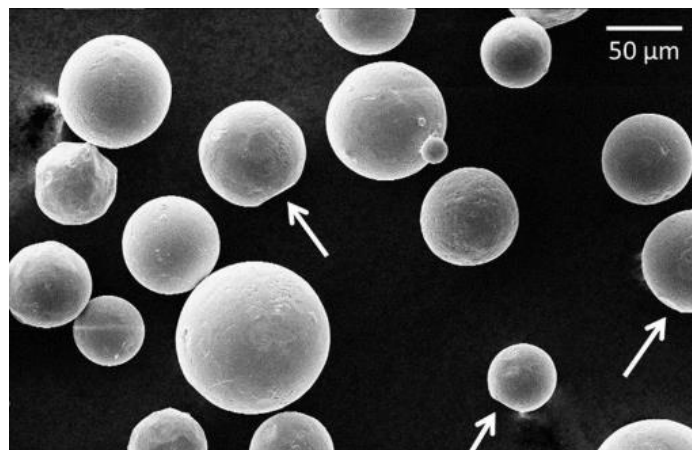


**Figure 66: Gas-atomized Ti-6Al-4V powder visualized under scanning electron microscopy. The white arrows represent the necks from previous building uses<sup>166</sup>**

The first step of the EBM process is the design of the part aimed to be built. This part is a geometric model generated in a 3D Computer Aided Design (CAD) file, which is then converted in the STL file format, a format that stores only surface features. This file is then imported into a specific software, Magics<sup>®</sup> (Materialise, Belgium) in our case, in order to position the part

and add if needed supporting structures on the building scene. Once the building scene is complete, the 3D model is sliced and converted into trajectories for the layer by layer melting.

**Figure 67** represents a schematic view of the EBM device. The machine can be divided into two parts: the electron beam column and the build chamber.

In the electron beam column, an electron beam is generated by applying a 60 kV accelerating electric field between a tungsten filament heated at 2600°C and an anode. Then, accelerated electrons forming the beam pass through different electro-magnetic coils. Those coils play a role of 3 different lenses:

- An astigmatism lens to reshape and concentrate the beam and obtain a spot
- A focus lens to focus the beam on a given plan
- A deflection lens to control the beam trajectory

The electron beam column is under a strong secondary vacuum of  $10^{-7}$  mbar to avoid the interaction of air particles with the beam. A secondary vacuum is also applied into the build chamber (around  $10^{-4}$  mbar) for the same motive and besides, to prevent the titanium oxidation with the high temperature.

Afterwards, the electron beam enters the build chamber. The build chamber is composed of two powder hoppers, a heat shield and a rake at the upper part of the build tank which contains the build platform. The hoppers store the powder, while the heat shield protects thermally and prevents the metallisation of the rest of the chamber. The translating rake deposits the powder on the build platform. Prior to the building start, the plate level is adjusted and the rake is activated in order to put a first layer of powder. When a layer is fused, the plate goes down at typically 50  $\mu\text{m}$  and a new layer of powder is deposited and the process is repeated until the building scene completion.

At the end of the process, the chamber is cooled down with Helium and the entire block of powder is transferred into the Powder Recovery System (PRS). In this hermetic chamber, the powder block is blasted at 8 bars with the building raw material. This last step allows to break necks between sintered particles and to take out the melted parts. The left particles are sieved and reused in the next buildings. The sieving allows the recycling of particles from 20 to 140  $\mu\text{m}$ .



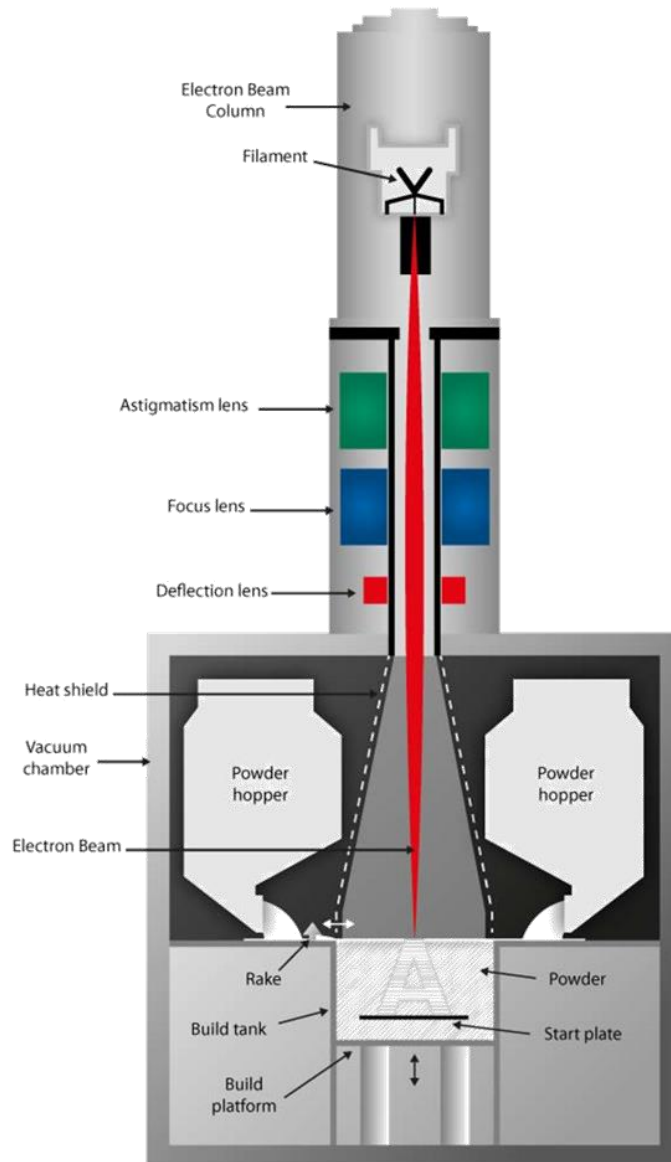


**Figure 67: Schematic presentation of the EBM machine.** The upper part is the electron beam column and the bottom part represents the build chamber<sup>168</sup>

In this project, we used the ARCAM A1 EBM machine (ARCAM, Sweden) whose characteristics are represented into **Table 6**. The height of a layer was defined and kept to the minimum possible distance of 50  $\mu\text{m}$ .

<b>Power</b>	50 – 3000 W
<b>Build temperature</b>	~ 700°C
<b>Deflection rate</b>	Up to 8000 m/s
<b>Maximum build size</b>	200 x 200 x 180 mm
<b>Beam spot size</b>	0.2 – 1mm
<b>Chamber pressure</b>	$10^{-4}$ mbar

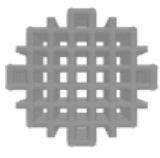


**Table 6: Main characteristics of the ARCAM A1 EBM machine**<sup>169</sup>

### 2.1.2.2 Scaffolds design by Computer Aided Design (CAD)

As explained above, the manufacturing of 3D structures using EBM technique requires a 3D CAD file. More particularly in the orthopaedic field, the two main strategies employed to generate this 3D file are:

- the use of computed tomography (CT) scans from the patient bone defect
- the use of geometrical structures available in the CAD software database

As illustrated in **Table 7**, we focused our investigations on geometric structures made of periodic cubic unit cells with 3 different porosities (73%, 80% and 85%) with the minimal strut size achievable of 600  $\mu\text{m}$ . For *in vitro* assay, disk-shaped scaffolds ( $\varnothing$  10 mm x L 7 mm) were designed to fit into 24 well plate cell culture wells, whereas cubic scaffolds (2 cm x 2 cm) were specifically manufactured to obtain a representative volume of the selected architectures for the mechanical tests.

<b>CAD representation</b>			
<b>Pore size</b>	830 $\mu\text{m}$	1070 $\mu\text{m}$	1400 $\mu\text{m}$
<b>Porosity</b>	73%	80%	85%

**Table 7: CAD representation, pore sizes and targeted porosities of Ti-6Al-4V architected scaffolds**

The scaffolds were generated using a previously homemade software from GPM2 team allowing the generation of lattice structures with periodic or random cells<sup>166</sup>. In a first step, a network of points is described by a connectivity table. In a second step, the lattices formed by the connected points were given specific dimensions and volume with the software Paraview (Kitware Inc, Sandia National Laboratories). Then, the scaffolds were nested on the computed building platform and the whole was sliced for the beam trajectory with the software Magics (Materialise, Belgium). To avoid the use of supports and make easier the scaffold removal from the plate, the scaffolds were manufactured on an edge with a 45° angle with respect to the build platform (**Figure 68**)<sup>170</sup>.

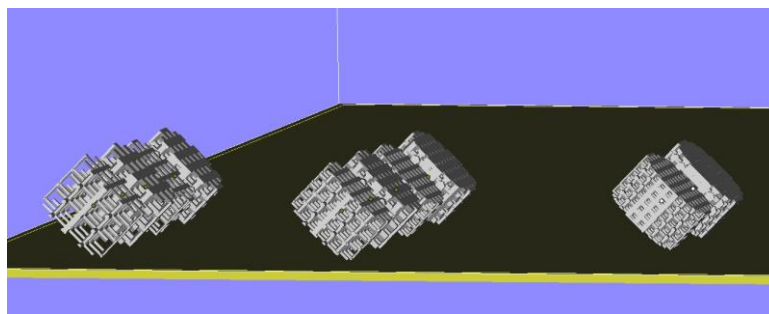


**Figure 68: Representation of the scaffolds placement into the build platform with a 45° angle**

### 2.1.2.3 Cleaning procedure

After the scaffolds building and de-powdering into the PRS, some powder remained in the structures, especially for scaffolds with the smallest pore sizes.

Prior to their use, scaffolds were further de-powdered and cleaned with a first sonicating phase (sonicator ultrasonic processors 130W, Branson processors, USA) at 20 kHz into water for 20 min. After total powder removal, the scaffolds were cleaned with isopropanol in an ultrasonic bath at the maximum frequency (FB 15051 ultrasonic bath 37 kHz 280 W, Fisher Scientific, USA) for 10 min. And finally, there were rinsed into ultrapure water and dried with Argon flux<sup>171</sup>.

### 2.1.3 Dimensional characterization

#### 2.1.3.1 Porosity measurement by hydrostatic weight

The porosity was determined by hydrostatic weight based on Archimedes' method. First, the scaffolds weight was measured successively in air and in ethanol, in order to determine the volume of the displaced fluid  $V_{fluid}$ .

$$V_{fluid} = \frac{m_{air} - m_{ethanol}}{\rho_{ethanol}} \quad Porosity = 1 - \frac{V_{fluid}}{V_{dense}}$$

By dividing the displaced fluid volume with the volume of a fully dense cylindrical structure with the scaffold's dimensions, we have access to the relative density and thus the porosity.



**Figure 69:** Weighting scale equipped with a hydrostatic weight platform

**Figure 69** displays the weighting scale used for the measurement. The weighting scale was equipped with a hydrostatic weighing platform and a beaker with ethanol to make possible the measurement procedure.

### 2.1.3.2 Structural characterization with X-ray tomography

X-ray tomography is a non-destructive method allowing the visualisation of the core structure of any materials or objects in 3D from cross-section images. This method is based on the measurement of X-rays attenuation (absorption, scattering) when X-rays pass through a section of matter. This absorption is related to the atomic number and the volumetric density of the crossed material. The principle of this technique is presented in **Figure 70**.

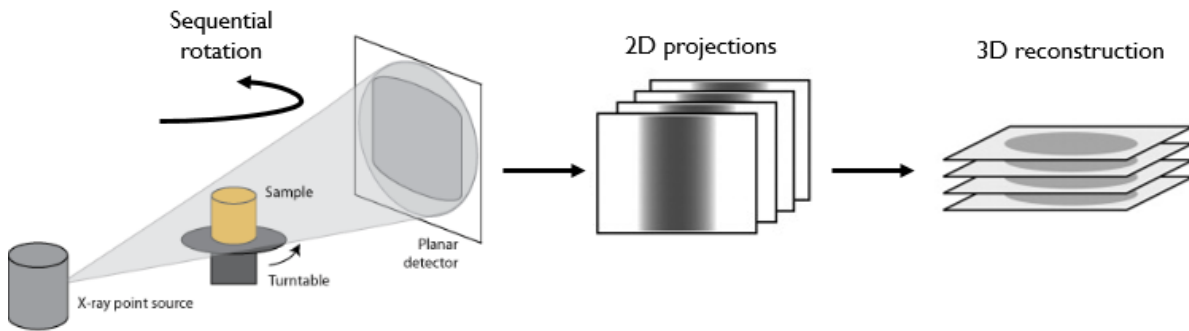


**Figure 70: Principle of the X-ray tomography imaging technique (adapted from<sup>172</sup>)**

X-rays are directed to the sample which was previously placed on a rotating platform. The absorption of X-rays on each projection is acquired in grayscale with a planar detector (CCD camera). Projections of the sample are obtained step by step at each rotation of the platform. By acquiring several 2D projections on different plans of the sample, it is possible to obtain a 3D reconstruction of the object using reconstruction algorithms and image segmentation<sup>173</sup>.

In this study, we used the EASYTOM XL tomography device (RX-solution®, France) available at the CMTC platform (“Consortium des Moyens Technologiques Communs” supported by the Centre of Excellence of Multifunctional Architected Materials “CEMAM”, Grenoble). The internal view of the tomograph chamber is exposed in **Figure 71**.

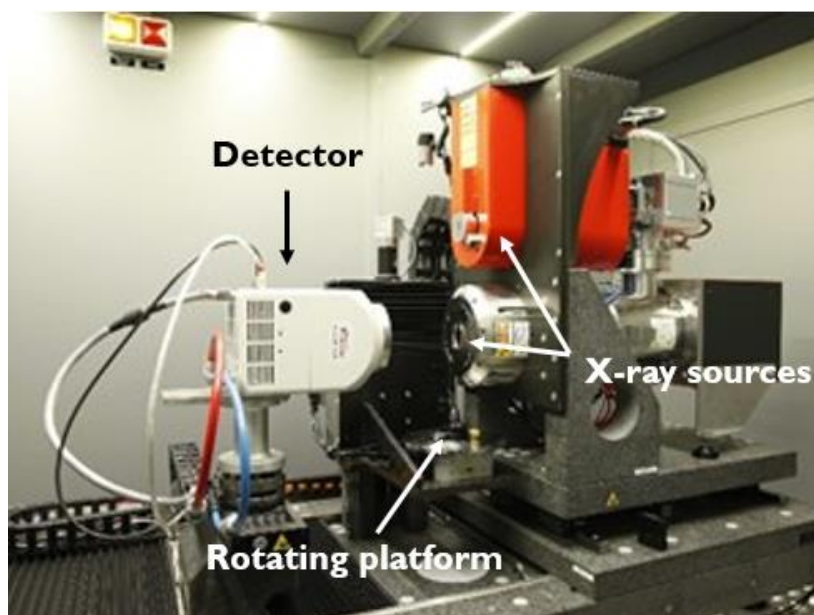


**Figure 71: Internal view of the EASYTOM XL tomograph (adapted from<sup>174</sup>)**

In order to obtain 3D reconstruction of EBM-built titanium scaffolds, scaffolds were scanned with a 140 kV tube voltage and 900 projections over a range of 360° for a voxel size of 11  $\mu\text{m}$ . The 3D images were reconstructed using a standard filtered back-projection algorithm with the software X-act (RX-solution®, France).

In order to design a custom-made implant for a critical size femoral bone defect reconstruction in rat, a rat bone femur was kindly donated by M.Bouyer (clinician, plastic and maxilla-facial surgery service in the University Hospital of Grenoble, PhD student at the LMGP team) and scanned by X-ray tomography. The images were acquired with a 50 kV tube voltage and 1600 projections with a voxel size of 3  $\mu\text{m}$ .

#### 2.1.4 Mechanical characterization by uniaxial compression test

Mechanical properties of bone implants play an important role in their appropriate integration, lifespan and in the viability of the surrounding bone tissue. The main mechanical property that describes the stiffness of any material or structure is the elastic modulus (Young's Modulus, E).

In this study, we measured the Young's modulus of architected Ti-6Al-4V scaffolds by uniaxial compression using a MTS 810 testing machine equipped with a 100 kN load sensor (MTS System Corporation, USA). The testing machine and the uniaxial compression test procedure were previously optimized in the frame of the PhD thesis of M.Suard<sup>175</sup>. A view of the machine is shown in **Figure 72**.

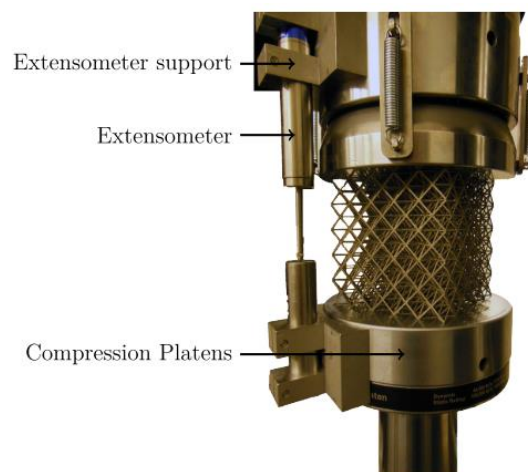


**Figure 72: Compression device used to perform mechanical tests on architected scaffolds**<sup>166</sup>

EBM build cubes of 2 cm x 2 cm and with the three different porosities of 73%, 80% and 85% were tested in this project. Cycles of loading-unloading were applied to the samples with a displacement rate  $v = 1 \text{ mm/min}$ , as illustrated in **Figure 73**.

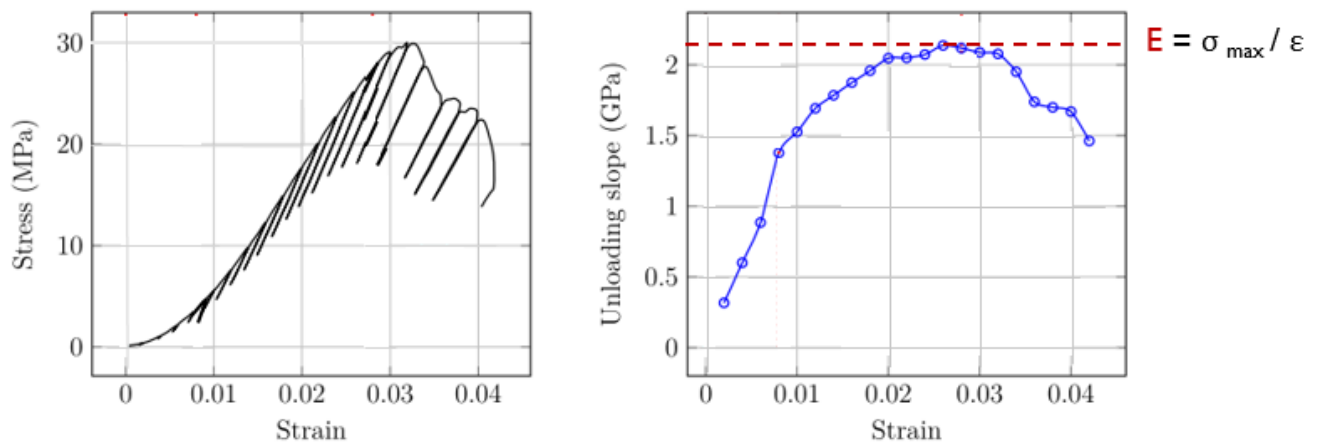


**Figure 73:** Example of the stress-strain cycles applied to architected Ti-6Al-4V scaffolds (left panel) and the corresponding representation of the unloading elastic modulus versus strain (right panel). The global elastic modulus was determined as the maximum value of the curve (adapted from <sup>166</sup>)

At each 0.02% of strain, the samples were unloaded until reaching 60% of the previous maximum load. The values of each unloading slope were then represented as a function of the strain and the global elastic modulus  $E$  of each structure was defined as the maximum value of the curve unloading slope vs strain (**Figure 73**).

## 2.2 Deposition of the polyelectrolyte multilayer (PEM) film

In this section, materials and methods used to obtain the osteoinductive coating will be presented and described.

### 2.2.1 PEM film deposition methods

#### 2.2.1.1 Film building and crosslinking

The PEM film used in this study is composed of 3 polyelectrolytes: poly (ethyleneimine) as the polycation anchoring layer, poly (L-Lysine) hydrobromide as the polycation and hyaluronic acid as the polyanion. Their characteristics are described in **Table 8**.



PE	Abv	Charge	pI	Structure	Working Concentration	Provider
Poly (ethylene imine)	PEI	+	10.8		[PEI] = 5 mg/mL	Sigma-Aldrich France
Poly (L-Lysine) hydrobromide	PLL	+	9		[PLL] = 0.5 mg/mL	Sigma-Aldrich France
Hyaluronic acid	HA	-	2.5		[HA] = 1 mg/mL	Lifecore USA

**Table 8: Detailed characteristics of the polyelectrolytes used** (PE: polyelectrolytes, Abv: abbreviation, pI: isoelectric point)<sup>176,177</sup>

Prior to the film buildup, hyaluronic acid (HA) and poly (L-Lysine) PLL were dissolved respectively at 1 mg/mL and 0.5 mg/mL into a HEPES-NaCl buffer composed of 20 mM HEPES at pH 7.4 and 0.15 M NaCl.

The film buildup starts with the deposition of an anchoring layer of polyethyleneimine at 5mg/mL (PEI, P3143, Sigma-Aldrich, France) dissolved in NaCl solution (0.15M NaCl at pH 6.5) for 20 min, followed by a layer of hyaluronic acid at 1 mg/mL (HA, 360 kDa, 02159933, Lifecore Biomedicals, USA) for 6 min.

Then, the successive bilayers deposition was made with poly(L-Lysine) hydrobromide at 0.5 mg/mL (PLL, 55 kDa, P2636, Sigma-Aldrich, France) and hyaluronic acid successively<sup>155</sup>. For each layer, the polyelectrolytes were left at rest for 6 min to allow their adsorption and then were rinsed (one quick rinsing and a 3 min rinsing) with a rinsing solution made of salt (0.15M NaCl at pH 6.4).

The (PLL/HA)<sub>x</sub> film (x corresponding to the number of layer pairs in the film, also called here bilayers) were crosslinked as previously described<sup>178</sup> using concentrations of EDC at 10 mg/mL, 30 mg/mL or 70 mg/mL (noted respectively EDC10, EDC30 and EDC70) and sulfo-NHS concentration was fixed at 11 mg/mL by incubation overnight (about 18h) at -4°C. Finally, the crosslinking agents were removed by rinsing thoroughly the film at room temperature with 6 washing steps of 20 min with HEPES-NaCl buffer (pH 7.4). The film was then stored in the fridge in HEPES-NaCl buffer.

#### 2.2.1.2 Film deposition in cell culture plates using an automated liquid handling robot

For 2D *in vitro* cellular assays, we built 12 and 24 bilayers of (PLL/HA)<sub>12/24</sub> into 96 well plate (Greiner Bio-One, Germany) in order to screen several conditions at the same time. The (PLL/HA)<sub>12/24</sub> film were automatically deposited into each well of the 96 well plate using an

automated liquid handling machine (TECAN Freedom EVO 100, France). This machine is equipped with liquid containers and tips to aspirate and dispense the polyelectrolytes on well plates that are disposed on a plate tilter, as described in the machine working table (**Figure 74**).

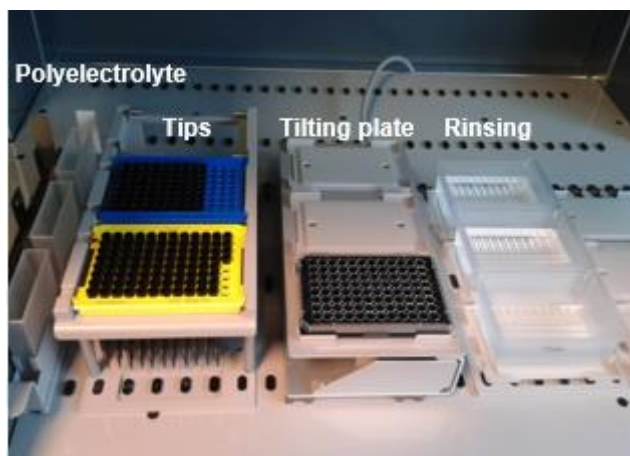


**Figure 74:** Working table of the automated liquid handling machine used for the film deposition in cell culture well plates. The polyelectrolyte solutions are in reservoirs, the tips on tip holders while the well plates are placed on a tilting plate carrier. The reservoir containing the rinsing solutions are placed on the right side of the working table.

The film buildup sequence is the same as previously described in 2.2.1.1. First the plates were tilted (**Figure 75**), the polyelectrolyte solutions were dispensed and the plates were set back in planar position for the incubation period. For the following polyelectrolyte removal and aspiration, the plates were tilted again to avoid the contact of the tip with the film. The remaining non-adsorbed polyelectrolyte was rinsed twice (2 min rinsing) following the same procedure. The sequence was then repeated until reaching the targeted number of bilayers<sup>179</sup>.

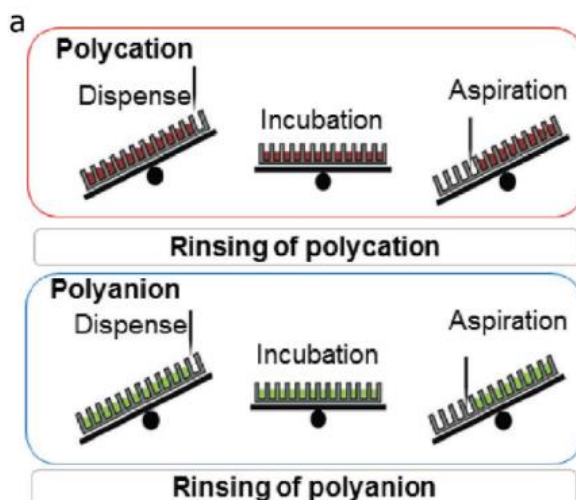


**Figure 75:** Schematic of layer-by-layer film deposit using the automated liquid handling machine into 96 well plates<sup>179</sup>

The film was then crosslinked manually by disposing 50  $\mu\text{L}$  of EDC/NHS solution into each well with a multichannel pipette as previously described in 2.2.1.1.

### 2.2.1.3 Film deposition on 3D scaffolds by automated dipping method

The films were deposited on 3D titanium scaffolds using the dip coating method<sup>150</sup> with an automated dipping machine (Dipping Robot DR3, Kirstein GmbH, Germany). The internal view of the DR3 is displayed in **Figure 76**.

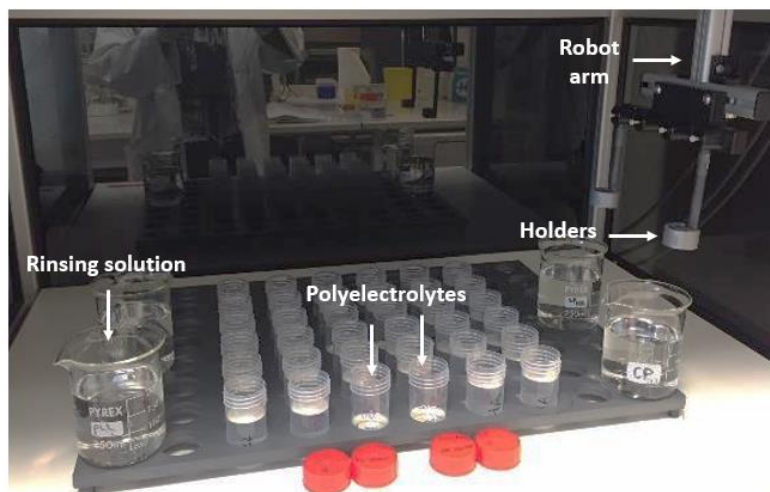


**Figure 76:** Picture of the automated dipping robot DR3 for the film deposition on 3D architected scaffolds. The polyelectrolytes and rinsing solutions are in beakers, where the robot arm is successively dipped into following a custom-made procedure. The total duration for the deposition of 12 layer pairs is about 8 h.

Instead of depositing a fixed amount of polyelectrolytes as for the 2D configuration, the scaffolds were placed into glass slides holders equipped with a homemade 3D printed crown (courtesy of C. Masse De La Huerta, PhD student at LMGP) and dipped into 13 mL of PLL or HA polyelectrolytes solutions, followed by rinsing steps into 150 mL and then 30 mL of rinsing solution after each adsorption of a polyelectrolyte layer (**Figure 77**).

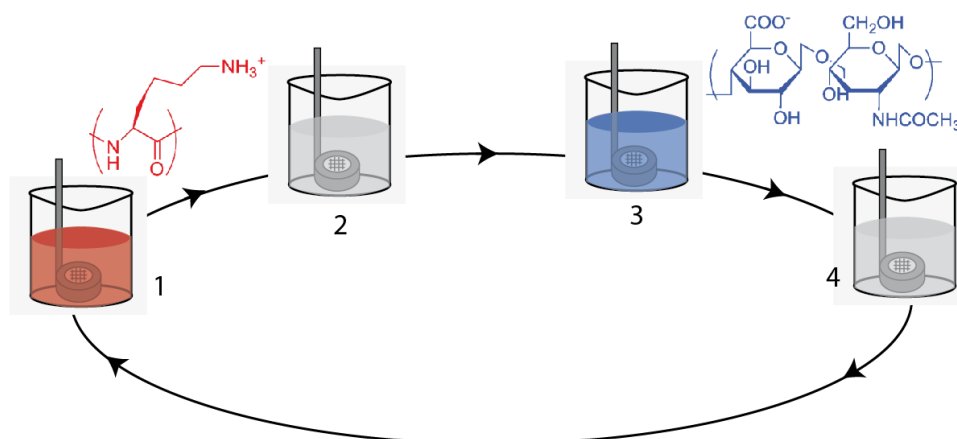


**Figure 77:** Schematic representation of the automated dipping method for the PEM film deposition into 3D architected scaffolds

At the end of the deposition, scaffolds were individually put into wells of a cell culture plate of 24 wells for the film crosslinking. The scaffolds ( $\varnothing$  10 mm x L 7 mm) were either coated with 12 and 24 bilayers of (PLL/HA) films respectively depending on their following use.

## 2.2.2 Loading of BMP-7 into PEM film

### 2.2.2.1 BMP-7 storage

In order to avoid a loss of bioactivity through protein aggregation or denaturation, BMP-7 (gift from Olympus Biotech, USA) was provided and stored in an acidic buffer composed of trehalose and acid lactic (trehalose 9% in acid lactic at pH 3) at the concentration of 1 mg/mL. It was stored at -20°C into 0.5 mL low-binding tubes (Eppendorf LoBind microcentrifuge tubes, Z666491, Sigma-Aldrich, France) and aliquoted at 500 µL.

Prior each use of the protein, an aliquot of BMP-7 (tub containing small amount of the protein) was thawed out slowly at room temperature and then gently agitated for the following recovery.

### 2.2.2.2 Loading procedure

The concentrated solution of BMP-7 was diluted into 1 mM HCl solution (filtered with a 20 µm filter) at pH 3. The concentration of the BMP-7 loading solution was varied between 2.5, 5, 10, 25, 50, 100 and 150 µg/mL. The BMP-7 loaded into the film will be thereafter designed as b-BMP-7.

After crosslinking, the films were kept in wet conditions into HEPES-NaCl buffer at pH 7.4. To load the protein, the left HEPES-NaCl at the top of the films was completely removed and the films were directly soaked with BMP-7 loading solutions for 1h30 at 37°C. Finally, films were rinsed with HEPES-NaCl buffer, for 1h every 10 min at room temperature, to remove any unbounded BMP-7 and were stored in HEPES-NaCl buffer<sup>153</sup>.

## 2.3 Characterization of the film deposition and the BMP-7 loading

After deposition, the osteoinductive film is hardly visible by eye. In this section, the different tools and equipment used for the film characterization and parts of the cellular studies will be detailed.

### 2.3.1 Film labelling with Rhodamine and FITC

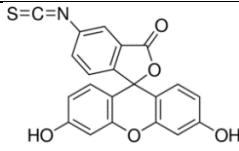
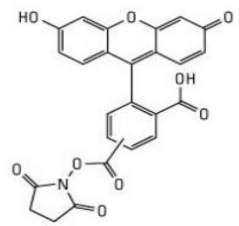
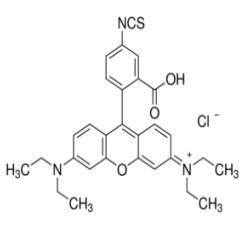
#### 2.3.1.1 Fluorophores

Fluorophores are fluorescent molecules able to adsorb light and that re-emit it with a higher wavelength (Stokes shift). Those molecules can be used on their own as a tracer in fluids or as a dye for staining cells, tissues or materials and can as well be employed as a labelling tool for antibodies or proteins<sup>180</sup>.

The 3 fluorophores used to label the PEM films or the BMP-7 were:

- FITC (fluorescein 5-isothiocyanate, ref 3326-32-7, Sigma-Aldrich)
- NHS-fluorescein (5(6)-carboxyfluorescein N-hydroxysuccinimide ester, ref 21878, Sigma-Aldrich)
- Rhodamine (rhodamine B isothiocyanate, ref 36877-69-7, Sigma-Aldrich)

Their characteristics are described in **Table 9**.

Abbreviation	Complete name	Structure	Molecular weight (g/mol)	Excitation wavelength $\lambda_{ex,max}$	Emission wavelength $\lambda_{em,max}$
FITC	fluorescein 5-isothiocyanate		389	492 nm	518 nm
NHS-fluorescein	5(6)-carboxyfluorescein N-hydroxysuccinimide ester		473	494 nm	518 nm
Rhodamine	rhodamine B isothiocyanate		536	543 nm	580 nm

**Table 9: Rhodamine, FITC and NHS-Fluorescein fluorophores main characteristics**

### 2.3.1.2 PEM film labelling with labelled PLL

Our strategy to verify the film deposition was to build the film with fluorescently labelled PLL or to add manually a last layer of PLL<sup>FITC</sup> or PLL<sup>rhod</sup> before the crosslinking step. To do so, the PLL was dissolved at 5 mg/mL in a sodium bicarbonate buffer (50 mM, pH 8.4) and the dye was added in the solution with a molecular ratio of 1/2.5 (PLL molecule/dye). The labelling reaction was performed under slow agitation and protected from light at room temperature for 2 h. Then, the free dye was removed by dialysis in 400 mL of HEPES/NaCl buffer at 4°C using a membrane with a 6-8 kDa cut off under gentle agitation. Then, the buffer was changed at least 4 times over 48 h and finally the labelled PLL was stored at -20°C.

### 2.3.2 BMP-7 labelling with NHS-fluorescein

In order to tag the BMP-7 protein, we used a previously established protocol using the NHS-fluorescein (5(6)-carboxyfluorescein N-hydroxysuccinimide ester, ref 21878, Sigma-Aldrich) whose characteristics are given in **Table 9**<sup>150,153</sup>.

To allow the grafting of the NHS-fluorescein on the BMP-7, the initial pH of 3.5 was raised at pH 7.5 with the sodium bicarbonate buffer (50 mM, pH 8.4). Then, the dye was directly added to the BMP-7 solution with a molecular ratio of 1:20 (BMP-7/dye) and slowly agitated for 2h at room temperature protected from light. Afterwards, the free NHS-fluorescein was removed

by dialysis in 2 x 1 L of 1mM HCl at 4°C using a membrane with a 6-8 kDa cut off under gentle agitation for 2h, with a renewal of the HCl solution after 1 h. The labelled BMP-7 was then stored at -20°C.

### 2.3.3 Spectrophotometry

The spectrophotometry consists in the quantitative measurement of the monochromatic light absorption or emission of a material as a function of the light wavelength in the visible light, near ultraviolet and near infrared ranges (**Figure 78**).

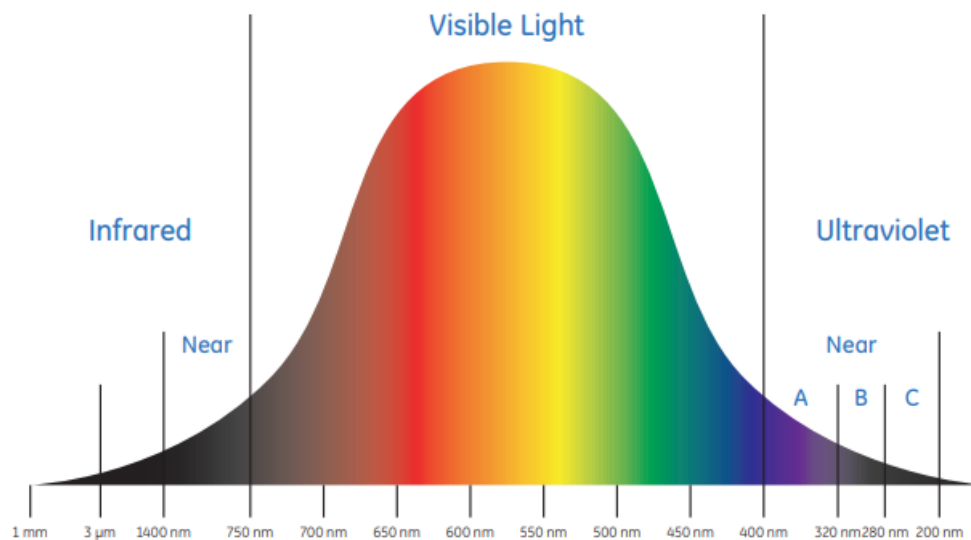


**Figure 78: Physical electromagnetic light spectrum**<sup>181</sup>

The associated apparatus for those measurements is called a spectrophotometer, a simplified overview of a spectrophotometer configuration is shown in **Figure 79**.

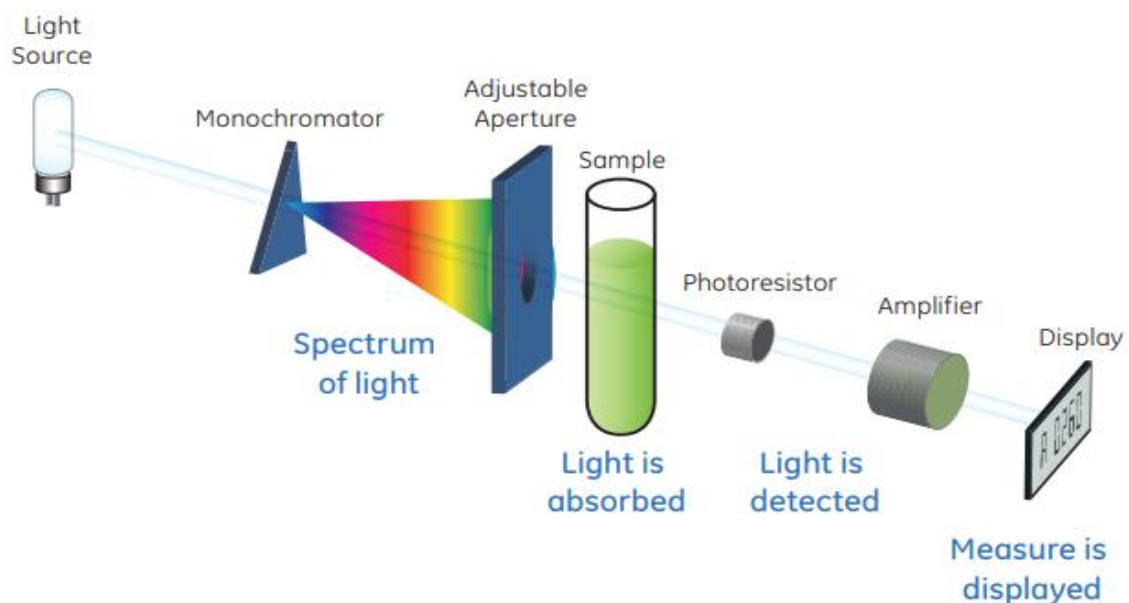


**Figure 79: General principle and components of a spectrophotometer.** The light is produced by a source light and travels through the monochromator and an adjustable aperture to illuminate the sample. The transmitted light is detected through a photoresistor<sup>181</sup>



First, the light from the source passes through a monochromator in order to select the desired wavelength. Then, the monochromatic light is directed to the probed sample and the transmitted light is detected through a photoresistor. The decreasing resistance with the increasing light intensity is detected and compared to the value from the original light source. In this study, the spectrophotometer we used was a TECAN Infinite M1000 microplate reader (Tecan France, Lyon).

### 2.3.4 BMP-7 quantification with BCA assay

The bicinchoninic acid (BCA) assay is a colorimetric technique used to measure proteins concentrations in a given volume. This assay is based on the alkaline reduction of  $\text{Cu}^{2+}$  ions into  $\text{Cu}^+$  ions by proteins and the following formation of a purple coloured complex derived from the reaction of the bicinchoninic acid with  $\text{Cu}^+$  ions (**Figure 80**).

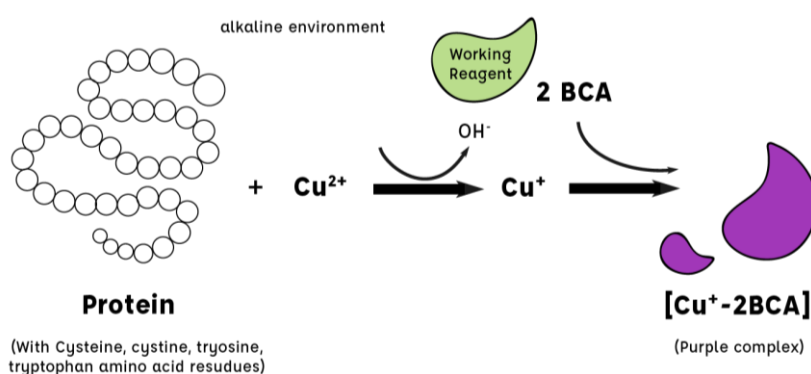


**Figure 80: Bicinchoninic acid BCA assay principle.** Available proteins reduce  $\text{Cu}^{2+}$  ions into  $\text{Cu}^+$  ions which reacts with bicinchoninic acid and form  $[\text{Cu}^+-2\text{BCA}]$  purple complex. The absorbance is then measured to quantify the amount of proteins<sup>182</sup>

The absorbance of the complex is then measured by spectrophotometry at  $562 \pm 10$  nm and a calibration curve, derived from successive dilutions of bovine serum albumin protein (BSA) at a fixed and known concentration, gives the corresponding protein concentration. Knowing the volume and concentration of proteins, it is possible to estimate the total protein mass.

The amount of BMP-7 loaded into the PEM film was quantified using QuantiPro™ micro BCA assay kit (Sigma-Aldrich, France) as previously done<sup>179</sup>. To this end, 96 well plates (Greiner Bio-One, Germany) were coated with PEM film and loaded with increasing BMP-7 concentrations from 2.5 to 100  $\mu\text{g}/\text{mL}$ .

To evaluate the mass of BMP-7 adsorbed in the film, the mass of BMP-7 in the loading solution before and after the loading were measured and subtracted to each other to determine the mass loss. Then, the adsorbed amount was obtained by dividing this mass by the surface area of the well ( $0.34 \text{ cm}^2$ ).

### 2.3.5 Fluorescence macroscopy and microscopy

#### 2.3.5.1 Fluorescence macroscopy

Fluorescence macroscopy combines the high resolution photography of reflected light, with relatively low enlargement zoom (0.5X to 10X), with the acquisition of fluorescent light. The

fluorescent sample is excited with a mercury halide external lamp (EL6000, Leica, France) and its fluorescent emitted light is acquired with a CCD digital camera directly located at the top of the observation column (**Figure 81**).

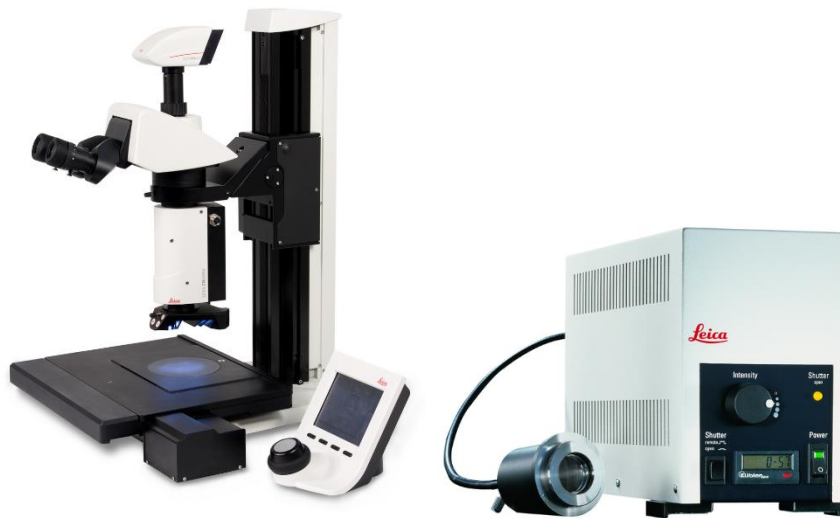


*Figure 81: Illustration of the macro microscope Leica Z16 and the external mercury halide lamp. The fluorescence macroscopy system used was the combination of the macro microscope and the external lamp with a CCD digital camera (not represented here)<sup>183</sup>*

In this study, we used a Leica Macrofluor (Z16 Apo, Leica, France) equipped with the external lamp for the fluorescence detection (at the objective 0.8X) available at the IAB (Institute for Advance Biosciences, Grenoble). The film was observed with a last layer of (PLL<sup>FITC</sup>/HA) deposited on Ti-6Al-4V scaffolds with an excitation wavelength at 492 nm.

#### 2.3.5.2 Epifluorescence microscopy

Epifluorescence microscopy is based on the detection of fluorescent light emitted by the observed sample, with the particular optical configuration where the excitation and emitted lights travel back through the same objective to the detector (either in the eyes through the ocular port or the camera).

**Figure 82** illustrates the working principle of epifluorescence microscopy. First, the light source is filtered through an excitation filter and guided to the sample by reflection on the dichroic mirror. Then, the excitation light is condensed by the objective and illuminates the sample. The emitted light from the sample passes by the same objective (“epi” meaning “same” in Greek) and the dichroic mirror, who reflects the excitation light and simultaneously transmits the emitted light to the emission filter before being detected by the camera or the eyes<sup>184</sup>.

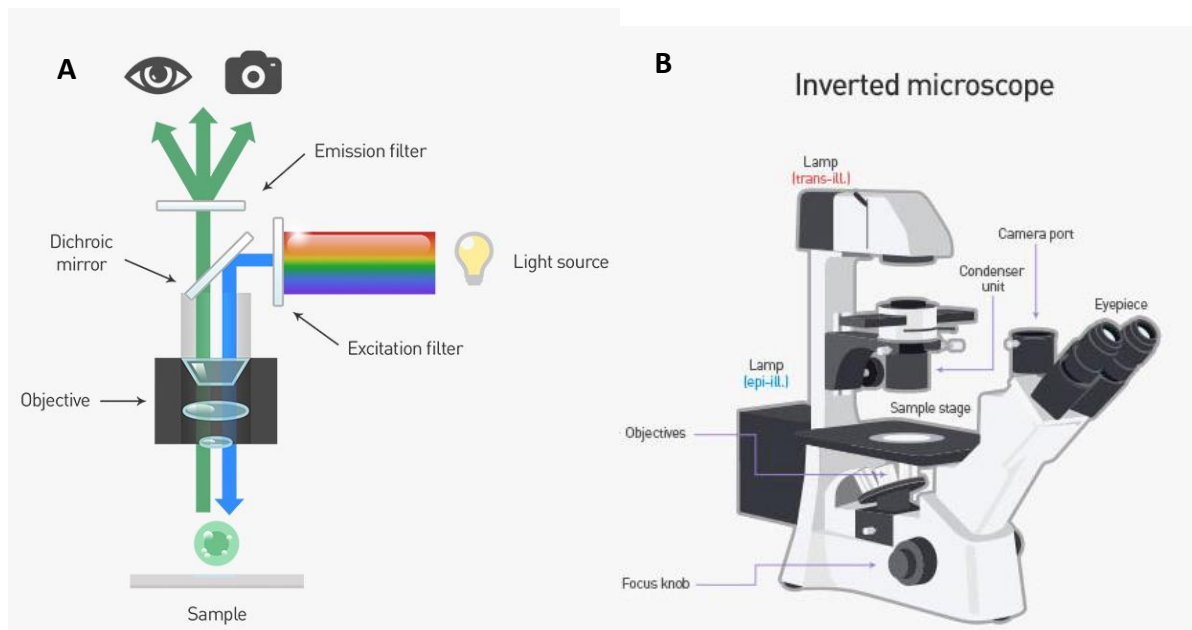


**Figure 82: Schematic presentation of the principle of epifluorescence microscopy (A) and the associated inverted fluorescence microscope (B).** The source light crosses the dichroic mirror and the objective to illuminate the sample. The light emitted by the sample passes through the same objective and mirror until reaching the emission filter<sup>184</sup>

In this project, we used the Zeiss Axio-observer 7 inverted microscope (Carl Zeiss, France) equipped with a LED light source (light-emitting diode, Solid-State Source light 7 Colibri). The 5X and 10X objectives were employed either in bright field, phase contrast or wide-field epifluorescence configuration to monitor and acquire images for 2D and 3D cell cultures.

### 2.3.5.3 Confocal microscopy

In epifluorescence microscopy, the fluorescent signal obtained from a sample is emitted from the entire field exposed to the microscope objective. However, those samples are generally 3D which means that the measured light is a volumetric contribution of the signals whether in or out of the focal plane of the objective. The latter raises issues in terms of resolution with a possible loss of finer details in the focal plane.

Confocal microscopy was developed to overcome this limitation and uses lasers sources combined with two pinhole apertures specifically located, as shown in **Figure 83**.

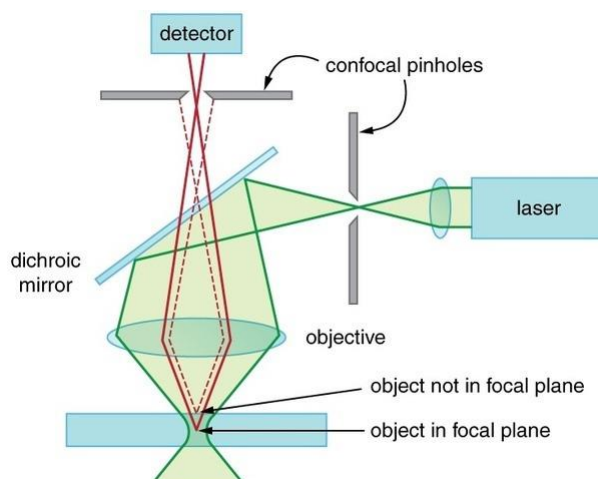


**Figure 83: Schematic representation of the confocal microscopy principle.** Pinholes are specifically placed after the laser source and before the detector on conjugate planes to the focal plan observed on the probed sample to increase the images resolution<sup>185</sup>

The first aperture is positioned directly after the excitation source in a conjugate plane (confocal) of the focal plan observed on the sample. The second aperture is also placed in a conjugate plane but located in front of the detector. This configuration allows the recovery of the emitted fluorescence light only generated by the selected focal plan. To obtain the global planar image and scan the focal plan, the focused laser beam is moved in the X, Y directions via motorized mirrors disposed on the optical path of the laser beam. The Z direction is also scanned by moving the objective along the optical axe with a stepper motor. Thus, it is possible to obtain images from different focal planes and to generate a 3D structure from the fluorescent light<sup>186</sup>.

LMGP laboratory is equipped with a confocal microscope Zeiss LSM 700 (Carl Zeiss, France) and more particularly in this study, the confocal microscopy was used to visualize the BMP-7 diffusion inside the PEM film with the 63X objective.

### 2.3.6 Scanning electron microscopy

Scanning electron microscopy (SEM) is a high resolution type of microscopy using the interaction of an electron beam with the atoms of the materials constituting the probed sample. The electron beam is scanned over the sample surface and the resulting signals emitted from the electrons/matter interaction are collected to obtain topographical and structural information.

In the case of SEM, three type of electron/matter interactions are measured: the secondary electrons (SE), the backscattered electrons (BSE) and the characteristic X-ray emitted from the atoms of the surface (**Figure 84**).

Secondary electrons (SE) enable the visualization of the topography. Backscattered electrons (BSE) allow the detection of the different sample phases at the surface depending on the atomic number. And finally, characteristic X-rays emitted enable the measurement of the atomic composition.

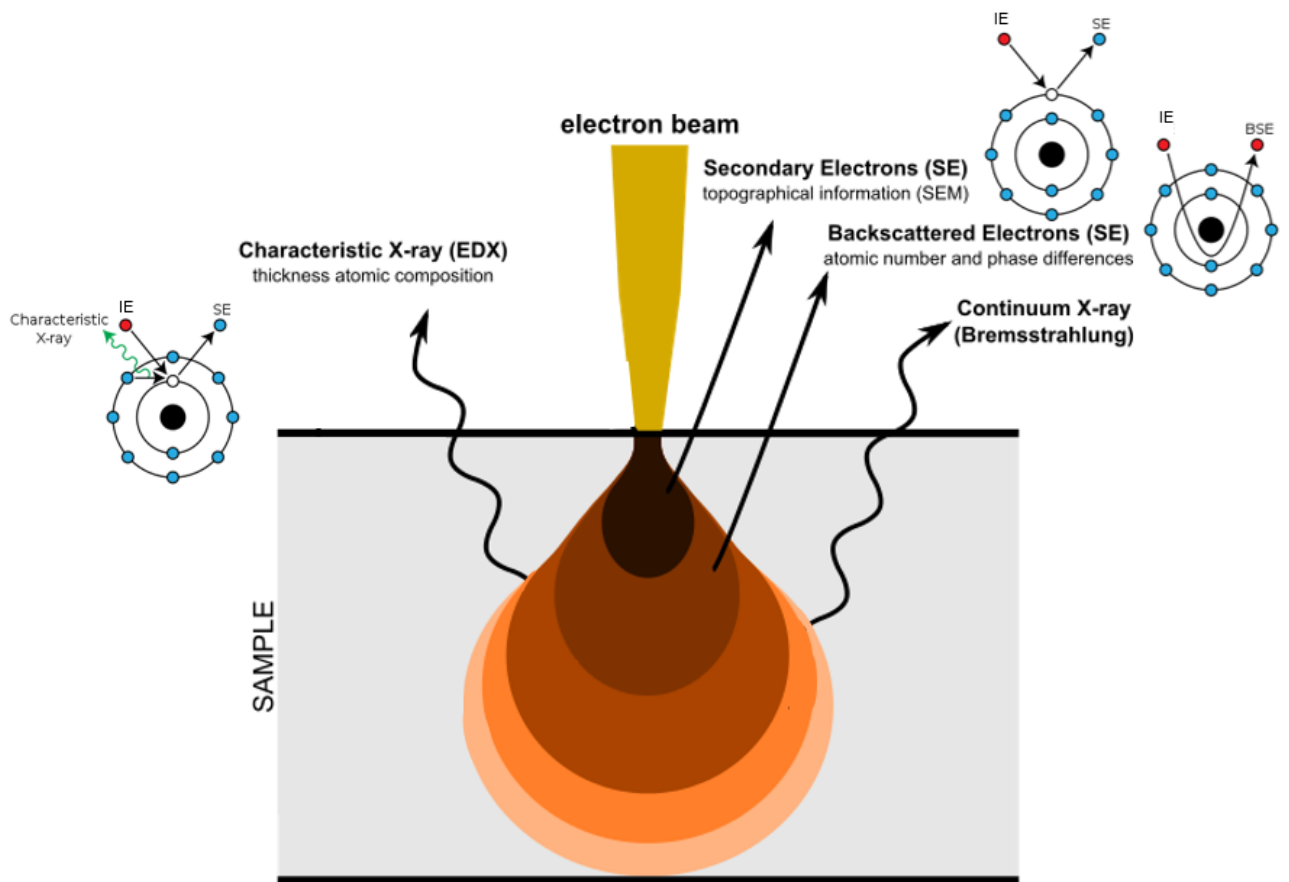


**Figure 84:** The different physical phenomena resulting from the electron/matter interaction detected by the scanning electron microscope. Secondary, backscattered electrons and characteristic X-rays are detected to image and analyse the sample composition<sup>187</sup>

**Figure 85** represents a schematic view of the internal elements constituting a scanning electron microscope. First in the column, electrons are thermally generated from the electron source by applying a high voltage between a filament cathode (generally tungsten) and an anode. The formed electron beam, whose energy can vary from 0.2 keV to 40 keV, is focused by two condenser lenses and its trajectory is controlled by the x, y scanning coils. The objective lens allows to focus the electron beam at the sample surface. Then, the electron beam enters the chamber and interacts with the sample and the emitted signals are measured by the 3 different detectors.

The electron beam requires to work under high vacuum to precisely control the electron beam trajectory. In the column, the vacuum is generally higher than in the chamber with values around 1 mPa for SEM equipped with tungsten filament. In the chamber, the pressure can vary between 1 and 0.01 mPa.

The SEM makes possible to observe areas ranging from approximately 1 to 5  $\mu\text{m}$  in width and the magnification is ranging from 20X to approximately 30 000X with a spatial resolution of 50 to 100 nm.

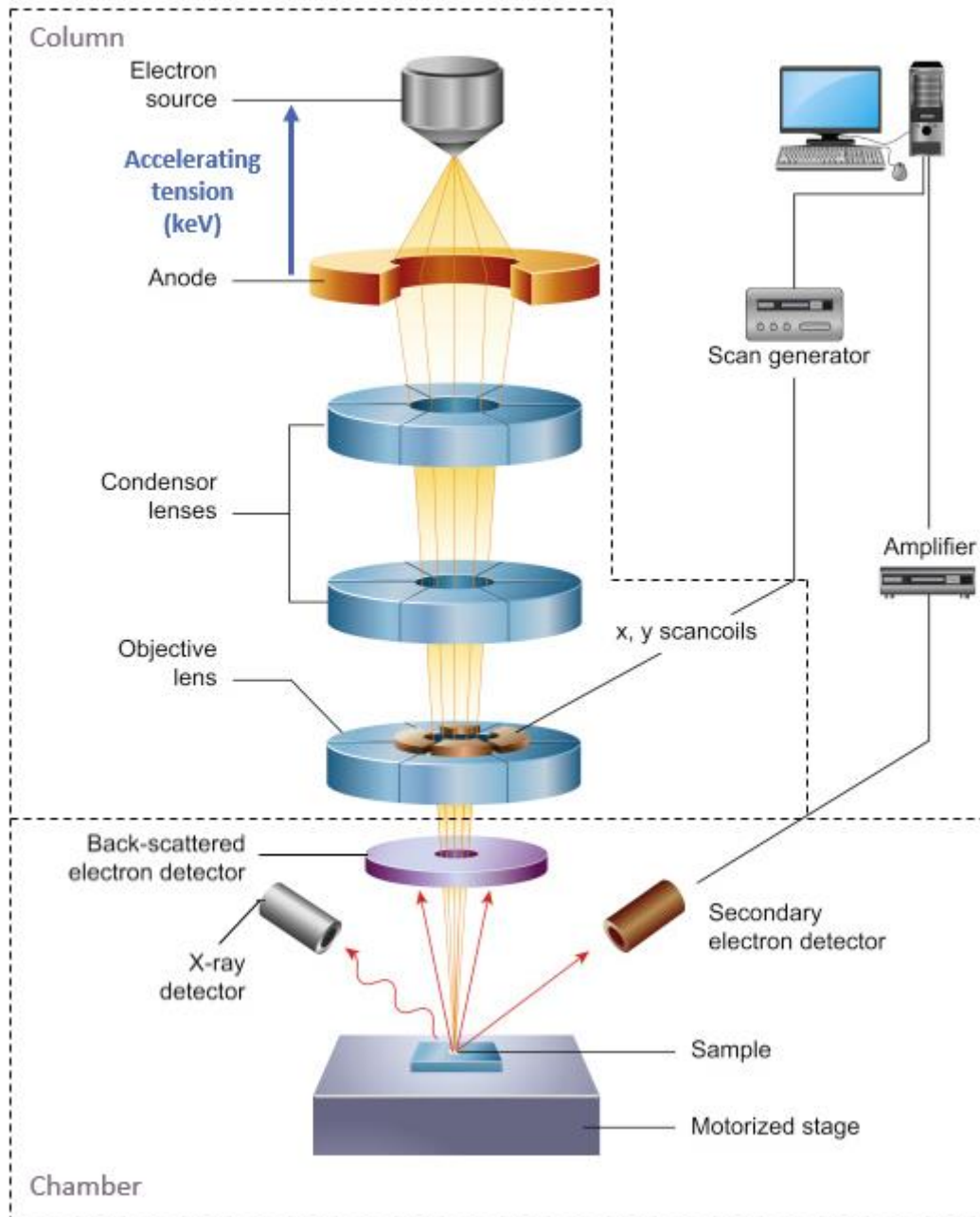


**Figure 85: Scheme of the scanning electron microscope.** The scanning electron beam is generated and controlled in the column, the emitted signals from the electrons/matter interaction are detected in the chamber (adapted from<sup>188</sup>)

In this thesis, we used the FEI-Quanta 250 SEM-FEG (Thermo Fisher, USA) in topography and chemical contrast modes (SE and BSE detections) for the film coating and cell morphology visualization at the scaffolds surface. Our imaging condition was settled at a low accelerating tension of 5 keV which is recommended for non-conductive materials.

## 2.4 Cell culture and biological investigations

In order to assess the osteoinductive capacity of the coating, *in vitro* cell cultures were performed on films and scaffolds. This section will described the type of cells used in this project and the associated biological assays.



## 2.4.1 D1 cell culture

### 2.4.1.1 D1 cell line

Among the stem cell population, mesenchymal stem cells (MSC) are known to be at the origin of the bone formation process through aggregation, condensation and chondrogenic and osteogenic differentiation, leading to the endochondral ossification<sup>189</sup>. In this project, we chose to use the D1 cell line as cellular model. D1 cells are murine mesenchymal stem cells that were isolated from mouse bone-marrow cells and cloned to obtain a cell line<sup>190</sup>.

The cells were obtained frozen in suspension from the American Type Culture Collection (D1 ORL UVA, < 16 passages, ATCC)<sup>191</sup>. D1 cells are adherent cells and thus need planar surfaces to be cultured. In this study, D1 cells were cultured either in Cellstar® 75cm<sup>2</sup> flasks (T-75 flask, Greiner Bio-One, Germany) for their amplification, or in 24 and 96 well plates (Greiner Bio-One, Germany) for the different experiments (**Figure 86**).

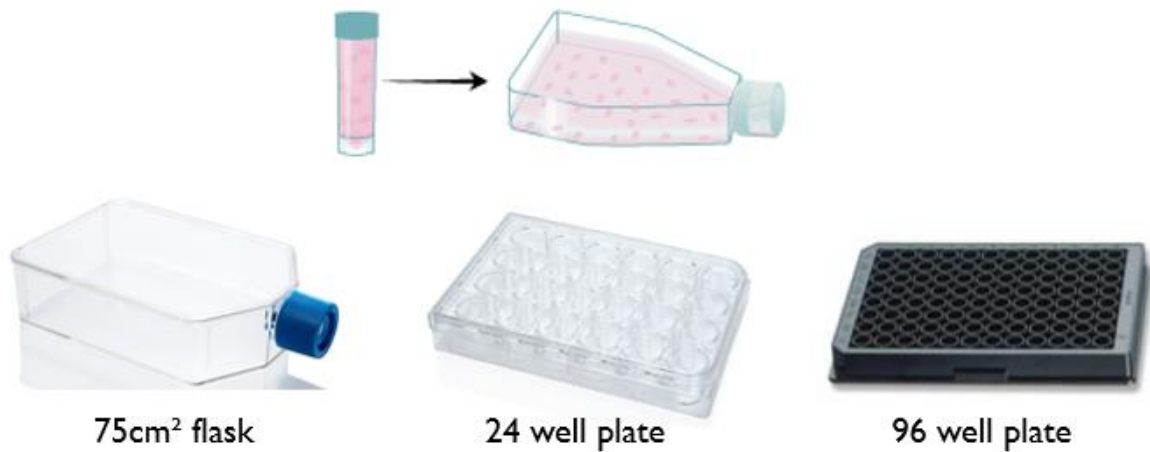


**Figure 86: Illustration of the different types of cell culture plates used in experiments.** From left to right: 75 cm<sup>2</sup> flasks used for cellular amplification, 24 and 96 well plates used to run experiments<sup>192</sup>

In our body, cells are constantly surrounded by an adjustable extracellular matrix which provides the supply of nutrients, allows the removal of waste and that provides the appropriate mechanical stability. To recreate this environment and maintain alive the cells, their culture is done in an aqueous environment at a physiological pH and temperature. The aqueous solution used is commonly called the cell culture medium.

The growth medium (GM) used in this study was composed of Minimum Essential Medium Eagle ( $\alpha$ MEM, Sigma-Aldrich, France) supplemented with 10% foetal bovine serum (FBS, PAA Laboratories, France), 1% GlutaMAX 100X (Gibco, ThermoFisher, France) and 100 U/mL penicillin and 100  $\mu$ g/mL streptomycin (Gibco, ThermoFisher, France). The GM was changed every 2 days to ensure the supply of nutrients and to maintain the pH. The temperature and also the pH were maintained at physiological levels (pH 7.4, 37°C) thanks to the cell incubator. The cell incubator is a hermetic and humid chamber which regulates the temperature and the CO<sub>2</sub> level (5% for mammalian cells). To avoid possible microorganisms (bacteria, fungi, yeast and virus) contaminations in the culture, all solutions, containers and disposable materials

used are sterile (directly bought sterilized or sterilized by the team with an autoclave) and the cell culture work was executed in a laminar flow hood (cell culture hood, **Figure 87**).

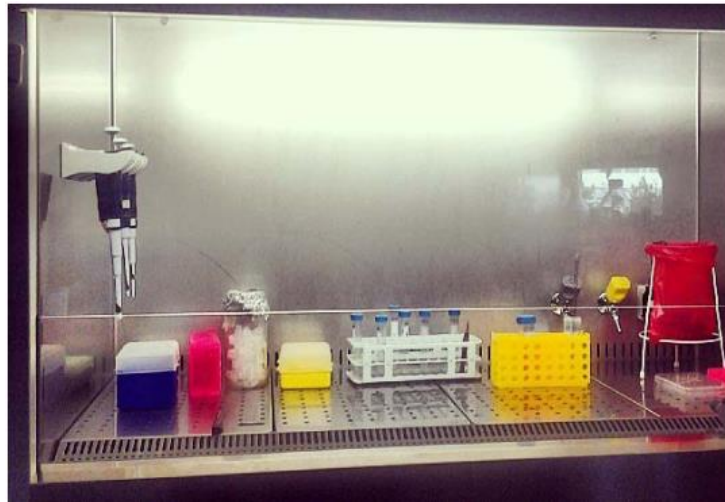


**Figure 87:** Picture of the cell culture hood with laminar flow available at the LMGP laboratory<sup>193</sup>

Cellular amplification does not only requires the change of the culture medium. Indeed, when cells divide and cover all the available surface of a cell culture dish (100% confluence), they stop replicating and can even lose their ability to proliferate. For those reasons, cells were sub cultured (transferred into new dishes at low density) prior reaching 60-70% confluence, approximately every 2 days (**Figure 88**).

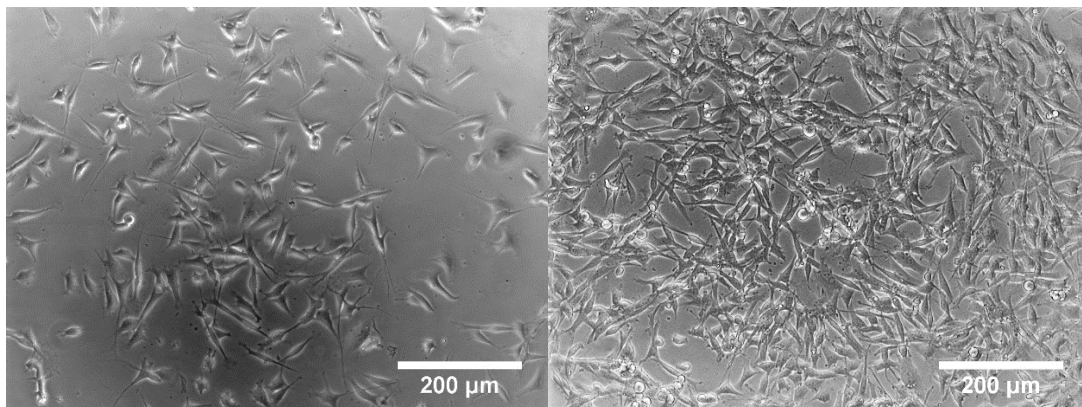


**Figure 88:** Phase contrast microscopy images of D1 cells at 20% (left) and 70% (right) confluence in 75 cm<sup>2</sup> flask in growth medium

#### 2.4.1.2 Culture procedure in 3D

To assess the osteoinductive capacity of coated scaffolds, D1 cells were also cultured *in vitro* into 3D scaffolds. To this end, the cell seeding and culture procedure in 3D conditions was adapted from a protocol published in the literature<sup>194</sup>. Prior to each 3D culture, scaffolds were sterilized with UV at 100 kJ/cm<sup>2</sup> (CL-1000 ultraviolet cross linker, UVP, USA) in HEPES/NaCl, 10 min by side (top-bottom-left-right) in a 24 well plate. The 360° multi-functional tube rotator (PTR-35, Grant-Bio, USA) and 3D multi-function rotator (PS-M3D, Grant-Bio, USA) required for the cell seeding and culture were cleaned with ethanol and UV sterilized into the cell culture hood 20 min per sides and kept in the hood until their use in the incubator. The cell seeding and culture procedure is represented in **Figure 89**.

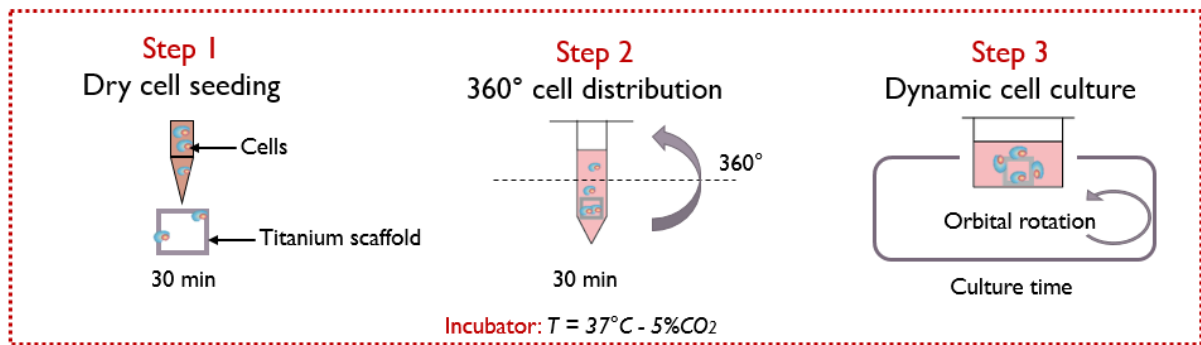


**Figure 89: 3D cell seeding and culture procedure on 3D architected titanium scaffolds.** Step 1: dry cell seeding. Step 2: homogenization of cell distribution. Step 3: dynamic cell culture.

First (**step 1** in **Figure 32**), sterilized scaffolds were placed into sterile 5mL Eppendorf low binding tubes, which were previously placed into the 360° rotator. Then, a highly concentrated cells suspension was prepared at  $5 \times 10^6$  cells/mL and 100  $\mu$ L of this suspension was drop-seeded randomly at the top of the scaffold, in order to obtain  $5 \times 10^5$  cells per scaffold. The 360° rotator holding the tubes with the cells seeded scaffolds was placed into the incubator without additional medium for a static incubation of 30 min to allow cell adhesion.

Secondly (**step 2** in **Figure 32**), 500  $\mu$ L of GM was added into each tube and the 360° rotator was activated for 30 min into the incubator to allow unattached cells to penetrate the scaffolds. Finally (**step 3** in **Figure 32**), the scaffolds containing cells were recovered, placed into a 24 well plate. 1 mL of GM was added and the set was put back into the incubator on the planar rotator with an orbital rotation (30 rpm, PS-M3D Grant Bio) for long term culture.

#### 2.4.2 Cell quantification with DNA-based cell proliferation assay

The strategy used to evaluate the cell proliferation was to count the number of cells at different time point. To this end, we used the CyQuant® Cell Proliferation assay kit (Molecular Probes, Invitrogen, France)<sup>195</sup>. This assay is based on the quantification of the total DNA amount by fluorescence associated with a cell number calibration curve. The procedure is detailed in **Figure 90**.

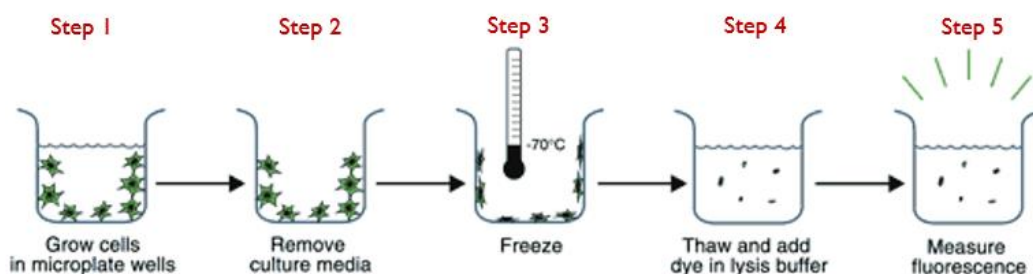


**Figure 90: Cell quantification with DNA-based cell proliferation assay.** After reaching the final time point, cells are frozen and lysed to obtain their DNA in the lysate. Then, the provided fluorescent dye in the kit binds to the available DNA<sup>195</sup>

At the corresponding time point (**step 1**), cell culture medium was removed (**step 2**) and cells were frozen at  $-80^\circ\text{C}$  overnight to damage their membrane and freeze their state (**step 3**). Then, they were thawed and the mix of lysis buffer and the green fluorescent dye (provided

in the kit) were added onto the cells (**step 4**). The aim of this buffer is to lyse (dissolve) the cell membrane and to allow the dye binding to DNA molecules. Once the dye is bound to nucleic acids, it exhibits an enhanced fluorescent light (**step 5**) which can then be compared to a cell number calibration curve (fluorescence as a function of the cell number) prepared with the same procedure. The fluorescence is then measured with an excitation light at  $485 \text{ nm} \pm 10 \text{ nm}$  and a detection of the emission light at  $530 \text{ nm} \pm 10 \text{ nm}$  by spectrophotometry. The range of this assay is generally linear from 50 to 50 000 cells per 200  $\mu\text{L}$ .

The proliferation of D1 cells on PEM film loaded with BMP-7 was determined in 2D using the kit as previously described<sup>178</sup>. To this end, 8500 cells/mL (5000 cells/cm<sup>2</sup>) in GM were seeded into 96 well plate loaded with BMP-7 and cultured for 1, 2 and 7 days. For each time points, the cells were washed twice with PBS and frozen at  $-80^\circ\text{C}$  overnight. The cell number was determined by fluorescent spectrophotometry (TECAN Infinite 1000, France) after doing a cell number standard calibration curve (**Figure 91**).

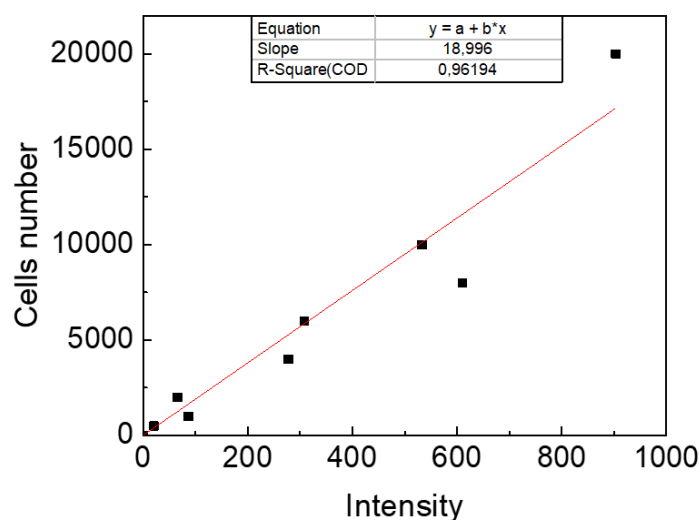


**Figure 91: Calibration curve of D1 cells number according to the DNA fluorescent intensity with Cyquant® kit (n=1)**

#### 2.4.3 Qualitative cell colonization evaluation with epifluorescence microscopy

In order to evaluate qualitatively the cell colonization after the 3D cell seeding and long term cell culture, D1 cells were seeded onto bare, only film-coated and film-coated and b-BMP-7 film coated scaffolds with  $5 \times 10^5$  cells per scaffolds and cultured for 3 days. Then, cells nuclei were stained by incubating Hoechst labelling (H3570, Invitrogen) into a serum-free medium (1:5000) for 10 min and visualized by epifluorescence microscopy with the 5X objective.

#### 2.4.4 Cell morphology with scanning electron microscopy

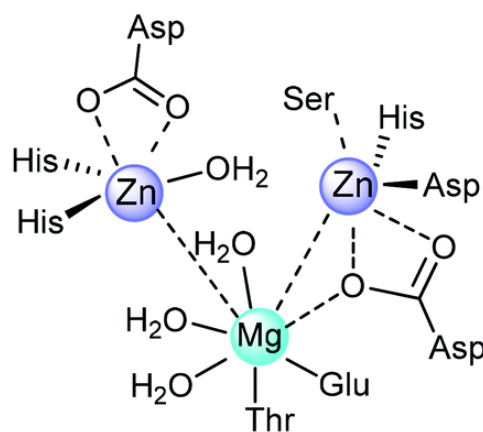
Due to the titanium non-transparent nature, we chose to observe D1 cellular morphology for cells cultured onto the 3D scaffolds with scanning electron microscopy (SEM). To maintain the cells structure and ensure appropriate visualization conditions under the SEM, the cells containing scaffolds were prepared using a dedicated protocol of the IMBM team (MODOP-110-022, I. Paintrand).

After evaluating cellular colonization by epifluorescence microscopy, cells onto scaffolds were chemically fixed with 2.5% glutaraldehyde in cacodylate buffer (0.1 M cacodylate-HCl, 0.1 M sucrose, pH 7.2) for 1 h at room temperature, followed by several rinsing steps in the same buffer. Then, the samples were slowly dehydrated to avoid cell membranes disruptions using a graded ethanol series from 30 to 100% and air-dried. Finally, to ensure the electron conduction at the cells surfaces, samples were sputtered with a thin layer of platinum (tilt 30°, 30 rpm, V=6kV, Precision Etching Coating System 682 (PECS) Gatan, “CMTC” facilities, Grenoble) for the imaging at 5 kV under the SEM.

#### 2.4.5 Evaluation of BMP-7 osteoinductivity with ALP expression

##### 2.4.5.1 Alkaline phosphatase (ALP) expression and activity

The alkaline phosphatase (ALP) is a metalloenzyme that hydrolyses phosphate monoester ( $-O-PO_3$ ) at alkaline (basic) pH environments. This enzyme contains two zinc ions and one magnesium ion which are known to participate actively in its catalytic activity (**Figure 92**). The ALP is located at the outer side of the cellular membrane and on matrix vesicles (lipid bilayers particles) in many tissues (intestine, placenta, liver, bone and kidney)<sup>196</sup>.



alkaline phosphatase

**Figure 92: Chemical structure of the alkaline phosphatase (ALP).** The ALP contains two zinc and one magnesium ions known to actively participate in its enzymatic catalytic activity<sup>197</sup>

In the case of bone tissue, ALP is expressed (produced) by bone progenitor cells and osteoblasts among other expressed proteins (**Figure 93**) and is also known to be involved in the extracellular mineralization. The ALP hydrolysing activity induces an increase of the local concentration of phosphate ions, which are essential for the calcium phosphate formation. This ALP induced hydrolyse decreases also the concentration of pyrophosphates which are inhibitors of the mineral formation<sup>196</sup>.

To identify whether a cell type starts its differentiation through bone progenitor, the ALP activity is commonly measured and considered as an important osteogenic differentiation marker<sup>198</sup>.



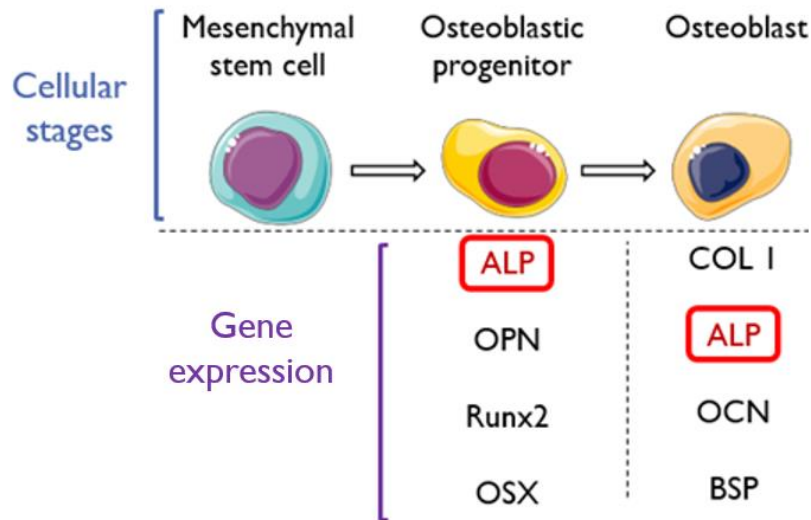


**Figure 93: Different stages of osteoblastic differentiation from mesenchymal stem cells to the formation of osteocytes.** Below are given the associated protein markers: membrane markers (CD105, CD73, CD90, CD271) as well as bone tissue markers (alkaline phosphatase ALP, osteopontin OPN, runt-related transcription factor 2 Runx2, osterix OSX, bone sialo protein BSP, adapted from<sup>199</sup>)

In this project, the BMP-7 loaded films bioactivity was assessed with D1 cells by quantifying the alkaline phosphatase (ALP) expression using two different methods adapted to 2D and 3D experiments.

#### 2.4.5.2 ALP staining assay for 2D experiments

The first method used to measure the ALP was a colorimetric staining. The staining is based on the hydrolysis of Naphtol AS-MX phosphate by the ALP. When associated with fast blue RR salt, the hydrolysed Naphtol AS-MX phosphate forms an insoluble blue product (**Figure 94**). The insoluble Azo blue product is produced where the ALP enzymes are located in the extracellular environment. This ALP staining technique was developed by the Sigma-Aldrich company (Leukocyte Alkaline Phosphatase Kit, 85L1 Sigma, France). This technique is done after cell fixation.



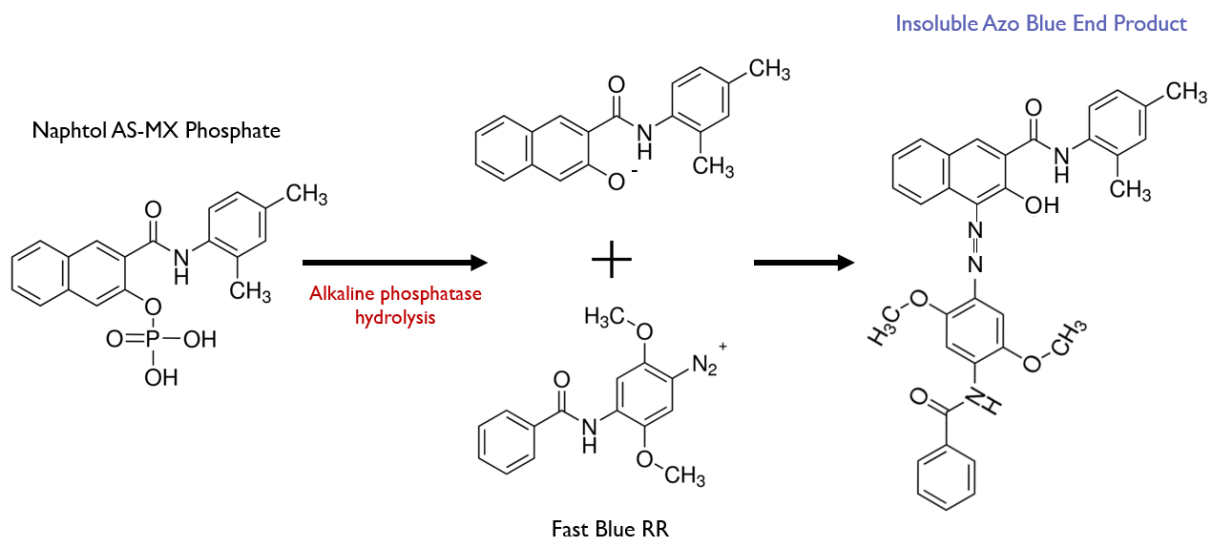


**Figure 94: ALP staining chemical reaction.** Naphtol AS-MX phosphate is hydrolysed by ALP and forms in presence of fast blue RR salt an insoluble azo blue end product at the ALP locations (adapted from<sup>200</sup>)

For 2D investigations, D1 cells were cultured into 96 well plate with BMP-7 loaded films and the ALP expression was measured using the previously described colorimetric staining<sup>179</sup>. For that, cells were seeded at 18 000 cells/mL in GM into each well containing a BMP-7 loaded film. After 3 days of culture, cells were washed with PBS and fixed with 3.7% paraformaldehyde in PBS. The expressed ALP was stained with Naphtol AS-MX phosphate kit (Sigma-Aldrich, France) and cells nuclei were labelled with 1:5000 DAPI (Invitrogen, France) in Tris buffer solid containing 0.2% of gelatine (Sigma-Aldrich, France). The ALP absorbance at  $570 \text{ nm} \pm 10 \text{ nm}$  was measured 5 times per well by spectrophotometry using the TECAN Infinite 1000. It was normalized by the nuclei fluorescence signal ( $\lambda_{ex,max} = 358 \text{ nm}$ ,  $\lambda_{em,max} = 461 \text{ nm}$ ) to account for the possible differences in cell number.

#### 2.4.5.3 ALP activity assay for 3D experiments

The method described above cannot be applied for 3D non-transparent substrate. The second used method was based on the kinetics of the ALP hydrolysis reaction of p-nitrophenylphosphate (pNPP) into p-nitrophenol (pNP) which is a yellow soluble compound. The reaction is shown in **Figure 95**.

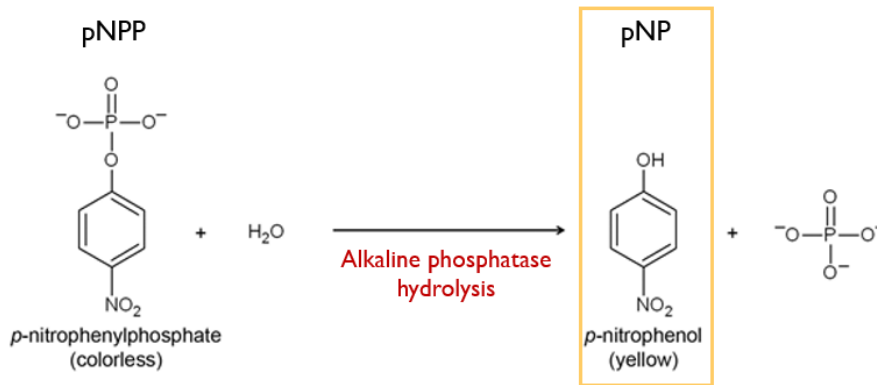


**Figure 95: ALP activity assay with pNPP hydrolysis into pN.** The kinetic of the pNP yellow insoluble compound formation is followed to determine the ALP enzymatic activity (adapted from<sup>201</sup>)

To quantify the ALP produced by the cells, cells are first lysed in 0.4% Triton-X100 in PBS. A buffer containing pNPP at basic pH is prepared to induce the reaction with the ALP contained into the cells lysate (mixture of proteins, DNA, lipids ...). After adding the buffer to the lysate, the kinetic of the pNPP → pNP reaction is followed by measuring the absorbance at 405 nm every 30 s during 10 min. The ALP activity is expressed as μmoles of pNP produced per minute per milligram of the total amount of protein (1).

$$ALP_{activity} = \frac{\alpha}{\epsilon \times l \times m_{tot,prot}} \quad (1)$$

Where:

$\alpha$  = slope (DO.min<sup>-1</sup>)

$\epsilon$  = molar attenuation coefficient of the pNP (18.75mM<sup>-1</sup>.cm<sup>-1</sup>)

$l$  = light pathlength (cm)

$m_{tot,prot}$  = total protein amount (mg)

The ALP activity of D1 cells cultured on BMP-7 loaded architected scaffolds was quantified with the pNPP colorimetric method (MODOP-110-030, R.Guillot). To this end, 5x10<sup>5</sup> cells in 100 μL of GM were seeded on the scaffolds. After 3 days of culture, GM was removed and cells on scaffolds were washed with PBS and lysed with a 10 min agitation on a plate agitator followed by 10 s of sonication into each well (20% intensity, ultrasonic processors 130W, Branson processors, USA) in 1mL of 0.4% Triton-X100 in PBS. 20 μL of the cell lysates were placed into wells of transparent 96 well plate and 180 μL of the buffer, containing 0.1M of 2-amino-2-methyl-1-propanol (Sigma-Aldrich, France), 1mM of MgCl<sub>2</sub> and 9mM of pNPP (Euromedex, France) adjusted to pH 10 with HCl, was added to the cell lysates to follow the pNPP → pNP reaction. The absorbance at 405 nm was measured with the spectrophotometer every 30 s during 10 min and the total protein contents of the cell lysates was determined by BCA assay (previously described in the 2.3.4 section)<sup>154</sup>.

## 2.4.6 Evaluation of the mineralization of the D1 cells extracellular matrix

### 2.4.6.1 Principle of the extracellular matrix mineralization

The extracellular matrix (ECM) mineralization consists in the formation of mineral compounds, mainly hydroxyapatite, into the ECM whether in extracellular fluids or into collagen fibres. The mineralization process is mediated by matrix vesicles released from osteogenic cells, as illustrated in **Figure 96**.

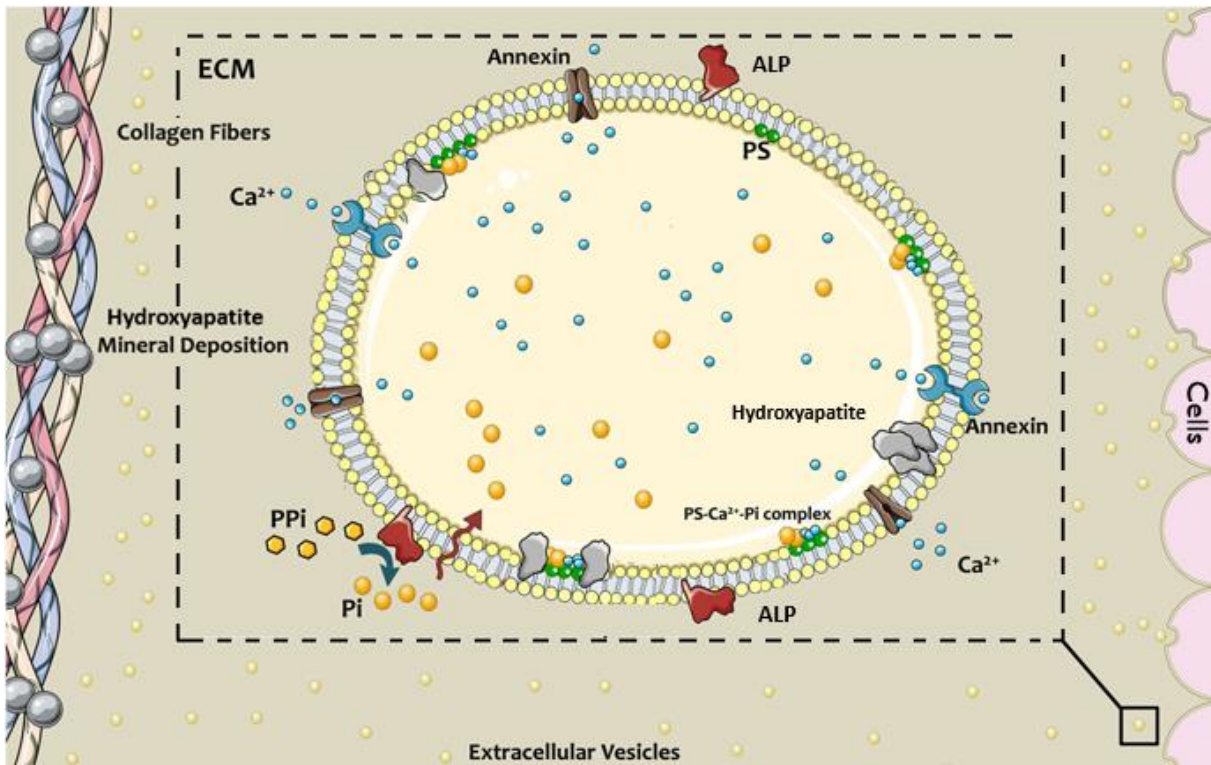


**Figure 96: Calcium and phosphate ions accumulation into matrix vesicle during the mineralization process.** Calcium and phosphate ions are attracted into matrix vesicles and form minerals within the vesicles (adapted from<sup>202</sup>)

At the membrane of the vesicles, molecules such as annexin, phosphatidylserine (PS) are attracting calcium ions  $\text{Ca}^{2+}$  into the vesicles. ALP are also found at the vesicles membrane and hydrolyse pyrophosphate (PPi) into phosphate ions ( $\text{PO}_4^{3-}$ , referred as Pi) which are then introduced into the vesicles by type III Na/Pi transporters. Due to the Pi introduction into vesicles, PS-  $\text{Ca}^{2+}$ -Pi complexes form and are at the origin of mineralization sites<sup>202</sup>.

Then, the mineralized vesicles membranes break and the preformed hydroxyapatite (HAP) crystals are exposed to extracellular fluids. At this stage, extracellular fluids contain homeostatically maintained levels of  $\text{Ca}^{2+}$  and  $\text{PO}_4^{3-}$  sufficient enough to support the propagation of new HAP crystals on the preformed HA crystals<sup>203</sup>.

### 2.4.6.2 Osteogenic differentiation medium

To induce the extracellular mineralization of mesenchymal stem cells *in vitro*, the composition of the cell culture medium has to be adapted to ensure the supply of crucial molecules involved in the mineralization process.

The common molecules added to trigger the osteogenic differentiation of multipotent stem cells are dexamethasone, ascorbic acid and  $\beta$ -Glycerophosphate ( $\beta$ -GP)<sup>204</sup>. Dexamethasone is known to induce the osteogenic differentiation by increasing the production of Runx2, an important transcription factor protein and bone marker involved in the osteogenic differentiation signalling pathway<sup>204</sup>. The ascorbic acid increases the secretion of collagen by cells and  $\beta$ -GP provides the phosphate required for the HAP crystals formation and the ECM mineralization<sup>204</sup>.

In our case, we were interested in the osteogenic differentiation of D1 cells, their ECM mineralization and how the osteoinductive film containing BMP-7 could affect this biological process. The osteogenic differentiation medium (DM) used in this project was directly derived from the GM supplemented with 50  $\mu$ g/mL L-Ascorbic acid-2-phosphate (A8960 Sigma-Aldrich, France) and with various concentration of  $\beta$ -Glycerol phosphate disodium salt pentahydrate (50020 Sigma-Aldrich, France) from 0.5 to 10 mM.

#### 2.4.6.3 Evaluation of the ECM mineralization by Alizarin Red S staining

To quantify the ECM mineralization *in vitro*, we used the Alizarin Red S staining. Alizarin Red S (3, 4-Dihydroxy-9, 10-dioxo-2-anthracenesulfonic acid sodium salt, A5533, Sigma-Aldrich) is a red dye that reacts with calcium salts and forms a calcium-alizarin red S product in a chelation process, their chemical structures are represented in **Figure 97**.

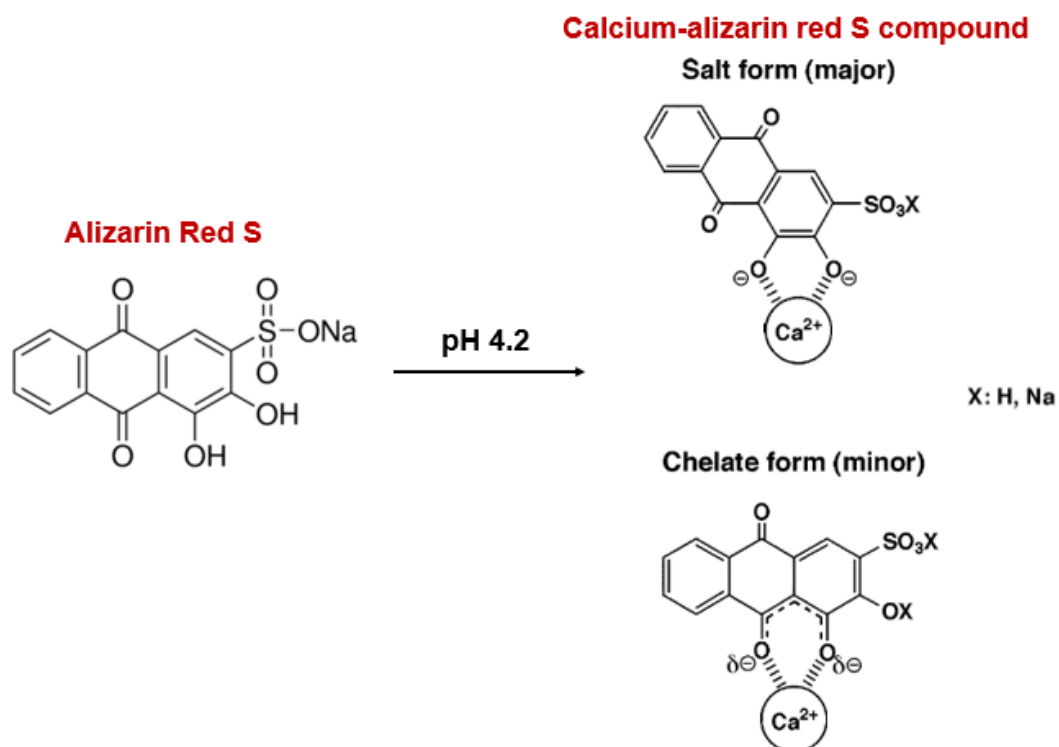


**Figure 97: Alizarin Red S and calcium-alizarin red S complex chemical structures.** The calcium-alizarin red S compound is formed at calcium salts locations and can be found in salt or chelate forms (adapted from<sup>205</sup>)

The final calcium-alizarin red S compound is also red and formed at calcium salts locations. This compound can be dissolved in an acidic solution and quantified by absorbance measurements with spectrophotometry.

For 2D studies of the ECM mineralization, D1 cells were cultured either into 24 or 96 well plates and quantified with ALZ staining. The cell density, the number of days of culture and the  $\beta$ -GP concentration in DM were varied as described in **Table 10**. After reaching the wanted number of days, cells were fixed in 3.7% formaldehyde in PBS for 15 min at room temperature.

The Alizarin Red S staining solution was prepared with 40 mM of Alizarin Red S in MilliQ water and the pH adjusted at 4.2 with 10 %  $\text{NH}_4\text{OH}$ . After fixation, cells were rinsed twice with PBS and incubated with the Alizarin Red S staining solution for 20 min at room temperature. Then, the staining solution was rinsed intensely with MilliQ water until all the unbound dye was removed and the absorbance was measured directly into wells at  $470 \text{ nm} \pm 10 \text{ nm}$  by spectrophotometry.

<b><math>\beta</math>GP (mM)</b>	10	8	6	5	4	2	1	0.5
<b>Days of culture</b>	14	12	10	9				
<b>Cell density (cell/cm<sup>2</sup>)</b>	25000	10000	5000					
<b>BMP-7 presentation</b>	Film	Solution						

*Table 10: Varied experimental parameters for the optimization of the osteogenic differentiation medium for D1 cell cultures in presence of BMP-7*

For 3D investigations, a preliminary experiment was done using bare titanium scaffolds. To this end,  $2 \times 10^5$  D1 stem cells were seeded and cultured on scaffolds for 14 days in a DM containing 10 mM of  $\beta$ -GP and was changed every 3 days. The calcium was stained following the same procedure as the 2D configuration.

After the last rinsing, calcium stained scaffolds were visualized under SEM at 5 keV to observe the ECM distribution. Finally, the ALZ staining on scaffolds was dissolved using a working solution of 0.5 M HCl with 5% SDS (Sodium Lauryl Sulfate, 151-21-3, Euromedex) in water and a 30 min incubation at room temperature. The absorbance of the resulting solution was measured at  $415 \text{ nm} \pm 10 \text{ nm}$  by spectrophotometry.

#### 2.4.7 Statistical analysis

Origin Pro 2016 9.3.2.303 (OriginLab Corporation, USA) was used for statistical analysis. All numerical values are expressed as means  $\pm$  standard deviation (SD). The means of continuous numerical variables were compared by one-way analysis of variance (ANOVA) with Kruskal-

Wallis test or Tukey-Kramer post-hoc test. For all analyses, levels of statistical significance were set at  $*p < 0.05$ .



## Chapter 3. Results: Osteoinductive coating on architected Ti-6Al-4V implants for bone regeneration (research article in preparation)

### 3.1 Preamble

Chapter 3 is written in the form of a research article that is in preparation.

By Antalya Ho-Shui-Ling <sup>1,2,3</sup>, Amandine Arnould <sup>1,2,3</sup>, Carole Fournier <sup>1,2</sup>, Paul Machillot <sup>1,2</sup>, Raphael Guillot <sup>1,2</sup>, Mathieu Suard <sup>3</sup>, Pierre Lhuissier <sup>3</sup>, Michael Bouyer <sup>4</sup>, Sanela Morand <sup>4</sup>, Georges Bettega <sup>5</sup>, Remy Dendievel <sup>3</sup>, Catherine Picart <sup>1,2</sup>

Affiliations:

<sup>1</sup> Grenoble Institute of Technology, Univ. Grenoble Alpes, 38000 Grenoble, France

<sup>2</sup> LMGP, University Grenoble Alpes & CNRS, F-38000 Grenoble, France

<sup>3</sup> SIMaP, University Grenoble Alpes & CNRS, F-38000 Grenoble, France

<sup>4</sup> CHU Service de chirurgie plastique et maxillo-faciale, Centre Hospitalier Universitaire de Grenoble, France

<sup>5</sup> Service de chirurgie maxillo-faciale, Centre Hospitalier Annecy Genevois, 1 avenue de l'hôpital, 74370, Epagny Metz-Tessy, France

### 3.2 Abstract

Bone cannot self-repair when there is a too severe injury and a large bone defect. Thus, there is a need for bone implants able to provide a mechanical support and a hosting structure to replace the damaged bone, and receive the new bone tissue. To date, titanium (Ti) based alloys remain the most used materials in bone implants for load-bearing applications. Emerging additive manufacturing processes such as electron beam melting (EBM) enable to custom-build Ti based alloys architected scaffolds. The main other strategy that entered the field one decade ago is the addition of biologic molecules to boost bone repair. Osteoinductive molecules such as bone morphogenetic proteins (BMPs) are currently employed for that purpose. However, one of the main limitations in their use is their appropriate delivery. Surface coatings made of biopolymers such as (PLL/HA) films have been successfully loaded with the bone morphogenetic proteins 2 and 7 (BMP-2,7)<sup>152-155</sup> and reached the pre-clinical stage. In this study, we aimed to develop architected and osteoinductive 3D titanium-based scaffolds as innovative bioactive bone implants using the EBM additive manufacturing technique and bone morphogenetic protein 7 (BMP-7). To this end, we built by EBM 3D porous Ti-6Al-4V scaffolds made of periodic cubic unit-cells with three different porosities. The porosity was well controlled with difference from CAD models of less than 1%. (PLL/HA) polyelectrolytes film were used to deliver the BMP-7. Their osteoinductive capacity was assessed on 2D surfaces with murine mesenchymal stem cells (MSCs) by quantifying their early ALP expression. The ALP expression of MSCs cultured on the BMP-7 loaded (PLL/HA) films increased in a dose-dependent manner. The bioactive film was effectively deposited on 3D architected scaffolds and MSCs cultured on BMP-7 loaded and film coated scaffolds also expressed ALP, proving the early osteoinductive capacity of functionalized scaffolds *in vitro*.

### 3.3 Introduction

Titanium and its alloys are currently the most widely used metallic materials in the orthopaedics field for their adequate properties for load-bearing applications. Presenting high strength with a low density, good corrosion resistance and improved osseointegration, their main limitations in use originate from their processing and their lack of osteoconduction and osteoinduction<sup>62,67</sup>.

Furthermore, in regards to the trabecular and cortical bone elastic modulus (from 0.01 to 30 GPa)<sup>206</sup>, the higher stiffness of titanium implants is known to induce the stress shielding effect<sup>207</sup>. As the mechanotransduction plays an important role in the bone regeneration and maintenance<sup>208</sup>, this effect might lead at long term to bone resorption at the surroundings and could eventually cause the implants loosening and failure<sup>207</sup>.

To reduce this effect, improve the implants integration and their lifespan, two main strategies are currently being explored in the orthopaedic field: the first strategy involves the modulation of the implant architecture<sup>84</sup> while the second strategy is focused on adding bioactive properties to the implant, mostly via surface coatings<sup>65</sup>.

Inspired by the structural organization of bones, intensive investigations on porous implant architectures are currently undertaken. They aim at reducing the implant high mechanical properties in regards to bone tissue and at understanding which structural features, such as surface curvature, pore shape, pore size, favour the implant integration and the bone regeneration<sup>84</sup>. Emerging metallic additive manufacturing processes such as Electron Beam Melting (EBM) and selective laser melting (SLM), allow to build highly porous titanium architectures with closer properties to bones in terms of mechanical matching and permeability, promoting mass transport and giving more space for the formation and vascularisation of the new bone tissue<sup>206</sup>.

Similarly, biomimetic strategies employed for the architecture at the macro scale (> 100  $\mu\text{m}$ ) and micro scale (< 100  $\mu\text{m}$ ) are translated to the cells levels through the addition of osteoinductive biomolecules. From large proteins or glycosaminoglycan, to growth factors, peptides, mass bone regulating and DNA molecules, biomolecules for bone repair are currently used at the research or clinical stages<sup>209</sup>. Some of the large proteins already approved for medical use, such as collagen or hyaluronic acid (HA) that are also part of the natural extracellular matrix, are currently used as material carriers for bioactive molecules<sup>210</sup>. The aim is to mimic the natural ECM and to act as carrier for active proteins such as growth factors. However in the case of active proteins, issues regarding the efficient loading, the controlled release and stability are of first importance and remain issues to tackle in order to obtain appropriate and controlled osteoinduction<sup>121</sup>.

Several techniques are used to store and deliver those molecules from metallic implants including surface functionalization with thiols or siloxane anchored to self-assembled monolayers<sup>69</sup>, RGD peptides immobilization<sup>211</sup> or using hydrogel carriers<sup>212</sup>. Among the available surface coating techniques employed to attach and deliver bioactive proteins at the implant surface, the layer-by-layer assembly of the polyelectrolytes (PEM) films appears

promising in terms of versatility and delivery capacities<sup>145</sup>. Several studies using those films, with either BMP-2 or BMP-7 incorporated, have proven that they can be effectively deposited on plastic<sup>153</sup>, ceramics<sup>154</sup> and metallic substrates<sup>155</sup>. PEM films sustained the growth factors osteoinductivity *in vitro* for both factors<sup>153,179</sup>. To date at the *in vivo* stage, only BMP-2 loaded PEM films have been tested and showed enhanced bone regenerative capacities<sup>152</sup>.

In this study, we aimed at developing porous Ti-6Al-4V implants with an osteoinductive capacity provided by a coating able to deliver various doses of BMP-7. The porous titanium scaffolds were built by EBM and coated with polyelectrolytes multilayer film containing the bioactive BMP-7. The scaffold architecture and BMP-7 amount were controlled to evaluate the scaffold osteoinductivity *in vitro*. Future *in vivo* investigations will be done with custom-made Ti-6Al-4V implants coated with the BMP-7 osteoinductive film in a critical-size femoral bone defect in rat.

## 3.4 Results

### 3.4.1 Architected Ti-6Al-4V scaffolds built by EBM additive manufacturing process

For *in vitro* cell studies, we chose to build architected scaffolds with periodic cubic unit-cell (UC). Other architecture with unit-cells such as diamond, dodecahedron, tetrahedron or octet-truss unit-cells were also already built by EBM and mechanically investigated<sup>4</sup>. For this study, scaffolds with cubic unit-cell were advantageous since pores are aligned and thus facilitate the UV sterilization, cell culture into well plates and imaging conditions. With this fixed geometry, our first goal was to test the EBM capacity to build ranges of cubic unit-cell porous scaffolds. Currently, the minimum strut size achievable with the EBM manufacturing process is about 600  $\mu\text{m}$ . In order to obtain the finest structures as possible with this process, we fixed the strut size of the scaffolds to 600  $\mu\text{m}$ . Due to these two structural requirements and our design methodology, we were able to generate three types of porous cubic unit-cell scaffolds with three different porosities of 73%, 80% and 85%. Those porosities are linked to the repetition number of unit-cells (either 7, 6 or 5) along the scaffold diameter. The CAD and EBM built corresponding scaffolds are represented in **Figure 98**.

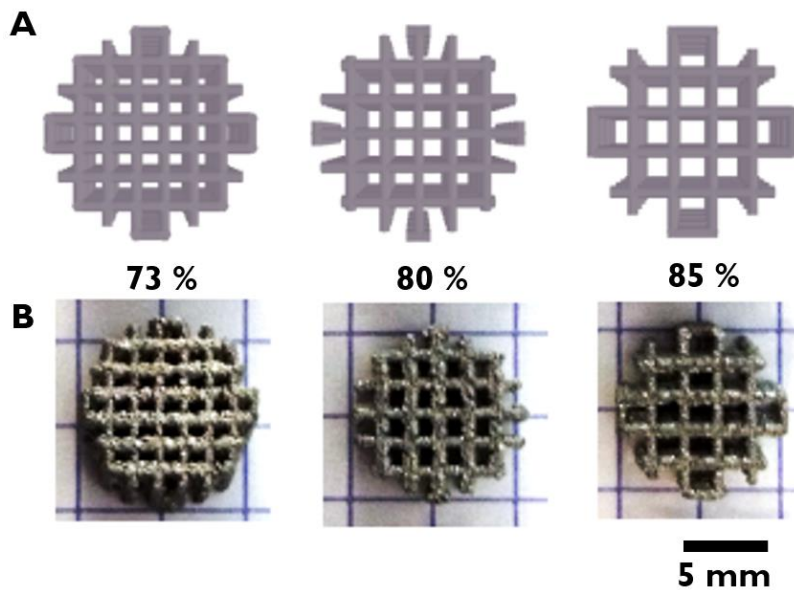


**Figure 98:** CAD (A) and EBM built (B) Ti-6Al-4V architected scaffolds with the expected porosities of 73%, 80% and 85%. Respectively corresponding to 7, 6 and 5 repeated unit-cells along the scaffold diameter

As seen on **Figure 98B** and **Figure 99**, EBM built scaffolds were inherently rough due two different effects. The first one is related to non-melted powders stuck or partially sintered at the scaffold surface. The second effect is due to irregularities in the layer stacking during the building. Those irregularities are the combined results of the spatial beam control and the local thermal history. It is called plate-pile like stacking defect and was described for example by Suard<sup>166</sup>.

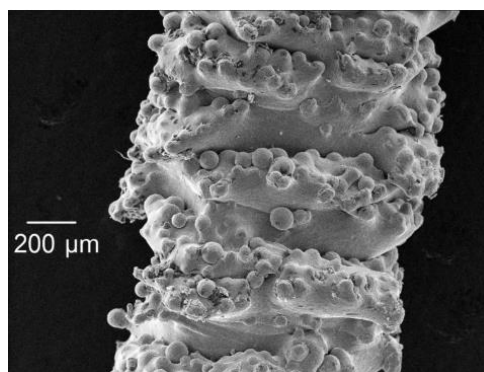


**Figure 99:** Rough surface of Ti-6Al-4V scaffolds built by EBM. The image was acquired by scanning electron microscopy<sup>166</sup>

Porosities of EBM-built scaffolds were measured by the hydrostatic weight method (**Table 11**). The obtained values were close to those from the CAD with differences equal or less than 1%. However, even if we were able to reach the expected porosities, we noticed a shape anisotropy on EBM-built scaffolds at the scale of the struts. This anisotropy was also previously described and was found to be dependent on the struts orientation during the build (**Figure 100**)<sup>166</sup>. Here, we built our scaffold with a 45° angle according to the build platform. With this setup, struts were either at 45° or 90° with respect to the build direction, which could explain this structural anisotropy. The fact that global porosities values were not affected might be due to a non-controlled compensation.

Unit-cell number	Porosity (%)			Young's Modulus (GPa)
	Expected	Obtained	Difference	
5	85	83.7 ± 0.1	1.3 ± 0.1	2.0
6	80	79.6 ± 0.1	0.4 ± 0.1	2.7
7	73	72.7 ± 0.3	0.3 ± 0.3	4.4

**Table 11: Structural characteristics of CAD and EBM-built architected Ti-6Al-4V scaffolds** ( $n = 3$  samples for porosities;  $n = 1$  per unit-cells scaffold type for compressive tests)

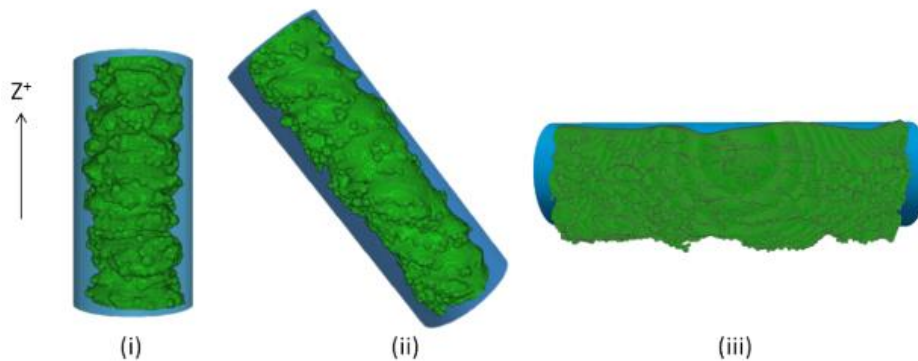


**Figure 100: Comparison of CAD (blue) and EBM built (green) struts as function of the strut orientation, either (i) 0°, (ii) 45° or (iii) 90° with respect to the build direction ( $Z^+$ )<sup>166</sup>**

The elastic modulus was determined for larger cubic scaffolds (2 cm x 2 cm) with the same previous porosities in order to be sure to measure the representative mechanical behaviour. The range of the Young's modulus was between 2 to 4.4 GPa which is between 50 to 25 times lower than the modulus of the bulk Ti-6Al-4V known to be around 110 GPa<sup>4</sup>. The elastic modulus of bone varies from 0.44 to 30 GPa depending on the bone nature and loading direction<sup>4</sup>. In regards to those values, architected structures possess a great potential in reducing stress shielding effects at the bone-implant interfaces<sup>207</sup>. The elastic modulus values obtained are consistent with the measured scaffold porosities. Indeed, if we consider that loads are transferred only in the axial compression direction, we can roughly estimate the elastic modulus with the equation (2).

$$E_{scaffold} = E_{Ti-6Al-4V} \times (1 - p) \times \frac{1}{3} \quad (2)$$

Where  $E_{scaffold}$  represents the Young's Modulus of porous scaffolds,  $E_{Ti-6Al-4V}$  the Young's Modulus of bulk Ti-6Al-4V and  $p$  the porosity. Elastic modulus estimated from this equation are two fold higher than the measured values. Due to the surface roughness, only an "efficient material" contributes to the mechanical properties of the EBM built structures (**Figure 101**). This phenomenon was described in the previous PhD work of M.Suard<sup>166</sup> where the concept of "mechanical equivalent diameter" was introduced to better predict the mechanical properties of such architected structures.

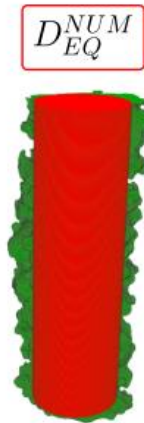


**Figure 101: Concept of mechanical equivalent diameter of EBM built struts.** The effective material involved in the mechanical response of EBM struts (represented by an equivalent cylinder of diameter  $D_{EQ}^{NUM}$ ) is lower than the total volume of the EBM built material (adapted from Suard<sup>175</sup>)

A down scaling factor was derived in order to estimate more accurately the mechanical properties of architected structures built by EBM. In the case of 600  $\mu\text{m}$  strut size, this down scaling down factor was about 2, which could explain the two fold higher values than the ones measured here<sup>170</sup>.

### 3.4.2 2D in vitro osteoinductive capacity of PEM film loaded with BMP-7

The osteoinductive strategy of this study consisted in combining layer-by-layer polyelectrolytes film with the osteogenic factor BMP-7<sup>113</sup>. PEM film were made either of 12 or 24 layer pairs of negatively charged PLL and positively charged HA which formed the film mainly by electrostatic interactions<sup>145</sup>. In order to mechanically reinforce the films, they were covalently cross-linked using an established protocol based on the carbodiimide chemistry, creating amine bonds between HA carboxylic groups and PLL ammonium groups<sup>146</sup>. Since films crosslinked at low EDC carbodiimide concentrations showed an higher stability upon storage<sup>155</sup>, we selected the two lowest EDC carbodiimide concentrations previously studied, namely 10 mg/mL (EDC10) and 30 mg/mL (EDC30). After cross-linking, the films were loaded with BMP-7 in the same manner as BMP-2 was loaded into (PLL/HA)<sub>12/24</sub> film in a previous study<sup>152</sup>.

In order to observe the BMP-7 loading into the films, cross-sections of (PLL/HA)<sub>24</sub> films built with red-labelled PLL and loaded with green-labelled BMP-7 were observed by confocal microscopy (**Figure 102A**). From these observations, the film thickness was evaluated at 5.4  $\mu\text{m}$  and the BMP-7 was distributed only at the top of the films. This phenomenon might be due to a limited diffusion of the BMP-7 into the film. It was also previously observed with labelled BMP-2<sup>213</sup> and might also be due to a structural anisotropy in the film depth.



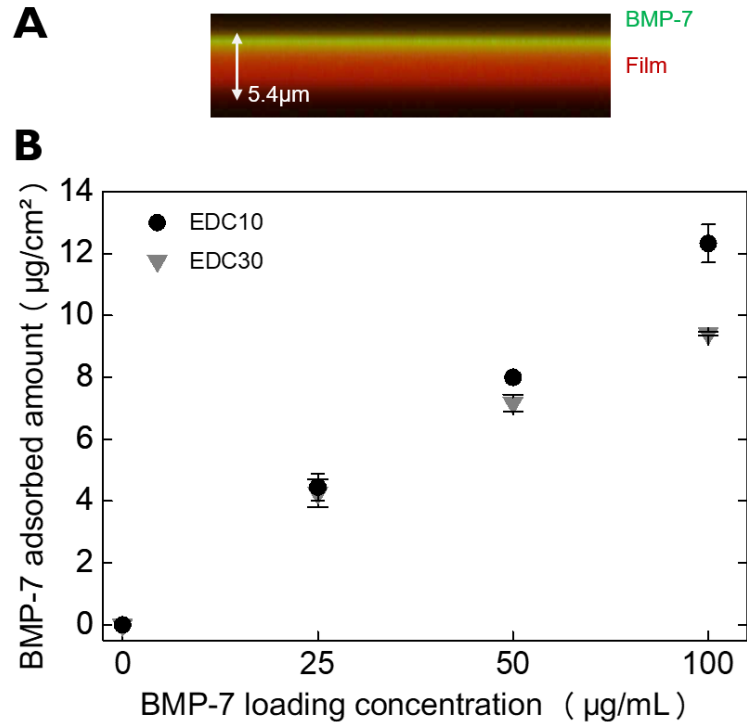


**Figure 102: Amount of BMP-7 loaded in (PLL/HA)<sub>24</sub> films.** (A) The diffusion of BMP-7 inside the films (PLL/HA)<sub>24</sub> PEM films was visualized using confocal microscopy and imaging transverse section. PLL<sup>Rho</sup> appears in red and BMP-7<sup>FNHS</sup> in green. (B) BMP7 adsorbed amount as a function of the initial BMP-7 loading concentration into (PLL/HA)<sub>24</sub> PEM films measured by micro BCA assay ( $n=3$  samples per condition in each experiment, with 3 independent experiments).

Then, the adsorbed amount of BMP-7 was quantified as a function of the initial BMP-7 loading concentration and the film crosslinking by micro BCA assay (**Figure 102B**). At low BMP-7 loading concentration ( $[BMP-7] \leq 25 \mu\text{g/mL}$ ), the film crosslinking did not affect the adsorbed amount of protein. However for  $[BMP-7] > 50 \mu\text{g/mL}$ , more BMP-7 adsorbed into the less crosslinked film with an adsorbed amount of  $12 \mu\text{g/cm}^2$  for EDC10 over  $9 \mu\text{g/cm}^2$  for EDC30. This might be due to the fact that higher crosslinked films are less permeable and have less space for the protein diffusion. In the following, only PEM film crosslinked at EDC10 were used.

(PLL/HA) films have already been shown to act as reservoir for BMP-7 and trigger ALP expression of C2C12 cells<sup>153</sup>. In terms of bone repair, this BMP-2 and BMP-7 responsive myoblast cellular model is interesting for *in vitro* experiments but cannot mimic a physiological situation since myoblast cells are not directly involved in the repair process<sup>25</sup>. After the initial inflammatory phase and hematoma formation, skeletal progenitor cells are recruited from the cortical bone, periosteum and bone marrow<sup>26</sup>. D1 mesenchymal stem cells are isolated from mouse bone marrow and known to differentiate into adipocyte, chondrocyte and osteoblast cells lineage<sup>191</sup>. Thus, in regards to the bone repair mechanism, we decided in this study to use the D1 stem cells line.

Prior to the evaluation of polyelectrolyte films containing BMP-7 with D1 cells, we investigated their response to soluble BMP-7 by quantifying their ALP expression after 3 days of culture on plastic (**Figure 103**). Their ALP expression in response to soluble BMP-2 was also assessed a reference osteogenic protein. D1 cells responded to both BMPs, with BMP-2 being more

potent than BMP-7, since a lowest concentration of BMP-2 was required to reach the maximum ALP level reached with BMP-7.

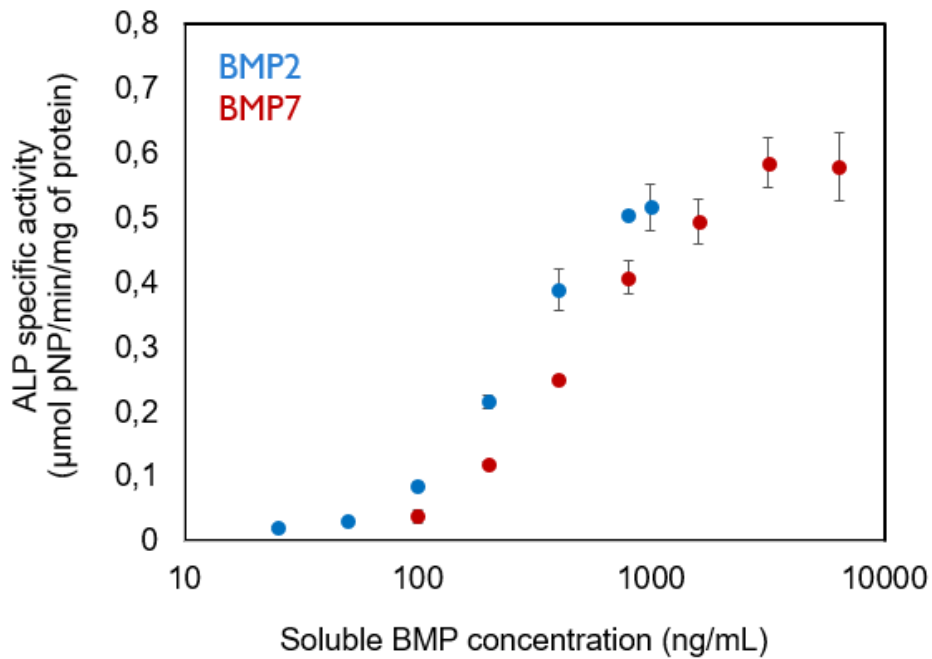


*Figure 103: D1 cells ALP expression in response to increasing soluble BMP-2 and BMP-7 concentrations after 3 days of culture in growth medium on plastic (n = 3, replicated 2 times)*

To investigate D1 cells behaviour in contact with the polyelectrolyte films containing BMP-7, their proliferation was measured after 1, 2 and 7 days of culture (**Figure 104A**). The cells adhered to PEM films and their number remained stable regardless of BMP-7 absence or presence. The presence of BMP-7 in the films did not affect the proliferation of D1 cells.

In order to evaluate the osteoinductive capacity of the PEM film loaded with BMP-7, we measured the ALP expression after 3 days of culture, this enzyme expression being widely recognised as an important marker of the osteogenic differentiation (**Figure 104B**). D1 cells expressed ALP in a BMP-7 dose-dependent manner, the highest expression being obtained for the highest BMP-7 loading concentration of 25  $\mu\text{g/mL}$ .

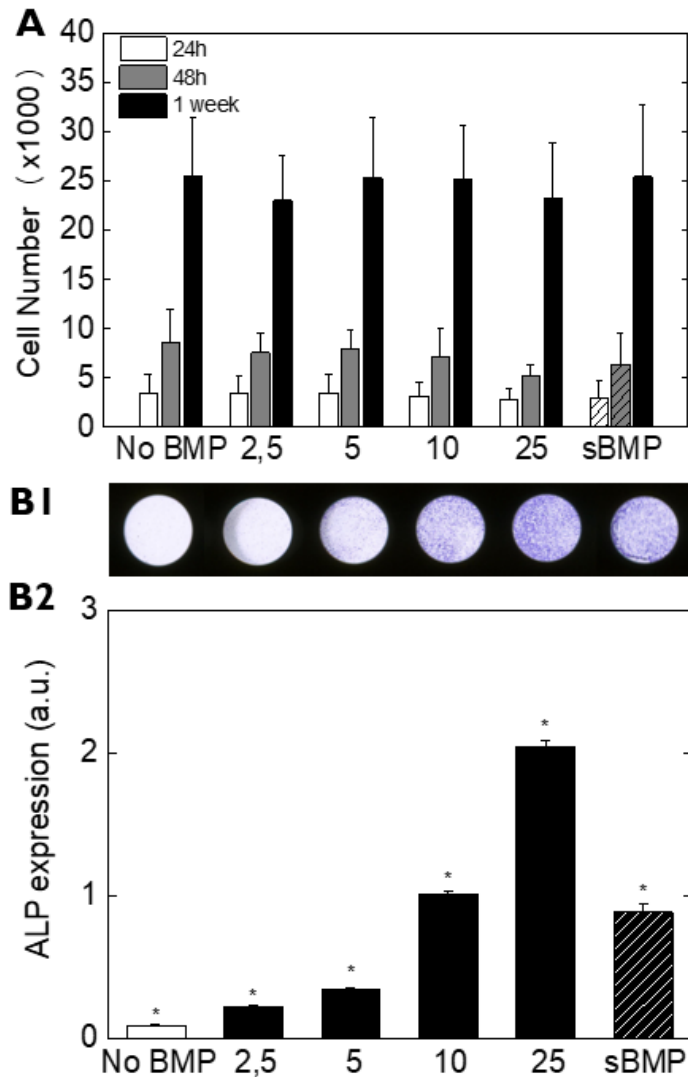


**Figure 104: Cell proliferation and osteoinduction with BMP-7 loaded into (PLL/HA)<sub>12</sub> films at [2.5, 5, 10 and 25 µg/mL] and at 800 ng/mL in solution (sBMP) as a positive control on 2D surfaces. (A) Proliferation of D1 cells on (PLL/HA)<sub>12</sub> film loaded with BMP-7 measured by quantifying the cell number after 1, 2 and 7 days culture in growth medium (B) Alkaline Phosphatase expression of D1 murine mesenchymal stem cells in response to increasing BMP-7 loading concentration after 3 days culture in growth medium. (B1) ALP staining representation into 96 well-plates (B2) Corresponding signal of absorbance measure normalized by the cells nuclei fluorescence signal from ALP staining into 96 well-plates (n =5 sample per experimental condition, experiments done 3 times,\*p < 0.05 with one-way analysis of variance (ANOVA) with Kruskal-Wallis test).**

According to the adsorbed amount measurements, the loading BMP-7 concentration = 10 µg/mL gives an adsorbed amount of 2 µg/cm<sup>2</sup> into EDC10 films. Here, we loaded EDC10 films into 96 well plate having a surface of 0.34 cm<sup>2</sup>. Thus, the total amount of BMP-7 into the film for the 10 µg/mL loading condition can be estimated to be at 680 ng. The BMP-7 concentration of the positive control was settled at 800 ng/mL. Knowing that we used 200 µL of growth medium per well, the starting amount of BMP-7 presented to the cells can be estimated at 160 ng.

With a 6-fold higher quantity of BMP-7 available in the film, we induced the same level of ALP expression than the soluble positive control. This result proves that the film delivered BMP-7 in a slower and more controlled manner. Moreover, the fact that the highest loading concentration induced a higher ALP expression shows that this delivered amount depends on the initially loaded amount. Altogether, those results show that the (PLL/HA) films loaded with BMP-7 are osteoinductive and this capacity increases with increasing concentrations of the BMP-7 loading solution.

### 3.4.3 Extracellular matrix mineralization of D1 cells in response to BMP-7

To further investigate the osteoinductive capacity of BMP-7 loaded (PLL/HA) films, we measured the mineralization of the extracellular matrix (ECM) produced by D1 cells *in vitro*. *In vitro* mineralization requires a specific cell culture medium, the osteogenic differentiation medium (DM). This medium ensures the phosphate supply for the formation of HA crystals. According to the literature, the standard composition of an osteogenic medium is the basal growth medium (GM) supplemented by dexamethasone (Dex), ascorbic acid and  $\beta$ -glycerophosphate ( $\beta$ GP)<sup>204</sup>. Our strategy was to use a minimal DM in order to minimise the possible interactions between the different substances and BMP-7 and thus highlighting the osteoinductive capacity of the film.

The first *in vitro* mineralization trial was conducted into a 96 well plate coated with (PLL/HA)<sub>12</sub> film, crosslinked at EDC10 and increasing concentrations of BMP-7: 2.5, 5, 10, and 25  $\mu$ g/mL. D1 cells were first cultured 2 days in growth medium (GM) prior changing to DM. In this medium, cells were cultured for 14 days, the standard time period for *in vitro* mineralization assessment (**Figure 105**, **Figure 106**, **Figure 108**, plate 1).

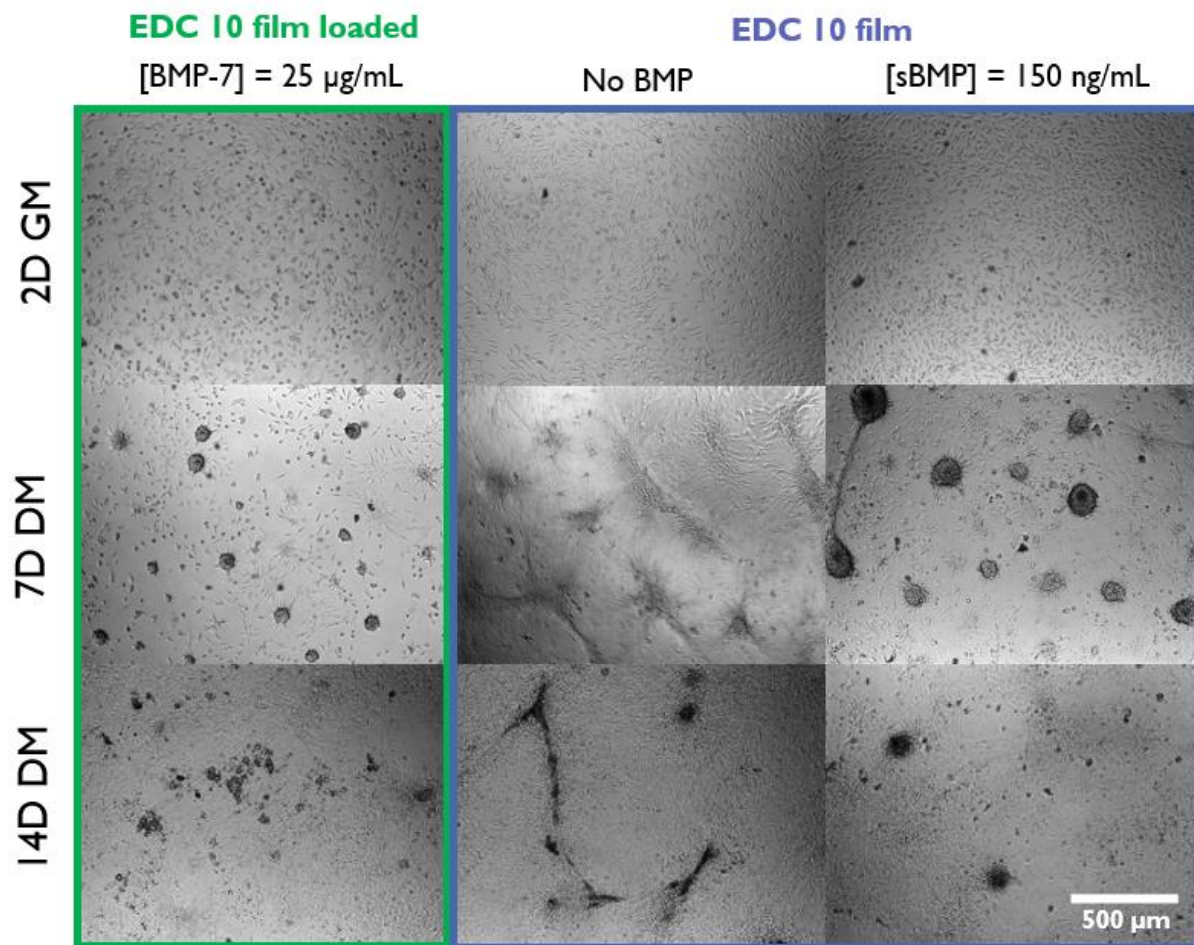


**Figure 105:** Phase contrast microscopic images of D1 cells after 2 days in growth medium GM, 7 days and 14 days in differentiation medium DM on  $(\text{PLL}/\text{HA})_{12}$  films crosslinked at EDC 10 and loaded with BMP-7 at [2.5, 5, 10, 25  $\mu\text{g/mL}$ ] and at 150 ng/mL in solution (sBMP) as positive control (Figure 108, plate 1)

In cultures on EDC10 films, cells first adhered and proliferated after 2 days in growth medium (GM). After changing to the differentiation medium (DM), cells gathered and aggregated (**Figure 105**). In the condition without BMP-7, they even formed an aggregation network. Black spots indicating the ECM mineralization were mostly located on the aggregates. However in the case of plastic substrates (**Figure 106**), cells were more spread in growth medium and kept their shapes after the medium changing. Signs of ECM mineralization were strongly appearing after 14 days of culture, as observed with dark areas on **Figure 106**. By optical microscopy, it was not possible to notice a difference between the different concentrations of loaded BMP-7 into films (not shown here).

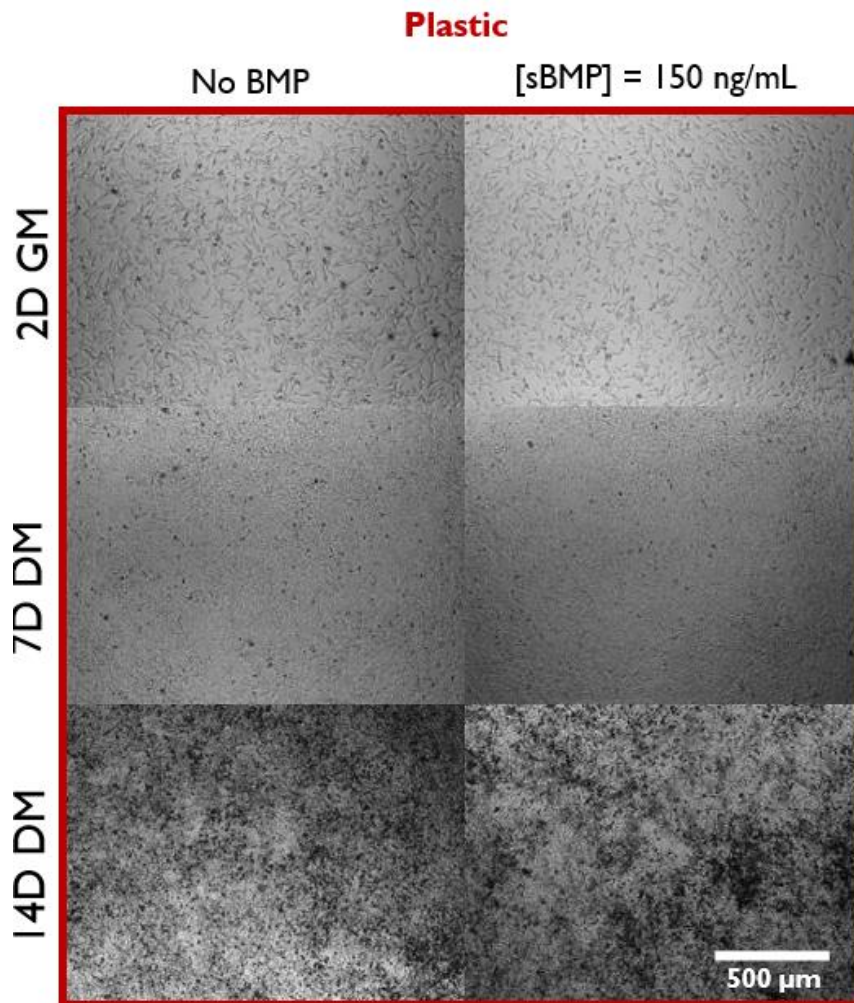


*Figure 106: Phase contrast microscopic images of D1 cells after 2 days in growth medium GM, 7 days and 14 days in differentiation medium DM on plastic without and with BMP-7 at 150 ng/mL in solution as positive control (Figure 108, plate 1)*

After 14 days of culture in DM, minerals from the ECM of D1 cells were stained by Alizarin Red S staining, the actual staining representation in a 96 well plate and the obtained absorbance values are shown in **Figure 107**. Unexpectedly, the mineralization was the strongest on plastic without BMP-7 (P No BMP, **Figure 107**) while on EDC10 films, the absorbance was the strongest in presence of BMP-7 in solution (sBMP, **Figure 107**). Those preliminary results indicated that BMP-7 may have an effect when presented in solution on soft substrates such as EDC10 but not when presented by the films.



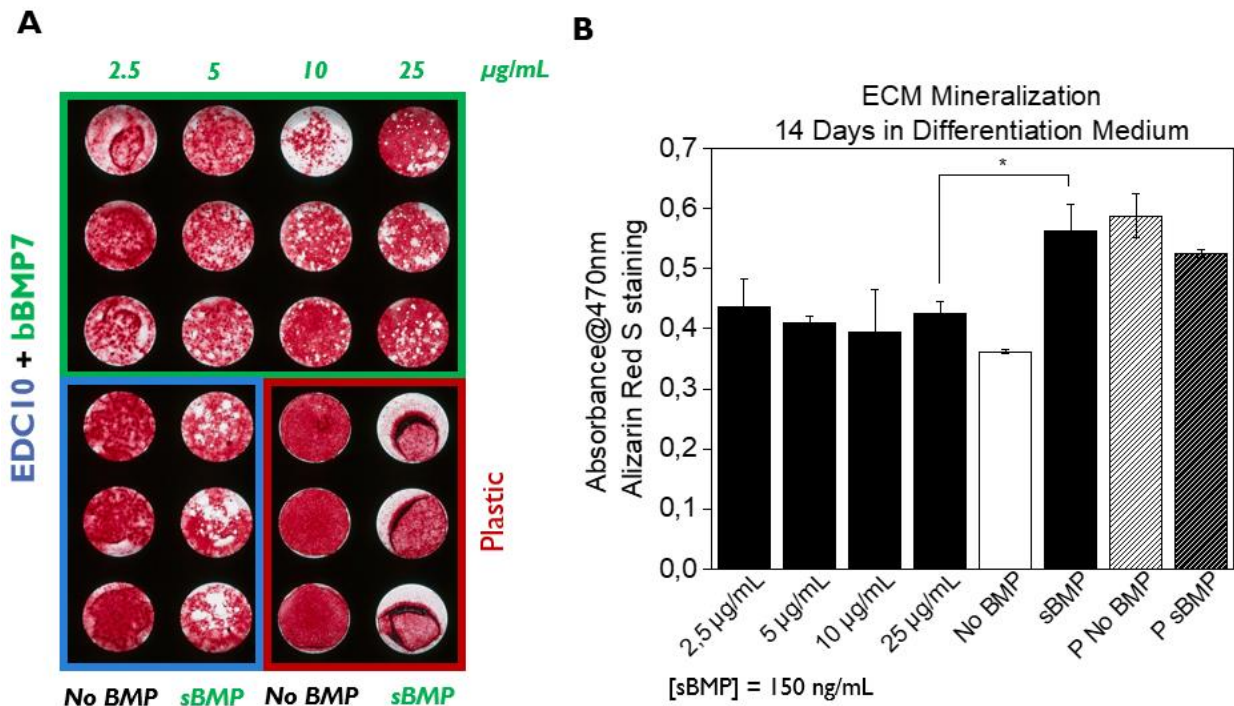


**Figure 107:** Alizarin Red S Staining of the extracellular matrix of D1 cells cultured on (PLL/HA)<sub>12</sub> films crosslinked at EDC10 loaded with BMP-7 at [2.5, 5, 10, 25 µg/mL] and on plastic P, with 150 ng/mL of BMP-7 in solution as positive control in differentiation medium for 14 days (A) and the corresponding absorbance at 470 nm (B) (\**p* < 0.05 with one-way analysis of variance (ANOVA) with Tukey-Kramer post-hoc test, Figure 108, plate 1)

Following those first results, we decided to investigate how we could highlight the BMP-7 effect on the mineralization process. To this end, we varied several cell culture parameters (cell density, days of culture, b-glycerolphosphate concentrations and BMP-7 presentation) in an incremental approach which chronology is detailed in **Figure 108**.

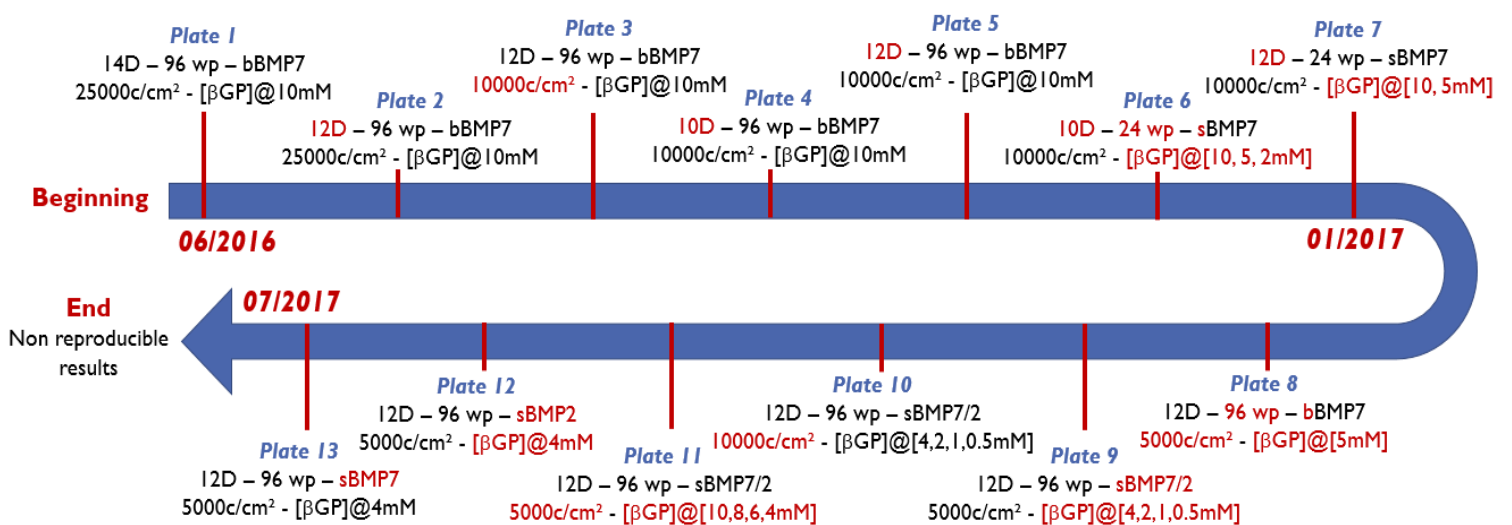


**Figure 108:** Experimental chronology of the ECM mineralization experiments. D: days - wp: well plate - bBMP7: bounded BMP7 - sBMP-7: soluble BMP-7 - parameters in red indicate the incremental changes

According to the previous enhanced ALP expression after 3 days of culture for only BMP-7 conditions (**Figure 104**), we hypothesized that the BMP-7 effect on the mineralization might be a competitive kinetic effect, namely that BMP-7 might induce an acceleration of the ECM mineralization. To verify this hypothesis, we first decided to reduce the cell culture time to an earlier time point of 12 days (**Figure 109**, plate 2 **Figure 108**). Also, we increased the soluble BMP-7 concentration from 150 ng/mL to 800 ng/mL, based on the higher ALP level that we obtained from the D1 cells response to soluble BMP-7 (**Figure 103**).

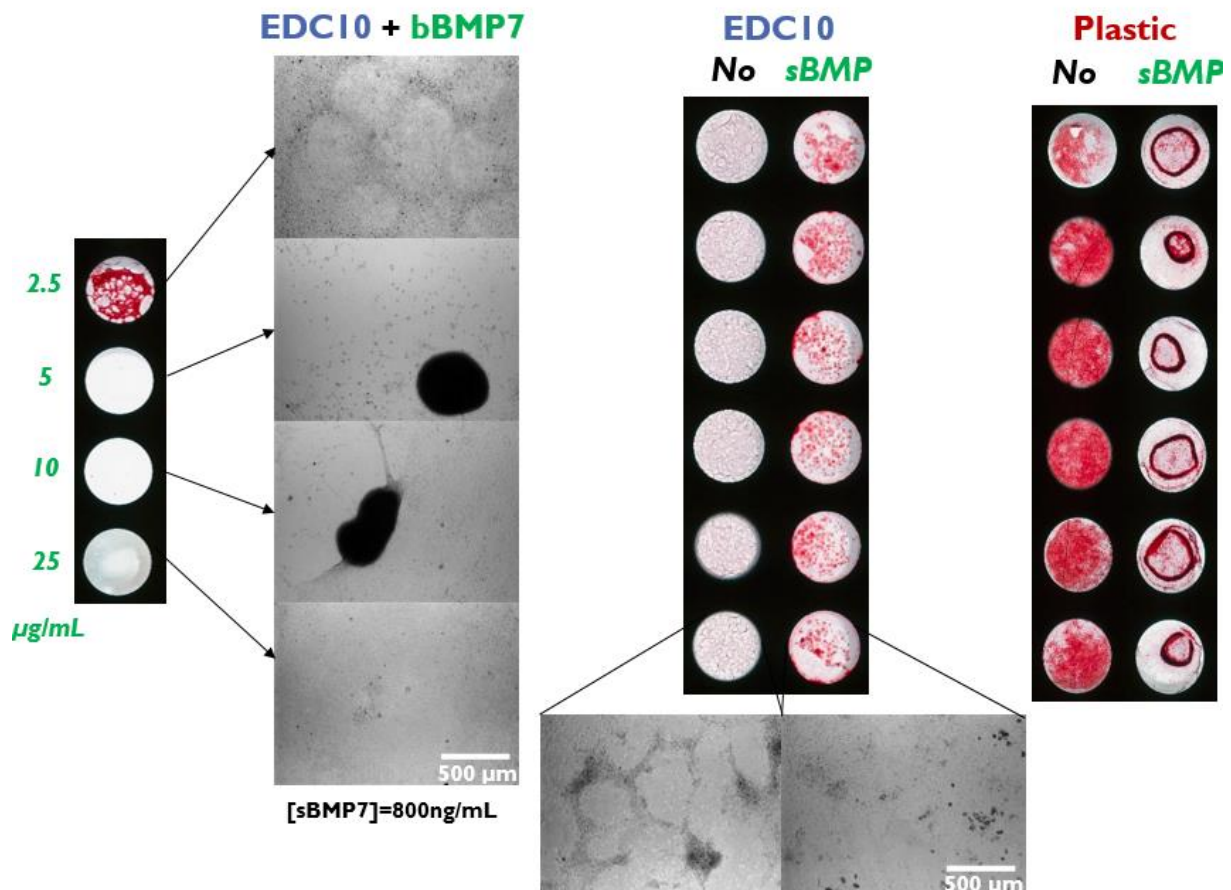
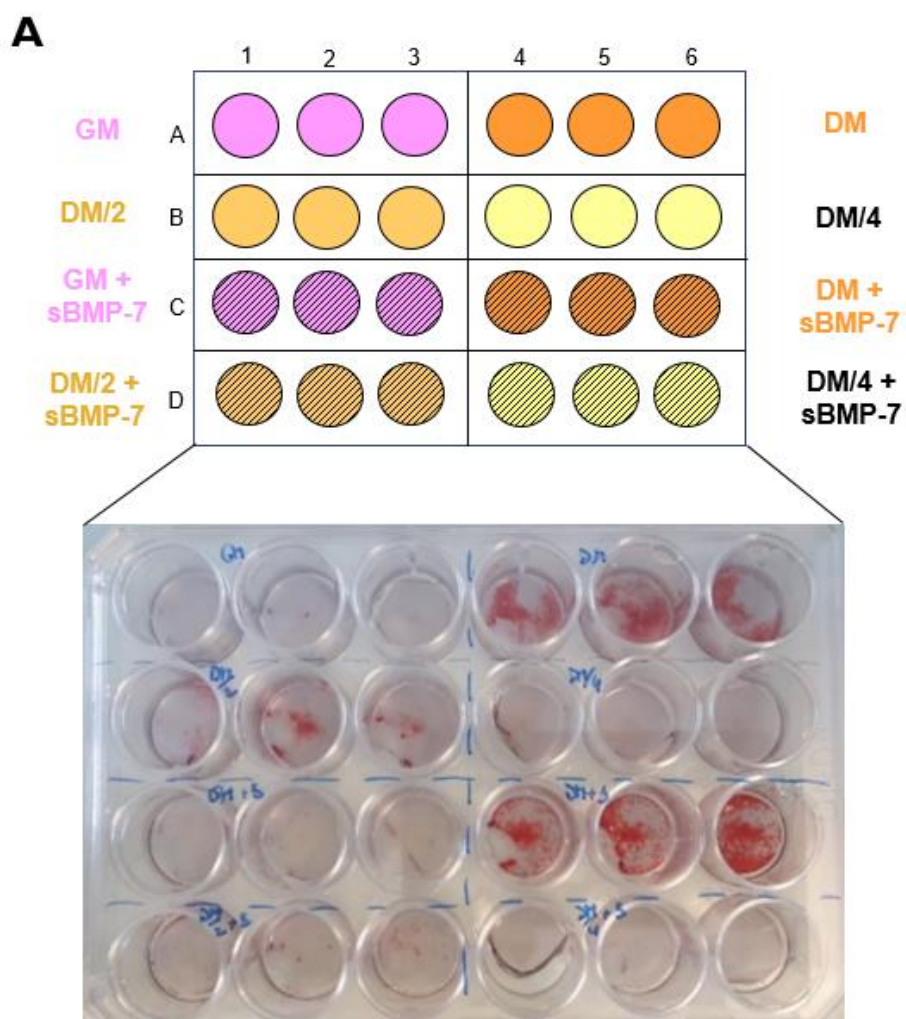


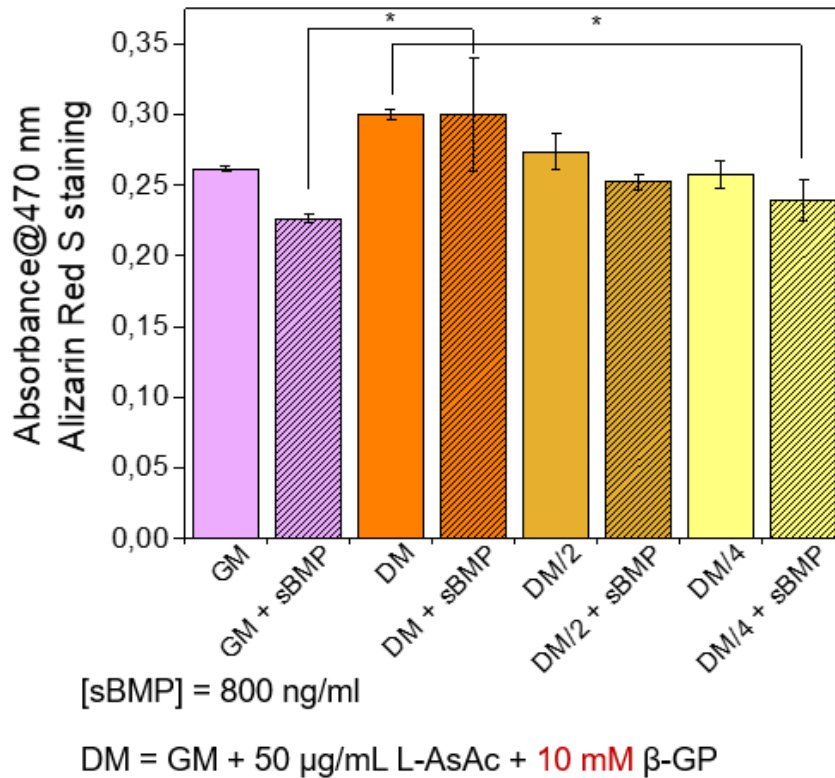
*Figure 109: Alizarin Red S staining of the extracellular mineralization of D1 cells seeded at 25000c/cm<sup>2</sup> cultured on (PLL/HA)<sub>12</sub> films crosslinked at EDC10 loaded with BMP-7 at [2.5, 5, 10, 25 µg/mL] and at 150 ng/mL in solution as positive control, in differentiation medium for 12 days (Figure 108, plate 2)*

Unfortunately, increasing the soluble BMP-7 concentration induced the cells carpet detachment on plastic (plastic, **Figure 109**), as we started to observe on the first experiment (plastic, **Figure 107**. **Figure 108**, plate 1). On EDC10 film loaded with BMP-7 conditions (EDC10 + bBMP7, **Figure 109**), we experienced a massive cell detachment and apoptosis. While on EDC10 film without loaded BMP-7, weak signals of mineralization were observed for wells with soluble BMP-7 (EDC10, **Figure 109**), with a negative control in absence of BMP-7.

In this experiment, the cell seeding density was settled at 25 000 cells/cm<sup>2</sup>. Observing the high rate of cells detachment, we reduced the cell seeding density at 10 000 cells/cm<sup>2</sup> and repeated the result obtained on EDC10 film with soluble BMP-7 (**Figure 108**, plate 3). Unfortunately, either after 10 and 12 days of culture (**Figure 108**, plate 4 and 5), we were not able to reproduce the result showing enhanced mineralization only in the case of soluble BMP-7 presentation on EDC10 film.

Then, to decouple as much as possible the parameters, we changed other cell culture parameters. First, we chose to work only on plastic substrates. Also, in view to offer more surface to cells and limit cellular detachment over time, we switched well plates from 96 to 24 well plates. Finally, we decided to decrease the  $\beta$ -glycerophosphate concentration to highlight the possible BMP-7 effect (**Figure 110**, plate 6 **Figure 108**).



**B**

**Figure 110:** Alizarin Red S staining of the extracellular mineralization of D1 cells cultured 2 days in growth medium and 10 days in differentiation medium with decreasing β-glycerophosphate concentrations of [10, 5, 2.5 mM] (A) and the corresponding absorbance measurement at 470 nm (B) (\* $p < 0.05$  with one-way analysis of variance (ANOVA) with Tukey-Kramer post-hoc test, **Figure 107**, plate 6)

From this additional trial, we observed very few cell detachment after 10 days of culture and a significantly higher ECM mineralization for the classic β-glycerophosphate concentration of 10 mM, nevertheless the effect of BMP-7 was still not noticeable. Other trials with BMP-2, which was known to be more potent than BMP-7 for D1 cells (**Figure 103**), were conducted without real success (**Figure 108**, plates 9 to 12).

We concluded that the D1 cells model presented a strong mineralization with solely the osteogenic differentiation medium. As a consequence and to prove the film osteoinductivity with BMP-7, we only focused on early stages of D1 cells osteogenic differentiation.



### 3.4.4 3D in vitro osteoinductivity of Ti-6Al-4V scaffolds coated with BMP-7

The ability to coat the Ti-6Al-4V scaffolds with (PLL/HA) films was investigated at the macro scale (> 1 cm) and micro scale (> 100  $\mu\text{m}$ ). For macro scale observations, the film deposition was slightly modified by the addition of a last layer of fluorescent FITC green-labelled PLL. The coated scaffolds were visualized using a fluorescence macroscopy system. **Figure 111** shows the film deposition in 73% porosity EBM built Ti-6Al-4V architected scaffold.

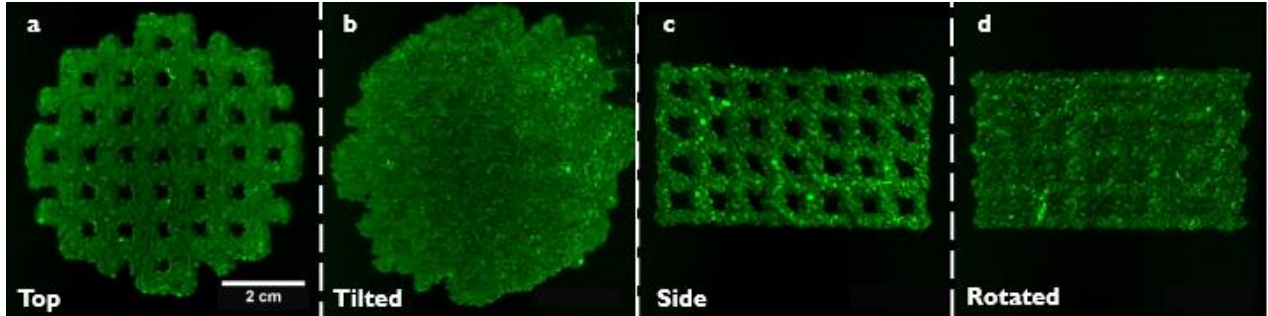


**Figure 111: Coating of architected Ti-6Al-4V scaffolds with  $(\text{PLL}/\text{HA})_{24}$  PEM film.** Ti-6Al-4V architected scaffolds coated with  $(\text{PLL}/\text{HA})_{24} + (\text{PLL}^{\text{-FITC}}/\text{HA})$  observed by fluorescence macroscopy with (a) top view, (b) tilted, (c) lateral view, (d) rotated

From a qualitative point of view, the film was homogeneously deposited along the entire scaffold length and inside the pores. For micro scale observations, the top surface of bare and coated scaffolds were intentionally scratched with a needle in some areas (**Figure 112**), in order to introduce chemical contrast between the damaged zone and the film itself. Both types of scaffolds were visualized by SEM with the topographical (secondary electrons, **Figure 112a, c**) and the chemical contrast modes (back scattered electrons, **Figure 112b, d**). Both bare and film coated scaffolds are inherently rough due to stuck or partially sintered powders, as clearly seen on **Figure 112**. In comparison to the bare scaffold surfaces, film coated scaffolds presented a smoother surface. Notably, the Ti-6Al-4V surfaces were homogeneously coated by the film as seen with all partially melted beads entirely covered by the film.

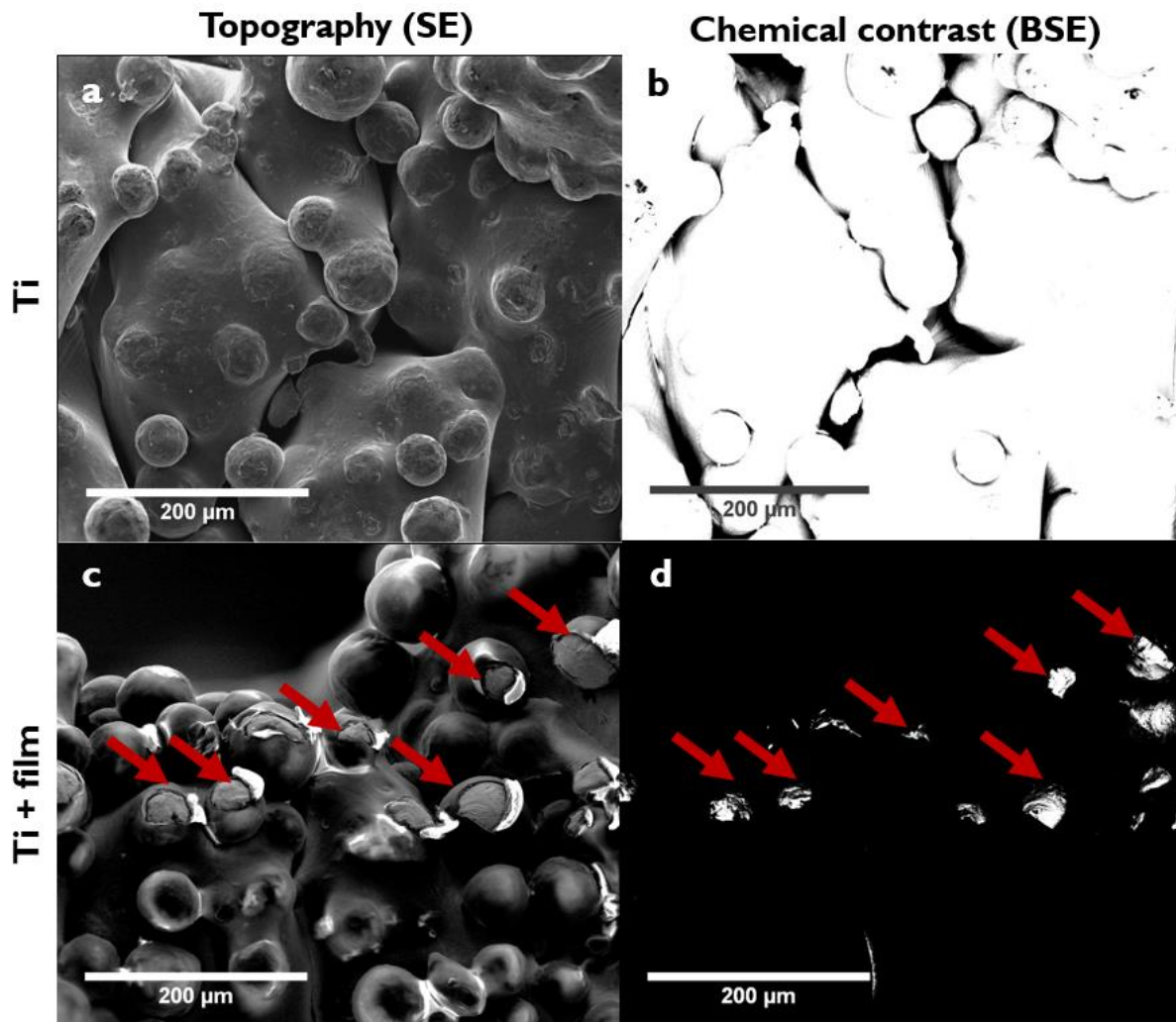


**Figure 112: Coating of architected Ti-6Al-4V scaffolds with (PLL/HA)<sub>24</sub> PEM film.** Ti-6Al-4V architected scaffolds bare and coated with (PLL/HA)<sub>24</sub> observed under scanning electron microscopy (SEM) in topography mode (secondary electrons, a and c panels) and chemical contrast mode (backscattered electrons, b and d panels). The red arrows show scratched and uncovered areas of the scaffold surface

Some of the film coated scaffolds were loaded with BMP-7 and the cellular adhesion and osteoinductive capacity of the bioactive implants were investigated *in vitro*. To this end, D1 cells were seeded into bare, only film coated and film coated and BMP-7 loaded Ti-6Al-4V scaffolds. Then, the cellular morphology was observed after 3 days of culture by phase contrast microscopy (**Figure 113A**), epifluorescence microscopy (**Figure 113B**), with the cells nuclei stained with DAPI (blue), and by SEM (**Figure 113C**).



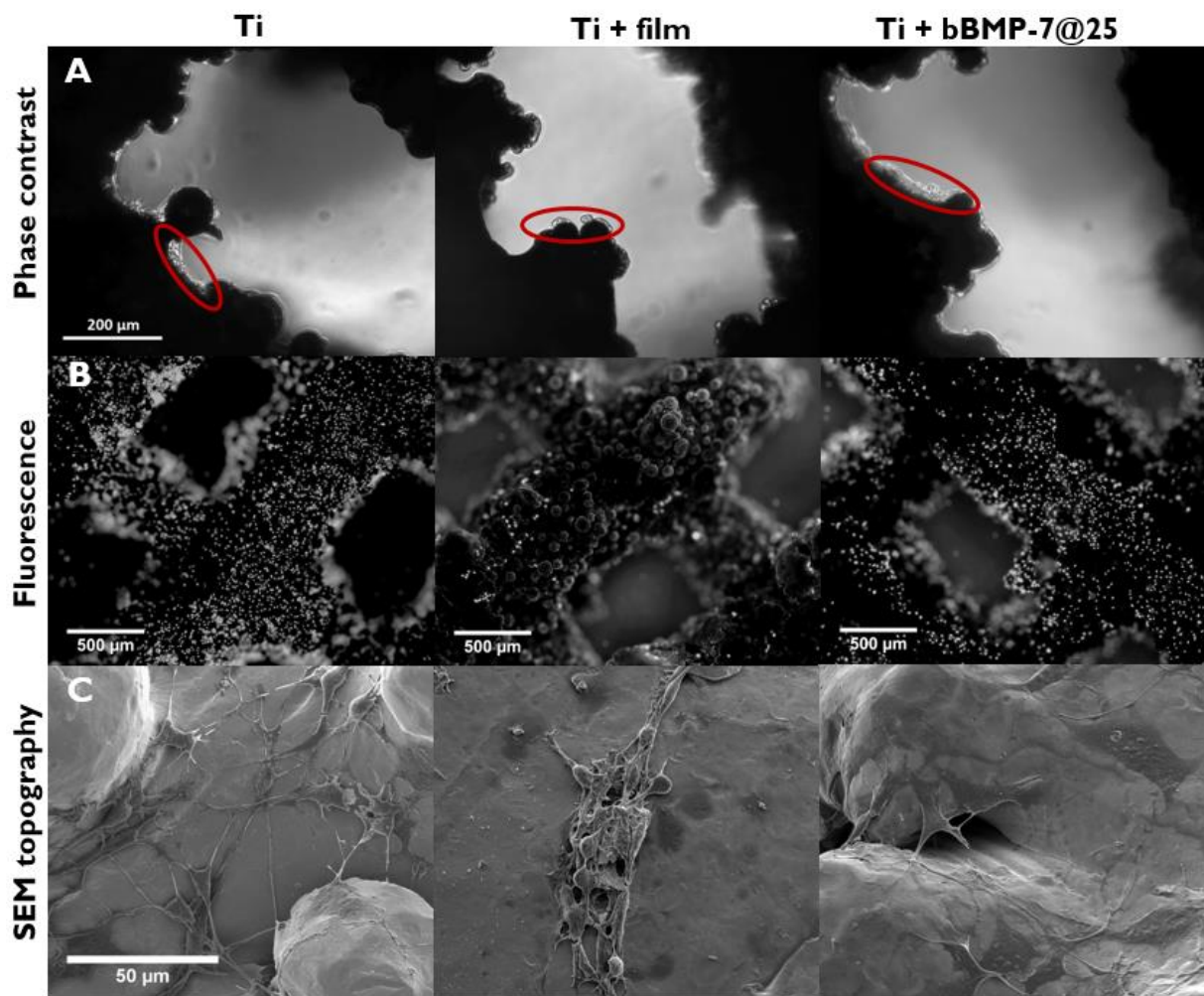


**Figure 113:** Cell morphology on bare, film-coated and BMP-7-film coated Ti-6Al-4V architected scaffolds after 3 days of culture in growth medium observed by phase contrast microscopy (A) fluorescence with cell nuclei stained with DAPI as fluorescent dye (B) and by SEM in topography mode (C). The red circles indicates cells at the surface of the scaffold.

In both bare (Ti) and BMP-7 loaded and film coated scaffolds (Ti + bBMP-7@25), cells colonized and spread at the surface with long protrusions (**Figure 113C**) while on film coated only (Ti + film), few cells are seen and aggregated, as seen on SEM observations. On fluorescence images (**Figure 113B**), the difference of nuclei number at the top and inside the scaffolds is noticeable with less fluorescent signal for the only film coated scaffold (Ti + film, **Figure 113B**). This observation is consistent with bright field microscopy and SEM images where on only film coated scaffolds (Ti + film), the few remaining cells aggregated and presented a round shape (Ti + film, **Figure 113A** and C). This might be due to the fact that EDC10 soft films solely are not sufficient enough to maintain the cellular adhesion. And then in order to survive, cells preferentially promote the cell-to-cell junctions. This survival mechanism indicates that BMP-7 loaded into films also increased the cellular adhesion at the scaffold surface.

Following those qualitative observations, the ALP expression was also measured after 3 days of culture (**Figure 114**). As shown by ALP levels expression, only D1 cells cultured on the BMP-7 loaded and film coated scaffolds exhibited a significant level of expression (Ti + bBMP-7@25,

**Figure 114).** This results proves that the bioactive implant can effectively trigger the osteogenic differentiation of murine stem cells.

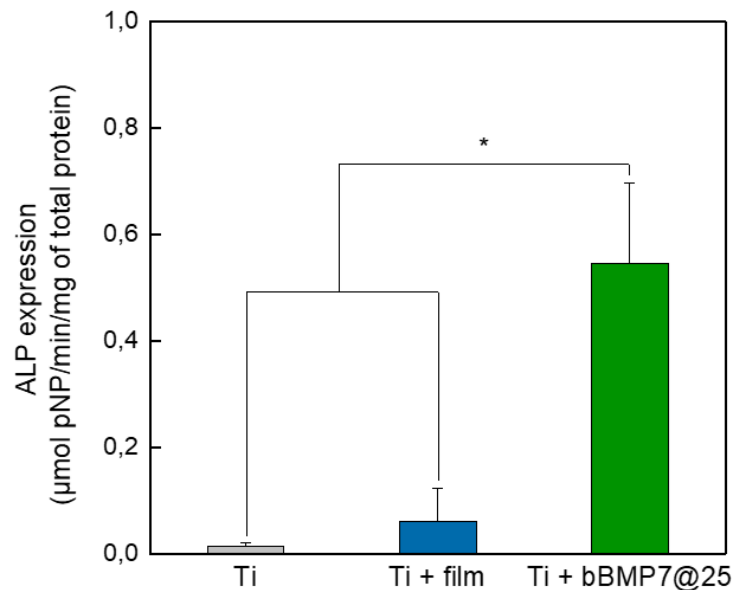


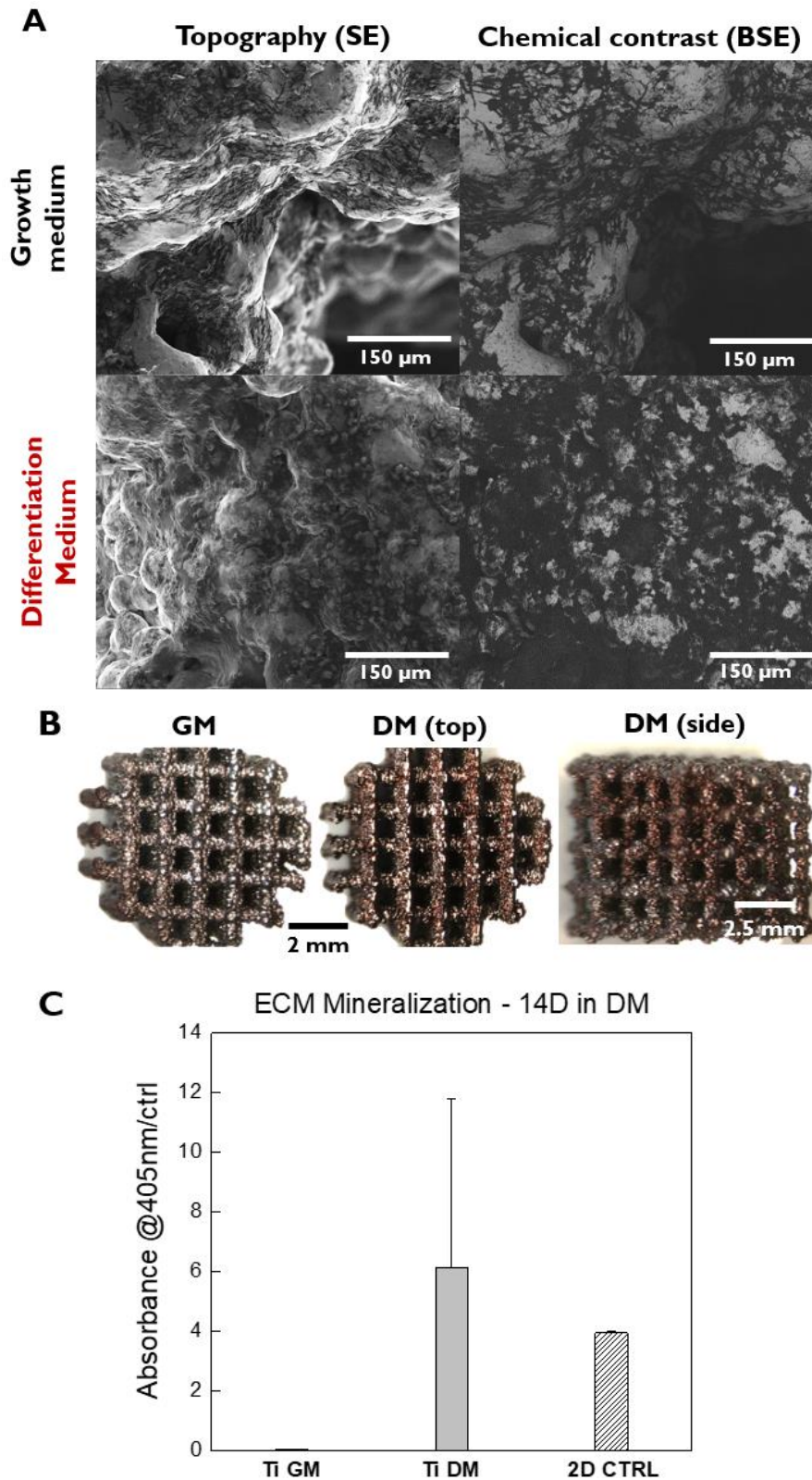
**Figure 114: ALP activity of D1 cells on osteoinductive and architected Ti-6Al-4V scaffolds.** Alkaline Phosphatase expression of D1 cells cultured onto osteoinductive and architected Ti-6Al-4V scaffolds after 3 days of culture in growth medium ( $n=3$ , replicated twice,  $*p < 0.05$  with one-way analysis of variance (ANOVA) with Kruskal-Wallis test)

The BMP-7 protein delivery was possible with the (PLL/HA) film surface coating into the 3D porous and architected structure without using additional filling material. Those *in vitro* results support the fact that BMP-7 loaded film coating Ti-6Al-4V scaffolds may accelerate bone regeneration *in vivo* while providing a hosting structure.

#### 3.4.5 3D *in vitro* extracellular matrix mineralization on bare Ti-6Al-4V scaffolds

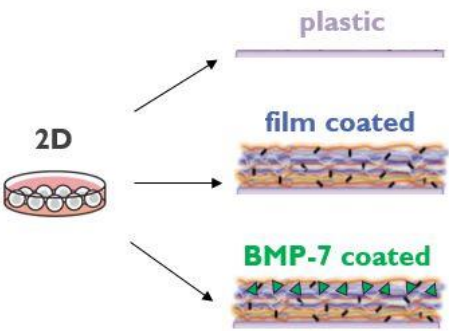
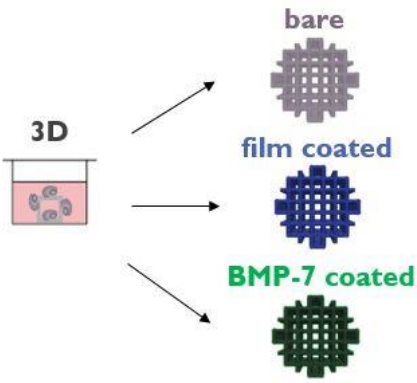
To assess long term cell cultures on architected scaffolds, D1 cells were cultured on bare Ti-6Al-4V scaffolds and the ECM mineralization of D1 cells was investigated by Alizarin Red S staining after 14 days of culture. Stained scaffolds were observed under SEM to visualize the cellular morphology and ECM deposition at the top of the scaffolds (**Figure 115A**).

From SEM images, we were able to distinguish a slight difference in the ECM deposition between the differentiation medium over the growth medium culture condition. In differentiation medium, more ECM was deposited by the cells compared the growth medium. From SEM chemical contrast observations, we noticed that the scaffold surfaces in DM were more homogeneously covered by organic material than in GM (chemical contrast BSE, **Figure 115**). This difference in the ECM deposition was confirmed by macroscopic observations with the red staining perceptible only for scaffolds with cells cultured in DM (**Figure 115B**). After staining, the red dye bound to the ECM deposited on scaffolds was dissolved to measure the corresponding absorbance values (**Figure 115C**). The results were positive only for scaffolds with cells cultured in DM even if we observed a high standard deviation among the samples. The latter was due to cells death in one of the samples, resulting in a negative result.



**Figure 115:** Alizarin Red S staining of the extracellular mineralization of D1 cells cultured on bare Ti-6Al-4V scaffolds for 14 days in growth and differentiation medium. Observed under scanning electron microscopy in topography and chemical contrast modes (A), macroscopic loupe (B) and the corresponding extracted absorbance at 405 nm from the dye solubilisation (C)

Those preliminary results demonstrated the effective ECM mineralization of D1 cells on bare Ti-6Al-4V scaffolds in DM, as previously demonstrated in 2D investigations (**Figure 116**). This experiment proved that we were able to maintain long term cell culture into 3D scaffolds *in vitro*.

	<b>Alkaline Phosphatase</b> early expression	<b>Mineralization</b> extracellular-matrix
 <p>2D</p> <p>plastic</p> <p>film coated</p> <p>BMP-7 coated</p>	<p>×</p> <p>×</p> <p>✓</p>	<p>✓</p> <p>×</p> <p>×</p>
 <p>3D</p> <p>bare</p> <p>film coated</p> <p>BMP-7 coated</p>	<p>×</p> <p>×</p> <p>✓</p>	<p>✓</p> <p>×</p> <p>×</p>
<b>Main Results</b>	<b>BMP-7</b> induces early osteogenic differentiation in 2D and 3D	<b>D1 cells</b> are not relevant for BMP-7 induced long term osteogenic differentiation

**Figure 116: Main results obtained from 2D and 3D *in vitro* osteoinductive investigations.** The ALP expression was studied in 2D on plastic, film coated and BMP-7 loaded substrates and in 3D on bare, film coated and film coated and BMP-7 loaded Ti-6Al-4V scaffolds. The ALP expression was induced by BMP-7 loaded (PLL/HA) film in 2D substrates and in 3D BMP-7 loaded and film coated scaffolds. The mineralization was studied in 2D on the three types of substrates and on bare Ti-6Al-4V scaffolds in 3D. The ECM mineralization obtained in 2D solely with the differentiation medium was also reproduced in 3D scaffolds

3.4.1 Design strategy for *in vivo* architected and osteoinductive Ti-6Al-4V implant for a critical size femoral bone defect in rat

For future investigations, we aimed to set up an *in vivo* experiment to repair a femoral bone defect in rat. According to the rat femoral critical size bone defect established in the literature<sup>152,160</sup>, the design of an architected titanium implant had to be specific for this bone



defect. To this end, a section of rat femur was scanned by X-ray micro tomography (**Figure 117** A and B). The femur cross section dimensions were measured with ImageJ software<sup>214</sup> and used to design two types of *in vivo* architected implants in Solid Edge software (Siemens®, USA).

In regards to the bone defect size fixed at 6 mm, the femur cross section dimensions and fixing requirements for the back of the implants (plate and screws), implants were designed with an elliptical cross section (3 mm x 4 mm) and a height of 6 mm. The CAD design of the first type of implants and the EBM-built implant are represented in **Figure 117** C and D.

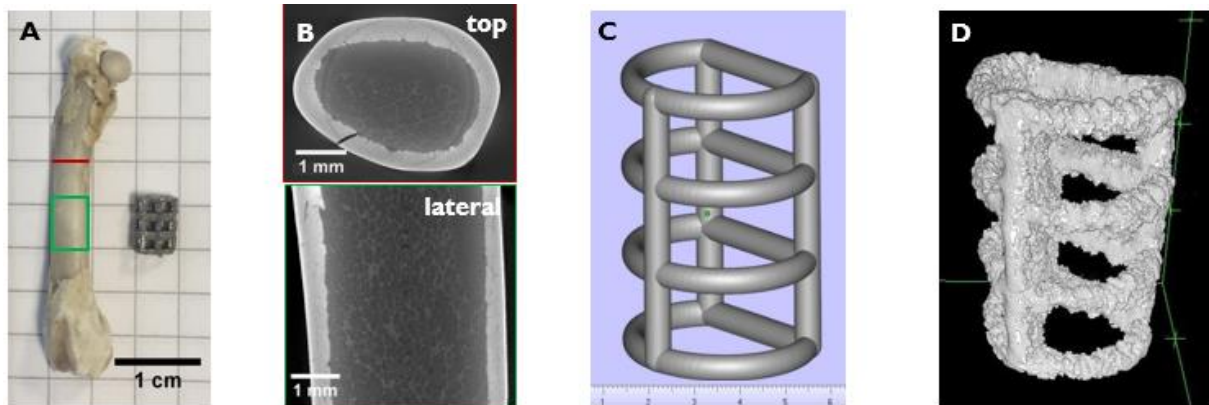


**Figure 117:** Design strategy for *in vivo* experiments using an architected Ti-6Al-4V implant adapted for a critical size femoral bone defects in rat. (A) Representation of the rat femur and one of the EBM built Ti-6Al-4V implant for implantation (B) Cross and lateral sections of the rat femur obtained by X-ray tomography prior implantation (C) Computed Aided Design of one of the Ti-6Al-4V implant (D) 3D representation of EBM built Ti-6Al-4V implant obtained by X-ray tomography

The surface of the first type of *in vivo* implant (**Figure 117C**) was estimated to be at 1 cm<sup>2</sup> according to the CAD. In order to increase the surface area and thus deliver a higher amount of BMP-7 in the same bone defect model, the second type of implants were designed and built with the same structure by adding two crossing struts at each levels of the first previous implant (**Figure 118**). This addition of material increased the implant surface at 1.5 cm<sup>2</sup> according to its CAD representation.

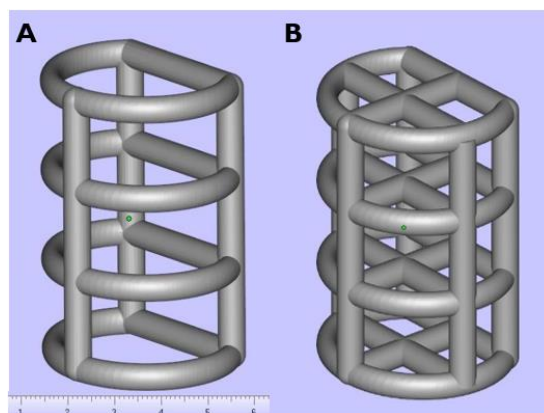


**Figure 118:** CAD representation of *in vivo* Ti-6Al-4V implants for critical size femoral bone defect in rat. The two type of implants with a 1 cm<sup>2</sup> (A) and 1.5 cm<sup>2</sup> (B) total surface areas are respectively represented

In order to know which amount of BMP-7 triggers an efficient bone repair in mouse and rat bone defects, a bibliographic research on the repair of bone defects using BMP-7 was undertaken (**Table 12**). The BMP-7 amounts are in the range of 1 to 100  $\mu\text{g}$  depending on the animal species. Beside, BMP-7 was always either delivered directly via injection or using a collagen carrier. For our preliminary trial, we decided to use a high BMP-7 concentration for the loading in order to reach a total amount of 20  $\mu\text{g}$ .

Animal	Model	Carrier material	Amount of BMP-7 ( $\mu\text{g}$ )	Main results	Ref
Mouse	Muscle pouch assay	Collagen granules	52.5	Bone formation	215
	Closed transverse mid-diaphyseal fractures of the tibia	10% lactose solution	10, 50	Repair and vascularization	216
Rat	Bilateral full-thickness diaphyseal segmental defects	Nanofiber mesh tubes	5	Bone repair	217
	Subcutaneously Intramuscular	Collagen sponge	0, 1, 3, 5, 10, 20	Inflammatory reaction and edema formation	218
	6-mm critical size defect	Collagen sponge	25, 50, 75, 100	100% union rate for 50, 75, and 100 25 too low	219
	Mid-diaphyseal closed transverse fracture	Collagen	50	At 4 week, 63% had healed At 6 weeks, 100% had healed	220

**Table 12: Literature research on appropriate BMP-7 amount for bone repair in mouse and rat bone defect models**

Thus, the two types of implants were coated with  $(\text{PLL}/\text{HA})_{24}$  film and loaded with BMP-7 in sterile conditions at the concentration of 150  $\mu\text{g}/\text{mL}$  for future *in vivo* implantation. The two architectures were loaded with the same BMP-7 concentration and have different surface area, of 1 and 1.5  $\text{cm}^2$  respectively. Since with a loading concentration of 100  $\mu\text{g}/\text{mL}$ , the delivered amount of BMP-7 is at 12  $\mu\text{g}/\text{cm}^2$ , we expect to deliver for the two implants at least more than 12 and 18  $\mu\text{g}$  of BMP-7 respectively, and see different bone regeneration kinetics. This kinetic could either be related to the different architectures or the BMP-7 dose.



## 3.5 Discussion

### 3.5.1 Better knowledge of the mechanical properties of EBM built cubic unit cell Ti-6Al-4V scaffolds

Thanks to emerging additive manufacturing (AM) processes, customized bone graft substitute can be built and structurally and mechanically optimized for a specific bone defect. EBM manufacturing process is one of the main AM technique that allows the building of highly porous structure with a medical grade metallic material, the Ti-6Al-4V alloy. In this study, we showed the versatility of this manufacturing technique by building porous Ti-6Al-4V scaffolds made of a repeated cubic unit cell with three different pores sizes and thus reaching different global porosities (**Figure 98, Table 11**). In a recent review establishing a state of the art of all the EBM-built Ti-6Al-4V scaffolds, cubic unit-cell scaffolds mechanical properties have been investigated for porosities ranging from 49.75% to 70.32%<sup>68</sup>. The reported values of elastic moduli and our measured values as a function of the relative density are presented in **Figure 119**.

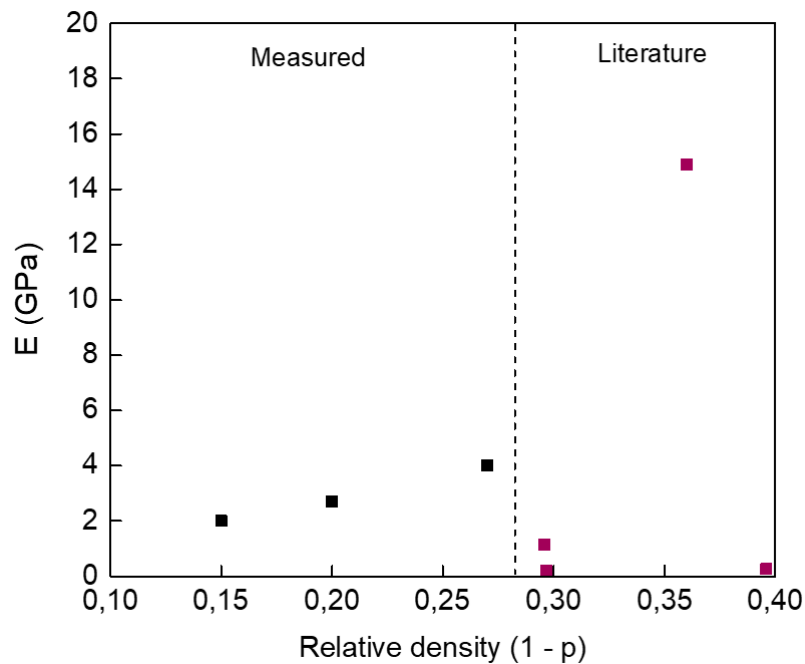


**Figure 119: Representation of the elastic modulus obtained by compression for Ti-6Al-4V cubic unit-cell scaffolds as a function of the relative density. Red dots represent the values obtained from the literature<sup>68</sup>**

Unexpectedly, reported values are either 10 times lower or 5 times higher than the obtained values of this study. This scattering in moduli is not only due the difference in relative density but also in the methods employed to measure the elastic modulus. In the reported values, only the scaffold with  $E = 15$  GPa was measured with cycles of loading-unloading while for others values, they were obtained by one-way compression tests to failure<sup>221</sup>. This demonstrates the remaining uncertainty in mechanical characterization for Ti-6Al-4V architected scaffolds.

In this study, we added to the knowledge of mechanical properties of EBM built cubic unit-cell scaffolds of porosities from 73% to 85% by measuring their compressive elastic modulus. Cubic unit-cell scaffold with 63% porosity (relative density 0.37,  $E = 14.9$  GPa red dot **Figure 119**) was found to be the closest structure, in terms of compressive strength, elastic modulus and fatigue strength, to human cortical tibia and femur<sup>68</sup>. In that sense, we selected a scaffold structure which has the potential to be translated to the clinical level in human patient for this type of bones.

### 3.5.2 BMP-7 incorporation into (PLL/HA) polyelectrolytes films

Depending on the bone trauma to be repaired, bone grafts are either autograft, allograft or synthetic scaffolds. Autograft or allograft treatments are limited in terms of available bone volume and possible risks of rejection in the case of allograft. Synthetic scaffolds made from biocompatible materials are the most used strategy for bone repair. The next generation of bone graft substitutes under development are now incorporating bioactive molecules such as BMP-7, in order to help the bone healing process. One of the main challenges to be resolved for those substitutes is the incorporation of bioactive molecules, their storage and appropriate delivery after implantation. In this study, we used a biopolymeric film made of two polyelectrolytes, poly(L-lysine) (PLL) and acid hyaluronic (HA) as a coating to deliver BMP-7, with PLL being approved for food application and HA being approved by the US Food and Drug Administration and the European Medicine Agencies (EMA) for bone tissue engineering. This specific PEM film has been investigated for bioactive molecule delivery of the well-known BMP-2 for bone regeneration investigations<sup>152,154,155,222</sup>. Here, we showed that this specific film can also incorporate BMP-7.

We also studied this incorporation depending on the films crosslinking level (EDC10 and EDC30) and on increasing BMP-7 loading concentrations. The quantification of the BMP-7 incorporated amount into (PLL/HA) film made of 12 bilayers was previously done by our team<sup>153</sup> for films crosslinked with EDC10: the maximum incorporated amount was  $2 \mu\text{g}/\text{cm}^2$  for an initial concentration of BMP-7 during the loading phase of  $100 \mu\text{g}/\text{mL}$ . Here, we showed that by doubling the number of bilayers from 12 to 24, the BMP-7 incorporated amount increased to  $12 \mu\text{g}/\text{cm}^2$  for the same loading concentration of  $100 \mu\text{g}/\text{mL}$ . Moreover, this amount was dependent on the EDC crosslinking level, with  $3 \mu\text{g}/\text{cm}^2$  less BMP-7 protein incorporated in the case of EDC30 films. Finally, EDC10 films with 24 bilayers are able to retain and deliver the largest amount of BMP-7.

### 3.5.3 (PLL/HA) polyelectrolytes films as BMP-7 carrier for human clinical trials

According to Reichert et al<sup>128</sup>, the recommended dose of rhBMP-7 for recalcitrant long bone non-union in humans was determined to be 7 mg, independently of the bone defect, size and site of fracture<sup>128</sup>. In the reported clinical uses, the BMP-7 amount used was more in the order of 3 mg<sup>223,224</sup>. By using a bone graft substitute having a surface area of  $250 \text{ cm}^2$ , we would be able to deliver the same amount of BMP-7 through our (PLL/HA) PEM film coating of 24 bilayers and a crosslinking level at  $[\text{EDC}] = 10 \text{ mg}/\text{mL}$ . However, those doses remain quite high comparing to the physiological doses that are in the nanogram range. Through the PEM film

coating, we would be able to deliver locally and more effectively smaller amount of BMP-7 and thus reduce possible adverse effects risks.

#### 3.5.4 BMP-7 bioactivity preserved into (PLL/HA) films for short term cell culture

To verify if BMP-7 remained osteoinductive after its incorporation into the PEM film, we conducted *in vitro* cell culture with the D1 cell line (murine mesenchymal stem cells). Their proliferation after 1, 2 and 7 days and their ALP expression after 3 days were assessed. BMP-7 loaded films induced a concentration dependent ALP expression, proving the effective osteoinductive capacity of the coating. In a previous study performed by Guillot et al., the same PEM film coating containing BMP-2 was proven to be stable at least one year after the storage at 4°C. Also, they showed that its osteoinductive capacity was preserved after exposure to clinically approved doses of  $\gamma$ -irradiation. Given that BMP-7 has very similar chemical structure and properties than BMP-2, we can assume that BMP-7 loaded films could also be sterilized and stored while preserving its osteoinductive capacity.

#### 3.5.5 Non BMP-7 dependant extracellular matrix mineralization of D1 cells

The ECM mineralization of D1 cells in regards to the BMP-7 presentation was assessed. Even if BMP-7 could induce the ALP expression at the early stage, the protein did not influence their ECM mineralization. In the literature, we found out an article that specifically studied the D1 cells line and the effects of BMP-2, BMP-4, BMP-6 and BMP-9 on their ECM mineralization<sup>225</sup>. After 7, 14 and 21 days of culture in osteogenic differentiation medium with soluble BMPs (BMP-2-4-6-9), they discovered that the mineralization could not be enhanced by BMPs with the Alizarin Red S staining. Then, they analysed the osteogenic differentiation by measuring the expression of osteogenic transcription factors, namely runX2 and osterix after 7, 14 and 21 days. The gene expression of transcription factors was also not influenced by the BMPs presence, indicating that D1 cells differentiation was mainly triggered by the osteogenic differentiation medium.

The D1 cell model we selected for this study was not adapted to highlight the osteoinductive effect of the BMP-7 loaded (PLL/HA) film coating for an *in vitro* ECM mineralization. This was specific to this cell line which naturally differentiates to an osteogenic lineage and which ECM mineralizes solely in presence of acid ascorbic and  $\beta$ -glycerophosphate, as proven for others BMPs<sup>225</sup>. Those results highlighted the strong dependence of *in vitro* results on the cellular model selected. This is the reason why human MSCs, which represent more physiological cellular models, are more and more used for *in vitro* studies.

#### 3.5.6 Effect of (PLL/HA) films on the topography of EBM built Ti-6Al-4V implants

To the best of our knowledge, bare surfaces of our EBM built Ti-6Al-4V scaffolds did not displayed any specific nanofeatures. Previous AFM measurements on Ti-6Al-4V casted substrates coated with (PLL/HA)<sub>24</sub> polyelectrolyte film indicated a smoother surface due the film addition<sup>193</sup>. The bare Ti-6Al-4V substrate had a roughness of 8.1 nm that was reduced to 1.2 nm by the (PLL/HA)<sub>24</sub> film coating.

In this study, the roughness of EBM built scaffolds was not measured. However, in a previous work done with the same EBM machine on single struts, the roughness was estimated at 35  $\mu\text{m}$  in average<sup>226</sup>. As we observed in **Figure 112**, the addition of (PLL/HA) film at the scaffold surface induced a surface smoothing. Compared to the actual scaffold roughness, the film addition without BMP-7 neither changes significantly the micro-topography roughness nor adds significant nano-features affecting the osteogenic differentiation.

### 3.5.7 BMP-7 surface delivery from porous and architected EBM built Ti-6Al-4V implants

Currently, several additive manufactured titanium bone graft substitutes are now available in the market for spinal replacement surgeries<sup>68</sup>. The first bioactive bone implant commercialized for spinal fusion surgeries was the Infuse<sup>®</sup> Bone Graft from Medtronic. This bone graft substitute consisted in a titanium cage containing a collagen type I paste in which rhBMP-2 was added for the delivery. Due to low-binding affinity of BMPs to collagen, this product required the use of supra-physiological dose of BMP-2 (1.5 mg/mL) which caused several adverse effects such as inflammation and pain<sup>115</sup>. Given the increasing use of AM for spinal implant and the potential use of bioactive molecule for spinal applications, combining our PEM film coating with architected AM scaffolds could meet the demand for this type of bone trauma. Here, we applied the PEM coating to AM cubic unit-cell scaffolds, loaded the PEM coating with BMP-7 and verified the osteoinductivity of the whole construct *in vitro*. The murine MSCs adhered and expressed ALP after 3 days of culture in presence of BMP-7 in the PEM film coating at the scaffold surface. At the best of our knowledge, we were the first to deliver a BMP from Ti-6Al-4V porous scaffolds without using an ECM based gel filling the pores.

### 3.5.8 Potential advantages of the combination of our architected and osteoinductive strategies

Combining 3D porous structures with 2D surface growth factor delivery present the advantage to leave enough space for the new bone to invade the structure while the surrounding cells are exposed to the growth factor and then performed the wanted biological healing cascade. The effectiveness of this 3D porous volume/2D surface delivery strategy was previously performed by Bouyer et al.<sup>152</sup> on a hollow PLGA tube coated with PEM film containing BMP-2. In this work, the bone defect were completely repaired after 2 weeks of implantation in critical size femoral bone defect of 6 mm in rat with 6.5  $\mu\text{g}$  of BMP-2 delivered from 1.34  $\text{cm}^2$  surface area. If we make the simplified assumption that BMP-2 is twice more potent than BMP-7 in regards to *in vitro* ALP expression level (**Figure 103**), we would require in the same configuration 13  $\mu\text{g}$  of BMP-7. In human, the critical size of bone defects was estimated to be in the order of 2.5 cm or greater<sup>227</sup>. Assuming that the defect is located in an adult femur with a diameter of 4.5 cm, the surface available on a cylindrical implant for a 2.5 cm bone defect would be of approximately 35.32  $\text{cm}^2$ , being 25 times more than in femoral critical size bone defect in rat. Knowing the fact that we can incorporate 12  $\mu\text{g}/\text{cm}^2$  of BMP-7 into the PEM film, we could easily incorporate 423  $\mu\text{g}$  (25 x 16.9  $\mu\text{g}$ ) of BMP-7 with the coating at the surface of an 35.32  $\text{cm}^2$  EBM built Ti-6Al-4V implant, while the maximum incorporation of BMP-7 would be of 423  $\mu\text{g}$ . Furthermore, EBM built parts are known to be inherently rough due to the

manufacturing process. The additional developed surface from this inherent roughness could be beneficial to increase the loaded amount of protein, especially since we proved that our coating fits closely this roughness (**Figure 112**).

In our particular case, the next step of this project would be to implant Ti-6Al-4V architected scaffold coated with the PEM film containing BMP-7 in a critical size femoral bone defect in rat to understand the dual effect of the architecture and the BMP-7 presentation on the bone regeneration. In view to assess this dual effect, architected Ti-6Al-4V implants were designed for *in vivo* experiments to repair a critical size femoral bone defect in rat.

### 3.6 Conclusions

Using an additive manufacturing process such as EBM, we were able to build highly porous cubic unit-cells scaffolds made of the medical grade Ti-6Al-4V alloy. The EBM built scaffolds exhibited an elastic modulus close to human cortical bones elastic modulus, showing the potential use of this type of architected structures to reduce the stress shielding effect. According to the increasing interest to incorporate and deliver bioactive molecule to help the bone regeneration process, we decided to use a surface coating made of (PLL/HA) polyelectrolyte films to deliver BMP-7 from the architected scaffolds. To this end, we studied the osteoinductive capacity of the BMP-7 loaded into PEM film with murine MSCs in 2D before coating the 3D structures. The scaffolds coated with the osteoinductive film showed an efficient osteoinductive capacity *in vitro* at the early stage. The combination of bioactivity and porous architecture in bone implants could be successfully translated in clinics and be used in patients who need a fast but long-term bone replacement and repair. Future *in vivo* investigations in animal models will bring more elements to assess the long term osteoinductivity and validate its potential application.

### 3.7 Acknowledgements

This work was supported by the European Commission under the FP7 program (European Research Council grant BIOMIM GA259370 and Proof of Concept REGENERBONE GA790435 to CP). CP is a senior member of the *Institut Universitaire de France*, whose support is greatly acknowledged. The Picart team is supported by the *Fondation Recherche Médicale* (Contract DEQ20170336746), the *Fondation Gueules Cassées* (dossier 21-2016) and the *Fondation de l'Avenir* (AP-RM-16-013). The European commission provided financial support in the frame of H2020/European Research Council (GA790435). WE acknowledge the Nanoscience foundation for support via the Chair of Excellence (FCN-2013-02CE) to Prof Amy Wagoner Johnson and the Center of Excellence of Multi-functional Architected Materials "CEMAM" (n° ANR-10-LABX-44-01). We thank A. Wagoner Johnson for her technical information on the D1 cells, C. Plettinx for assistance in the mechanical tests, C. Masse De La Huerta for designing and building the plastic holders, I. Paintrand, I. Gelard, S. Coindeau and J. Volaire for their technical support in optical, electron microscopy and X-ray tomography imaging.

## Chapter 4. Conclusions and perspectives

### 4.1 Conclusions

The aim of this thesis was to develop 3D architected and osteoinductive titanium-based scaffolds for bone regeneration applications, presenting at the same time porosity and bioactivity. The project was divided into three main parts constituting the main steps of the implant development. First, we had to build the Ti-6Al-4V architected scaffolds by additive manufacturing using the EBM technology. The structural properties of the 3D structures, especially their porosities and elastic modulus, were characterized.

Secondly, we focused on the bioactive surface functionalization technique by working on biomimetic films (considered as 2D surfaces) prior to their coating on the 3D scaffolds. To this end, we used an osteoinductive coating made of several bilayers of two polyelectrolytes (PLL/HA) to form a film that can be loaded with BMP-7. We evaluated the diffusion of BMP-7 and its incorporation in (PLL/HA)<sub>24</sub> films depending on their cross-linking level. After the selection of the films trapping the highest amount of BMP-7, we conducted *in vitro* cellular assays using murine MSCs to test their ability to be differentiated in bone cells.

Finally, after the evaluation of the biomimetic 2D surfaces, we coated the film on 3D scaffolds and characterized their coating at the macro (> 1 mm) and micro (> 100 μm) scales. Then, the osteoinductive capacity of the 3D architected and osteoinductive titanium-based scaffolds was assessed *in vitro* with murine MSCs.

#### 4.1.1 Architected Ti-6Al-4V scaffolds built by EBM additive manufacturing process

The EBM process allowed us to build architected scaffolds with periodic repetitions of cubic unit-cells of three different porosities of 73%, 80% and 85%. The porosities of EBM-built scaffolds were the same as their CAD representation with differences equal or less than 1%. The elastic modulus of the EBM-built structures were obtained by compression test and compared to values from the literature<sup>68</sup>. The modulus values of 2.0 GPa for 73% scaffold porosity, 2.7 GPa for 80% and 4.4 GPa for 85%, were between 50 to 25 times lower than the modulus of bulk Ti-6Al-4V. This first mechanical characterization suggests the potential of the architecture to reduce stress shielding effects.

#### 4.1.2 2D *in vitro* osteoinductive capacity of PEM film loaded with BMP-7

The BMP-7 loading, diffusion and incorporated amount were evaluated in 2D for biomimetic films deposited into plastic well plates. The use of fluorescently-labelled PLL and BMP-7 allowed to observe the BMP-7 diffusion in the (PLL/HA)<sub>24</sub> films. The protein only partially diffused into the film and was mainly localized at the upper side. The two lowest levels of film cross-linking (EDC10 and EDC30) were studied for the BMP-7 incorporation. The film crosslinked with EDC10 was able to retain more BMP-7, with an incorporation of 12 μg/cm<sup>2</sup> for the maximum loading concentration of 100 μg/mL. Thus, this film was selected for further studies. Then, we evaluated the osteoinductive capacity of BMP-7 loaded films by measuring



the early ALP expression of murine MSCs after 3 days of culture. We demonstrated that BMP-7 loaded films were osteoinductive at the early stages in a dose-dependent manner.

#### 4.1.3 Extracellular matrix mineralization of D1 cells in response to BMP-7

The *in vitro* mineralization of the extracellular matrix is one of the late stage assessment of the osteogenic differentiation. We aimed at evaluate the osteoinductive effect of BMP-7 on the mineralization process. However, the murine MSCs used in this project strongly mineralized even in the presence of minimally osteoinductive differentiation medium. Thus, we were not able to highlight the osteoinductive effect of the BMP-7 loaded films on the matrix mineralization using those cells. Findings from the literature confirmed that this effect was not specific to BMP-7 but was also found out for BMP-2, -4, -6 and -9<sup>225</sup>.

#### 4.1.4 3D *in vitro* osteoinductivity of Ti-6Al-4V scaffolds coated with BMP-7

The 3D architected scaffolds were coated with the (PLL/HA) films and fluorescently labelled PLL for qualitative microscopic observations. Fluorescence macroscopy and scanning electron microscopy images confirmed the homogeneous coating of the film at the surface of the scaffolds, even on partially-fused Ti-6Al-4V beads. After the loading of BMP-7, the osteoinductive capacity of the 3D architected scaffold was assessed *in vitro* with murine MSCs after 3 days of culture. Cellular morphology and colonization were qualitatively evaluated on scaffolds by epifluorescence and scanning electron microscopies. Cells were well spread and distributed on bare and on BMP-7 loaded film-coated scaffolds, while there were only little spreading on the film-coated scaffolds (in the absence of BMP-7). The ALP expression on film-coated scaffolds was significantly increased in the presence of matrix-bound BMP-7. This proved that the 3D coated scaffolds were osteoinductive and that they properly delivered BMP-7.

Altogether, our results proved that the titanium-based implant with a 3D porous architecture and the bioactive surface was effectively osteoinductive *in vitro*.

## 4.2 Perspectives

### 4.2.1 Architectural characterization of EBM-built scaffolds

The structure of bone implants was found to play an important role in bone regeneration<sup>83</sup>. Mechanical properties, such as elastic modulus, ultimate yield or compressive strengths and fatigue strength, are also important to ensure the viability of the surrounding bone tissues and implant stability in their lifespan<sup>68</sup>. In term of architecture, features such as nano-micro topographies, pore interconnectivity, size and shape, and surface curvature were identified for guiding and controlling the bone tissue formation<sup>84</sup>. Future strategies to deepen our view on those aspects will be presented in this section.

Additional structural characterization

To better characterize our structures, it would be interesting to further analyse their structural dimensions (pores, surface topography and curvature) with X-ray tomography scans of EBM-

built scaffolds. Then, additional mechanical tests with different EBM-built specimens such as tensile and fatigue tests could be done to complete their mechanical characterization in view of future implantation applications.

#### Pore size and surface curvature

In this study, *in vitro* titanium scaffolds were made of a periodic repetition of cubic unit-cells of three different porosities. The longest period of cell culture using the 80% porous scaffold was of 14 days. At this time point, the cells did not secrete enough ECM to visualize the pore size nor a curvature-dependent tissue formation. However, we could expect a tissue growth starting from the corners at the location of crossing struts, as seen in square-shaped hydroxyapatite plates<sup>92</sup>. A way to study pore size or curvature effects on EBM-built scaffolds would be to use smaller scaffolds in their height with a cellular model known to secrete large amounts of extracellular matrix proteins.

#### Prediction of bone regeneration with a curvature-driven tissue growth model

A discrete model of curvature-driven tissue prediction into 2D<sup>228</sup> and 3D structures<sup>93,229</sup> was previously developed by Cécile Bidan (Team leader at Max Planck Institute in Golm). In 2D, this model is a cellular automaton based on the discretization of surfaces with pixels and the determination of the local curvature in a defined mask. When the local mean curvature is negative (concave surface) voids pixels in the mask are filled and thus simulate the tissue growth driven by the curvature.

This model could be used on EBM-built scaffolds tomographic representations to predict the tissue growth and extracellular matrix deposit inside the architectures solely based on the local mean curvature. Preliminary trials on *in vitro* scaffolds were conducted by Pierre Lhuissier (CNRS researcher at SIMAP) using this model. However, there are some limitations with the definition of the local mean curvature that leads to a null mean curvature, which is stopping the growth process. The improvement of this model in 3D is still in progress. In the future, it would be interesting to compare *in vitro* and *in vivo* tissue formation from explanted structures with *in vivo* formed bone tissue.

#### 4.2.2 Assessment of the film osteoinductivity

The osteoinductive capacity of the BMP-7 loaded films was investigated with D1 murine mesenchymal stem cells. We measured their early ALP expression in 2D and 3D configurations to quantify this capacity. The current limitations and possible future strategies are presented in this section.

#### Cellular model

After the second wave of inflammatory cells, next implicated cells at the implantation site are progenitor cells. In that sense, stem cells are appropriate cellular model to assess the osteoinductive potential of a bioactive molecule. Human MSCs such as marrow stromal cells (BMSCs), adipose-derived mesenchymal cells (ASCs) and periosteum-derived stem cells (PDSCs) are currently used in pre-clinical and clinical trials for bone repair strategies based on

cells<sup>21</sup>. Those cells represent more physiological models than the murine mesenchymal stem cells used here.

Further experiments with human mesenchymal stem cells or human periosteum stem cells<sup>230,231</sup> could be done to confirm the long-term osteoinductive effect of the bioactive films. Even if those cells are more difficult to harvest and have longer proliferation time than murine cells, it would have been interesting to assess our film osteoinductivity with at least one type of human MSCs. Since February 2017, the LMGP lab is equipped with a L2 facility that enables the culture of human stem cells and has established a partnership with the French blood institute “Etablissement Français du Sang” in June 2017 to obtain human MSCs. These MSCs are now available at LMGP and preliminary experiences have been done recently.

## 2D osteoinductive biological tests

In order to further assess the osteoinductive capacity of the coating, it would be interesting to quantify the expression of early and late genes considered as bone markers, including transcription factors and extracellular matrix proteins, using quantitative polymerase chain reaction (qPCR). The most commonly investigated markers either at the gene or protein levels are:

- runt-related transcription factor 2 (RunX2) which is considered as the master regulator of the osteogenic differentiation<sup>232</sup>
- osterix (OSX) transcription factor during preosteoblast progenitor differentiation<sup>233</sup>
- alkaline phosphatase (ALP) enzyme, expressed early during differentiation, responsible for the ECM mineralization<sup>234</sup>
- osteopontin (OPN) non-collagenous bone ECM protein, expressed at early stages<sup>235</sup>
- osteocalcin (OCN) non-collagenous bone ECM protein, expressed at late stages<sup>235</sup>

These markers could also be visualized using immunofluorescence with appropriate antibodies.

## 3D cell culture

*In vitro* 3D cell culture into scaffolds raises issues in term of cell survival and long term viability. In this study, we cultured cells on titanium scaffolds with constant orbital agitation to ensure a flow in the culture medium, supply of oxygen and removal of cellular wastes. However, we were not sure that cells inside the 3D scaffolds were maintained appropriately. Currently for this type of 3D construct, bioreactors are used to maintain a constant medium flow inside 3D structures<sup>236</sup>.

Another strategy to facilitate 3D *in vitro* culture, reduce the number of cells and depth issues regarding the imaging or the cellular viability, would be to reduce the dimensions of the scaffolds, notably their height. Indeed, 3D-mimetic platforms with heights ranging from 0.5 to 2 mm are already employed for studying the effects of pore shapes on tissue formation *in vitro*<sup>92</sup>.

## In vivo experiments in critical-size femoral bone defect

In view to further assess the osteoinductive potential of our architected and bioactive scaffolds, one of the future steps would be to evaluate them with *in vivo* investigations. It was initiated in a 6 mm critical-size femoral bone defect in rat with two types of porous EBM-built implants. Both implants were coated with (PLL/HA)<sub>24</sub> film and loaded with BMP-7. Since they displayed different surface areas, a higher and lower dose of BMP-7 are presented. We expect that these BMP-7 loaded architected implants will be osteoinductive *in vivo* and that there will be a difference in the bone regeneration kinetics. This kinetic could either be related to the different architectures or the BMP-7 dose. One of the next steps could be to compare the (experimentally) regenerated bone tissues to the model tissues obtained using the curvature-driven bone model. This would enable to better understand the distinct effect of the scaffold architecture. Alternately, different doses of BMP-7 may be tested. Finally, we could design implants for larger animal models such as mini pig, goat or sheep, which are the common animal models for large bone defects.

## Bibliographic References

1. Michel S. Circulatory system. In: *Larousse*.
2. Alan M. Essentials of anatomy & physiology 4th edition martini/bartholomew. In: *Duke University*.
3. Chai YC, Carlier A, Bolander J, et al. Current views on calcium phosphate osteogenicity and the translation into effective bone regeneration strategies. *Acta Biomater*. 2012;8(11):3876-3887. doi:10.1016/j.actbio.2012.07.002.
4. Wang X, Xu S, Zhou S, et al. Topological design and additive manufacturing of porous metals for bone scaffolds and orthopaedic implants: A review. *Biomaterials*. 2016;83:127-141. doi:10.1016/j.biomaterials.2016.01.012.
5. Dufort CC, Paszek MJ, Weaver VM. Balancing forces: Architectural control of mechanotransduction. *Nat Rev Mol Cell Biol*. 2011;12(5):308-319. doi:10.1038/nrm3112.
6. Hussey GS, Dziki JL, Badylak SF. Extracellular matrix-based materials for regenerative medicine. *Nat Rev Mater*. 2018;3(7):159-173. doi:10.1038/s41578-018-0023-x.
7. Uings IJ, Farrow SN. Cell receptors and cell signalling. *Mol Pathol*. 2000;53(6):295-299. doi:10.1136/mp.53.6.295.
8. Ten Dijke P, Arthur HM. Extracellular control of TGF $\beta$  signalling in vascular development and disease. *Nat Rev Mol Cell Biol*. 2007;8(11):857-869. doi:10.1038/nrm2262.
9. Wang RN, Green J, Wang Z, et al. Bone Morphogenetic Protein (BMP) signaling in development and human diseases. *Genes Dis*. 2014;1(1):87-105. doi:10.1016/j.gendis.2014.07.005.
10. Eliceiri BP. Integrin and growth factor receptor crosstalk. *Circ Res*. 2001;89(12):1104-1110. doi:10.1161/hh2401.101084.
11. Long F. Building strong bones : molecular regulation of the osteoblast lineage. *Nat Rev Mol Cell Biol*. 2012;13. doi:10.1038/nrm3254.
12. Crockett JC, Rogers MJ, Coxon FP, Hocking LJ, Helfrich MH. Bone remodelling at a glance. *J Cell Sci*. 2011;124(7):991-998. doi:10.1242/jcs.063032.
13. Viswanath B, Raghavan R, Ramamurty U, Ravishankar N. Mechanical properties and anisotropy in hydroxyapatite. Viswanath B, Raghavan R, Ramamurty U, Ravishankar N. Mechanical properties and anisotropy in hydroxyapatite single crystals. *Scr Mater*. 2007;57(4):361-364. doi:10.1016/j.scriptamat.2007.04.027. te sing. *Scr Mater*. 2007;57(4):361-364. doi:10.1016/j.scriptamat.2007.04.027.
14. Bala Y, Seeman E. Bone's material constituents and their contribution to bone strength in health, disease, and treatment. *Calcif Tissue Int*. 2015;97(3):308-326. doi:10.1007/s00223-015-9971-y.
15. Weinkamer R, Fratzl P. Mechanical adaptation of biological materials — The examples of bone and wood. *Mater Sci Eng C*. 2011;31(6):1164-1173. doi:10.1016/j.msec.2010.12.002.
16. Ogata S, Uhthoff H. The early development and ossification of the human clavicle--an embryologic study. *Acta Orthop Scand*. 1990;Aug;61(4):
17. Hill MA. Embryology timeline human development. <https://embryology.med.unsw.edu.au/embryology/index.php/>.
18. Creative Commons Attribution 4.0 International License. Anatomy and physiology. Rice University. <https://opentextbc.ca/anatomyandphysiology/chapter/6-4-bone-formation-and-development/>.
19. Bonomo A, Monteiro AC, Gonçalves-Silva T, Cordeiro-Spinetti E, Galvani RG, Balduino A. A T Cell View of the Bone Marrow. *Front Immunol*. 2016;7(MAY). doi:10.3389/fimmu.2016.00184.
20. Pria Bankoff AD. Biomechanical characteristics of the bone. In: *Human Musculoskeletal Biomechanics*. InTech; 2012. doi:10.5772/19690.
21. Ho-shui-ling A, Bolander J, Rustom LE, Wagoner A, Luyten FP, Picart C. Bone regeneration strategies : Engineered scaffolds , bioactive molecules and stem cells current stage and future

- perspectives. *Biomaterials*. 2018;180:143-162. doi:10.1016/j.biomaterials.2018.07.017.
22. Inc O. *The Orthopaedic Industry Annual Report: 2010-2011*.
  23. Austin V. Bones and skeletal tissues. Bluegrass Technical and Community College.
  24. Holmes D. Non-union bone fracture: a quicker fix. *Nature*. 2017;550(7677):S193-S193. doi:10.1038/550S193a.
  25. Seeman E. Bone quality: The material and structural basis of bone strength. *J Bone Miner Metab*. 2008;26(1):1-8. doi:10.1007/s00774-007-0793-5.
  26. Gerstenfeld LC, Cullinane DM, Barnes GL, Graves DT, Einhorn TA. Fracture healing as a post-natal developmental process: Molecular, spatial, and temporal aspects of its regulation. *J Cell Biochem*. 2003;88(5):873-884. doi:10.1002/jcb.10435.
  27. Phillips AM. Overview of the fracture healing cascade. *Injury*. 2005;36(3):S5-S7. doi:10.1016/j.injury.2005.07.027.
  28. Claes L, Recknagel S, Ignatius A. Fracture healing under healthy and inflammatory conditions. *Nat Rev Rheumatol*. 2012;8:133. <http://dx.doi.org/10.1038/nrrheum.2012.1>.
  29. Kolar P, Schmidt-Bleek K, Schell H, et al. The early fracture hematoma and its potential role in fracture healing. *Tissue Eng Part B Rev*. 2010;16(4):427-434. doi:10.1089/ten.teb.2009.0687.
  30. Street JT, Wang JH, Wakai A, McGuinness A, Redmond HP. †Is human fracture hematoma inherently angiogenic? *J Orthop Trauma*. 2000;14(2).
  31. Prystaz K, Kaiser K, Kovtun A, et al. Distinct effects of IL-6 classic and trans-signaling in bone fracture healing. *Am J Pathol*. 2018;188(2):474-490. doi:10.1016/j.ajpath.2017.10.011.
  32. Schlundt C, El T, Serra A, et al. Macrophages in bone fracture healing : Their essential role in endochondral ossification ☆. *Bone*. 2018;106:78-89. doi:10.1016/j.bone.2015.10.019.
  33. Gerstenfeld L, Kon T, Aizawa T, et al. Impaired fracture healing in the absence of TNF-α signaling: The role of TNF-α in endochondral cartilage resorption. *J Bone Miner Res*. 2003;18(9):1584-1592.
  34. Yang X, Ricciardi BF, Hernandez-Soria A, Shi Y, Pleshko Camacho N, Bostrom MPG. Callus mineralization and maturation are delayed during fracture healing in interleukin-6 knockout mice. *Bone*. 2007;41(6):928-936. doi:10.1016/j.bone.2007.07.022.
  35. Raggatt LJ, Wulschleger ME, Alexander KA, et al. Fracture healing via periosteal callus formation requires macrophages for both initiation and progression of early endochondral ossification. *Am J Pathol*. 2014;184(12):3192-3204. doi:10.1016/j.ajpath.2014.08.017.
  36. Hall BK, Miyake T. All for one and one for all: condensations and the initiation of skeletal development. *BioEssays*. 2000;22(2):138-147. doi:10.1002/(SICI)1521-1878(200002)22:2<138::AID-BIES5>3.0.CO;2-4.
  37. Hall BK, Miyake T. Divide, accumulate, differentiate: Cell condensation in skeletal development revisited. *Int J Dev Biol*. 1995;39(6):881-893. doi:10.1387/IJDB.8901191.
  38. Dunlop LLT, Hall BK. Relationships between cellular condensation, preosteoblast formation and epithelial-mesenchymal interactions in initiation of osteogenesis. *Int J Dev Biol*. 1995;39(2):357-371.
  39. Colnot C. Skeletal cell fate decisions within periosteum and bone marrow during bone regeneration. *J Bone Miner Res*. 2009;24(2):274-282. doi:10.1359/jbmr.081003.
  40. Duchamp De Lageneste O, Julien A, Abou-Khalil R, et al. Periosteum contains skeletal stem cells with high bone regenerative potential controlled by Periostin. *Nat Commun*. 2018;9(1):1-15. doi:10.1038/s41467-018-03124-z.
  41. Schindeler A, McDonald MM, Bokko P, Little DG. Bone remodeling during fracture repair: The cellular picture. *Semin Cell Dev Biol*. 2008;19(5):459-466. doi:10.1016/j.semcdb.2008.07.004.
  42. Al-Aql ZS, Alagl AS, Graves DT, Gerstenfeld LC, Einhorn TA. Molecular mechanisms controlling bone formation during fracture healing and distraction osteogenesis. *J Dent Res*. 2008;87(2):107-118. doi:10.1177/154405910808700215.
  43. Riddle RC, Clemens TL. Bone cell bioenergetics and skeletal energy homeostasis. *Physiol Rev*. 2017;97(2):667-698. doi:10.1152/physrev.00022.2016.
  44. Thompson Z, Miclau T, Hu D, Heims J a. A model for intramembranous bone healing during



- fracture repair. *J Orthop Res.* 2002;20(0):1091-1098.
45. Shen X, Wan C, Ramaswamy G, et al. Prolyl hydroxylase inhibitors increase neoangiogenesis and callus formation following femur fracture in mice. *J Orthop Res.* 2009;27(10):1298-1305. doi:10.1002/jor.20886.
  46. Gerstenfeld LC, Cho TJ, Kon T, et al. Impaired intramembranous bone formation during bone repair in the absence of tumor necrosis factor-alpha signaling. *Cells Tissues Organs.* 2001;169(3):285-294. doi:10.1159/000047893.
  47. Schmid GJ, Kobayashi C, Sandell LJ, Ornitz DM. Fibroblast growth factor expression during skeletal fracture healing in mice. *Dev Dyn.* 2009;238(3):766-774. doi:10.1002/dvdy.21882.
  48. Yu YY, Lieu S, Lu C, Miclau T, Marcucio RS, Colnot C. Immunolocalization of BMPs, BMP antagonists, receptors, and effectors during fracture repair. *Bone.* 2010;46(3):841-851. doi:10.1016/j.bone.2009.11.005.
  49. Giannoudis P V., Dinopoulos H, Tsiridis E. Bone substitutes: An update. *Injury.* 2005;36(3):S20-S27. doi:10.1016/j.injury.2005.07.029.
  50. Laurencin C, Khan Y, El-Amin SF. Bone graft substitutes. *Expert Rev Med Devices.* 2006;3(1):49-57. doi:10.1586/17434440.3.1.49.
  51. Whitehead T. Tissue engineering and regenerative medicine. Summer Course. <https://slideplayer.com/slide/4494601/>.
  52. Vanderstappen J, Lammens J, Berger P, Laumen A. Ilizarov bone transport as a treatment of congenital pseudarthrosis of the tibia: a long-term follow-up study. *J Child Orthop.* 2015;9(4):319-324. doi:10.1007/s11832-015-0675-7.
  53. Einhorn TA, Gerstenfeld LC. Fracture healing: Mechanisms and interventions. *Nat Rev Rheumatol.* 2015;11(1):45-54. doi:10.1038/nrrheum.2014.164.
  54. Albrektsson T, Johansson C. Osteoinduction, osteoconduction and osseointegration. *Eur Spine J.* 2001;10:S96-S101. doi:10.1007/s005860100282.
  55. Ratner BD, Bryant SJ. Biomaterials: where we have been and where we are going. *Annu Rev Biomed Eng.* 2004;6(1):41-75. doi:10.1146/annurev.bioeng.6.040803.140027.
  56. Piconi C, Porporati AA. Bioinert ceramics: zirconia and alumina. In: Antoniac IV, ed. *Handbook of Bioceramics and Biocomposites.* Cham: Springer International Publishing; 2016:59-89. doi:10.1007/978-3-319-12460-5\_4.
  57. Renovis®. Total hip replacement information for patients. <http://www.renovis-surgical.com/2011/09/hip-replacement-information-for-patients/>.
  58. Ohtsuki C, Kamitakahara M, Miyazaki T. Bioactive ceramic-based materials with designed reactivity for bone tissue regeneration. *J R Soc Interface.* 2009;6:S349-S360. doi:10.1098/rsif.2008.0419.focus.
  59. Hench LL. Bioceramics: From concept to clinic. *J Am Ceram Soc.* 1991;74(7):1487-1510. doi:10.1111/j.1151-2916.1991.tb07132.x.
  60. Stevens MM. Biomaterials for bone Materials that enhance bone regeneration have a wealth of potential. *Mater Today.* 2008;11(5):18-25. doi:10.1016/S1369-7021(08)70086-5.
  61. Göpferich A. Mechanisms of polymer degradation and erosion. *Biomaterials.* 1996;17(2):103-114. doi:10.1016/0142-9612(96)85755-3.
  62. Navarro M, Michiardi A, Castano O, Planell J. Biomaterials in orthopaedics. *J R Soc Interface.* 2008;5(27):1137-1158. doi:10.1098/rsif.2008.0151.
  63. Gao C, Deng Y, Feng P, et al. Current progress in bioactive ceramic scaffolds for bone repair and regeneration. *Int J Mol Sci.* 2014;15(3):4714-4732. doi:10.3390/ijms15034714.
  64. Roseti L, Parisi V, Petretta M, et al. Scaffolds for bone tissue engineering: State of the art and new perspectives. *Mater Sci Eng C.* 2017;78:1246-1262. doi:10.1016/j.msec.2017.05.017.
  65. Amini AR, Laurencin CT, Nukavarapu SP. Bone tissue engineering: Recent advances and challenges. *Crit Rev Biomed Eng.* 2013;40(5):363-408.
  66. Wikipedia. Metallic bonding. [https://en.wikipedia.org/wiki/Metallic\\_bonding](https://en.wikipedia.org/wiki/Metallic_bonding).
  67. Geetha M, Singh AK, Asokamani R, Gogia AK. Ti based biomaterials, the ultimate choice for orthopaedic implants – A review. *Prog Mater Sci.* 2009;54(3):397-425.

- doi:10.1016/j.pmatsci.2008.06.004.
68. Zhang XZ, Leary M, Tang HP, Song T, Qian M. Selective electron beam manufactured Ti-6Al-4V lattice structures for orthopedic implant applications: Current status and outstanding challenges. *Curr Opin Solid State Mater Sci*. 2018;22(3):75-99. doi:10.1016/j.cossms.2018.05.002.
  69. Hanawa T. Research and development of metals for medical devices based on clinical needs. *Sci Technol Adv Mater*. 2012;6996(Topical Review). doi:10.1088/1468-6996/13/6/064102.
  70. Agarwal S, Curtin J, Duffy B, Jaiswal S. Biodegradable magnesium alloys for orthopaedic applications : A review on corrosion , biocompatibility and surface modifications. *Mater Sci Eng C*. 2016;68:948-963. doi:10.1016/j.msec.2016.06.020.
  71. Quinn RK, Armstrong NR. Electrochemical and surface analytical characterization of titanium and titanium hydride thin film electrode oxidation. *J Electrochem Soc*. 1978;125(11):1790-1796. doi:10.1149/1.2131295.
  72. Elias CN, Lima JHC, Valiev R, Meyers MA. Biomedical applications of titanium and its alloys. *JOM*. 2008;60(3):46-49. doi:10.1007/s11837-008-0031-1.
  73. Rack HJ, Qazi JI. Titanium alloys for biomedical applications. *Mater Sci Eng C*. 2006;26:1269-1277. doi:10.1016/j.msec.2005.08.032.
  74. Kobelco. Manufacturing Processes. *Kobe Steel Gr*. <http://www.kobelco.co.jp/english/titan/files/process.pdf>.
  75. Trotman S. Orthopaedics machining case study. PCML. <http://www.pcml.net/orthopaedics-machining.htm>.
  76. Beeby D. Design and manufacture considerations for medical implants. TCT Mag. <https://www.tctmagazine.com/blogs/guest-column/design-manufacture-considerations-medical-implants/>.
  77. Pallone T. The making of a dental implant. Engineering 360. <https://insights.globalspec.com/article/8101/the-making-of-a-dental-implant>.
  78. Kang CW, Fang FZ. State of the art of bioimplants manufacturing: part I. *Adv Manuf*. 2018;6(1):20-40. doi:10.1007/s40436-017-0207-4.
  79. Kerns J. Powder-metallurgy processes. MachineDesign. <https://www.machinedesign.com/metals/powder-metallurgy-processes>.
  80. Frazier WE. Metal additive manufacturing: A review. *J Mater Eng Perform*. 2014;23(6):1917-1928. doi:10.1007/s11665-014-0958-z.
  81. Sing SL, An J, Yeong WY, Wiria FE. Laser and electron-beam powder-bed additive manufacturing of metallic implants: A review on processes, materials and designs. *J Orthop Res*. 2016;34(3):369-385. doi:10.1002/jor.23075.
  82. Murr LE, Gaytan SM, Ramirez DA, et al. Metal fabrication by Additive Manufacturing using Laser and Electron Beam Melting technologies. *J Mater Sci Technol*. 2012;28(1):1-14. doi:10.1016/S1005-0302(12)60016-4.
  83. Karageorgiou V, Kaplan D. Porosity of 3D biomaterial scaffolds and osteogenesis. *Biomaterials*. 2005;26(27):5474-5491. doi:10.1016/j.biomaterials.2005.02.002.
  84. Zadpoor A a. Bone tissue regeneration: the role of scaffold geometry. *Biomater Sci*. 2015;3(2):231-245. doi:10.1039/C4BM00291A.
  85. Murr LE, Gaytan SM, Medina F, et al. Next-generation biomedical implants using additive manufacturing of complex, cellular and functional mesh arrays. *Philos Trans R Soc A Math Phys Eng Sci*. 2010;368(1917):1999-2032. doi:10.1098/rsta.2010.0010.
  86. Amin Yavari S, Wauthle R, Van Der Stok J, et al. Fatigue behavior of porous biomaterials manufactured using selective laser melting. *Mater Sci Eng C*. 2013;33(8):4849-4858. doi:10.1016/j.msec.2013.08.006.
  87. Amin Yavari S, Ahmadi SM, Wauthle R, et al. Relationship between unit cell type and porosity and the fatigue behavior of selective laser melted meta-biomaterials. *J Mech Behav Biomed Mater*. 2015;43:91-100. doi:10.1016/j.jmbbm.2014.12.015.
  88. Kuboki Y, Takita H, Kobayashi D, et al. BMP-Induced osteogenesis on the surface of

- hydroxyapatite with geometrically feasible and nonfeasible structures: Topology of osteogenesis. *J Biomed Mater Res*. 1998;39(2):190-199. doi:10.1002/(SICI)1097-4636(199802)39:2<190::AID-JBM4>3.0.CO;2-K.
89. Hulbert SF, Young FA, Mathews RS, Klawitter JJ, Talbert CD, Stelling FH. Potential of ceramic materials as permanently implantable skeletal prostheses. *J Biomed Mater Res*. 1970;4(3):433-456. doi:10.1002/jbm.820040309.
  90. Zhang Q, Lu H, Kawazoe N, Chen G. Pore size effect of collagen scaffolds on cartilage regeneration. *Acta Biomater*. 2014;10(5):2005-2013. doi:10.1016/j.actbio.2013.12.042.
  91. Doktor T, Valach J, Kytýr D, Jiroušek O. *Pore Size Distribution of Human Trabecular Bone - Comparison of Intrusion Measurements with Image Analysis.*; 2011.
  92. Rumpler M, Woesz A, Dunlop JWC, Van Dongen JT, Fratzl P. The effect of geometry on three-dimensional tissue growth. *J R Soc Interface*. 2008;5(27):1173-1180. doi:10.1098/rsif.2008.0064.
  93. Paris M, Götz A, Hettrich I, et al. Scaffold curvature-mediated novel biomineralization process originates a continuous soft tissue-to-bone interface. *Acta Biomater*. 2017;1-17. doi:10.1016/j.actbio.2017.07.029.
  94. Dobbenga S, Fratila-Apachitei LE, Zadpoor AA. Nanopattern-induced osteogenic differentiation of stem cells – A systematic review. *Acta Biomater*. 2016;46:3-14. doi:10.1016/j.actbio.2016.09.031.
  95. Gittens RA, McLachlan T, Olivares-Navarrete R, et al. The effects of combined micron-/submicron-scale surface roughness and nanoscale features on cell proliferation and differentiation. *Biomaterials*. 2011;32(13):3395-3403. doi:10.1016/j.biomaterials.2011.01.029.
  96. Lord MS, Foss M, Besenbacher F. Influence of nanoscale surface topography on protein adsorption and cellular response. *Nano Today*. 2010;5(1):66-78. doi:10.1016/j.nantod.2010.01.001.
  97. Flemming RG, Murphy CJ, Abrams GA, Goodman SL, Nealey PF. Effects of synthetic micro- and nano-structured surfaces on cell behavior. *Biomaterials*. 1999;20(6):573-588. doi:10.1016/S0142-9612(98)00209-9.
  98. Nikkhah M, Edalat F, Manoucheri S, Khademhosseini A. Engineering microscale topographies to control the cell-substrate interface. *Biomaterials*. 2012;33(21):5230-5246. doi:10.1016/j.biomaterials.2012.03.079.
  99. Holthaus MG, Stolle J, Treccani L, Rezwani K. Orientation of human osteoblasts on hydroxyapatite-based microchannels. *Acta Biomater*. 2012;8(1):394-403. doi:10.1016/j.actbio.2011.07.031.
  100. Kirmizidis G, Birch MA. Microfabricated grooved substrates influence cell–cell communication and osteoblast differentiation in vitro. *Tissue Eng Part A*. 2008;15(6):1427-1436. doi:10.1089/ten.tea.2008.0137.
  101. Fu J, Wang YK, Yang MT, et al. Mechanical regulation of cell function with geometrically modulated elastomeric substrates. *Nat Methods*. 2010;7(9):733-736. doi:10.1038/nmeth.1487.
  102. Goriainov V, Cook R, Latham JM, Dunlop DG, Oreffo ROC. Bone and metal : An orthopaedic perspective on osseointegration of metals. *Acta Biomater*. 2014;10(10):4043-4057. doi:10.1016/j.actbio.2014.06.004.
  103. Sharan J, Lale S V, Koul V, Mishra M, Kharbanda OP. An overview of surface modifications of Titanium and its alloys for biomedical applications. *Trends Biomater Artif Organs*. 2015;29(2):176-187.
  104. Wennerberg A, Albrektsson T. Effects of titanium surface topography on bone integration: A systematic review. *Clin Oral Implants Res*. 2009;20(SUPPL. 4):172-184. doi:10.1111/j.1600-0501.2009.01775.x.
  105. Gittens RA, Olivares-Navarrete R, Schwartz Z, Boyan BD. Implant osseointegration and the role of microroughness and nanostructures: Lessons for spine implants. *Acta Biomater*.

- 2014;10(8):3363-3371. doi:10.1016/j.actbio.2014.03.037.
106. Heini P, Müller L, Körner C, Singer RF, Müller FA. Cellular Ti–6Al–4V structures with interconnected macro porosity for bone implants fabricated by selective electron beam melting. *Acta Biomater.* 2008;4(5):1536-1544. doi:10.1016/j.actbio.2008.03.013.
  107. Li X, Feng Y, Wang C-T, et al. Evaluation of Biological Properties of Electron Beam Melted Ti6Al4V Implant with Biomimetic Coating In Vitro and In Vivo. Zheng J, ed. *PLoS One.* 2012;7(12):e52049. doi:10.1371/journal.pone.0052049.
  108. Amin Yavari S, Van der Stok J, Chai YC, et al. Bone regeneration performance of surface-treated porous titanium. *Biomaterials.* 2014;35(24):6172-6181. doi:10.1016/j.biomaterials.2014.04.054.
  109. Li X, Wang L, Yu X, et al. Tantalum coating on porous Ti6Al4V scaffold using chemical vapor deposition and preliminary biological evaluation. *Mater Sci Eng C.* 2013;33(5):2987-2994. doi:10.1016/j.msec.2013.03.027.
  110. Li X, Gao P, Wan P, et al. Novel bio-functional magnesium coating on porous Ti6Al4V orthopaedic implants: in vitro and in vivo study. *Sci Rep.* 2017;7(1):40755. doi:10.1038/srep40755.
  111. Ceramed. Medical coatings. <http://www.ceramed.pt/servicos>.
  112. DOT. Dental Coatings - PVD Coating. Medical implant solutions. <http://www.dot-coating.de/index.php/en/coatings/dental/pvd-coating>.
  113. Carreira AC, Alves GG, Zambuzzi WF, Sogayar MC, Granjeiro JM. Bone Morphogenetic Proteins: Structure, biological function and therapeutic applications. *Arch Biochem Biophys.* 2014;561:64-73. doi:10.1016/j.abb.2014.07.011.
  114. Gandhi NS, Mancera RL. Prediction of heparin binding sites in bone morphogenetic proteins (BMPs). *Biochim Biophys Acta - Proteins Proteomics.* 2012;1824(12):1374-1381. doi:10.1016/j.bbapap.2012.07.002.
  115. Carragee EJ, Hurwitz EL, Weiner BK. A critical review of recombinant human bone morphogenetic protein-2 trials in spinal surgery: Emerging safety concerns and lessons learned. *Spine J.* 2011;11(6):471-491. doi:10.1016/j.spinee.2011.04.023.
  116. Simmonds MC. Food and Drug Administration executive summary for P050036 Medtronic's AMPLIFY™ rhBMP-2 Matrix Orthopaedic and Rehabilitation Devices Advisory Panel. *FDA.* 2010;p.2013.
  117. Zara JN, Siu RK, Zhang X, et al. High doses of bone morphogenetic protein 2 induce structurally abnormal bone and inflammation in vivo. *Tissue Eng Part A.* 2011;17(9-10):1389-1399. doi:10.1089/ten.tea.2010.0555.
  118. Kim JW, Jeong IH, Lee K II, et al. Volumetric bone regenerative efficacy of biphasic calcium phosphate-collagen composite block loaded with rhBMP-2 in vertical bone augmentation model of a rabbit calvarium. *J Biomed Mater Res - Part A.* 2012;100 A(12):3304-3313. doi:10.1002/jbm.a.34278.
  119. Hwang DY, On SW, Song SI. Bone regenerative effect of recombinant human bone morphogenetic protein-2 after cyst enucleation. *Maxillofac Plast Reconstr Surg.* 2016;38(1):22. doi:10.1186/s40902-016-0070-4.
  120. Cho JH, Lee JH, Yeom JS, et al. Efficacy of Escherichia coli-derived recombinant human bone morphogenetic protein-2 in posterolateral lumbar fusion: an open, active-controlled, randomized, multicenter trial. *Spine J.* 2017;17(12):1866-1874. doi:10.1016/j.spinee.2017.06.023.
  121. King WJ, Krebsbach PH. Growth factor delivery : How surface interactions modulate release in vitro and in vivo ☆. *Adv Drug Deliv Rev.* 2012;64(12):1239-1256. doi:10.1016/j.addr.2012.03.004.
  122. El Bialy I, Jiskoot W, Reza Nejadnik M. Formulation, delivery and stability of bone morphogenetic proteins for effective bone regeneration. *Pharm Res.* 2017;34(6):1152-1170. doi:10.1007/s11095-017-2147-x.
  123. Yu X, Suárez-González D, Khalil AS, Murphy WL. How does the pathophysiological context

- influence delivery of bone growth factors? *Adv Drug Deliv Rev.* 2015;84:68-84. doi:10.1016/j.addr.2014.10.010.
124. R&DSystems. Recombinant human BMP-7 protein. [https://www.rndsystems.com/products/recombinant-human-bmp-7-protein\\_354-bp#product\\_datasheets](https://www.rndsystems.com/products/recombinant-human-bmp-7-protein_354-bp#product_datasheets). Published 2018.
  125. Mitu G, Hirschberg R. Bone morphogenetic protein-7 (BMP7) in chronic kidney disease. *Front Biosci.* 2008;13:4726-4739.
  126. Cecchi S, Bennet SJ, Arora M. Bone morphogenetic protein-7: Review of signalling and efficacy in fracture healing. *J Orthop Transl.* 2016;4:28-34. doi:10.1016/j.jot.2015.08.001.
  127. Wei K, Yin Z, Xie Y. Roles of the kidney in the formation, remodeling and repair of bone. *J Nephrol.* 2016;29(3):349-357. doi:10.1007/s40620-016-0284-7.
  128. Reichert JC, Cipitria A, Epari DR, et al. A tissue engineering solution for segmental defect regeneration in load-bearing long bones. *Sci Transl Med.* 2012;4(141):141ra93. doi:10.1126/scitranslmed.3003720.
  129. Ozaki Y, Nishimura M, Sekiya K, et al. Comprehensive analysis of chemotactic factors for bone marrow mesenchymal stem cells. *Stem Cells Dev.* 2007;16(1):119-129. doi:10.1089/scd.2006.0032.
  130. DiGiovanni CW, Lin SS, Baumhauer JF, et al. Recombinant human platelet-derived growth factor-BB and beta-tricalcium phosphate (rhPDGF-BB/ $\beta$ -TCP): An alternative to autogenous bone graft. *JBJS.* 2013;95(13).
  131. DiGiovanni CW, Lin SS, Daniels TR, et al. The importance of sufficient graft material in achieving foot or ankle Fusion. *JBJS.* 2016;98(15).
  132. Arrighi I, Mark S, Alvisi M, von Rechenberg B, Hubbell JA, Schense JC. Bone healing induced by local delivery of an engineered parathyroid hormone prodrug. *Biomaterials.* 2009;30(9):1763-1771. doi:10.1016/j.biomaterials.2008.12.023.
  133. Kuros. KUR-111. Kuros Biosciences. <http://www.kuros.ch/products/orthobiologics/fracture-repair/kur-111.html>.
  134. Fuerst A, Derungs S, Von Rechenberg B, Auer JA, Schense J, Watson J. Use of a parathyroid hormone peptide (PTH1–34)-enriched fibrin hydrogel for the treatment of a subchondral cystic lesion in the proximal interphalangeal joint of a warmblood filly. *J Vet Med Ser A.* 2007;54(2):107-112. doi:10.1111/j.1439-0442.2007.00890.x.
  135. Van der Stok J, Wang H, Amin Yavari S, et al. Enhanced bone regeneration of cortical segmental bone defects using porous titanium scaffolds incorporated with colloidal gelatin gels for time- and dose-controlled delivery of dual growth factors. *Tissue Eng Part A.* 2013;19(23-24):2605-2614. doi:10.1089/ten.tea.2013.0181.
  136. Van der Stok J, Lozano D, Chai YC, et al. Osteostatin-coated porous titanium can improve early bone regeneration of cortical bone defects in rats. *Tissue Eng Part A.* 2015;21(9-10):1495-1506. doi:10.1089/ten.tea.2014.0476.
  137. Van Der Stok J, Koolen MKE, De Maat MPM, et al. Full regeneration of segmental bone defects using porous titanium implants loaded with BMP-2 containing fibrin gels. *Eur Cells Mater.* 2015;29:141-154.
  138. Hess M, Jones RG, Kahovec J, et al. Terminology of polymers containing ionizable or ionic groups and of polymers containing ions (IUPAC Recommendations 2006). *Pure Appl Chem.* 2006;78(11):2067-2074. doi:10.1351/pac200678112067.
  139. Decher G. Fuzzy nanoassemblies: Toward layered polymeric multicomposites. *Science (80- ).* 1997;277(5330):1232-1237. doi:10.1126/science.277.5330.1232.
  140. Guyomard A, Muller G, Glinel K. Buildup of multilayers based on amphiphilic polyelectrolytes. *Macromolecules.* 2005;38(13):5737-5742. doi:10.1021/ma050867n.
  141. Sukhishvili SA, Granick S. Layered, erasable polymer multilayers formed by hydrogen-bonded sequential self-assembly. *Macromolecules.* 2002;35(1):301-310. doi:10.1021/ma011346c.
  142. Wang F, Ma N, Chen Q, Wang W, Wang L. Halogen bonding as a new driving force for layer-by-layer assembly. *Langmuir.* 2007;23(19):9540-9542. doi:10.1021/la701969q.

143. Sukhorukov GB, Donath E, Lichtenfeld H, et al. Layer-by-layer self assembly of polyelectrolytes on colloidal particles. *Colloids Surfaces A Physicochem Eng Asp.* 1998;137(1-3):253-266. doi:10.1016/S0927-7757(98)00213-1.
144. Sukhorukov GB, Möhwald H, Decher G, Lvov YM. Assembly of polyelectrolyte multilayer films by consecutively alternating adsorption of polynucleotides and polycations. *Thin Solid Films.* 1996;284-285(95):220-223. doi:10.1016/S0040-6090(95)08309-X.
145. Boudou T, Crouzier T, Ren K, Blin G, Picart C. Multiple functionalities of polyelectrolyte multilayer films: New biomedical applications. *Adv Mater.* 2010;22(4):441-467. doi:10.1002/adma.200901327.
146. Richert L, Boulmedais F, Lavallo P, et al. Improvement of stability and cell adhesion properties of polyelectrolyte multilayer films by chemical cross-linking. *Biomacromolecules.* 2004;5(2):284-294. doi:10.1021/bm0342281.
147. ThermoFisherScientific. Carbodiimide crosslinker chemistry. <https://www.thermofisher.com/fr/fr/home/life-science/protein-biology/protein-biology-learning-center/protein-biology-resource-library/pierce-protein-methods/carbodiimide-crosslinker-chemistry.html>.
148. Johansson J, Halthur T, Herranen M, Söderberg L, Elofsson U, Hilborn J. Build-up of collagen and hyaluronic acid polyelectrolyte multilayers. *Biomacromolecules.* 2005;6(3):1353-1359. doi:10.1021/bm0493741.
149. Mendelsohn JD, Barrett CJ, Chan V V., Pal AJ, Mayes AM, Rubner MF. Fabrication of microporous thin films from polyelectrolyte multilayers. *Langmuir.* 2000;16(11):5017-5023. doi:10.1021/la000075g.
150. Crouzier T, Ren K, Nicolas C, Roy C, Picart C. Layer-by-layer films as a biomimetic reservoir for rhBMP-2 delivery: Controlled differentiation of myoblasts to osteoblasts. *Small.* 2009;5(5):598-608. doi:10.1002/smll.200800804.
151. Schneider A, Francius G, Obeid R, et al. Polyelectrolyte multilayers with a tunable young's modulus: Influence of film stiffness on cell adhesion. *Langmuir.* 2006;22(3):1193-1200. doi:10.1021/la0521802.
152. Bouyer M, Guillot R, Lavaud J, et al. Surface delivery of tuneable doses of BMP-2 from an adaptable polymeric scaffold induces rapid bone regeneration. *Biomaterials.* 2016;104:168-181. doi:10.1016/j.biomaterials.2016.06.001.
153. Almodóvar J, Guillot R, Monge C, et al. Spatial patterning of BMP-2 and BMP-7 on biopolymeric films and the guidance of muscle cell fate. *Biomaterials.* 2014;35(13):3975-3985. doi:10.1016/j.biomaterials.2014.01.012.
154. Crouzier T, Sailhan F, Becquart P, Guillot R, Logeart-Avramoglou D, Picart C. The performance of BMP-2 loaded TCP/HAP porous ceramics with a polyelectrolyte multilayer film coating. *Biomaterials.* 2011;32(30):7543-7554. doi:10.1016/j.biomaterials.2011.06.062.
155. Guillot R, Gilde F, Becquart P, et al. The stability of BMP loaded polyelectrolyte multilayer coatings on titanium. *Biomaterials.* 2013;34(23):5737-5746. doi:10.1016/j.biomaterials.2013.03.067.
156. Reichert JC, Saifzadeh S, Wullschlegler ME, et al. The challenge of establishing preclinical models for segmental bone defect research. *Biomaterials.* 2009;30(12):2149-2163. doi:10.1016/j.biomaterials.2008.12.050.
157. Li Y, Chen S, Li L, Qin L, Wang X-L, Lai Y-X. Bone defect animal models for testing efficacy of bone substitute biomaterials. *J Orthop Transl.* 2015;3(3):95-104. doi:10.1016/j.jot.2015.05.002.
158. Wancket LM. Animal models for evaluation of bone implants and devices: Comparative bone structure and common model uses. *Vet Pathol.* 2015;52(5):842-850. doi:10.1177/0300985815593124.
159. Peric M, Dumic-Cule I, Grcevic D, et al. The rational use of animal models in the evaluation of novel bone regenerative therapies. *Bone.* 2015;70:73-86. doi:10.1016/j.bone.2014.07.010.
160. Lammens J, Maréchal M, Geris L, et al. Warning about the use of critical-size defects for the



- translational study of bone repair: Analysis of a sheep tibial model. *Tissue Eng Part C Methods*. 2017;23(11):694-699. doi:10.1089/ten.tec.2017.0147.
161. Colquhoun R, Tanner KE. Mechanical behaviour of degradable phosphate glass fibres and composites - A review. *Biomed Mater*. 2015;11(1). doi:10.1088/1748-6041/11/1/014105.
  162. Martino MM, Briquez PS, Maruyama K, Hubbell JA. Extracellular matrix-inspired growth factor delivery systems for bone regeneration. *Adv Drug Deliv Rev*. 2015;94:41-52. doi:10.1016/j.addr.2015.04.007.
  163. Mani G, Feldman MD, Patel D, Agrawal CM. Coronary stents: A materials perspective. *Biomaterials*. 2007;28(9):1689-1710. doi:10.1016/j.biomaterials.2006.11.042.
  164. Ashby M. Designing architected materials. *Scr Mater*. 2013;68(1):4-7. doi:https://doi.org/10.1016/j.scriptamat.2012.04.033.
  165. Arcam AB. Ti6Al4V ELI Titanium Alloy. www.arcam.com.
  166. Suard M. Characterization and optimization of lattice structures made by Electron Beam Melting. *Thesis Univ Grenoble Alpes*. 2015.
  167. Petrovic V, Haro JV, Blasco JR, Portolés L. *Biomedicine*. (Lin C, ed.). InTech; 2012. doi:10.5772/2321.
  168. Parthasarathy J, Starly B, Raman S, Christensen A. Mechanical evaluation of porous titanium (Ti6Al4V) structures with electron beam melting (EBM). *J Mech Behav Biomed Mater*. 2010;3(3):249-259. doi:10.1016/j.jmbbm.2009.10.006.
  169. Arcam AB. EBM Hardware. <http://www.arcam.com/technology/electron-beam-melting/hardware/>.
  170. Suard M, Lhuissier P, Dendievel R, Blandin J-J, Vignat F, Villeneuve F. Towards stiffness prediction of cellular structures made by electron beam melting (EBM). *Powder Metall*. 2014;57(3):190-195. doi:10.1179/1743290114Y.0000000093.
  171. Park JH, Olivares-Navarrete R, Baier RE, et al. Effect of cleaning and sterilization on titanium implant surface properties and cellular response. *Acta Biomater*. 2012;8(5):1966-1975. doi:10.1016/j.actbio.2011.11.026.
  172. Landis EN, Keane DT. X-ray microtomography. *Mater Charact*. 2010;61(12):1305-1316. doi:https://doi.org/10.1016/j.matchar.2010.09.012.
  173. Ketcham R. X-ray Computed Tomography (CT). Montana State University. [https://serc.carleton.edu/msu\\_nanotech/methods/CT.html](https://serc.carleton.edu/msu_nanotech/methods/CT.html).
  174. CMTc. Tomographe EASYTOM. <http://cmtc.grenoble-inp.fr/equipements/tomographe-easytom-xl-nanofoyer-862781.kjsp?RH=1484417245091>.
  175. Suard M, Martin G, Lhuissier P, et al. Mechanical equivalent diameter of single struts for the stiffness prediction of lattice structures produced by Electron Beam Melting. *Addit Manuf*. 2015;8:124-131. doi:10.1016/j.addma.2015.10.002.
  176. Narayan RJ, Kumta PN, Wagner WR. Advances in biomedical and biomimetic materials. In: The American Ceramic Society, ed. *Advances in Biomedical and Biomimetic Materials*. The American Ceramic Society; 2008.
  177. Hyldgaard M, Mygind T, Vad BS, Stenvang M, Otzen DE. The antimicrobial mechanism of action of epsilon-poly-L-lysine. *Appl Environ Microbiol*. 2014;80(24):7758-7770. doi:10.1128/AEM.02204-14.
  178. Ren K, Crouzier T, Roy C, Picart C. Polyelectrolyte multilayer films of controlled stiffness modulate myoblast cell differentiation. *Adv Funct Mater*. 2008;18(9):1378-1389. doi:10.1002/adfm.200701297.
  179. Paul Machillot, Catarina Quintal, Fabien Dalonneau, Loic Hermant PM, Kelsey Matthews, Vincent Fitzpatrick, Jie Liu IP-P, Picart\* and C. Automated buildup of biomimetic films in cell culture microplates for high-throughput screening of cellular behaviors. *Adv Mater*. 2018;30(10):1801097. doi:10.1002/adma.201801097.
  180. Wikipedia. Fluorophore. <https://en.wikipedia.org/wiki/Fluorophore>.
  181. GE. Spectrophotometry Handbook. GE Healthcare Life Sciences.
  182. VisualProtein. Dual-Range™ BCA Protein Assay Kit.

- <http://www.visualprotein.com/vispro/index.php/western-blotting/dualrange-bca-protein-assay-kit>.
183. Leica. Leica Z16 APO A. <https://www.leica-microsystems.com/fr/produits/stereomicroscopes-et-microscopes/macrosopes/informations-detaillees/product/leica-z16-apo-a/gallery/>.
  184. ThermoFisherScientific. Epifluorescence microscope basics. <https://www.thermofisher.com/fr/fr/home/life-science/cell-analysis/cell-analysis-learning-center/molecular-probes-school-of-fluorescence/fundamentals-of-fluorescence-microscopy/epifluorescence-microscope-basics.html>.
  185. Harsh O. Confocal microscopy. Quora. <https://www.quora.com/How-does-confocal-microscopy-work#HDPmR>.
  186. Olympus. Introduction to Confocal Microscopy. <https://www.olympus-lifescience.com/en/microscope-resource/primer/techniques/confocal/confocalintro/>.
  187. Claudionico. Electron interaction with matter. In: *Wikimedia Commons*. [https://commons.wikimedia.org/wiki/File:Electron\\_Interaction\\_with\\_Matter.svg](https://commons.wikimedia.org/wiki/File:Electron_Interaction_with_Matter.svg).
  188. Inkson BJ. Scanning electron microscopy (SEM) and transmission electron microscopy (TEM) for materials characterization. In: *Materials Characterization Using Nondestructive Evaluation (NDE) Methods*. Elsevier; 2016:17-43. doi:10.1016/B978-0-08-100040-3.00002-X.
  189. Arvidson K, Abdallah BM, Applegate LA, et al. Bone regeneration and stem cells. *J Cell Mol Med*. 2011;15(4):718-746. doi:10.1111/j.1582-4934.2010.01224.x.
  190. Diduch, D R; Coe, M R; Joyner, C; Owen, M E; Balian G. Two cell lines from bone marrow that differ in terms of collagen synthesis, osteogenic characteristics, and matrix mineralization. *J Bone Jt Surg*. 1993;American V.
  191. SIB Swiss Institute of Bioinformatic. Cellosaurus D1 ORL UVA (CVCL\_6495). [https://web.expasy.org/cellosaurus/CVCL\\_6495](https://web.expasy.org/cellosaurus/CVCL_6495).
  192. GreinerBioOne. Flask and plates. <https://shop.gbo.com/en/france/products/bioscience/cell-culture-products/cellstar-cell-culture-flasks/>.
  193. Gilde S. Présentation de la BMP-2 par un film biomimétique : structure de la protéine , stabilité à long terme et internalisation cellulaire. *Thesis Univ Grenoble Alpes*. 2014.
  194. Chai YC, Roberts SJ, Bael S Van, et al. Multi-level factorial analysis of Ca<sup>2+</sup> / P<sup>i</sup> supplementation as bio-instructive media for in vitro biomimetic. *Tissue Eng Part C*. 2012;18(2):90-103. doi:10.1089/ten.TEC.2011.0248.
  195. ThermoFisherScientific. CyQUANT Cell proliferation assays. <https://www.thermofisher.com/fr/fr/home/brands/molecular-probes/key-molecular-probes-products/cyquant-cell-proliferation-assays.html>.
  196. Golub EE, Boesze-Battaglia K. The role of alkaline phosphatase in mineralization. *Curr Opin Orthop*. 2007;18(5):444-448. doi:10.1097/BCO.0b013e3282630851.
  197. Info M helfen. Alkaline phosphatase lewis structure. <http://mahnwachen-helfen.info/mmp/c/ch3no-lewis-structure/>.
  198. Sharma U, Pal D, Prasad R. Alkaline phosphatase: An overview. *Indian J Clin Biochem*. 2014;29(3):269-278. doi:10.1007/s12291-013-0408-y.
  199. Guerrero J. Devenir des cellules souches mesenchymateuse humaines dans un environnement tridimensionnel: application à l'ingénierie du tissu osseux. *Thesis Univ Bordeaux*. 2014.
  200. Sigma-Aldrich. Colorimetric alkaline phosphatase and peroxidase substrate detection systems. BioFiles. <https://www.sigmaaldrich.com/technical-documents/articles/biofiles/colorimetric-alkaline.html>. Published 2008.
  201. NPTEL. Enzyme activity. Module 2 : Spectroscopic Methods. <https://nptel.ac.in/courses/102103047/module2/lec12/2.html>.
  202. Bakhshian Nik A, Hutcheson JD, Aikawa E. Extracellular vesicles as mediators of cardiovascular calcification. *Front Cardiovasc Med*. 2017;4. doi:10.3389/fcvm.2017.00078.
  203. An J, Leeuwenburgh S, Wolke J, Jansen J. 4 - Mineralization processes in hard tissue: Bone. In: Aparicio C, Ginebra M-PBT-B and B, eds. *Biomaterialization and Biomaterials*. Boston: Woodhead Publishing; 2016:129-146. doi:<https://doi.org/10.1016/B978-1-78242-338->

- 6.00005-3.
204. Langenbach F, Handschel J, Robey P, et al. Effects of dexamethasone, ascorbic acid and b-glycerophosphate on the osteogenic differentiation of stem cells in vitro. *Stem Cell Res Ther.* 2013;4(5):117. doi:10.1186/scrt328.
  205. Moriguchi T, Yano K, Nakagawa S, Kaji F. Elucidation of adsorption mechanism of bone-staining agent alizarin red S on hydroxyapatite by FT-IR microspectroscopy. *J Colloid Interface Sci.* 2003;260(1):19-25. doi:10.1016/S0021-9797(02)00157-1.
  206. Bobbert FSL, Lietaert K, Eftekhari AA, et al. Additively manufactured metallic porous biomaterials based on minimal surfaces: A unique combination of topological, mechanical, and mass transport properties. *Acta Biomater.* 2017;53:572-584. doi:10.1016/j.actbio.2017.02.024.
  207. Ridzwan MIZ, Shuib S, Hassan AY, Shokri AA, Mohammad Ibrahim MN. Problem of stress shielding and improvement to the hip implant designs: A review. *J Med Sci.* 2007;7(3):460-467. doi:10.3923/jms.2007.460.467.
  208. Papachroni KK, Karatzas DN, Papavassiliou KA, Basdra EK, Papavassiliou AG. Mechanotransduction in osteoblast regulation and bone disease. *Trends Mol Med.* 2009;15(5):208-216. doi:10.1016/j.molmed.2009.03.001.
  209. Goodman SB, Yao Z, Keeney M, Yang F. The future of biologic coatings for orthopaedic implants. *Biomaterials.* 2013;34(13):3174-3183. doi:10.1016/j.biomaterials.2013.01.074.
  210. Lo KW, Ulery BD, Ashe KM, Laurencin CT. Studies of bone morphogenetic protein-based surgical repair ☆. *Adv Drug Deliv Rev.* 2012;64(12):1277-1291. doi:10.1016/j.addr.2012.03.014.
  211. Elmengaard B, Bechtold JE, Søballe K. In vivo study of the effect of RGD treatment on bone ongrowth on press-fit titanium alloy implants. *Biomaterials.* 2005;26(17):3521-3526. doi:10.1016/j.biomaterials.2004.09.039.
  212. Rammelt S, Illert T, Bierbaum S, Scharnweber D, Zwipp H, Schneiders W. Coating of titanium implants with collagen, RGD peptide and chondroitin sulfate. *Biomaterials.* 2006;27(32):5561-5571. doi:10.1016/j.biomaterials.2006.06.034.
  213. Gilde F, Fourel L, Guillot R, et al. Stiffness-dependent cellular internalization of matrix-bound BMP-2 and its relation to Smad and non-Smad signaling. *Acta Biomater.* 2016;46:55-67. doi:10.1016/j.actbio.2016.09.014.
  214. Schneider CA, Rasband WS, Eliceiri KW. NIH Image to ImageJ: 25 years of image analysis. *Nat Methods.* 2012;9(7):671-675. doi:10.1038/nmeth.2089.
  215. Barr T, McNamara AJA, Sándor GKB, Clokie CML, Peel SAF. Comparison of the osteoinductivity of bioimplants containing recombinant human bone morphogenetic proteins 2 (Infuse) and 7 (OP-1). *Oral Surgery, Oral Med Oral Pathol Oral Radiol Endodontology.* 2010;109(4):531-540. doi:10.1016/j.tripleo.2009.10.027.
  216. Lu C, Xing Z, Yu Y, Colnot C, Miclau T, Marcucio RS. Recombinant human bone morphogenetic protein-7 enhances fracture healing in an ischemic environment. *J Orthop Res.* 2010;28(5):687-696. doi:10.1002/jor.21033.
  217. Berner A, Boerckel JD, Saifzadeh S, et al. Biomimetic tubular nanofiber mesh and platelet rich plasma-mediated delivery of BMP-7 for large bone defect regeneration. *Cell Tissue Res.* 2012;347(3):603-612. doi:10.1007/s00441-011-1298-z.
  218. Lee K, Taghavi CE, Murray SS, Song K, Keorochana G, Wang JC. BMP induced inflammation: A comparison of rhBMP-7 and rhBMP-2. *J Orthop Res.* 2012;30(12):1985-1994. doi:10.1002/jor.22160.
  219. Williams JC, Maitra S, Anderson MJ, Christiansen BA, Reddi AH, Lee MA. BMP-7 and bone regeneration: evaluation of dose-response in a rodent segmental defect model. *J Orthop Trauma.* 2015;29(9):e336-41. doi:10.1097/BOT.0000000000000307.
  220. Makino T, Hak DJ, Hazelwood SJ, Curtiss S, Reddi a H. Prevention of atrophic nonunion development by recombinant human bone morphogenetic protein-7. *J Orthop Res.* 2005;23(3):632-638. doi:10.1016/j.orthres.2004.09.009.

221. Parthasarathy J, Starly B, Raman S. A design for the additive manufacture of functionally graded porous structures with tailored mechanical properties for biomedical applications. *J Manuf Process*. 2011;13(2):160-170. doi:10.1016/j.jmapro.2011.01.004.
222. Guillot R, Pignot-Paintrand I, Lavaud J, et al. Assessment of a polyelectrolyte multilayer film coating loaded with BMP-2 on titanium and PEEK implants in the rabbit femoral condyle. *Acta Biomater*. 2016;36:310-322. doi:10.1016/j.actbio.2016.03.010.
223. Kanakaris NK, Calori GM, Verdonk R, et al. Application of BMP-7 to tibial non-unions: A 3-year multicenter experience. *Injury*. 2008;39:S83-S90. doi:10.1016/S0020-1383(08)70019-6.
224. Papanagiotou M, Dailiana ZH, Karachalios T, et al. Heterotopic ossification after the use of recombinant human bone morphogenetic protein-7. *World J Orthop*. 2017;8(1):36-41. doi:10.5312/wjo.v8.i1.36.
225. Madhu V, Li CJ, Dighe AS, Balian G, Cui Q. BMP-non-responsive Sca1+CD73+CD44+ mouse bone marrow derived osteoprogenitor cells respond to combination of VEGF and BMP-6 to display enhanced osteoblastic differentiation and ectopic bone formation. *PLoS One*. 2014;9(7):1-11. doi:10.1371/journal.pone.0103060.
226. Lhuissier P, de Formanoir C, Martin G, Dendievel R, Godet S. Geometrical control of lattice structures produced by EBM through chemical etching: Investigations at the scale of individual struts. *Mater Des*. 2016;110:485-493. doi:10.1016/j.matdes.2016.08.029.
227. Schemitsch EH. Size matters: defining critical size in bone defect. *J Orthop Trauma*. 2017;31(10):S20-S22. doi:10.1097/BOT.0000000000000978.
228. Bidan CM, Kommareddy KP, Rumpler M, et al. How linear tension converts to curvature: Geometric control of bone tissue growth. *PLoS One*. 2012;7(5). doi:10.1371/journal.pone.0036336.
229. Bidan CM, Wang FM, Dunlop JWC. A three-dimensional model for tissue deposition on complex surfaces. *Comput Methods Biomech Biomed Engin*. 2013;16(10):1056-1070. doi:10.1080/10255842.2013.774384.
230. Bolander J, Ji W, Geris L, et al. The combined mechanism of bone morphogenetic protein- and calcium phosphate-induced skeletal tissue formation by human periosteum derived cells. *Eur Cells Mater*. 2016;31:11-25. doi:10.22203/eCM.v031a02.
231. Bolander J, Ji W, Leijten J, et al. Healing of a large long-bone defect through serum-free in vitro priming of human periosteum-derived cells. *Stem Cell Reports*. 2017;8(3):758-772. doi:10.1016/j.stemcr.2017.01.005.
232. Chen G, Deng C, Li YP. TGF- $\beta$  and BMP signaling in osteoblast differentiation and bone formation. *Int J Biol Sci*. 2012;8(2):272-288. doi:10.7150/ijbs.2929.
233. Sinha KM, Zhou X. Genetic and molecular control of osterix in skeletal formation. *J Cell Biochem*. 2013;114(5):975-984. doi:10.1002/jcb.24439.
234. Marom R, Shur I, Solomon R, Benayahu D. Characterization of adhesion and differentiation markers of osteogenic marrow stromal cells. *J Cell Physiol*. 2005;202(1):41-48. doi:10.1002/jcp.20109.
235. Aubin JE. Regulation of osteoblast formation and function. *Rev Endocr Metab Disord*. 2001;2(1):81-94. doi:10.1023/A:1010011209064.
236. Markhoff J, Wieding J, Weissmann V, Pasold J, Jonitz-Heincke A, Bader R. Influence of different three-dimensional open porous titanium scaffold designs on human osteoblasts behavior in static and dynamic cell investigations. *Materials (Basel)*. 2015;8(8):5490-5507. doi:10.3390/ma8085259.

## Curriculum Vitae

### HO-SHUI-LING Antalya

French nationality  
28 rue Alphonse Terray  
38000 GRENOBLE  
antalya.ho@gmail.com/+33665477967

Material Science Engineer, Grenoble INP

PhD in Bioengineering



### Work experiences

<b>3 years (2015-2018)</b>	<b>PhD in Bioengineering: bone regeneration into 3D architected and osteoinductive titanium scaffolds (defence planned on December 5<sup>th</sup> 2018)</b> <i>Grenoble Alpes University UGA COMUE - Grenoble</i> Host laboratories: <i>LMGP : Laboratoire des Matériaux et du Génie Physique - Supervisor : Prof. C.PICART</i> <i>SIMaP : Laboratoire Sciences et Ingénierie des Matériaux et Procédés - Supervisor : Prof. R.DENDIEVEL</i> Research project: 3D scaffolds design and building by additive manufacturing, surface bio functionalization with polyelectrolytes and proteins, in vitro 3D cell culture, structural and biological characterizations <b>Benefits:</b> Strong development in experimental and team work, scientific and non-scientific writing and communication skills
<b>6 months (2015)</b>	<b>Rheological characterization of Sheet Moulding Compounds on manufactured items</b> <i>Research Engineer Training</i> <i>Research &amp; Innovation department – Plastic Omnium, Sainte-Julie (3 months) - Supervisor: M.SAGER</i> <i>Laboratoire sols solides structures et risques – 3SR, Grenoble (3 months) - Supervisor: L.ORGEAS</i> Tasks : Compression moulding manufacturing, density measurement, calcination, X-ray tomography, image analysis <b>Benefits:</b> Experience in a R&D center, work in a corporate environment, achievement of a scientific project
<b>3 months (2014)</b>	<b>Transdifferentiation of endothelial cells to smooth muscle cells in presence of TGF-β1 protein</b> <i>Traning as Assistant Engineer in the frame of the PHC Cai YuanPei (French/Chinese collaborative program)</i> <i>Department of polymer science and engineering – Zhejiang University, China (3 months) – Supervisor: Assistant Prof. K.REN</i> <i>Laboratoire des matériaux et génie physique – LMGP, Grenoble (2 weeks) – Supervisor : Prof. C. PICART</i> Tasks : Polymer films building, human cells culture in situ, image analysis, working with a PhD team <b>Benefits :</b> Discovery of laboratory research and the biomaterial field, experience abroad

### Written scientific communication

<b>In preparation</b>	<b>Osteoinductive coating on architected Ti-6Al-4V implants for bone regeneration (research article)</b> <i>A. Ho-Shui-Ling, A. Arnould, C.Fournier, P. Machillot, M.Suard, P.Lhuissier, M.Bouyer, S.Morand, G.Bettega, R.Dendievel, C.Picart</i> Article in preparation
<b>2018</b>	<b>Bone regeneration strategies: Engineered scaffolds, bioactive molecules and stem cells current stage and future perspectives (review article)</b> <i>A. Ho-Shui-Ling, J. Bolander, L. E. Rustom, A. W. Johnson, F. P. Luyten, C. Picart</i> <i>Biomaterials,180: 143-162, 2018</i>

## Oral scientific communication

- 2017** **Berlin brandenburg school for regenerative therapies (BSRT) symposium**  
**Poster + Audio flash presentation – Berlin, Germany**  
PhD poster presentation, 3 days, November 2017
- 2<sup>nd</sup> BIOMAT Congress**  
**Oral presentation – Ambleteuse, France**  
15min oral presentation, 4 days, June 2017
- 2016** **Biointerfaces International Zurich**  
**Poster presentation – Zurich, Switzerland**  
Team poster presentation, 3 days, August 2016

## Education

- 2012-2015** **Engineering school in Material science – PHELMA (Physics Material Electronic)**  
**Grenoble Institute of Technology PHELMA – Grenoble, France**  
French engineering school ranked in the top 100 of the QS World University Rankings 2016 in Material science
- 2009-2012** **Post-secondary preparatory school in Physics and engineering science**  
**Léon Gontran Damas High-School – French Guiana**  
Intensive classes on physics, mathematics, chemistry and engineering science

## Skills

### Linguistic

**English:** fluent (TOEFL ITP B2 level)

**Spanish:** written and oral comprehension

### IT

**Image processing:** Image J - **Material selection:** CES Selector

**Numerical modelling:** Matlab, Solidworks, Paraview, Magics

### Technical

**Cell culture:** murine mesenchymal stem cells (D1 cell line), murine myoblast cells (C2C12 cell line)

**Additive Manufacturing:** electron beam melting (EBM)

**Microscopy:** scanning electron (SEM), epifluorescence and confocal laser scanning (CLS) microscopies

## Interests

**Science outreach:** “Fête de la science” 2016 LMGP laboratory workshop animation - Liquid Nitrogen workshop animation **Nano@school** 2015 + 2016 – Ninth grade students (troisième) supervision to present laboratory research

**Sport:** Running: 5 to 10 km.

Races: **EKIDEN** 2016 + 2017 – **Run In Lyon** 2016 + 2017 - **ASPARUN** Meylan 2018

**Art practice:** Saxophone – 2 years. Member of “**Fanfar’naque**” brass band – 1<sup>st</sup> price “fanfare” CDMGE 2018 Paris



## Abstract

To date, titanium-based alloys (Ti) remain the most used implantable materials for load-bearing applications. Emerging additive manufacturing techniques such as electron beam melting (EBM) enable to custom-build architected scaffolds of controlled macroporosity. In very difficult clinical situations, potent bioactive signals are needed to boost stem cells: osteoinductive molecules such as bone morphogenetic proteins (BMP-2) are currently used for this purpose. However, one of their limitations is their inappropriate delivery with collagen sponges. Biomimetic surface coatings made of the biopolymers poly(L-lysine) and hyaluronic acid, (PLL/HA) polyelectrolyte films, have recently been engineered as nanoreservoirs for BMP proteins. The aim of this PhD thesis was to develop architected and osteoinductive 3D titanium-based scaffolds as innovative synthetic bone grafts. To this end, we used the EBM additive manufacturing technique to engineer porous scaffolds with cubic unit-cells. Their surface was coated with biomimetic films containing the bone morphogenetic protein 7 (BMP-7). The porosity was well controlled with a difference from CAD models of less than 1%. The osteoinductive capacity of BMP-7 loaded films was assessed using murine mesenchymal stem cells (MSCs) by quantifying their alkaline phosphatase (ALP) expression, which increased in a dose-dependent manner. The coating of the 3D architected scaffolds by the bioactive film was characterized using optical and electron microscopy techniques. Finally, the 3D architected scaffolds coated with BMP-7-loaded films were proved to be osteoinductive at the early stage *in vitro*. Preliminary experiments are currently done to assess their performance in an *in vivo* model of a critical size femoral bone defect in rat.

## Résumé

A l'heure actuelle, les alliages à bases de titane sont les matériaux les plus utilisés en implantologie osseuse. Les procédés émergents de fabrication additive, tel que la fusion par faisceau d'électrons (EBM), permettent de fabriquer des structures architecturées sur-mesure en titane. Dans les cas cliniques difficiles, il est nécessaire de stimuler activement les cellules souches osseuses pour qu'elles produisent de l'os. Les protéines osseuses morphogénétiques (BMP-2, BMP-7) ont cette capacité d'ostéo-induction et sont utilisées en clinique. Cependant, leur délivrance par matrice de collagène est très mal contrôlée. Des revêtements de surface à base de polymères naturels, tels que la poly(L-lysine) et l'acide hyaluronique (PLL/HA), peuvent former des films biomimétiques servant de nanoréservoir pour ces protéines. L'objectif de cette thèse était de développer un implant innovant constitué de structures 3D en titane à la fois architecturées et ostéo-inductrices. Pour cela, des structures 3D poreuses en alliage de titane (Ti-6Al-4V) constituées de cellules cubiques ont été construites par EBM. La porosité a été bien contrôlée avec une différence par rapport aux modèles CAO de moins de 1%. La BMP-7 a été chargée et quantifiée dans les films biomimétiques. La capacité d'ostéo-induction des films a été évaluée avec des cellules souches mésenchymateuses de souris par leur expression de la phosphatase alcaline. L'expression de cette enzyme a augmenté de façon dose-dépendante avec la dose de BMP-7 initialement chargée. Le dépôt du film ostéo-inducteur sur les structures 3D architecturées a été caractérisé par microscopies optique et électronique. Les cellules souches cultivées au sein des structures 3D bioactives se différencient en cellules osseuses démontrant ainsi leur capacité ostéo-inductrice sur le court terme *in vitro*. Des tests préliminaires *in vivo* sont actuellement réalisés pour tester ces structures 3D bioactives dans un modèle fémoral de défaut osseux chez le rat.